REALISATION OF A HOT CARRIER PHOTOVOLTAIC CELL

James Palles-Dimmock

Quantum Photovoltaics Group

Imperial College London

Department of Physics

This dissertation is submitted for the degree of Doctor of Philosophy (PhD)

October 2017

DECLARATION & COPYRIGHT

I hereby declare that the work presented in this document is my own, except where specifically described and referenced in the text. Some of the work described in this thesis has been previously published in first author journal articles of James Dimmock and are referenced in the publications section. The work of others has been acknowledged and list of references provided.

ABSTRACT

The hot carrier solar cell is a heat engine; supplementing or supplanting the photovoltaic action of a traditional solar cell with a thermally driven current, analogous to a thermoelectric device. With this additional channel for energy extraction it is, in principle, possible for these cells to achieve efficiencies up to 85%, since the thermalization loss of high energy carriers is mitigated through their contribution to the heat current. In this thesis, three different hot carrier solar cell concepts are presented and experimentally investigated to probe their efficacy.

Firstly, a hot carrier solar cell structure is presented, in which photogenerated carriers are extracted from a narrow band gap semiconductor to a wider bandgap semiconductor through a double barrier quantum well, providing energy selective extraction through resonant tunnelling. Current-voltage characteristics of this cell are presented along with time-resolved and temperature-dependent photoluminescence data, supporting the conclusion that this cell is operating as a hot carrier cell.

Secondly, the idea of a metallic absorber for a solar cell is proposed, in order to provide ultra-high absorption of light (>99%) in metallic films thinner than 10nm. This idea is realised in two different cells, with silver and chromium absorbers. The absorption of light in the metal film, followed by extraction of heated electrons over a Schottky barrier, is demonstrated.

Thirdly, the combination of these ideas is discussed, and a solar cell with a metallic absorber and selective extraction of heated electrons through resonant tunneling is realised. The current-voltage characteristics of all cells are modelled theoretically, and key signatures are revealed in both experimental and theoretical work showing the extraction of heated carriers.

ACKNOWLEDGEMENTS

I would like to start by thanking Ned Ekins-Daukes for agreeing to take me on after I proposed this project with only a few weeks remaining before the funding proposal was due to the Royal Commission. Ned has been instrumental in the success of this project and it has been a great privilege to be able to work with someone of his experience and with his passion for photovoltaics for three years. I would also like to thank Matthias Kauer at Sharp for suggesting I take up this Industrial Fellowship PhD and being my industrial supervisor throughout. Matthias has been an enormous support throughout my career at Sharp, giving me the freedom to pursue interesting research and providing direction to make sure it is industrially useful.

My thanks are also owed to the Royal Commission for the exhibition of 1851, who agreed to fund this work and to Sharp Laboratories of Europe for allowing me to focus my research slightly more academically for a period of three years while I undertook this PhD.

Two other academics in particular deserve thanks for their important input into this project. Firstly, Huiyun Liu grew all the samples investigated in this project and without his MBE skill and experience, none of this work would be possible. Secondly, Paul Stavrinou was one of the most committed and useful joint-supervisors that one could have. His semiconductor modelling knowledge was particularly important and useful in the discussions of this project.

Finally, I would like to thank my wife Katherine and my wonderful daughters, Lucy and Jemima. Katherine allowed me to spend part of the first night of our honeymoon in Australia interviewing by skype to secure the funding for this PhD, she then continued to support me throughout, during which time we have moved house and had two children. Without her love and support, none of this would have been possible, and whatever was possible would have been a lot less enjoyable.

CONTENTS

LIST OF TABLES

LIST OF FIGURES

ABBREVIATIONS

ΔE	–	*Energy Width*
E_{off}	–	*Energy Offset*
EQE	–	*External Quantum Efficiency*
IPE	–	*Internal Photoemission*
IV	–	*Current-Voltage*
J_{sc}	–	*Short Circuit Current (density)*
LA	–	*Longitudnal Acoustic (Phonon)*
LO	–	*Longitudnal Optical (Phonon)*
k	–	*Imaginary part of the refractive index (extinction coefficient)*
MQW	–	*Multiple Quantum Well*
n	–	*Real part of the refractive index*
PL	–	*Photoluminescence*
QD	–	*Quantum Dot*
QDSL	–	*Quantum Dot Super Lattice*
QW	–	*Quantum Well*
RTD	–	*Resonant Tunnelling Diode*
TDPL	–	*Temperature Dependent Photoluminescence*
T_e	–	*Electron Temperature*
T_s	–	*Semiconductor Temperature*
TMM	–	*Transfer Matrix Method*
TRPL	–	*Time Resolved Photoluminescence*
V_{oc}	–	*Open Circuit Voltage*

PUBLICATIONS &C.

Journal Articles (2014-2016)

[1] J. A. R. Dimmock, S. Day, M. Kauer, K. Smith, and J. Heffernan, "Demonstration of a hot-carrier photovoltaic cell," Prog. Photovolt. Res. Appl., vol. 22, no. 2, pp. 151–160, 2014.

[2] P. N. Taylor, M. A. Schreuder, T. M. Smeeton, A. J. D. Grundy, J. A. R. Dimmock, S. E. Hooper, J. Heffernan, and M. Kauer, "Synthesis of widely tunable and highly luminescent zinc nitride nanocrystals," J. Mater. Chem. C, 2014.

[3] J. A. R. Dimmock, M. Kauer, K. Smith, H. Liu, P. N. Stavrinou, and N. J. Ekins-Daukes, "Optoelectronic characterization of carrier extraction in a hot carrier photovoltaic cell structure," J. Opt., vol. 18, no. 7, p. 74003, 2016.

[4] J.A.R. Dimmock, "Improving the efficiency of solar cells: hot carrier photovoltaics," Eng. Technol. Ref., ISSN 2056-4007, 2016.

Patents (2014-2016: related to Hot Carrier Photovoltaics)

[1] J. A. R. Dimmock, S. Day, M. Kauer, and J. Heffernan, "Energy conversion device with selective contacts," US8975618 B2, granted 10-Mar-2015

[2] J. A. R. Dimmock, M. Kauer, N. J. Ekins-Daukes, and P. N. Stavrinou, "Energy Selective Photodetector," Application 15/269168, granted 10-Feb-2017.

[3] D. Gallardo, J. A. R. Dimmock, M. Kauer, V Bousquet, "Ballistic Carrier Spectral Sensor," Application 15/160417, granted 15-Feb-2017.

Conference Presentations (2014-2016)

[1] J. A. R. Dimmock, S. Day, K. Smith, J. Heffernan, and M. Kauer, "Hot Carrier Solar Cells: Efficiency Limits and Realisation," in Proceedings of the 10th Photovoltaic Science Applications and Technology Conference, Loughborough, UK, 2014.

[2] J. A. R. Dimmock, S. Day, K. Smith, J. Heffernan, and M. Kauer, "A Hot Carrier Photovoltaic Cell by Offset Resonant Tunnelling," in Proceedings of the 40th IEEE Photovoltaic Specialists Conference, Denver, CO, 2014. (invited)

[3] J. A. R. Dimmock, M. Kauer, K. Smith, P. N. Stavrinou, and N. J. Ekins-Daukes, "The Development of a Hot Carrier Photovoltaic Cell," in Conference Record of the 2014 6th World Conference on Photovoltaic Energy Conversion, 2014.

[4] J. A. R. Dimmock, M. Kauer, P. N. Stavrinou, and N. J. Ekins-Daukes, "Metallic Absorbers and the Hot Carrier Photovoltaic Cell," EDISON-19, Salamanca, Spain, 2015

[5] J. A. R. Dimmock, M. Kauer, P. N. Stavrinou, and N. J. Ekins-Daukes, "A metallic hot carrier photovoltaic cell," in Proc. SPIE 9358, Physics, Simulation, and Photonic Engineering of Photovoltaic Devices IV, 2015, p. 935810.

[6] J. A. R. Dimmock, M. Kauer, Alex V. Mellor, P. N. Stavrinou, and N. J. Ekins-Daukes, "Current Voltage Characteristics of a Metallic Structure for a Hot-Carrier Photovoltaic Cell," in Proceedings of the 43rd IEEE Photovoltaic Specialists Conference, Portland, OR, 2016.

[7] J. A. R. Dimmock, M. Kauer, P. N. Stavrinou, and N. J. Ekins-Daukes, "Generating and exploiting hot carriers in a metallic solar cell," High Energy Materials for Photovoltaics Workshop, London, UK, 2016 (invited)

Invited Seminars (2014-2016)

[1] Oklahoma University, Physics Department: "Hot Carrier Solar Cells: Efficiency Limits and Realization", 6th June 2014

[2] Tokyo University, RCAST: "Hot Carrier Solar Cells – Theoretical Requirements and Experimental Demonstration", 28th November 2014

[3] Sheffield University, Low Dimensional Structures & Devices Group: "Hot Carrier Solar Cells", 25th March 2015

[4] London, Royal Commission for the exhibition of 1851: "Realisation of a Hot Carrier Solar Cell", 16th February 2016

Prizes

[1] Best Paper Award, 10th Photovoltaic Science Applications and Technology Conference (PVSAT-10), 2014.

[2] Best Paper Award, Topic area 1: Fundamentals and New Concepts for Future Technologies, 6th World Conference on Photovoltaic Energy Conversion (WCPEC-6), 2014.

[3] Student Poster Award, 19th International Conference on Electron Dynamics in Semiconductors, Optoelectronics and Nanostructures (EDISON-19), 2015

[4] Certificate of Outstanding Contribution in Reviewing – Solar Energy Materials and Solar Cells, Elsevier, September 2015

1 CONTEXT AND CONCEPT

1.1 Motivation

Two driving forces motivate the search for new methods to harness the power of the sun, necessity and curiosity. Pragmatically, it is necessary to transition from a society dependent on non-renewable sources of energy to one that uses the abundant, sustainable, energy that we receive from the sun. Over 78% of worldwide electricity generation is currently from non-renewable sources [1], a situation which is both depleting remaining energy reserves and contributing to global warming through burning fossil fuels. While photovoltaics is the fastest growing source of electricity generation, with more photovoltaic installations in 2014 in the UK than all other sources combined [2], this should not lead to complacency, but rather recognition that this is the result of an impressive research, development, engineering and deployment effort which must be continued.

The second driving force is the curiosity to discover new physics and to better understand how light interacts with materials. The photovoltaic effect has been the subject of fascination and research since Becquerel made his discovery almost 200 years ago [3], however there remains substantial work to do to build upon the existing body of work. New materials, cell designs and concepts are challenging the incumbent methods of energy conversion and revealing new and exciting physics, such as multiple exciton generation and hot carrier extraction.

It is in this context that this work is carried out; to understand the current limitations of solar energy conversion with the aim of improving efficiency and contributing to the understanding of the physics of photovoltaic energy conversion.

1.2 The limitations of first generation PV

Solar cells harness the renewable and virtually unlimited solar resource, significantly reducing humankind's dependence on non-renewable energy sources such as fossil fuels. Photovoltaic cells convert the sun's power into electricity, but with various intrinsic and extrinsic loss mechanisms that are present in the current first generation of cells.

Extrinsic cell losses are, in principle, avoidable. These are familiar mechanisms, like series resistance, for which one can imagine methods, however expensive and contrived, which could reduce them to zero. By contrast, intrinsic losses are those which are unavoidable and would still exist in some hypothetical, perfect, Platonic solar cell, existent only in our imaginations. These intrinsic loss mechanisms have been previously studied in great detail [4] to show the highest efficiency that such a Platonic solar cell could reach is 32.5% under single sun illumination or 42% under maximally concentrated sunlight. While it is beyond the scope of this introduction to explore each of the intrinsic loss mechanisms in detail, it is instructive, for the purpose of motivating and focusing our search for higher efficiency concepts, to understand that the biggest contribution to these losses is from what could be termed "spectral losses". While approximately one third of the sun's power can be converted into useful energy, almost 60% of the light incident on the Platonic cell is wasted because sunlight comprises a broad spectrum of wavelengths, rather than being a single monochromatic source. The remaining ~10% of losses will not be discussed in depth, but Hirst [4] has covered these in great detail, terming them the "Boltzmann" loss, the "Carnot" loss and the "Emission" loss:

- The Boltzmann loss is attributable to the fact that absorption of light occurs from a smaller solid angle than the Kirchoff necessitated re-emission of light from the cell, giving rise to an entropy increase. This loss is actually not so "intrinsic" and can be removed by concentrating the light on the cell, e.g. by a lens, thus increasing the apparent solid angle of the light hitting the cell. This makes the absorption/re-emission balance closer to reversible and reduces the entropy gain.
- The Carnot loss is attributable to the finite temperature of the absorber, thermally smearing the energy of the electrons in this region resulting in non-optimal extraction. This can be reduced by reducing the cell temperature, and is zero at 0K.
- The Emission loss is due to spontaneous emission from a cell, resulting from running the cell under a non-zero bias in order to extract power, and appears truly unavoidable if one wishes to extract power from a cell.

These loss mechanisms will not be addressed in this thesis and it is generally "spectral" losses that are addressed when designing a next generation solar cell.

1.2.1 Spectral losses

The broad spectral nature of sunlight results in a large efficiency penalty (~60%) because a standard solar cell operates as a two level system, with an energy gap (or band gap) separating a mobile (conduction band) and non-mobile (valence band) electron energy level. Light with energy equal to, or in excess of this band gap can be absorbed, promoting an electron to the mobile level for extraction, but any light with an energy below the band gap is not able to be used by the cell. Similarly, because it is a two level system, only the difference in energy between the two levels is able to be exploited. Light with an energy in excess of the band gap is absorbed and contributes to the current, but the extra energy is lost as heat to the rest of the cell in a process termed "thermalisation". These two loss mechanisms, and the broad solar spectrum that gives rise to them, are illustrated in Figure 1-1, with the energy gap plotted at the optimum value of 1.31eV, which results in a maximum efficiency of 32.5% under single-sun illumination.

All incident light which is of too low an energy to be absorbed is shaded in red, and all light which is absorbed, but with a thermalisation loss, is shaded in blue. An illustration of how light with these energies interacts with our two level system is shown below the spectral plot. These energy momentum diagrams in particular show an important feature of the interaction of high energy light with matter, which will be important to overcome. This is the loss of energy of a high-energy electron via a series of discrete steps in which it interacts with the lattice. This process is discussed in more detail in section 1.4.1.

This limit represents a fundamental limit on conversion efficiency. Many commercial groups are approaching this limit, and any further gains are being made subject to a law of diminishing returns, with Sharp [5] and Panasonic [6] achieving efficiencies in excess of 25% in silicon photovoltaic cells and Alta devices of nearly 29% [7] in GaAs. To achieve significantly higher efficiencies it will be necessary to change the way solar cells operate and address their intrinsic loss mechanisms.

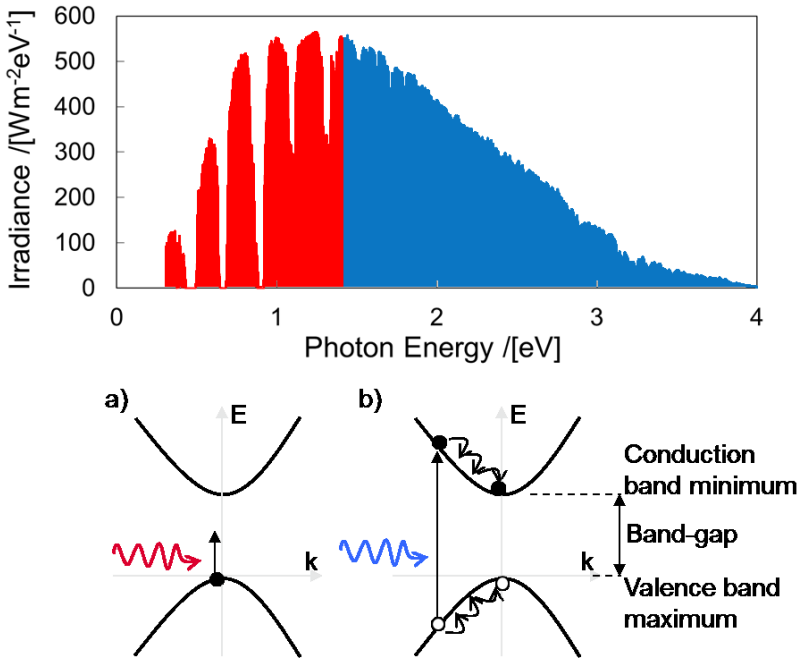

Figure 1-1. Top: Solar Spectrum [8] replotted as a function of photon energy with red/blue indicating unabsorbed/absorbed light incident on a cell with an optimum energy gap of 1.31eV. Bottom: Energy-momentum diagrams for electrons in a semiconductor showing the effect of absorption of light with different energies. a) No absorption of light with energy less than the band gap b) Absorption of light with energy in excess of the band gap followed by energy loss to thermalisation

1.3 Overcoming the first generation limit

Next generation solar cell concepts seek to remove or reduce the intrinsic energy losses already discussed by reformulating how a cell operates. As previously mentioned the largest energy losses are from not absorbing light beneath the band gap and from thermalisation of electrons generated by light with energy in excess of the cell's energy gap.

Figure 1-2 shows how much more efficient a solar cell can be if this thermalisation energy can instead be used in the cell. This is calculated by comparing the "detailed balance" efficiency limit [9], in which power is generated by extracting carriers against a voltage drop (equation 1-1), with a limit based on extracting hot carriers against a thermal drop (equation 1-2) to give the thermodynamic limit of a heat engine trying to extract power under the same conditions.

$$\eta(E_g,V)=\frac{q\left[2\pi\sin^2\theta\int_{E_g}^{\infty}\frac{E^2}{e^{E/k_BT_h}-1}dE-2\pi\int_{E_g}^{\infty}\frac{E^2}{e^{(E-qV)/k_BT_c}-1}dE\right].V}{2\pi\sin^2\theta\int_{0}^{\infty}\frac{E^3}{e^{E/k_BT_h}-1}dE} \quad (1\text{-}1)$$

$$\eta(E_g,T_c)=\frac{\left[2\pi\sin^2\theta\int_{E_g}^{\infty}\frac{E^3}{e^{E/k_BT_h}-1}dE-2\pi\int_{E_g}^{\infty}\frac{E^3}{e^{E/k_BT_c}-1}dE+\dot{Q}(T_c)\right].\left(1-\frac{T_a}{T_c}\right)}{2\pi\sin^2\theta\int_{0}^{\infty}\frac{E^3}{e^{E/k_BT_h}-1}dE} \quad (1\text{-}2)$$

These equations are explained more fully in appendix 1, but essentially equation 1-1 models a cell in which absorption and emission of light are balanced to give a net current, which is multiplied by an applied voltage to give an extracted power. This equation assumes that the electrons are extracted at one particular energy and that they are extracted at ambient temperature (i.e. incorporating thermalisation losses). Equation 1-2 models a cell in which the extraction of electrons happens over the range of energies at which they are photo-generated, modelling the case for which there is no thermalisation loss when the cooling term *(Q)* is equal to zero. To determine the maximum efficiency for each band gap (E_g), in equation 1-1 the efficiency is maximised as a function of applied voltage and in equation 1-2 the efficiency is maximised as a function of the carrier temperature (for a fixed ambient temperature).

In Figure 1-2 the efficiency of a cell under maximally concentrated solar illumination is plotted against the cell's energy gap; using maximum concentration for this comparison removes any impact of the previously discussed Boltzmann loss. The maximum efficiency of 42% for a single junction cell is achieved at a band gap which balances the low energy non-absorption loss with the high energy thermalisation loss. However, if the thermalisation loss could be circumvented, then the optimum energy gap would be zero, there would be no non-absorption loss, and an efficiency of 85% could, in principle, be achieved if we found some new way to exploit absorption in a material with no energy gap. This efficiency is the same as that calculated for a monochromatic beam under the same conditions [10], and shows how important the spectral losses are in a solar cell.

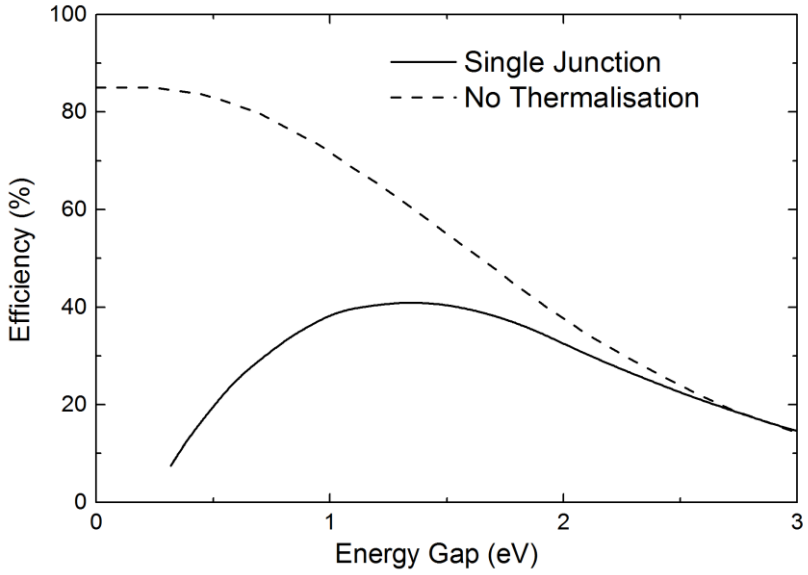

Figure 1-2. A comparison of the limiting efficiency as a function of band gap for a standard single junction solar cell (solid) with the efficiency of cell without thermalisation losses (dashed)

Fundamentally, all next generation photovoltaic concepts are methods to solve this issue and seek to either minimize or use this extra thermalisation energy rather than waste it. The most prominent next generation concepts are briefly discussed in the following subsections and separate into two categories. Those which seek to minimize the extra energy given to the electrons on absorption, such as the multi-junction and intermediate band solar cells, and those which seek to exploit the extra energy given to the electrons, such as the multiple-exciton generating and hot carrier solar cells.

1.3.1 Multi-junction solar cells

The most successful next generation concept in photovoltaics to date has been the multijunction solar cell. This addresses the thermalisation loss by splitting the cell into a multitude of sub-cells, with the intention that light of different wavelengths is absorbed in the sub-cell most closely matched to it in energy. This reduces the thermalisation loss by effectively narrowing the spectrum of light for which each sub-cell is optimized. In the limit of an infinite number of sub-cells this technology has an efficiency limit of 85% and in practice efficiencies of up to 46% [11] have been achieved by splitting light absorption over four sub-cells. Such technology finds a place in satellites and also terrestrially in concentrator photovoltaic (CPV) systems. However, price is still an issue with this technology, in order to compete with Silicon, and efficiency gains have slowed due to the

complications associated with stacking or growing multiple single junction cells on top of one another.

1.3.2 Intermediate band solar cell

A related concept to the multijunction solar cell is the intermediate band solar cell (IBSC), in which a third level is introduced into the energy gap of the previous two level system. In this way the energy gap can be widened and the intermediate energy level acts as a stepping stone for absorption of lower energy light, allowing it to contribute to the current. With a single intermediate level the efficiency of a solar cell could increase to 63.2% [12] and in the case of infinitely many intermediate bands the limit is again 85% [13].

In practice the intermediate band cell has proven difficult to achieve, essentially due to reciprocity; any intermediate states which absorb light necessarily emit light. This means that adding such a state needs to be carried out exceptionally carefully unless it is to be a net detriment to the cell and act as a way for electrons to be removed from the conduction band. One possible method has been proposed to overcome this by inserting a non-radiative "ratchet" state in addition to the intermediate energy level [14], though this work is at an early stage.

1.3.3 Multiple exciton generation

It has been noticed that in some materials, rather than the excess energy generated by high energy light being lost to thermalisation it can instead be used to generate further electrons via so-called multiple exciton generation (MEG). The extra electrons provide extra current in the cell under higher energy illumination and can increase the efficiency from 32% to 42% [15] under single-sun illumination. While not as high an efficiency increase as the previous methods, the idea of simply using a different material and generating more current is appealing. In common materials this process has been found to be generally of low efficiency with only a 5% efficiency gain in Silicon when illuminated at 4eV although with possibly higher efficiencies in quantum dots [16]. A similar process exists in molecular chromophores, singlet fission, whereby two triplet states are formed following the decay of a singlet state [17] allowing a similar multiplication of charge carriers.

1.3.4 Hot carrier solar cell

Our chosen method to address the thermalisation loss is perhaps the most direct and involves directly using the hot carriers in something more like a heat engine than a solar cell, and will be briefly described in this section. Prior to thermalisation with the lattice the electrons in the conduction band of the prototypical two level system have an energy in excess of the conduction band minimum, which in a first generation cell is lost as heat. The distribution of energies present in this electron system is akin to the distribution of energies present in a population of gas molecules and analogously it can be represented by a characteristic temperature, which defines the distribution. The temperature of these electrons can be thousands of Kelvin, and significantly higher than the lattice temperature of the cell, which is defined by the spread of energies of the phonons in the system, hence the term hot carriers. In the hot carrier solar cell, this higher temperature of electrons is directly used by setting up a heat engine between a hot part of the cell, where light absorption takes place, and a cold part of the cell, which is held at ambient temperature.

To further understand the concept it is useful to compare the hot carrier cell with the thermophotovoltaic (TPV) system [18], another next generation concept which addresses the thermalisation loss, with both concepts schematically illustrated in Figure 1-3.

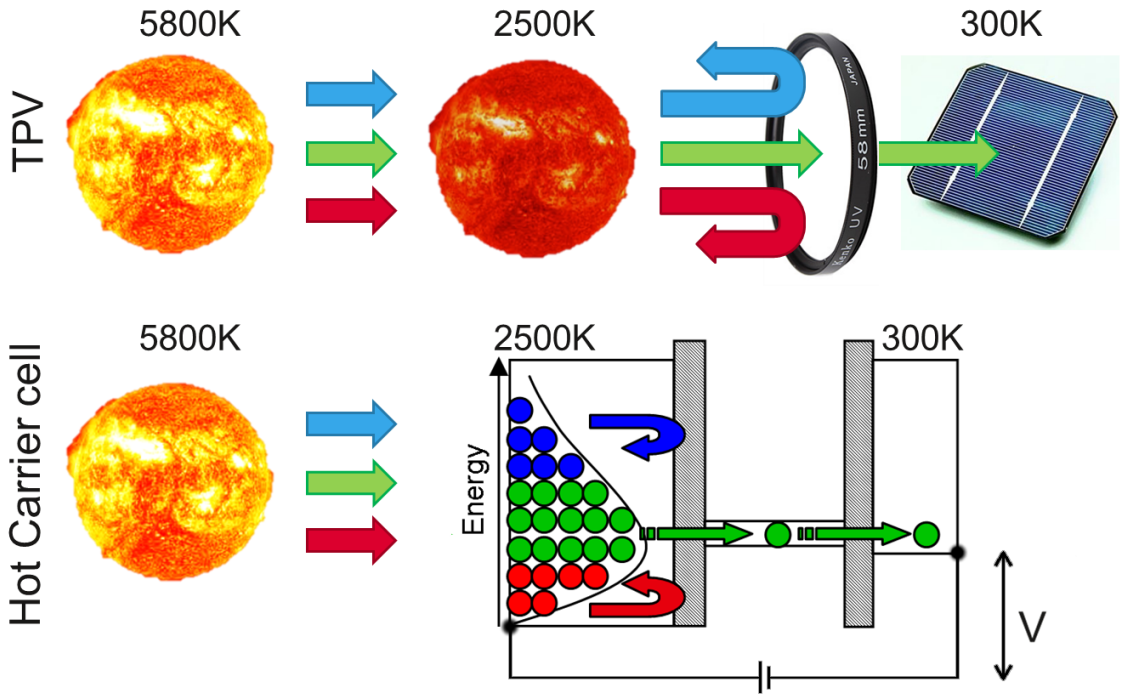

Figure 1-3. Comparison of the working scheme of a thermophotovoltaic (TPV) setup (top) with a hot carrier solar cell (bottom)

In a TPV system light from the sun is absorbed by an intermediate body, causing it to heat up and radiate. The radiation from the intermediate body is filtered such that only light optimally matched to the band gap of an adjacent solar cell is allowed to pass to it. The rest of the radiation is reflected back to the intermediate body and reheats it. This scheme has an efficiency limit of 85% as well [19], since it deals comprehensively with the thermalisation loss in the cell. However, to reach this efficiency limit it presents several complex engineering challenges, not least to find an intermediate body and a filtering mechanism which can both withstand temperatures up to 2500K and avoid any other heat losses such as to convection.

The hot carrier solar cell is similar to the TPV system, but instead of holding this energy as a lattice temperature it is held as an electron temperature after absorption of light from the sun. Electrons at an optimum energy are then allowed to leave this absorption region to a cooler region, while electrons at non-optimum energies are reflected back to re-heat the rest of the electrons and re-populate the optimum energy level. In this way it was shown as long ago as 1982 that this concept could reach 85% efficiency too [20].

1.3.4.1 The hot carrier solar cell in the literature

Building on the initial conceptual work by Ross and Nozik [20], Würfel refined the idea to demonstrate the necessity of relaxing the constraint of particle conservation [21]. We explore this requirement and how it can be physically implemented in section 4.1 through impact ionisation in systems with a very high electron density (e.g. metals).

This initial conceptual work has been extended by a number of groups to theoretically assess the loss mechanisms and give a more realistic limiting efficiency of such cells [22]–[24]. We evaluate the loss mechanisms and limiting efficiency of hot carrier cells, in the context of previous work, in the following sections 1.4 and 1.5, building towards a list of requirements in section 1.6 with reference to other such lists in the literature [25].

Experimental work on hot carrier photovoltaics has generally been focused on addressing individual items from this list of requirements, such as achieving slowed electron cooling rates in quantum wells [26], [27]. We shall discuss this prior experimental work in the introductory section 1.5.2.3 and further in section 2.1.1.

It is the aim of this work to use our own and others' theoretical assessments, lists of requirements and experimental verifications to construct a device which demonstrates the exploitation of hot carriers in a photovoltaic cell.

1.4 The requirements for a hot carrier solar cell

The previous sections reveal the gains that can be made if the thermalisation loss can be avoided; however, first we must understand how this energy is lost before understanding how it might be circumvented. This requires us to understand two features of any such system, how the electron energy is lost, which is covered in section 1.4.1, and how the electrons should be extracted after photogeneration, which is covered in section 1.4.2.

1.4.1 Thermalisation

Until this point the thermalisation energy loss has been treated as a numerical parameter which affects the efficiency of the cell but was ascribed no particular physical mechanism. However, in order to overcome this loss, it is important to understand how it occurs and the speed at which it occurs.

The cooling rate of hot electrons in semiconductor structures is dependent on the interaction between electrons and phonon modes, in particular longitudinal optical (LO) phonons. Hot electrons initially lose energy to LO phonons on a timescale of 165fs in GaAs [28], however these lattice modes cannot directly dissipate energy as they are defined by standing wave oscillations. Without dissipation of energy from these modes, they would re-scatter with the electron distribution and a hot LO phonon and hot electron distribution would result, without any irreversible energy "loss".

The main dissipation mechanism for these LO modes (the Klemen's mechanism [29]) is through the decay of a single LO phonon into two longitudinal acoustic (LA) phonons, which are travelling modes and so can dissipate energy, resulting in lattice heating. The timescale for this interaction is 8ps for GaAs at 10K [30], but gets faster as temperature increases, due to the increase in acoustic phonon modes, to 7ps at 77K [31] and 4ps at 300K [32]. It is this mechanism which gives the effective "cooling rate" of electrons in semiconductors and has become the focus of several experimental groups investigating hot carrier cells. Their aim is to frustrate the Klemen's mechanism, either through choosing materials with a high anion/cation mass disparity such as HfN [33] or InGaN[34], or through careful heterostructure design [35] (e.g. of quantum wells) which might act to "reflect" LA phonons, effectively turning them into stationary modes. In this way several groups have observed a reduction in the electron cooling rate in quantum wells compared with bulk [26], [27], [36] which has recently resulted in the observation of a hot carrier photocurrent observed from a quantum well [37]. However, whether this is strictly caused

by a frustration of phonon decay or a reduction in electron density of states is still debatable, and perhaps our calculations in the following section 1.5.2 reveal more about this. Furthermore, even with frustration of the Klemen's mechanism other decay paths for hot electrons can be as important, for which a full density functional theory analysis of the decay modes might be required [22].

1.4.2 Electron extraction

An important feature of the hot carrier solar cell is not just that the absolute cooling rate of hot electrons in the absorber region should be below some critical threshold, but that this rate of cooling should be slower than the rate at which the electrons are extracted from this region. In this way, the extra energy in the electron distribution can be extracted prior to its irreversible loss through thermalisation with the lattice.

Continuing the comparison with a TPV cell, it is also necessary that the electrons are extracted in an energy selective way. They must be extracted over a narrow range of energies in what is generally termed an energy selective contact [38]. This narrow range is necessarily in excess of the minimum electron energy in order to provide some increase in the operating voltage of the device; however, it is also necessary to stop high-energy electrons from leaving the region of photogeneration through this contact. Stopping high-energy electrons from leaving the device allows for the redistribution of their energy to the lower energy electrons and stops this energy being wasted by thermalisation in the contact. This point is made clearer in section 1.5.3, in which we calculate the optimum values for these energy selectivity parameters.

However, it is not only the extraction speed and energy selectivity parameters which are important, it is also the properties of the electron-electron interaction in the absorber region which contribute to an operational hot carrier cell. In a TPV cell, the energy is re-used after reflection from the wavelength selective filter by re-heating the emitter. The redistribution of energy through lattice vibrations in the TPV case is performed analogously by electron-electron scattering in the hot carrier photovoltaic cell.

A method to achieve these extraction requirements is proposed in the following section (1.5), and the impact of varying the parameters of this extraction and further discussion of them is presented in section 1.5.3.

1.5 Concept

Based on the arguments of the previous section, previously presented in [39], for a device to function as a hot carrier photovoltaic cell the structure needs to meet two key criteria:

1. Minimise the loss of energy from photo-generated electrons to the lattice in the absorber.
2. Maintain photo-generated electrons in the absorber at a different temperature to the rest of the cell, while allowing them to be extracted.

These two fundamental criteria are at the foundation of any attempt to create a hot carrier solar cell; showing that in order to realize a hot-carrier cell we need not only an energy selective filter but also the extraction of hot carriers from one region of the cell and the formation of a thermalised distribution in another without losing the thermalisation energy to the lattice.

In the thermophotovoltaic structure this is achieved by having an optical filter and the band gap of the receiving cell energetically aligned. To achieve this in the hot carrier cell we have proposed [40] a solar cell structure using the concept of 'offset' resonant tunnelling, in which photo-generated carriers tunnel from a narrow band gap semiconductor to a wider band gap semiconductor, as shown in Figure 1-4.

The schematic illustration in Figure 1-4 demonstrates structural and material requirements sufficient to achieve the two criteria above. In this approach to hot carrier extraction, carriers are photo-generated in an absorber region, followed by fast, energy selective extraction through tunnelling to a collector region. In this cell the energy selectivity is only in the conduction band, a simplification on the standard picture of a hot carrier solar cell [20] in which energy selective contacts are present for both the valence and conduction bands. This simplification is proposed for two reasons:

1. The excess energy distribution to the electron (ΔE_e) upon photogeneration of an electron-hole pair depends on their relative masses (m_e and m_h) according to $\Delta E_e = \frac{(E_\gamma - E_g)}{1+{}^{m_e}/_{m_h}}$ (by a conservation of energy and momentum argument, with E_γ the photon energy and E_g the band gap). In the materials investigated, hole masses are generally substantially bigger than electron masses, resulting in a lot more energy being given to the hot electron distribution (e.g. for GaAs, 88% of the extra photon energy in excess of the band gap is given to the electron distribution).

2. In the vast majority of cases, and certainly in the materials of interest in this investigation, the hole cooling rate is significantly faster than the electron cooling rate [41], essentially attributable to the hole's much higher density of states mass.

These two factors mean that the hole temperature can be assumed to be at ambient temperature, while fast extraction is only necessary from the hotter electron distribution.

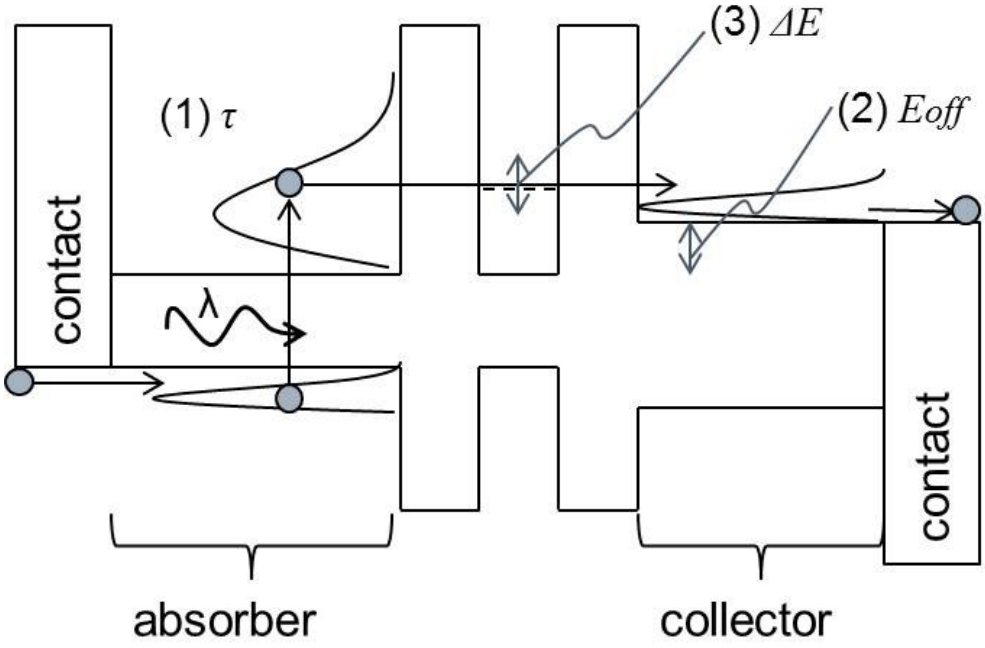

Figure 1-4. The schematic band structure and mode of operation of the hot carrier offset tunnelling cell from [40], showing important features necessary to realise hot carrier extraction and exploitation

Three features which are key to achieving a hot carrier solar cell are highlighted in Figure 1-4, the slowed electron thermalisation rate (τ), an energy offset (E_{off}) and energy filtering (ΔE). These are described in the following subsections and explored more thoroughly in the following sections 1.5.2 and 1.5.3.

1.5.1.1 Thermalisation rate (τ)

To meet criterion 1, the thermalisation rate of photo-generated electrons in the absorber must be slower than the rate of their extraction. Significant theoretical and experimental work has been carried out in this area, as previously addressed in section 1.4.1 and is the focus of most groups active in the hot carrier photovoltaics field. The offset tunnelling structure that we propose approaches this in a different way, rather than slow the cooling it increases the rate of extraction. By extracting electrons quickly through tunnelling, the rate

of electron energy loss to the lattice is minimized. This is not an alternative method, but rather complementary, and a material with a reduced thermalisation rate would simply be an additive benefit to our proposed structure. We will summarise the impact of the thermalisation rate on hot carrier solar cell efficiency in section 1.5.2.

1.5.1.2 Energy offset (E_{off})

An energy offset in the conduction band between the absorber and collector addresses criteria 1 and 2. By introducing an energy offset, electrons can be extracted from energies in excess of the conduction band minimum of the absorber without losing energy in the collector following selective tunnelling. Optimisation of this offset will depend on the temperature of the electron distribution and will be explored further in section 1.5.3.2.

1.5.1.3 Energy filtering (ΔE)

Energy filtering of extracted electrons addresses criterion 2. In order to maintain different electron temperatures in two different regions of the cell it is necessary to only allow the two populations to interact over a narrow range of energies, otherwise both populations will reach an equilibrium at the same temperature, causing irreversible energy loss. The wider the energy filter the more the populations will interact and the larger this energy loss will be. The effect of the width of the energy filter on efficiency is explored through a theoretical analysis in section 1.5.3.1.

1.5.2 Modelling the impact of thermalisation

1.5.2.1 A hot carrier cell with no electron thermalisation

Using equation 1-2, we previously showed that the maximum theoretical efficiency for a hot carrier cell was 85%, this was carried out by varying the carrier temperature (T_c) to maximise the efficiency for a given absorber energy gap (E_g), which was plotted in Figure 1-2. To identify the impact that carrier temperature has on efficiency we can instead choose an optimum (zero) band gap absorber and plot the efficiency of such a cell as the carrier temperature is varied. This is plotted in Figure 1-5, in which we can also see the impact that concentrating the incident light has on optimum temperature and cell efficiency.

For the hot carrier solar cell increasing the carrier temperature is equivalent to (and controlled by) raising the applied bias on the cell. I.e. at the V_{oc} point for a hot carrier solar cell operating under maximum concentration we should expect a carrier temperature equal to the solar temperature, similarly at the J_{sc} point we should expect a carrier temperature

equal to ambient. These effects are seen at the points at which the efficiency as a function of temperature goes to zero in Figure 1-5.

The lower efficiency under one-sun illumination compared with full concentration is a manifestation of the Boltzmann loss, already discussed in section 1.2. The smaller solid angle of solar influx, for the same solid angle of emission, also results in a lower temperature at the point where incoming and outgoing radiation are balanced (V_{oc}).

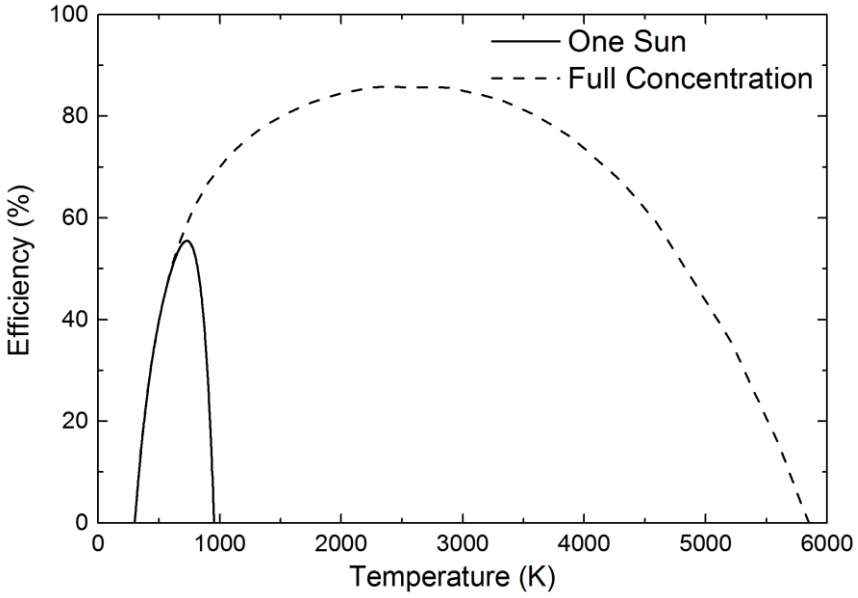

Figure 1-5. The efficiency of a hot carrier cell as a function of the electron temperature in the absorber region under single sun (solid) and full concentration (dashed) illumination.

The results presented in Figure 1-5, with no impact from electron thermalisation, can be compared with results for a real material, in which we include realistic values of electron cooling and a non-zero band gap. These cooling rate values ($\dot{Q}$) are calculated as a function of electron temperature, then inserted into equation 1-2. Our method for calculating this cooling rate is outlined below, and detailed in appendix 3.

Marti has presented calculations for the cooling rate of electrons due to electron-phonon interactions for a for 3D electron phonon interaction [24]. We extended this work to the 2D case to compare electron cooling rates between 2D and 3D absorbers based on acoustic phonons (so this treatment is only strictly valid for non-polar semiconductors, but gives a good start for comparing the electron cooling rates based only on dimensionality).

1.5.2.2 Summary of the cooling rate calculation

Fermi's Golden rule is used to calculate the transition rate between states:

$$S(\underline{p},\underline{p}') = \tfrac{2\pi}{\hbar}\left|H_{\underline{p},\underline{p}'}\right|^2 \delta\left(E(\underline{p}) - E(\underline{p}') - \Delta E\right) \tag{1-3}$$

Where S is the transition rate between states with momentum $\underline{p}$ and $\underline{p}'$ separated by an energy ΔE. $H_{p,p'}$ is the matrix element joining the two states through their interaction via a potential U:

$$H_{\underline{p},\underline{p}'} = \left\langle \psi_{\underline{p}} \left| \hat{U} \right| \psi_{\underline{p}'} \right\rangle \tag{1-4}$$

It is through this matrix element, and the electron states $\psi_{\underline{p}}$ that the dimensionality of the electrons presents itself and affects the scattering rate.

The transfer of energy to a state $\underline{k}$ ($W(\underline{k})$) is then given by integrating the transfer rate (1-3) over all states $\underline{k}'$ to which and from which energy can be transferred to/from state $\underline{k}$ (multiplied by the amount of energy transferred ($n\hbar\omega$) and the occupation numbers of initial and final states $f(\underline{k})$:

$$W(\underline{k}) = \frac{2}{8\pi^3}\hbar\omega\left\{\begin{array}{l}\int\left[S^-(\underline{k},\underline{k}')nf(\underline{k})(1-f(\underline{k}')) - S^-(\underline{k},\underline{k}')(n+1)f(\underline{k}')(1-f(\underline{k}))\right]d^3\underline{k}' - \\ \int\left[S^+(\underline{k},\underline{k}')(n+1)f(\underline{k})(1-f(\underline{k}')) - S^+(\underline{k},\underline{k}')nf(\underline{k}')(1-f(\underline{k}))\right]d^3\underline{k}'\end{array}\right\} \tag{1-5}$$

Integrating this transfer of energy over all $\underline{k}$ and multiplying by the number of degenerate valleys (Z) between which scattering takes place yields the cooling rate (equation 1-6) which is used in equation 1-2 to calculate the efficiency of a hot carrier cell in which electrons cool through 2D interactions.

$$\dot{Q} = Z(Z-1)\frac{D_i^2 k_B T_a m_e^2 (2+\delta_{fi})\Omega}{2\pi\hbar^3\rho w^2(\hbar\omega)}\left\{\begin{array}{l}n\int f(E)(1-f(E+\hbar\omega)dE - (n+1)\int f(E+\hbar\omega)(1-f(E)dE \\ -(n+1)\int f(E)(1-f(E-\hbar\omega)dE + n\int f(E-\hbar\omega)(1-f(E)dE\end{array}\right\} \tag{1-6}$$

A similar equation exists for the 3D interaction; this along with a more thorough derivation of the cooling rate can be found in appendix 3.

1.5.2.3 A hot carrier cell with 2D and 3D electron thermalisation

Figure 1-6 presents the efficiency of a hypothetical absorber based on Silicon as a function of electron temperature, with illumination at full concentration. The dashed line of Figure 1-6 presents the efficiency as a function of electron temperature for the case where there are still no electron-phonon interactions. The efficiency maximum is reduced to 68.7%, in comparison with the 85% maximum in Figure 1-5 due to the higher (than zero) band gap

leading to lower absorption. This lower absorption results in a lower optimum operating temperature.

The red and blue lines in Figure 1-6 reveal the impact of putting in calculated values for the electron cooling rate for the case of 2D and 3D electrons as the $\dot{Q}$ value in equation 1-2. These are calculated in appendix 3 and are based on evaluating Fermi's golden rule for transitions between two electron energy states, in one case the states are bulk-like plane waves and in the other case the states are sinusoidal functions. The sample thickness used in both calculations is 10nm, so this gives the impact of quantising the electron modes in the structure versus using plane wave modes. The result of including electron cooling in the structure is to dramatically lower the optimum electron temperature and also to lower efficiency, to a maximum of 43% and 50% for the 3D and 2D cases respectively. An important feature to notice is that while this is a large decrease in efficiency from the theoretical maximum, this shows that an increase in efficiency over a standard first generation solar cell can be achieved in a readily available material if we can operate the cell as an electron heat engine.

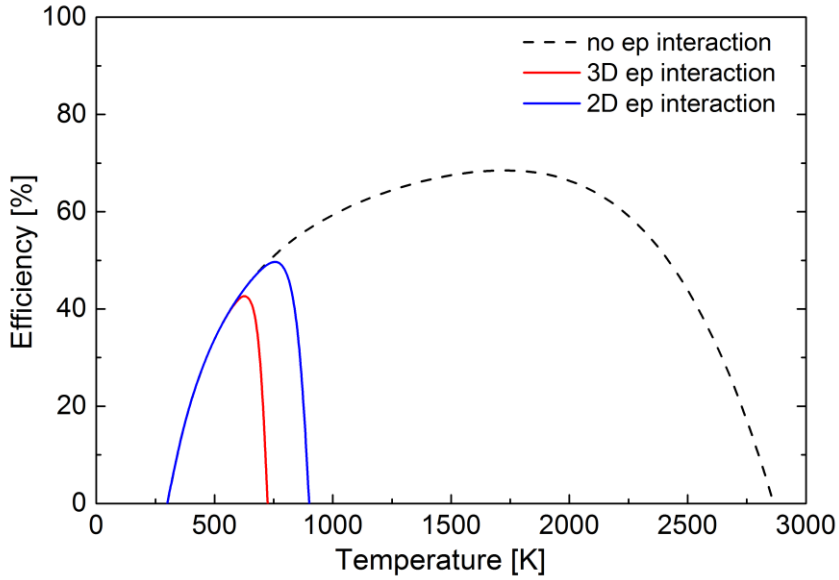

Figure 1-6. The modelled efficiency as a function of electron temperature for a hot carrier solar cell, illuminated at full concentration, with a Silicon absorber with no electron-phonon (ep) interaction to cool the electrons (dashed line), ep interactions in a 3D structure (red line) and ep interactions in a 2D structure.

The results from this theoretical work show the same trend as the experimental work mentioned in section 1.4.1, which found that lower cooling rates are observed in 2D materials than 3D materials, and consequently higher efficiencies are possible. In particular,

the scattering times (from the Fermi's golden rule calculation) that we calculate for a 2D material are 2 orders of magnitude higher than for a 3D material, as plotted in Figure 1-7. This is the same order of magnitude increase that has been observed in the literature [26] and has been reproduced for convenience as Figure 1-8.

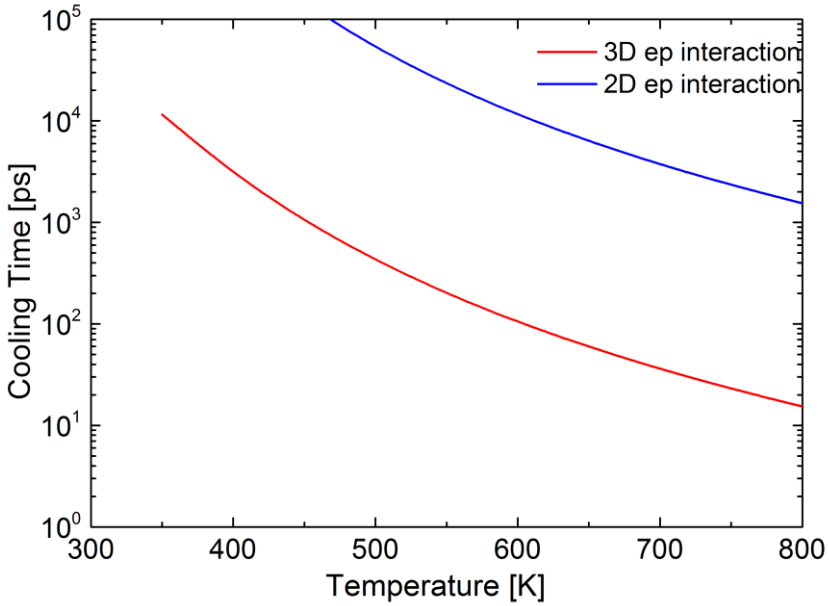

Figure 1-7. The modelled cooling time for the case of a 2D and 3D ep interaction in a 10nm slab of Silicon as modelled using the results of appendix 3.

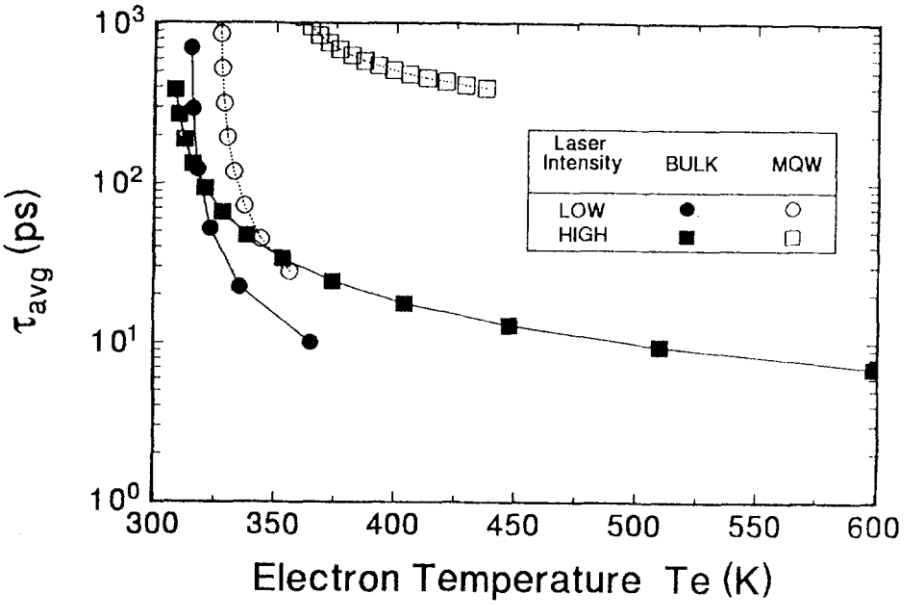

Figure 1-8. The time constant for hot electron cooling vs electron temperature for bulk GaAs and GaAs MQW's at high and low excitation intensities (from [26])

The qualitative comparison of Figure 1-7 and Figure 1-8 is remarkably good, given the simple input parameters. Both show a dramatic decrease in cooling time as electron temperature increases, and both show a ~100x lower cooling time for the 3D electron states when generated with "high" laser intensity (corresponding to a photogenerated electron density of ~$3x10^{18}cm^{-3}$ compared with $3x10^{17}cm^{-3}$ in the "low" intensity case). In the theoretical model this cannot be anything to do with a change in phonon modes, or the nature of the ep interaction, as both are modelled identically in the 2D and 3D case. Ridley has investigated this previously [42] and shown only a 10-20% decrease in the energy loss from hot electrons from quantising the phonon modes. This agrees with the data for "low" illumination intensity in Figure 1-8 (circles), but is significantly lower than the experimentally observed difference for high illumination intensity (squares), implying a larger contribution from the quantisation of electron modes under these conditions. That is, a reduced density of electron states for the 2D electron case means that electron state filling occurs more readily under high intensity illumination conditions, which gives rise to a reduction in available states to which electrons can scatter, which results in a significant increase in the thermalisation time when compared with a system with 3D electron states.

The only thing that changes in our analysis is the electron modes and consequently their density of states. The quantisation of the electron states results in a reduction in their density of states, resulting in a lower number of states for hot electrons to scatter to, as schematically illustrated in Figure 1-9 in which the density of states is plotted for a 10nm slab of material with either quantised or continuous electron states (2D or 3D). The difference between the cumulative density of states up to a certain energy level is shown as the right chart of Figure 1-9, more clearly showing the lower number of potential states to which a 2D electron of a given energy could scatter.

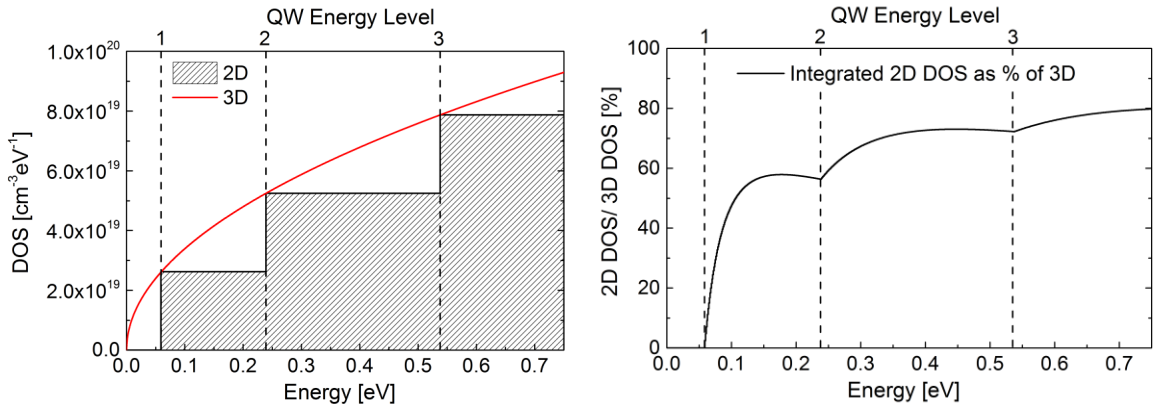

Figure 1-9. Left: Density of states per unit volume and energy for a 3D semiconductor (red line) and a 10nm quantum well (black line and shaded region). Right: Integrated 2D density of states as a percentage of the integrated 3D density of states to a particular energy.

Equation 1-7 presents the value of this cumulative density of states in 2D divided by the value in 3D at the bottom of each quantum well sub-band (calculated in appendix 3 [eq A3-18]) and is instructive to further illustrate the difference in the density of states in the 2D and 3D case.

$$\frac{g_c^{2D}}{g_c^{3D}} = \frac{(4N+1).(N-1)}{4N^2} \tag{1-7}$$

N in this case is the highest sub-band of the well which can be filled by illumination with an incident light source $\left[N = \sqrt{\frac{8m^*c}{h\lambda}}w\right]$, so increasing N in this equation can either be viewed as making the well wider (w) or illuminating with a shorter wavelength of light (λ).

So as N→∞ (shorter wavelengths or wider wells) the difference between the scattering rates should disappear as the cumulative density of states in 2D and 3D is identical, but as N→0 (longer wavelengths and narrow wells) a difference in the scattering rates should be apparent due to the large difference in the cumulative density of states.

This quick analysis should motivate us, as it is clear that even with existing materials a hot carrier solar cell should be possible, and furthermore that there exists a simple method to increase the efficiency further simply by absorbing light in a quantum well. Taking this confinement further (i.e. to 1D or 0D structures) might seem like an intuitive way to further increase efficiency, however it turns out that such structures fail in one of the other requirements of a hot carrier cell, namely the redistribution of electron energy, as described at the end of section 1.5.3.1.

1.5.3 Energy selective extraction

1.5.3.1 Energy filtering width (ΔE) and energy redistribution

In order to maintain different electron temperatures in two different regions of the cell it is necessary to only allow the two populations to interact over a narrow range of energies, otherwise both populations will reach an equilibrium temperature, causing irreversible energy loss. The broader the energy selectivity the more the populations will interact and the larger this energy loss will be.

The impact of ΔE on the efficiency of the hot carrier cell can be explored using the Landauer formalism [43] to model the heat and particle flux between two reservoirs of electrons held at two different temperature. This method is outlined fully in Appendix 2, but relies on calculating the heat flux ($\dot{Q}_h$) from one reservoir to another by integrating over the particle distribution functions for a given transmission probability. For example, the heat flux from the hot to the cold reservoir is given in equation (1-3):

$$\dot{Q}_h = \frac{2N}{h}\int_{E_{off}}^{E_{off}+\Delta E}(E-\mu_h)(f_h(E)-f_c(E))dE \qquad (1\text{-}3)$$

With N representing an areal density of contacts between the two reservoirs, T_h and T_c representing the temperatures of the Fermi distribution of electrons in the hot and cold reservoir respectively, μ_h and μ_c the chemical potential of the hot/cold reservoirs.

In this model the transmission probability for electrons is modelled as a top hat function of width ΔE and height E_{off}, giving unity transmission probability over this narrow range.

Figure 1-10 shows the results of this modelling, demonstrating the improvement that comes from energy selectivity. At the extreme limit as $\Delta E \rightarrow 0$ we obtain the Würfel [21] limit of 85% for a hot carrier solar cell. In this limit, infinitesimal power is extracted, owing to the maximum efficiency being achieved at the reversible condition of f_h being set infinitesimally larger than f_c (with reference to equation Appendix 2, A1) at the infinitesimally narrow energy of extraction.

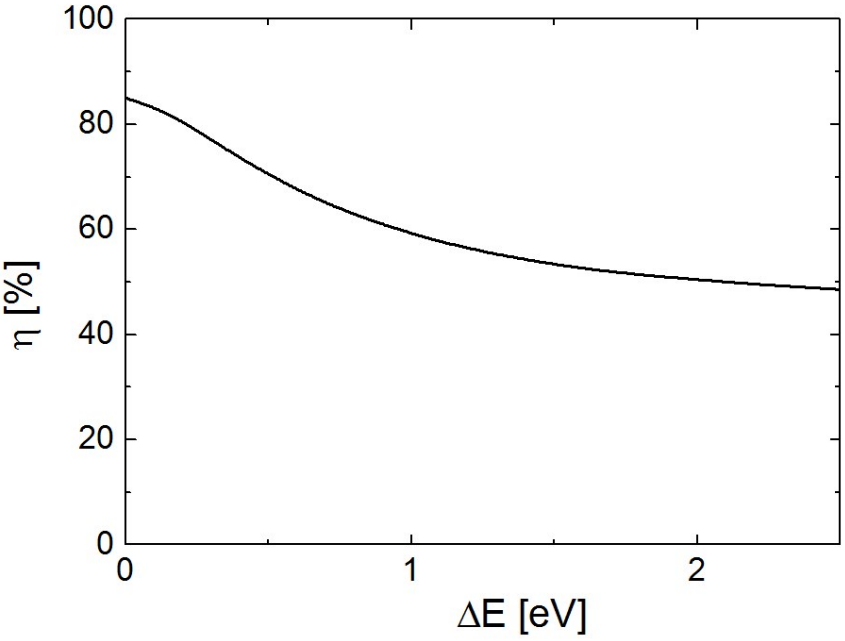

Figure 1-10. Efficiency of a hot carrier solar cell as a function of energy extraction width

It is interesting to note that appreciable conversion efficiency (~50% for the contact density chosen in this work) is possible for a "semi-selective contact $\Delta E \rightarrow \infty$. This is higher than a superficially similar cell, the thermionic "internal photo-emission (IPE)" cell [44], which has an efficiency of 7-22.6% (depending on density of states assumptions), due to the benefit that the hot carrier cell derives from electron energy redistribution. A thorough comparison of the function and efficiency of these two cells is presented in section 4.4.3, but the essential difference which gives rise to this increase in efficiency in the hot carrier cell is the equilibration of electrons amongst themselves, through electron-electron scattering, allowing a redistribution of energy. This allows electrons generated at an energy below the extraction energy to contribute to the overall device efficiency.

It is this necessity of equilibration amongst the electron distribution which leads us to the conclusion that structures in lower dimensions than 2 would not operate as effective hot carrier solar cell absorbers. This follows Ridley's comment (speaking of the electron-electron interaction) that *"it turns out that the restriction of motion to one dimension completely eliminates any effect of the interaction, at least to lowest order"* [p. 236 [32]].

We carried out an analysis of the strongly interacting electron gas for 3D, 2D and 1D to verify this comment (Appendix 4) and showed that electrons can indeed exchange energy and momentum in 3D and 2D, with an interaction strength given by the reciprocal of the

momentum exchange, but that in 1D this momentum exchange is not possible. This is graphically represented in Figure 1-11.

This can also be understood from an intuitive perspective by imagining the collision of billiard balls. A head on collision results in the velocities of two balls switching (equivalent to a 1D interaction); whereas after a glancing collision the subsequent velocities depend on the angle of collision (equivalent to a 2D interaction).

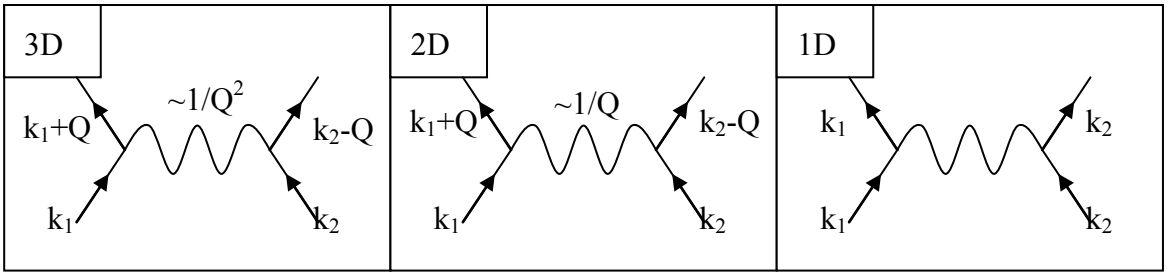

Figure 1-11. Scattering diagrams for electron-electron interactions in 3D, 2D and 1D

Therefore, in a perfect 1D material the electrons cannot redistribute their energy and momenta through (direct) electron-electron collisions[1] and this redistribution is likely to be significantly slower. This appears to find support in experimental work on hot carrier effects in 1D structures, e.g. finding orders of magnitude differences in scattering rates between an effective 1D quantum dot superlattice and a 2D multiple quantum well [46]. Though undoubtedly other mechanisms also contribute to this observed effect, in particular it is likely that there is also a contribution from a reduced density of states, akin to those for the 2D case presented in section 1.5.2.

1.5.3.2 Energy offset (E_{off})

In addition to the energetic width variations, the energy offset also strongly impacts the efficiency. Figure 1-12 shows that the efficiency is maximized for an energy offset between absorber and collector of 0.09eV. For this energy offset it is interesting to note that the optimum electron temperature for the absorber region is identical to the optimum lattice

[1] In fact electrons in such a 1D material are generally modelled as a Luttinger liquid [45], but this is beyond the scope of this very quick justification that 1D materials are less interesting for hot carrier cells.

temperature for the re-emitter in a thermophotovoltaic conversion device (~2600K). At this optimum temperature both cells also show the same efficiency of 85% (calculated using Würfel's equation (1-4) for the thermophotovoltaic cell from [19]).

$$\eta_{TPV} = \left(1 - \frac{T_h^4}{T_{SUN}^4}\right)\left(1 - \frac{T_c}{T_h}\right) \tag{1-4}$$

This again shows the similarity between these two approaches to energy conversion, and also illustrates some interesting features of the hot carrier cell. Firstly, an energy offset of 0.09eV acts to minimize the optimum temperature for the electrons in the absorber region (Figure 1-12, Top), for all other offsets a higher temperature is required to maximize efficiency. Furthermore, this energy offset also minimizes ΔE for a fixed N (areal contact density, from equation 1-3).

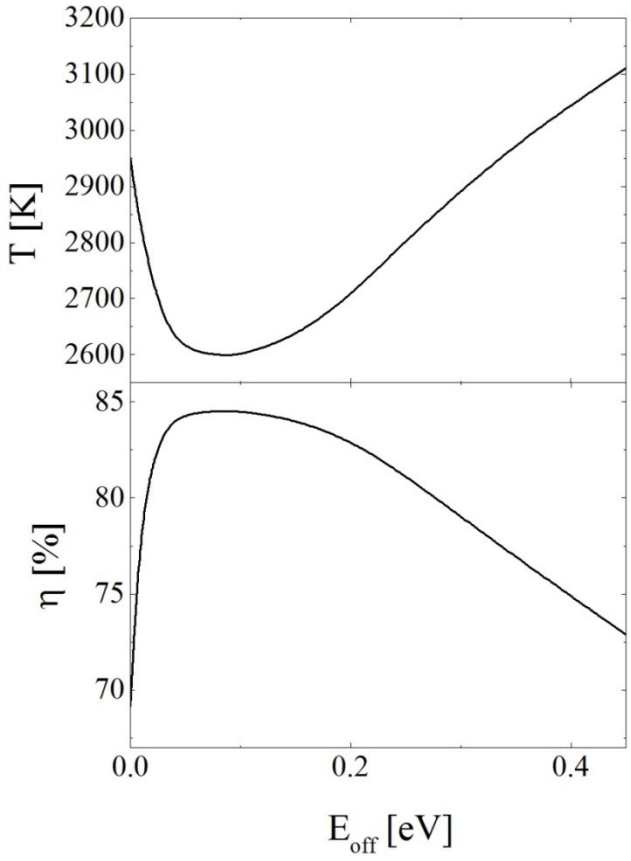

Figure 1-12. Top: temperature of the absorber region at maximum efficiency as a function of energy offset. Bottom: efficiency as a function of energy offset

One important feature to take from these previous sections, summarising the dependence of the efficiency on the electron extraction, is that the efficiency is not exceptionally sensitive to these parameters (the energy offset and the energy filtering width). While optima do exist, the region for which greater than 75% efficiency is possible is actually quite wide,

both in terms of the selectivity of extraction and the energy at which this extraction occurs. This should give encouragement that such structures should be realisable and is investigated in the following section with respect to existing materials.

1.6 Feasibility assessment

The concept that we propose to realise a hot carrier cell is theoretically promising, but it is important to verify whether the constraints imposed on the materials system are realistic and achievable in readily available materials so that prototypes can be constructed and the concept validated. These materials requirements are summarised in the following subsections and compared with those available in contemporary semiconductor systems.

1.6.1 Requirements

To add to the design rules that we have calculated in the previous sections, Takeda [25] has proposed "material rules" for the hot carrier solar cell. These specify constraints on the loss rate from electrons to the phonons and its relationship to other rates in the system, such as the rate of redistribution of electron energy after non-optimum energy carriers are reflected. These can be summarised as follows:

1. Carrier thermalization time in the absorber τ_{th}>1-10ns
2. Carrier equilibration time in the absorber $\tau_{eq} < \tau_{th}$ /100
3. Energy-selection width ΔE <0.1eV

The third rule gives the higher end of device efficiency that we calculated in Figure 1-10, resulting in >80% efficiency, while the two prior rules are much more "material specific". While rule 2 seems like a necessary constraint in order to refill the energy level from which carriers are extracted, it seems rule 1 should have a similar comparator in it, rather than being a strict lower limit. The comparator in this case would be that the carrier thermalisation time should be longer than the carrier extraction time, allowing extraction before thermalisation.

With regard to a particular material which we will investigate in this work it is clear that these requirements can be met. For a GaAs/AlAs system we have the following parameters:

- <5ps tunnelling time for an electron through a double barrier quantum well of GaAs/AlAs with AlAs barriers less than 2nm (from both calculations using a transmission linewidth model [47] and experimental results [48], [49]).

- 10-15ps thermalisation time for hot carriers in bulk GaAs or 350-550ps cooling rate for hot carriers in a GaAs quantum well [26].
- 0.1ps equilibration time for non-thermal electrons in GaAs to form a thermalised fermi distribution [50].

While improving these characteristics further is an important task to improve efficiency, it is clear that we can already start making prototype devices in a very well understood material system (GaAs/AlGaAs) and expect it to be able to operate as a hot carrier cell. Starting work on device structures will allow whatever materials and structures might be designed in the future, perhaps even with tailored properties [51], to be incorporated.

1.6.2 Absorber material

In addition to the electronic thermalisation and extraction requirements that we have already commented on, it is necessary that a cell should absorb a substantial amount of the light incident on it to operate as an efficient solar cell. This is a non-trivial requirement in most solar cells, where a balance of absorption depth and recombination length is required, but is even more restrictive in the case of the hot carrier cell. Not only do we need to extract carriers before they recombine with holes in the valence band, we need to extract them faster than they can relax to the conduction band minimum. Meeting this constraint may pose a significant challenge, since a thin layer generally has a very low absorption.

While this might seem like a difficult problem to overcome, various groups have in fact already observed hot carrier effects in some of the most unlikely materials, in particular amorphous silicon [52], where the thin layers have permitted hot carrier effects to be directly observable [53], however often resulting in a decrease in efficiency in these cells [54].

We will start by looking at hot carrier extraction from thin semiconductor layers in Chapter 3, however to enhance the absorption that is achievable in a thin film we also investigate metallic absorbers for a hot carrier solar cell in chapters 4 and 5, showing that these can give up to 99% broadband absorption in a layer thinner than 10nm.

1.7 Summary

This Chapter has described what we mean by a hot carrier photovoltaic cell and provided motivation that realising one should be an achievable goal given the current state of materials science. The following chapter outlines the theoretical tools that we will use in pursuing this goal; these will be used in Chapters 3-5, which detail experimental work on three embodiments of a hot carrier cell.

2 THE ASSESSMENT OF HOT CARRIERS

In the previous chapter we discussed how hot carriers could be used in order to increase the efficiency of a solar cell, however we did not discuss how such carriers were identified as being "hot". In this chapter, we will discuss the characterisation methods that are used to reveal the temperature of carriers, and also present theoretical work that is used to support this. Hot carrier effects are generally probed indirectly, through a photoluminescence (PL) or current-voltage (IV) signature. For this reason, modelling these characteristics accurately is essential, so that we can correctly predict the changes in these signatures that are associated with changes in carrier temperature.

We start by summarising the optical methods used to assess hot carriers in section 2.1, then explain the model that we use to evaluate the IV characteristics of hot carrier cells in section 2.2 and in mathematical appendices 5-7.

2.1 Methods of measuring carrier temperature

In Chapter 1, we differentiated between the thermalisation time and the equilibration time, stating that to operate as a hot carrier solar cell the equilibration time for electrons must be sufficiently short such that electrons are always extracted from a fermi distribution of "hot" electrons. Being part of a hot, thermalised distribution means that these carriers have an associated temperature and to prove that a cell is operating as a hot carrier solar cell we need to show that this carrier temperature is in excess of the lattice temperature.

Various optical methods exist to indirectly determine the electron temperature in a material, such as:

- Steady state intensity dependent photoluminescence [55]
- Transient (time resolved) photoluminescence [56]
- Transient absorption methods [57]
- Time resolved reflectivity [58]
- Electroluminescence [59]
- Time and angle resolved photoemission spectroscopy [60], [61]

The calculation of the electron temperature in all of these methods relies on using a Fermi-Dirac (or Maxwell-Boltzmann) distribution to model the carrier distribution in the material and adjusting the temperature of the distribution until the modelled data matches with the experimental data. These various techniques all have their own advantages and disadvantages, with the luminescence techniques being easier to apply to thicker samples and in more geometries, while the transient absorption/reflection techniques are capable of better time resolution. However, a more in depth discussion of each technique is beyond the scope of this chapter, instead we will briefly introduce the steady state photoluminescence technique in section 2.1.1 since it is the method that we use to characterise the cells used in this thesis.

In addition to these optical methods, there also exist IV characteristics which are dependent on the temperature of electrons. Changes in these IV characteristics reveal information about the electron distribution and, again, require comparison with modelled data using a heated Fermi-Dirac electron distribution. Two IV signatures, which are particularly relevant to our concept (and later structures), are introduced in section 2.1.2 and the modelling of the IV response of the illuminated hot carrier cell is explained in section 2.2.

2.1.1 Photoluminescence

Steady state (or continuous-wave) photoluminescence (PL) is the most common method to measure carrier temperature in semiconductors. Shah pioneered work in this field [55], showing that the gradient of high energy tail of a PL peak reveals the temperature of the carriers which are recombining to yield the PL. This is because the intensity of the photoluminescence (I) from band-to-band recombination can be described by the expression shown in equation 2-1.

$$dI(E) = A(E)E^2\left[\exp\left(\frac{E-\Delta\mu}{kT_e}\right)-1\right]^{-1}dE \quad (2\text{-}1)$$

In which A is the absorptivity of the material, T_e is the carrier temperature and $\Delta\mu$ is the quasi-Fermi level splitting between electrons and holes. This can be simplified for the case where the carrier energy is significantly larger than the carrier temperature and the absorptivity is more slowly varying than the exponential PL decrease (i.e. the high energy side of a PL peak), to show that the gradient of the PL in this region is proportional to the exponential of the carrier temperature, as in equation 2-2.

$$\frac{dI}{dE} \propto \exp\left(-\frac{E}{kT_e}\right) \quad (2\text{-}2)$$

Since Shah's early work, this has now become the standard method for determining the carrier temperature in an emissive material, particularly so in the research of hot carrier solar cells. One particularly commonly used method is to vary the intensity of the illumination source and show that the peak wavelength of the PL does not shift in wavelength (which would indicate lattice heating) but that the high temperature tail gradient shallows with increasing intensity. Various authors have already used this technique to successfully demonstrate hot carriers in photovoltaically relevant structures [35], [37], [62]–[64].

This method is generally very good for assessing hot carrier temperatures, but care must be taken, as there are three main sources of error if the underlying assumptions are not valid:

1. The absorption must not change with intensity (e.g. by Pauli blocking)
2. The low energy tail of the PL should not also broaden (a sign of state filling rather than carrier heating)
3. The hole and the electron which recombine to give the PL should be at the same temperature.

These assumptions are generally good, with the exception of 3, which is almost never true due to the much faster relaxation of the holes when compared with electrons. This is of no particular concern if one simply wants a temperature comparison (e.g. to show that the electron temperature is increasing with illumination intensity), but for an absolute measurement of temperature Gibelli et al have recently extended this PL analysis with a two temperature approximation to take into account the differences in the electron and hole temperature [65]. This can be further enhanced by fitting over the entire PL spectrum rather than simply linearizing the high-energy slope of the PL.

2.1.2 IV characteristics

In addition to the CWPL method, we will use two signatures of hot carriers which appear in a hot carrier cell's IV characteristic. Both signatures rely on the fact that our realisation of a hot carrier cell uses resonant tunnelling as the carrier extraction method. The unique and sensitive IV characteristics of resonant tunnelling diodes (RTDs) have been extensively studied (e.g. [66], [67]) and shown to be acutely sensitive to the temperature of the sample in question. This is largely due to the quantum mechanical nature of the current being disrupted by phonon scattering, though also due to the necessary alignment of occupied states and tunnelling resonances to provide a current. As such, these structures' IV response provides a sensitive probe through which we can examine the carrier temperature changes in devices that rely upon them.

The first signature of interest in a resonant tunnelling structure is the value of the voltage at the current peak. An RTD has a peak in current at the bias where the peak of the electron distribution (in the region providing electrons for extraction) is aligned with the energy resonance of the quantum well through which tunnelling occurs, schematically represented in Figure 2-1.

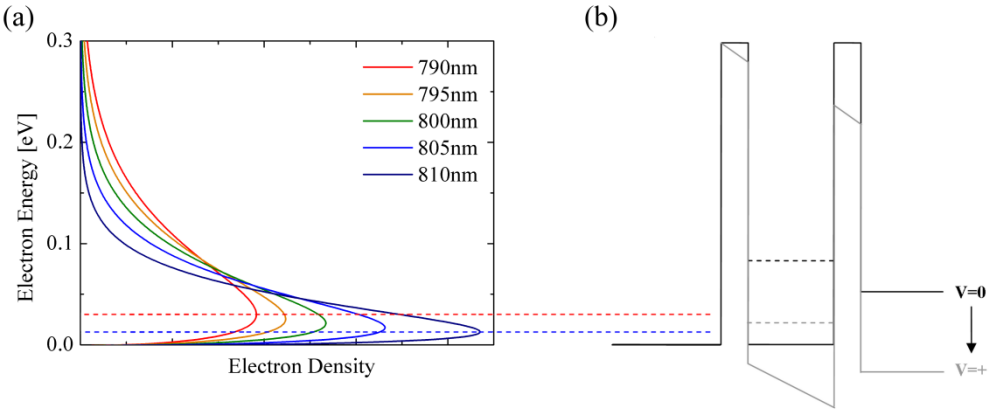

Figure 2-1. Explanation of the voltage shift in the peak of the current in the IV characteristic of a DBRTD when illuminated with different wavelengths of light

Since the peak in the electron distribution is related to the average energy of the carriers, which is, by definition, related to the carrier temperature, the carrier temperature can be inferred by the voltage of the current peak. This was confirmed by Yagi et al [68] in an early prototype of a hot carrier extraction structure. They demonstrated that by illuminating a double barrier RTD structure with different wavelengths of light a voltage shift was observed in the IV characteristics of the device, reproduced in Figure 2-2.

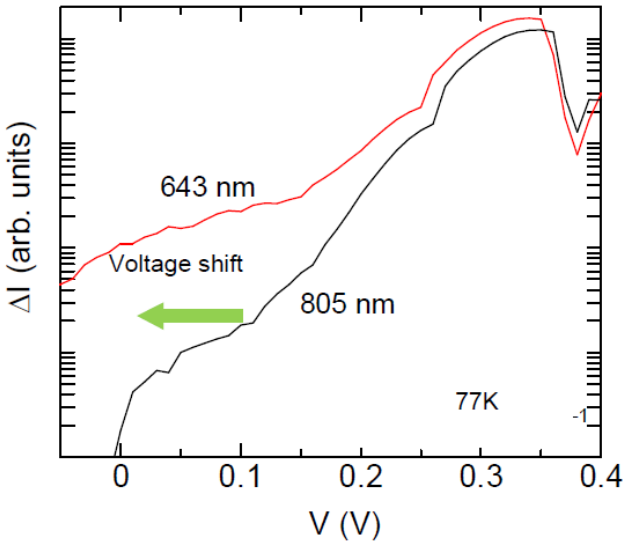

Figure 2-2. Experimental voltage shift in the IV characteristic of a double barrier resonant tunnelling diode when illuminated with two different wavelengths of light from [68]

This characteristic is important to prove that a device is operating as a hot carrier solar cell. The PL measurements show that the carriers are hot, but changes in the IV characteristics show that they can be extracted before thermalisation occurs.

Further examination of the IV characteristics, which result from electron transfer from a heated distribution through a tunnelling resonance, reveal a second characteristic that can be used to infer a change in carrier temperature. Further to a peak in the IV characteristic RTDs also have a "valley", where their current reaches a minimum. This is when the device is biased in excess of the resonance voltage, but before thermionic emission starts to dominate the current behaviour. Since the current at this point is determined by electrons from the (high-energy) tail of the distribution, the ratio of the peak current to this valley current (the peak to valley ratio or PVR) gives another probe for the electron temperature. For such a device we would expect the PVR to decrease as the temperature increases and more non-resonant current is present. While this ratio is also affected by the lattice temperature, the two signatures in combination (the peak shift and the PVR change) reveal important information about the carrier temperature in a device and how it changes.

We have seen both of these effects in our work prior to this PhD [40], with both the peak and PVR shifting in accordance with expectations in a hot carrier solar cell structure. Figure 2-3 shows the outcomes of this work, demonstrating the sensitivity of the IV characteristics of such a device to a change in illumination conditions.

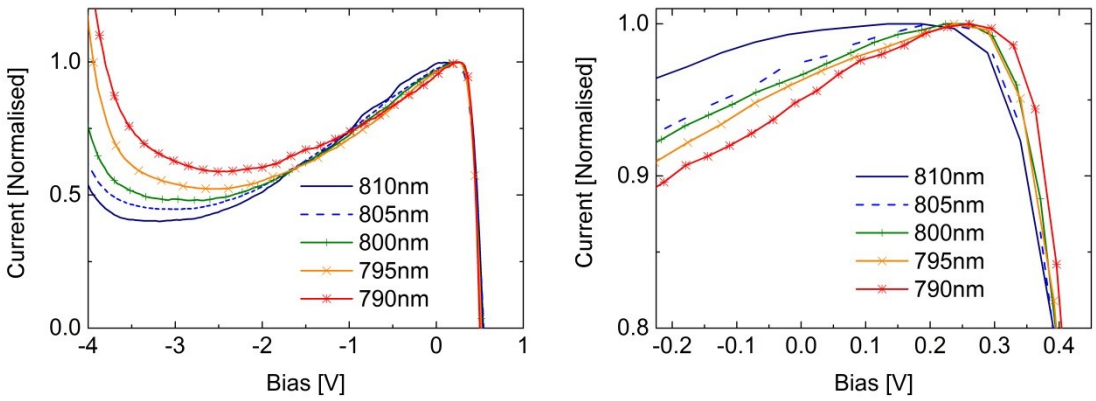

Figure 2-3. IV characteristics of a RTD structure operating as a hot carrier solar cell under illumination with different wavelengths of light from 790-810nm at a temperature of 93K from [69] (left shows full IV characteristic, right shows an enhanced view of the peak region to reveal the peak shift).

This work on an n-i-n tunnelling device will not be taken further in this PhD, however a related structure will be investigated in chapter 3, and the idea that IV characteristics are a sensitive probe of carrier temperature will be important throughout.

2.2 Modelling the IV characteristics of a hot carrier photovoltaic cell

Section 2.1.2 presented two signatures in the IV characteristics of hot carrier solar cells, which have been experimentally shown to be correlated with hot carriers. However, to build on these findings and to find other signatures which are dependent on the carrier temperature it is important to accurately model hot carrier cells using a robust theoretical method. In this way, novel cells can be characterised and evidence for their operation is clear. In particular, while optical characterisation is possible for the semiconductor-based cells presented in chapter 3, we will have to rely on IV differences to characterise the metallic cells presented in chapters 4 and 5, since the (metallic) absorbers do not luminesce and the fully processed cells are not able to be probed with differential absorption techniques.

Accurate modelling of cell operation is crucial to understand how signatures in the IV characteristics reveal important information about the cell. This necessitates a good assessment of absorption of light in the cell and also of the electron transport in these cells. Perfect modelling and quantitative accuracy is not required, but reliable qualitative

indications of trends is vital so that we can evaluate and understand experimental data. We explain in the following two subsections how we model carrier excitation (section 2.3) and carrier transport (section 2.4) in order to understand these photovoltaic devices and derive the signatures which reveal the presence of hot carriers.

2.3 Carrier excitation

2.3.1 Modelling the absorption via TMM

The absorption of light in a multi-layer structure cannot be expected to follow Beer-Lambert exponential attenuation, as it does in a thick, homogeneous material. This is important for our understanding of hot carrier cells, as their structure will likely be a multi-layer heterostructure, and their IV characteristics (e.g. those mentioned in section 2.1.2) can depend sensitively on the density of carriers photogenerated in the absorber region of the device. For this reason, it is necessary to model the generation of carriers using an appropriate method.

The location of the carrier generation ($G_j(x)$) in a material layer (j) can be inferred from the strength of absorption of the electromagnetic field ($E_j(x)$) in that location, as shown in equation 2-3, detailed in appendix 5.

$$G_j(x) = \frac{1}{\hbar}\varepsilon_0 k_j(\lambda) n_j(\lambda) \left|E_j(x)\right|^2 \qquad (2\text{-}3)$$

With this value for its absorption, and the subsequent generation of carriers, it is necessary to compute the electric field throughout the structure as a function of the electric field incident on it. This can be carried out by discretising the structure in a direction perpendicular to the incident field and computing the transfer of the electromagnetic field between these discrete layers. We use the transfer matrix method (TMM), or more precisely the scattering matrix method, to perform this calculation.

The basic method is to describe each interface by a matrix, wherein the relationship between the electric field on either side of the interface is determined by the Fresnel complex reflection and transmission coefficients, as documented in e.g. [70]. We wrote a program in FORTRAN to evaluate this absorption for an arbitrary layered structure, presented in appendix 5, which was used extensively in this work to model the absorption, reflection and transmission of light through layered structures.

2.3.2 Comparison of TMM results with Sentaurus FDTD

In order to validate the model it was compared with both experimental results (presented throughout chapter 4, e.g. in section 4.2.2 for a chromium based structure) and also with existing validated theoretical models. In particular we validated it with the finite difference time domain (FDTD) solver present in the proprietary software "Sentaurus TCAD" [71] from Synopsys®.

This comparison was carried out for a GaAs heterostructure, which will be experimentally probed in chapter 3, and the layer structure of which is presented in Table 1.

Table 1. The layer structure and refractive indices (n,k) of the p-i-n device explored in chapter 3

Layer	**Material**	**Thickness [nm]**	**N**	**K**
Air	Air	0	1.000000	0.000000
Absorber	GaAs	150	3.659100	0.066012
barrier1	AlAs	2	2.956100	0.000000
Well	GaAs	6	3.659100	0.066012
barrier2	AlAs	2	2.956100	0.000000
Collector	7% AlGaAs	150	3.571887	0.000000
Contact	7% AlGaAs	500	3.571887	0.000000
Insulation	AlAs	100	2.956100	0.000000
Buffer	GaAs	4090	3.659100	0.066012

The structure was modelled with both our TMM solver and the Sentaurus FDTD solver for the case of illumination with monochromatic light at 790nm and an intensity of 50mW/cm². The resulting optical generation profile (of excited electrons) showing the carrier generation as a function of distance from the surface in the cell is shown in Figure 2-4, showing an excellent agreement between the two methods. The big benefit of using our FORTRAN based TMM solver over the Sentaurus FDTD offering is that it is over 10,000 times faster and can easily be interfaced with other modules, such as the carrier extraction calculation presented in the following section.

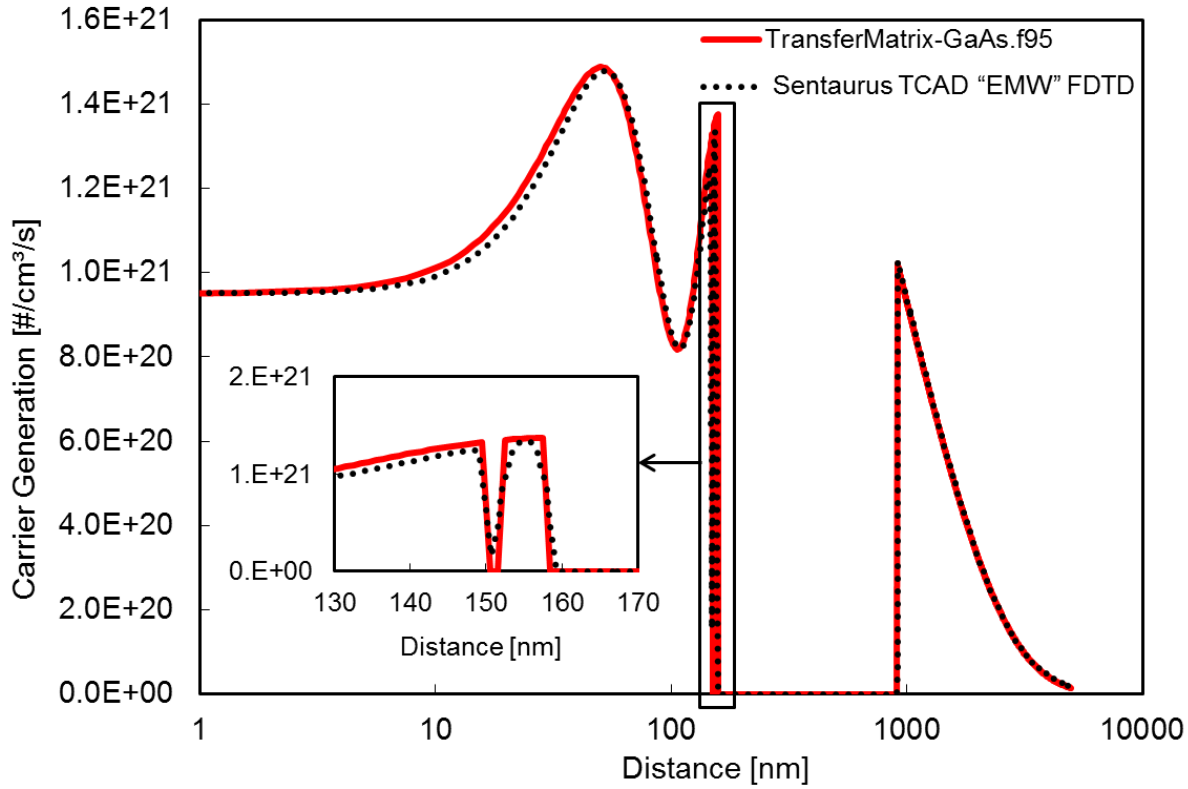

Figure 2-4. The carrier generation in the p-i-n structure when illuminated with 790nm light at 50mW/cm² at 93K modelled by the transfer matrix solver written for our program compared with the result from modelling with a proprietary FDTD solver packaged with Sentaurus TCAD.

The TMM model also accurately predicts experimentally determined values of reflection as a function of wavelength, as presented in section 4.2.2.

In the present work, it is never the intention to absorb light in the quantum well, the aim being to absorb in the lower band gap "absorber region" only. Experiments are carried out using wavelengths of light which are below the energy required to excite carriers anywhere else in the structure. As such we do not need to be concerned with increases of absorption in the well region due to confinement effects, though these could be modelled by altering the absorption coefficient [72] if desired.

2.4 Carrier transport

2.4.1 Self-consistent Schrödinger-Poisson formalism

In order to calculate the current in a quantum mechanical device, we use the relationship between the wavefunction (Ψ) and particle flux (I) of equation 2-4:

$$I(x_i) = \frac{q\hbar}{m^*} \sum_k \mathrm{Im}(\psi_k^*(x_i) \nabla \psi_k(x_i)).(f_k^L - f_k^R) \tag{2-4}$$

As such, it is necessary to determine the wavefunction for electrons in the system for a given potential. The wavefunction determines the distribution of electrons in the system, which in itself changes the potential, as such, it is necessary to compute the distribution of electrons in the device, such that it self-consistently solves both the Poisson equation and the Schrödinger equation. A derivation and justification of this approach is presented in appendix 6, but the method and key equations are summarised in the flow diagram of Figure 2-5 and equations 2-4, 2-5, 2-6 and 2-7.

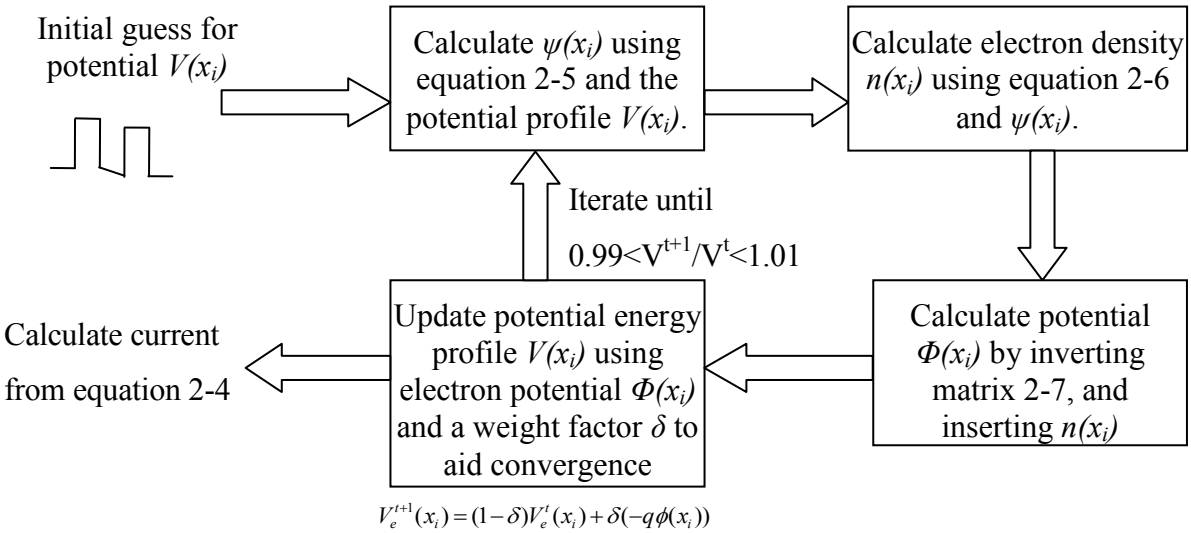

Figure 2-5. A schematic illustration of the discretised Schrödinger based program, used to calculate the current and electron distribution in a device self-consistently

$$\psi(x_{i+1}) = \left\{ \frac{2m^*(\Delta x)^2}{\hbar^2} (V(x_i) - E) + 2 \right\} \psi(x_i) - \psi(x_{i-1}) \tag{2-5}$$

$$n(x_i) = \sum_k |\psi_k(x_i)|^2 \left[f_k^L - f_k^R \right] \tag{2-6}$$

$$-\begin{bmatrix} 1 & 0 & 0 & 0 & 0 \\ 1 & -2 & 1 & 0 & 0 \\ 0 & \ddots & \ddots & \ddots & 0 \\ 0 & 0 & 1 & -2 & 1 \\ 0 & 0 & 0 & 0 & 1 \end{bmatrix} \begin{bmatrix} \varepsilon(x_1)\phi(x_1) \\ \varepsilon(x_2)\phi(x_2) \\ \dots \\ \varepsilon(x_{nx-1})\phi(x_{nx-1}) \\ \varepsilon(x_{nx})\phi(x_{nx}) \end{bmatrix} = q(N(x_i) - n(x_i)) \tag{2-7}$$

2.4.2 Determining the transmission function – analytical Tsu-Esaki equation

To simplify the evaluation of equations 2-4 and 2-6, which in their current form are three-dimensional integrals over all k-space, these equations are analytically evaluated over the two dimensions perpendicular to the confined direction in our devices. In this work, we assume that the *y* and *z* directions (the unconfined directions) have a parabolic dependence of energy on momentum and can therefore be analytically integrated over. This approach follows the work of Esaki and Tsu [73] to calculate the current through a heterostructure. This has previously been expanded to take into account different effective masses [74], but here we extend it further to take into account different electron temperatures and fermi energies. This is necessary in our device, as the transfer is necessarily from two regions which are not in thermal equilibrium, as schematically illustrated in Figure 2-6.

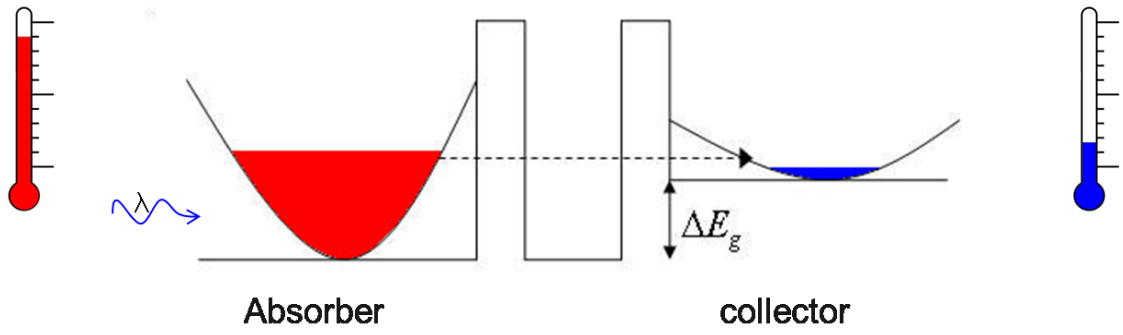

Figure 2-6. A schematic of the hot carrier solar cell, which was modelled through the self-consistent Schrödinger-Poisson formalism

The analytical integration over the unconfined directions is laid out in appendix 7, and results in a simplified 1 dimensional integral in the confined directions, yielding the current transfer from the absorber (region subscript *L*) to the collector (region subscript *R*), documented in equations 2-8 and 2-9:

$$J = \frac{q\hbar}{m_R}\sum_{k_x} A_{k_x}\,\mathrm{Im}(\psi_k^*(x_i)\nabla\psi_k(x_i)) \tag{2-8}$$

$$A_{k_x} = \frac{m_R k_B T \Delta k_x}{\pi\hbar^2}\ln\left[\left(\frac{1+e^{(E_{fL}-E_x-eV)/k_BT_1}}{1+e^{(E_{fL}-\alpha E_x-eV)/k_BT_1}}\right)^{T_1/T_2}\cdot\left(\frac{1+e^{(E_{fR}-\alpha E_x)/k_BT_2}}{1+e^{(E_{fR}-E_x)/k_BT_2}}\right)\right] \tag{2-9}$$

This scheme was written into a FORTRAN program to provide us with fast and accurate modelling of new structures and a way to analyse experimental results.

2.4.2.1 The benefit of self-consistency

Various authors have covered the benefits of providing self-consistency between the Schrödinger and Poisson equations in great detail (e.g. [75]), so we shall not explore this in depth, as the main improvement we make over the conventional methods is the inclusion of a different electron temperature in the absorber and collector regions, as previously described. However, it is worth quickly summarising the benefit of such a self-consistent formalism, justifying its numerical cost.

The benefits of the self-consistent approach are clear when we compare the output of this modelling with and without self-consistency between the Poisson and Schrödinger equations. We have carried out such a comparison for a simple RTD structure, with 1.7nm AlAs barriers and a 4nm well, which is compared with a literature calculation on a similar structure [76] to validate this model. The calculated IV characteristics for this structure are shown in Figure 2-7, showing a higher peak voltage and a more natural RTD IV characteristic.

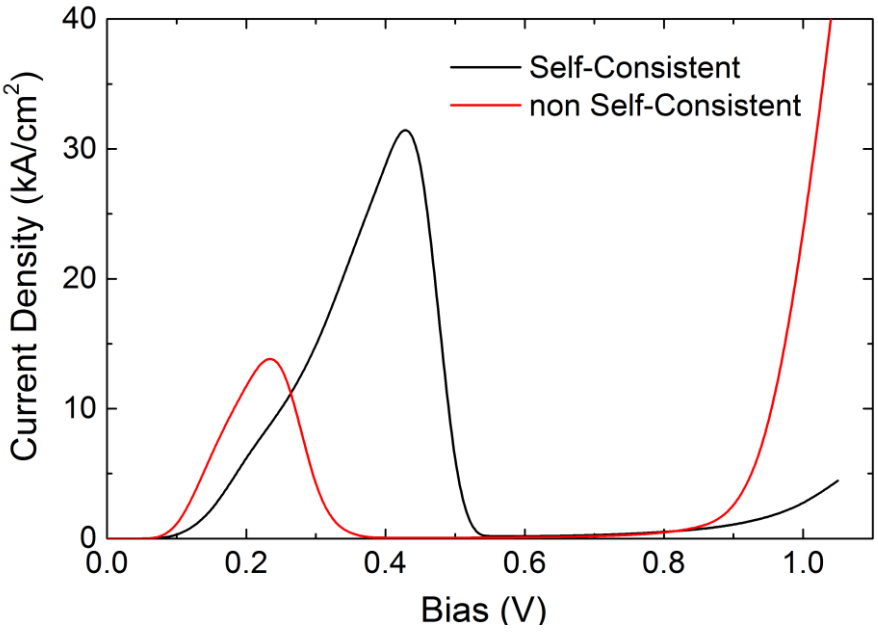

Figure 2-7. The modelled IV characteristic of a RTD with 1.7nm AlAs barriers and a 4nm GaAs well modelled using self-consistency between the Poisson and Schrödinger solutions (black) and without self-consistency (red).

Our model provides a good comparison with the model of REF [76], with a similar IV characteristic shape and numerically similar values for the absolute current density at peak current and a similar voltage value. In keeping with earlier findings in the literature [75], [77] we observe two benefits of this self-consistent approach:

- The voltage for the current peak is shifted higher, attributable to an accurate modelling of space-charge effects, i.e. charge building up in the device during operation
- The PVR is reduced, leading to a more realistic shape for the IV characteristic

Importantly for the hot carrier cells, the altered charge distribution changes the transmission characteristics, for example the extraction energy and the average tunnelling time, which, as previously mentioned, can be calculated from the inverse of the transmission linewidth [47]. These differences are important, as they will change the optimum design of the cell, and so should be taken into account.

2.4.3 Extension to metals

In this work, both semiconductor absorbers and metallic absorbers are investigated, necessitating a method to model metals, as the previous method was implicitly developed for semiconductors. This was carried out, by moving the contact point of the absorber to one grid cell to the left of the metal/semiconductor junction, which had a starting "guessed" potential of a Schottky barrier. In effect this removed the charge self-consistency for the metallic region, while leaving it for the semiconductor region. This was necessary, as otherwise the large charge density of the metallic region caused convergence problems for the iterative solver. This was possible, and a reasonable assumption, as the band structure of the metallic region remains unperturbed in spite of electron transfer to/from the semiconductor region due to its very high electron density. Essentially, the conduction band is flat and is always equal to the potential applied by the external field, by the definition that a metallic layer is an iso-potential. For this reason it is justifiable to model the one metallic cell next to the semiconductor layer in our self-consistent solver, as Poisson's equation in the rest of the metallic layer is, in effect, already solved.

With this slight change, the only inputs required for the metallic region are the electron temperature in the "contact" region, which is simply taken to be a Fermi distribution, and the electron mass for the metal.

Modelling a metal/semiconductor junction in this way produces very good results, with the Schottky junction behaviour emerging naturally from the self-consistent solution of how the electron wavefunction is affected by the barrier. This method is used semi-empirically for our experimental structures, as the Schottky barrier height is determined experimentally and forced upon the model. Figure 2-8 shows the IV output from the model when a 1eV Schottky barrier is modelled between a metallic layer and a GaAs semiconductor layer with a donor dopant concentration of $5x10^{17}cm^{-3}$. In this case, the absorber temperature and collector temperature for the cell are equal, simply yielding Schottky diode dark IV characteristics. This IV characteristic is compared with a fit to the classical diode equation to show that the shape of the current predicted by this model is physically reasonable.

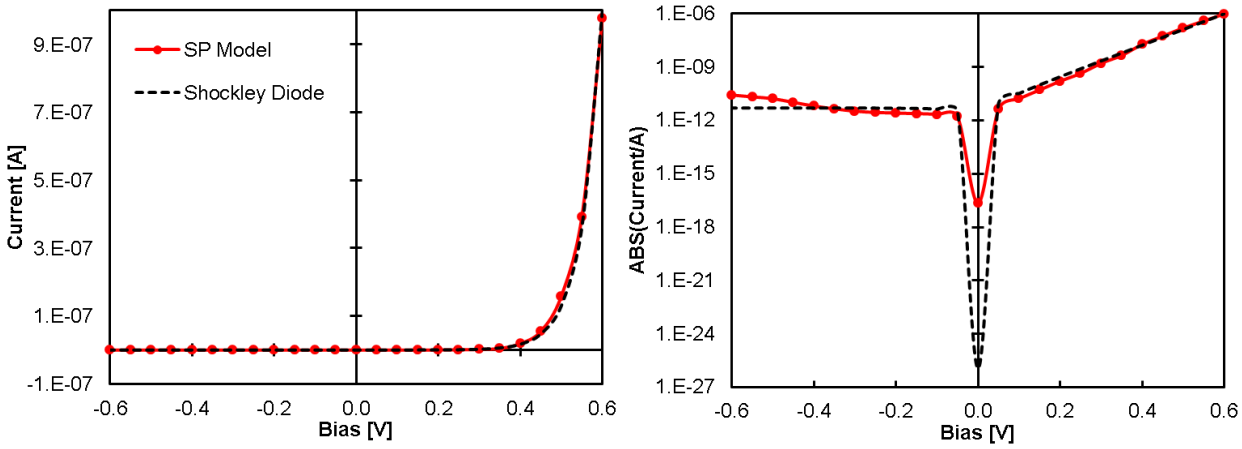

Figure 2-8. Right: The IV output from the Schrödinger-Poisson (SP) model of a metal/semiconductor junction (red) compared with the Shockley diode equation. Left: Plot of the same with a logarithmic ordinate axis

One particular benefit of modelling a Schottky junction in this way is the natural inclusion of a reverse bias current. Using the diode equation the current in reverse bias will decrease exponentially ad infinitum, whereas using the Schroedinger-Poisson formalism allows some ohmic behaviour in this contact, depending on the properties of the materials. This is significantly closer to the real life IV characteristics observed in chapter 5.

This method will be extended in section 4.4.2, when the electron temperatures will be different and it will be seen that power generation naturally emerges from the temperature gradient in this cell.

2.5 Summary

The methods in this chapter, both theoretical and experimental, will be used in the following three chapters to design and probe devices that we expect to operate as hot carrier solar cells. Firstly, in chapter 3, a semiconductor based hot carrier solar cell will be explored, mostly with a PL based study to examine electron extraction in a tunnelling structure. Secondly, in chapters 4 and 5 the IV based theoretical work will be used to design a hot carrier cell using a metal absorber and describe its operation in comparison with experimental findings.

3 DEVELOPMENT OF A SEMICONDUCTOR HOT CARRIER PV CELL

In this chapter, we shall investigate the experimental realisation of a semiconductor based hot carrier photovoltaic cell. In previous work [40], predating this PhD and mentioned in section 2.1.2, we showed a hot carrier photovoltaic cell which approached the demonstration of a hot carrier solar cell through fast extraction, rather than slowed carrier thermalisation. This work showed a hot carrier photocurrent, which was dependent on the wavelength of light used to illuminate the cell, demonstrating the extraction of carriers prior to their thermalisation. The structure used was based on ultra-fast extraction of carriers from a narrow band gap semiconductor absorber to a wider band gap semiconductor collector through an energy selective tunnelling contact. While this previous structure provided an important proof of principle, showing hot carrier electrical extraction, as a solar cell it was limited by a low open circuit voltage (V_{oc}) and the carrier transport was not directly explored.

In this chapter, based on work published in [78], we explore this device concept further by investigating the structural and carrier transport properties of two related structures.

3.1 A P-i-N semiconductor hot carrier solar cell

Previously [40], and in section 2.1.2 we showed a structure which extracted carriers from an absorber region to a collector region through resonant tunneling before the

photogenerated carriers could thermalise with the lattice. This demonstration was carried out by separating two intrinsic regions of semiconductors with different band gaps by a double barrier quantum well. These two intrinsic regions were electrically contacted by thin layers of n-doped material, such that electron transport could occur through the device and be measured in the form of an output current between two terminals. This cell provided an unambiguous signal showing hot carrier extraction, but its voltage output was limited, as the electrical connection was only to the conduction band, so no field assisted extraction could take place.

To extend this work, we propose a different contacting scheme in this chapter so that an offset tunneling structure is contacted with p and n contacts more commonly used in a photovoltaic cell. In this way the heat driven current that has already previously been shown in an n-i-n cell can supplement the field driven current that is commonplace in a p-i-n cell. This supplementary thermal current is similar in principle to a thermoelectric current [79] and is what allows these cells to be capable of reaching ultra-high efficiencies.

We will investigate two structures (HYL5 and HYL6) in this chapter, which will explore the possibilities provided by a p-i-n hot carrier solar cell. The first structure investigated, HYL6 has an increased V_{oc} by using a p-i-n structure rather than an n-i-n structure as used in [40]. The second structure HYL5 is structurally similar to HYL6 but has a multiple quantum well (MQW) region embedded in the wider band gap collector to provide a signature region for photoluminescence (PL) characterization of the device.

In the following section we will outline the conceptual aim behind developing and examining these two samples, their sample design and fabrication, followed by low temperature current-voltage (IV) analysis of HYL6 (the p-i-n structure) in section 3.2. We will then present a photoluminescence investigation of HYL5 (the MQW structure), with section 3.3 exploring its temperature dependent PL (TDPL) in order to determine the relevant energy levels in the structure and section 3.5 showing time resolved PL (TRPL) in order to characterize the decay constants of electrons in the device.

3.1.1 Concept

The key concept that we seek to exploit in the two structures to follow is that of energy selective tunnelling from a narrow bandgap to a wider bandgap semiconductor. This mechanism, driven by a difference in electron temperature between the two regions, is the driving force for our cell. This method of realizing a hot carrier cell relies crucially on the

transport of electrons from the absorber region to the collector region at a rate faster than they can thermalize with the phonon bath. This mechanism has been shown previously in Figure 1-4.

The rate of carrier transfer by tunnelling through a double barrier quantum well region is strongly influenced by the barrier thickness, with thin barriers giving a wider transmission line width and consequently a faster speed of electron transfer [47]; therefore our structures have potential barriers of 2nm thickness or less to achieve picosecond transfer rates.

3.1.2 Samples

Samples to explore these concepts were grown by molecular beam epitaxy by Professor Huiyun Liu at University College London. HYL6 is a p-i-n structure, used to assess IV characteristics and HYL5 is an MQW structure used to investigate band structure and carrier transport properties through PL measurements.

3.1.2.1 P-i-n structure

The p-i-n structure was grown to study how an improved extraction for holes over an existing n-i-n hot carrier structure [40] would increase the photocurrent and voltage of the cell. The p-i-n structure uses GaAs as the narrow-band-gap semiconductor (the absorber) and $Al_{0.07}Ga_{0.93}As$ as the wide-band-gap semiconductor (the collector) with an intervening AlAs/GaAs double-barrier quantum well, as shown schematically in Figure 3-1. The layer structure was grown on a GaAs substrate by molecular beam epitaxy (MBE) and then processed into mesas. An annular Au/Zn/Au metallisation was used as the top contact to a thin (10nm) $5\times10^{17}cm^{-3}$ p-doped GaAs region directly adjacent to the intrinsic GaAs absorber region. This allowed photogeneration in the GaAs layer before the quantum well region and limited the impact of excess doping in the absorbed region, while still providing a good quality contact. The GaAs and AlGaAs regions on either side of the AlAs/GaAs/AlAs double-barrier quantum well were undoped, with contact to the n-doped AlGaAs region made by an InGe/Au contact.

Processing into the mesa structure shown in Figure 3-1 was carried out by using a calibrated and timed non-selective AlGaAs/GaAs etch and the contacts were annealed to provide a resistivity of less than $10^{-5}\Omega cm^2$.

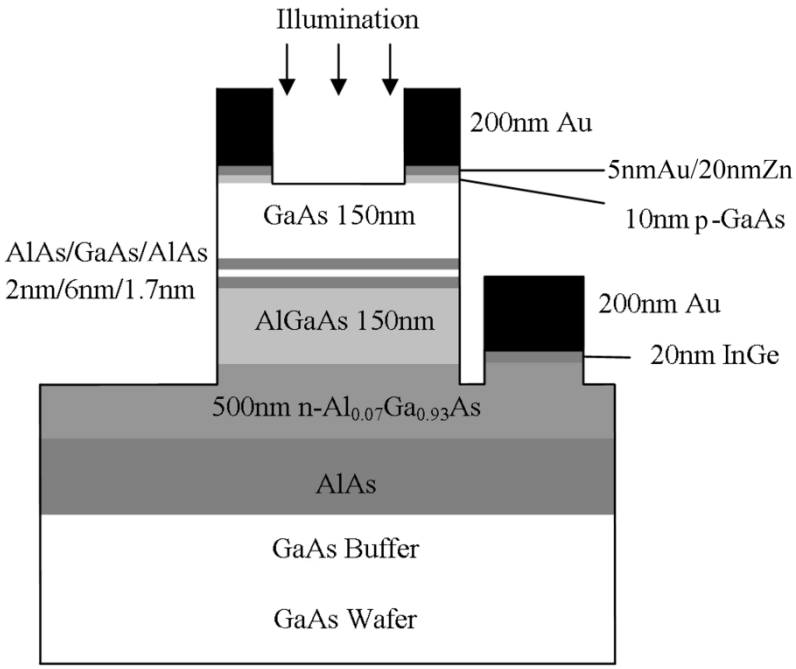

Figure 3-1. A schematic illustration of the layer and processed mesa structure of the p-i-n device, HYL6

3.1.2.2 MQW structure

The MQW band structure, HYL5, is shown in Figure 3-2, along with the wavefunctions for the three important states in this structure modelled with the Schrödinger-Poisson program described in section 2.4 and appendices 7 and 8. The structure has a 10nm p-doped GaAs cap and a 150nm intrinsic GaAs absorber region, the last 5nm of which is shown as the region between 155-160nm in Figure 3-2. This region is followed by a 6.5nm wide GaAs QW, confined by AlAs barriers. Up to this point HYL6 and HYL5 are identical; however, from this point while HYL6 has a bulk AlGaAs collector, HYL5 has a GaAs/AlGaAs MQW region followed by a bulk AlGaAs region. As illustrated in Figure 3-2, our transfer matrix calculations predict that the 6.5nm GaAs well gives rise to a transmissive (between absorber region and collector region) energy state which is 0.069eV above the GaAs conduction band minimum at the absorber/AlAs barrier (labelled ΔE_1); we will refer to this state and region as the "RTD" state and region, since it acts similarly to the transmissive tunnelling state in a resonant tunnelling diode. In addition to this state the MQW region gives two additional non-transmissive energy states, a higher energy state MQW+ and a lower energy state "MQW". These states are termed "non-transmissive", as they have a negligibly weak transmission with a very low tunnelling probability between the MQW and

RTD regions. Other states are also present, but only the states relevant to the following analysis are presented in Figure 3-2 for clarity.

The aim of this structure is to provide signature PL emission from four regions of the device (GaAs absorber, RTD state, MQW state, and AlGaAs collector and barrier regions). The MQW+ state is important for the scattering of electrons from the RTD state but is not observed in PL, presumably due to rapid decay of carriers from MQW+ to the MQW state, so we only refer to PL from the MQW state. In addition to this signature region for PL examination, HYL5 was prepared by mounting on a glass cover-slip and removing the GaAs substrate up to an AlAs etch stop directly beneath the AlGaAs region; this allowed us to focus on the PL from the four regions previously mentioned and remove any impact from the substrate. The emission from these regions will be explored both in its temporal evolution and temperature dependence in order to reveal the structure of the device and show the nature of electron transport through it.

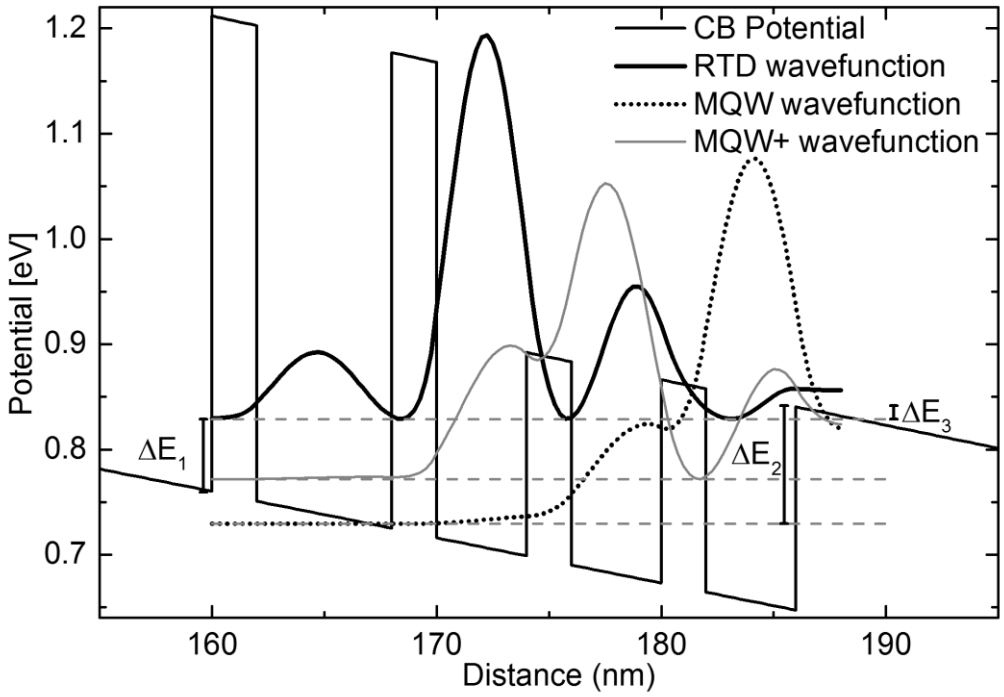

Figure 3-2. The schematic band structure of the MQW sample (HYL5) with confined state wavefunctions overlaid as calculated by transfer matrix calculations. Activation energies for PL analysis are labelled as ΔE_1=69meV, ΔE_2=111meV, ΔE_3=12meV

3.2 IV results from a P-i-N device

HYL6 was illuminated with monochromatic light at wavelengths from 805-815nm and at temperatures from 88K-293K. The illumination wavelengths and temperatures were chosen so as to excite carriers in the absorber region but not in the collector region or the confined regions.

Similarly to the previously presented n-i-n device described in section 2.1.2, HYL6 shows an IV curve characteristic of resonant tunnelling, showing a pronounced peak and valley characteristic, Figure 3-3 shows the IV characteristic of HYL6 under 805nm illumination at a lattice temperature of 115K. For these experiments the illumination source was a wavelength tuneable Ti–sapphire laser (Millennia pumped Tsunami), focused to a spot size of 50μm with an objective lens. The laser wavelengths were measured with a calibrated Anritsu MS9710C spectrum analyser. The structure was cooled on a Linkam THMSE600 cryogenic microscope stage.

Figure 3-3 shows the dependence of the IV of HYL6 on the laser power (measured at source) normalized such that the current peak for each illumination power is equal to 1 to allow comparison between different powers of illumination.

The right hand axis of Figure 3-3 demonstrates the success of the p-i-n contacting of the device, showing the raw current density for 15mW device illumation, showing that it is capable of sustaining the high current densities (over $3A/cm^2$) that a photovoltaic cell requires under concentrated illumination [80]. In addition to this high current density, the device also has a high V_{oc}, in excess of 1V in comparison to the previously presented n-i-n cell which had a V_{oc} of 0.5V. The significantly higher V_{oc} for the p-i-n structure is a result of the greater quasi-Fermi level separation between the absorber and collector, owing to the p-doping. In the n-i-n structure the only driving force was the photogenerated electron temperature and density difference between the absorber and the collector, whereas in the p-i-n structure there is also a field driving electrons into the collector. In this way the n-i-n structure is a clearer demonstration of a thermally driven current (since there is no other driving force present) while the p-i-n structure shows that this thermally driven current can supplement a field driven current and give rise to higher device performance. Given the mesa diameter of 15um we can use this JV to determine an approximate monochromatic efficiency at this wavelength and temperature of 1.6% for this device.

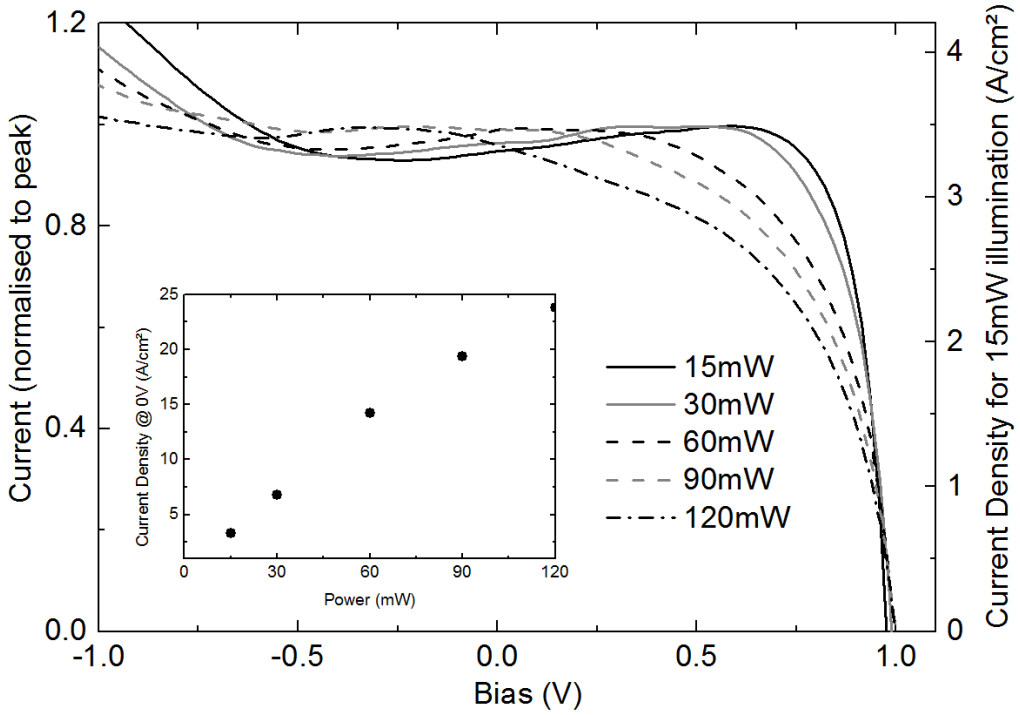

Figure 3-3. Experimental IV characteristic of the p-i-n structure held at a temperature of 115K and illuminated with 805nm laser light of power between 15-120mW focused on a 50um spot size. Left axis shows current of structure A normalized at 1 for current peak at all intensities, right axis shows absolute current density of structure A illuminated with 15mW laser output power. Inset shows linearity of response of J_{sc} with increasing power.

There is, however, a drawback with the p-i-n device in the dependence of the device characteristics on changes in light intensity that was not present in the n-i-n device. The dependence on light intensity was explored as this is a key factor to control for when determining the hot carrier IV response of a cell to different wavelengths of light. Previously other authors [35], [37], [62] have shown strong hot carrier effects based on heating electron populations through increased light intensity, observing carrier temperature dependent features in the PL emission of their structures. However, this method of generating hot carriers (generating different temperatures with different illumination intensities) causes difficulty in analysis and interpretation when we examine the current from the structure rather than solely its optical emission. In particular, features that are caused by hot carrier effects can also be attributed to changes in electron density.

Previously we demonstrated the hot carrier characteristics of an n-i-n structure by showing a wavelength dependence of the current peak position of the IV curve in section 2.1.2 arguing that this showed hot carrier transport from the absorber to the collector and showed that this was not sensitive to changes in electron density. This was necessary to rule out

fluctuations in photogenerated electron density contributing to any observed effect. The high sensitivity of the p-i-n sample to changes in light intensity, observed in Figure 3-3, means that analysing the wavelength dependence of the IV characteristic would be subject to much higher errors than the n-i-n analysis.

The difference between the two devices' response to changes in light intensity arises from the change in position of the quasi-Fermi level for electrons under illumination. For the n-i-n device absorption of light in the absorber region adjacent to the n-doped contact will not significantly alter the electron quasi-Fermi level, so the voltage response of the device is insensitive to changes in light intensity since the IV characteristic is determined by conduction band properties (i.e. tunnelling from the electron population). This is demonstrated in Figure 3-4 showing that the normalised IV characteristic changes very little for the n-i-n device for a doubling light intensity.

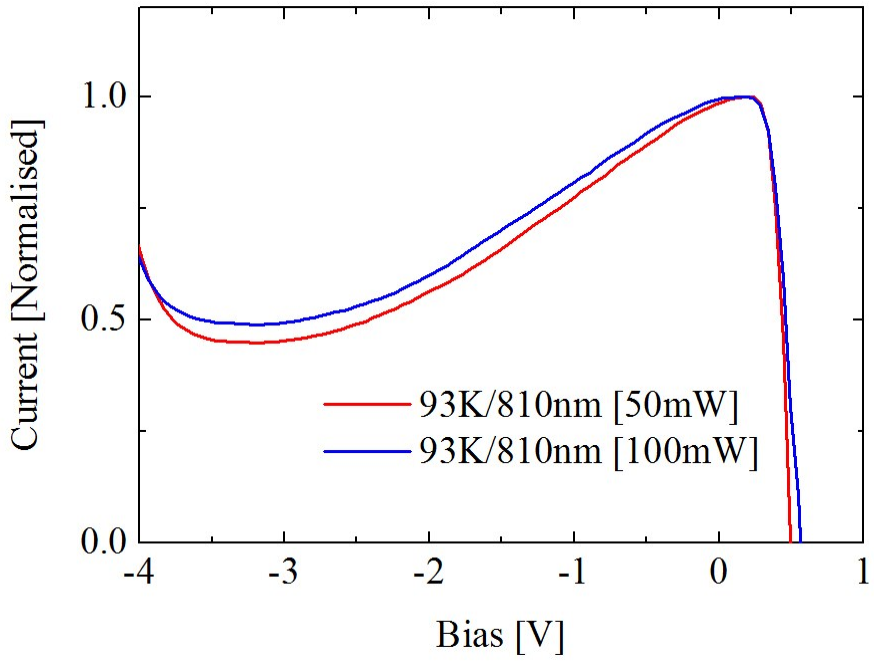

Figure 3-4. Power dependence of the n-i-n structure showing a limited change in the peak location and PVR in comparison to the equivalent p-i-n structure (Figure 3-3)

By contrast, for the p-i-n device absorption of light in the absorber region adjacent to a p-doped contact will significantly alter the electron quasi Fermi-level. This change in the electron quasi-Fermi level as a function of illumination intensity gives rise to the peak shift that is observed in Figure 3-3, with higher intensities giving a current peak at more negative biases.

Because the light intensity has such a large effect on the IV properties, significantly larger than any hot carrier effects we might expect to observe through either intensity or wavelength variations, examining the IV characteristics is not helpful in discriminating any hot carrier effects for this structure; though they are likely to exist due to the structure's similarity to the n-i-n structure, for which such effects have been shown. As such, the investigation of p-i-n hot carrier structures is continued in the rest of this chapter through purely optical means in order to explore the device structure and carrier transport.

3.3 Measurement of bandstructure by TDPL

HYL5 was designed to explore the carrier transport properties through the RTD state, which is a common feature across all our hot carrier photovoltaic structures, allowing for energy selective extraction from an absorber region to a collector region. In order to characterize the signature PL peaks of HYL5 we carried out TDPL on the sample, illuminating at 660nm with a diode laser and varying the lattice temperature of the sample between 88-293K. The PL emission peaks were assigned by fitting their temperature dependent peak shift to the Varshni equation [81], with material dependent parameters obtained from the IOFFE database [82]. The rms errors in these fits were lower than 1%.

Figure 3-5 shows three of the PL spectra obtained from HYL5 (at 88K, 153K and 293K) along with data points showing the assignment and location of the peaks at the other intermediate temperatures. An important feature of this set of spectra is the change in the relative intensity of the RTD and MQW peaks as temperature is decreased. At 293K the MQW and RTD peaks are of approximately equal intensity, as expected from a transfer matrix analysis of the absorption through the structure. However, as the temperature is reduced the RTD peak is strongly quenched relative to the MQW peak, reducing to nearly an order of magnitude lower in intensity than the MQW peak at 88K. This feature can be explained by carriers scattering into the MQW state from the RTD state, this scattering will presumably occur via the MQW+ state since these states are each separated by a little over 1LO phonon in energy and have a strong wavefunction overlap. The temperature dependence of this quenching is important in the analysis of the TRPL data in section 3.5 and will be investigated further by plotting the integrated PL of each peak in Figure 3-5 as a function of temperature in an Arrhenius plot.

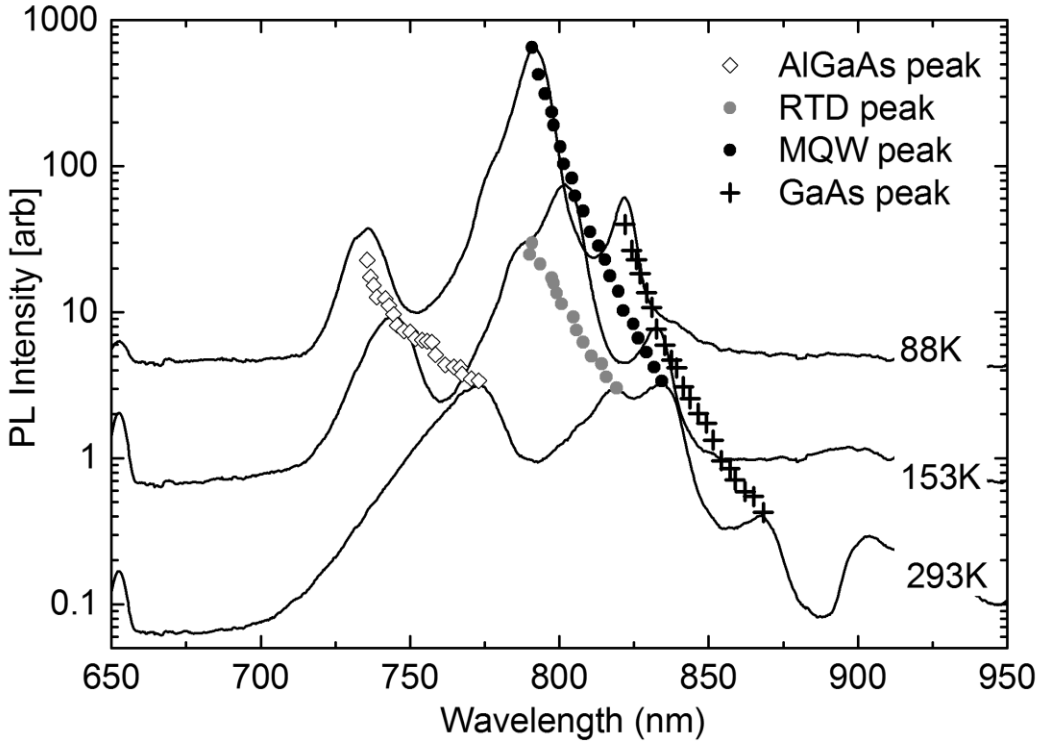

Figure 3-5. PL spectra for temperatures from 88K→293K, showing the low temperature quenching of the RTD peak relative to the MQW peak, the initial peak at 660nm is the diode laser used to illuminate the sample.

Figure 3-6 is an Arrhenius plot of the integrated PL of the GaAs, MQW and RTD regions, calculated from Gaussian fits to the peaks in the spectra shown in Figure 3-5. An Arrhenius equation representing the temperature dependence of the luminescence is then fitted to each plot with a least squares fit, revealing the activation energy required to quench the PL for each region [83].

The most important feature of Figure 3-6 is the activation energy for the GaAs peak, which is experimentally observed to be 74meV, within 5meV of the calculated value for the RTD transmissive state relative to the GaAs CB minimum (ΔE_1 in Figure 3-2). This is a strong indication that the quenching of the PL from the GaAs region is occurring through carriers transferring from the GaAs absorber through the RTD state, this will be further elaborated upon in section 3.5, in which the rate of the PL decay in this region is examined and it is determined whether this rate is compatible with tunnelling transfer and therefore hot carrier extraction as previously proposed.

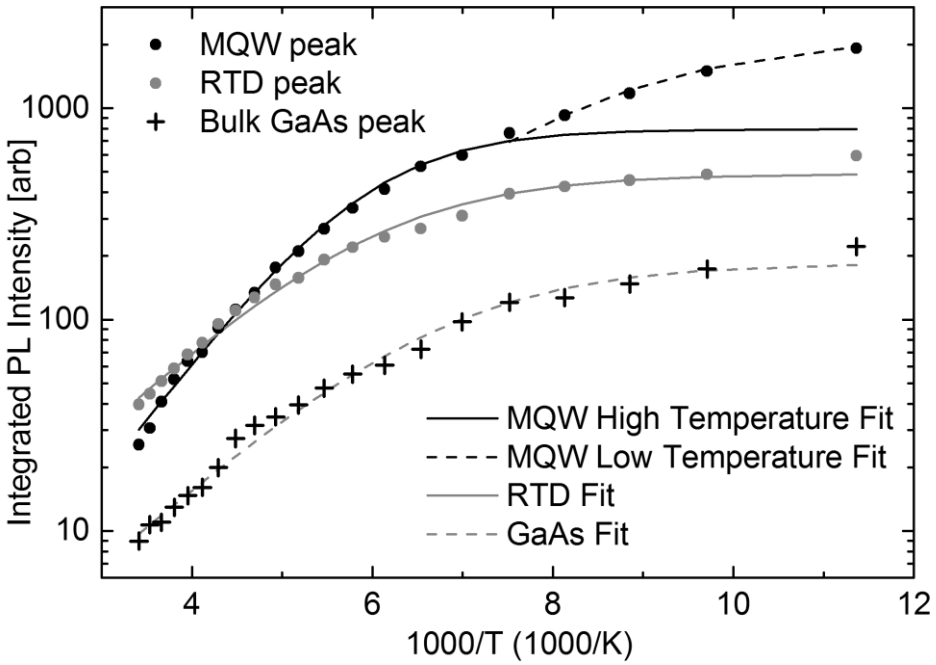

Figure 3-6. Arrhenius plot of integrated PL vs temperature for the key peaks

In addition to this important feature, a second feature of Figure 3-6 reveals further information suggesting the reason behind the temperature dependence of the quenching of the RTD peak relative to the MQW peak. The integrated PL of the MQW peak shows different behaviour either side of a critical temperature of approximately 140K, showing a transition to a higher activation energy required to quench the PL at higher temperatures (solid black line) than lower temperatures (dashed black line). This behaviour can be explained, with reference to Figure 3-2, as resulting from electrons in the RTD state in the MQW region (between 180-186nm in Figure 3-2) being able to be thermally excited out of the RTD state and into the AlGaAs continuum at higher temperatures. Our band structure calculations presented in Figure 3-2 show that the RTD state is 12meV below the AlGaAs continuum (ΔE_3 in Figure 3-2), meaning that for temperatures in excess of 140K carriers are able to be thermally excited from this region rather than decaying into the bound MQW state. This mechanism results in the behaviour observed in Figure 3-5, whereby at low temperatures carriers scatter from the RTD state into the MQW state quenching the RTD PL relative to the MQW PL, whereas at high temperatures this does not occur. It also means that carriers cannot escape from the MQW state via the RTD state at higher temperatures, but must go directly to the continuum, resulting in a higher activation energy (ΔE_2=110meV in Figure 3-2, agreeing exactly with the experimentally determined activation energy) for PL quenching at high temperatures for the MQW PL.

The two features revealed through the TDPL analysis, GaAs PL quenching from carrier escape through the RTD state and the temperature dependence of carrier transfer from the RTD to the MQW state, are important for the device operation of the hot carrier photovoltaic cell and are built upon further in section 3.5 to reveal their time dependence. In particular, due to the thermal escape from the RTD state to the continuum, this device only operates as designed below 140K.

3.4 Measurement of carrier temperature

With knowledge of the bandstructure obtained by the TDPL data in the previous section we now investigate the temperature of photogenerated carriers in the two particular areas of the device as a function of illumination intensity. As explained fully in section 2.1.1, the slope of the high-energy side of a PL peak can be used to infer the characteristic temperature of the electrons, which are decaying from the conduction band to the valence band and emitting the photons to yield the luminescence. Using this formalism, the temperature of the electrons in the absorber and collector of the cell is determined as a function of illumination intensity. The temperature of electrons as a function of illumination intensity with a 660nm laser in the absorber region (GaAs) and the collector region (MQW) is plotted in Figure 3-7.

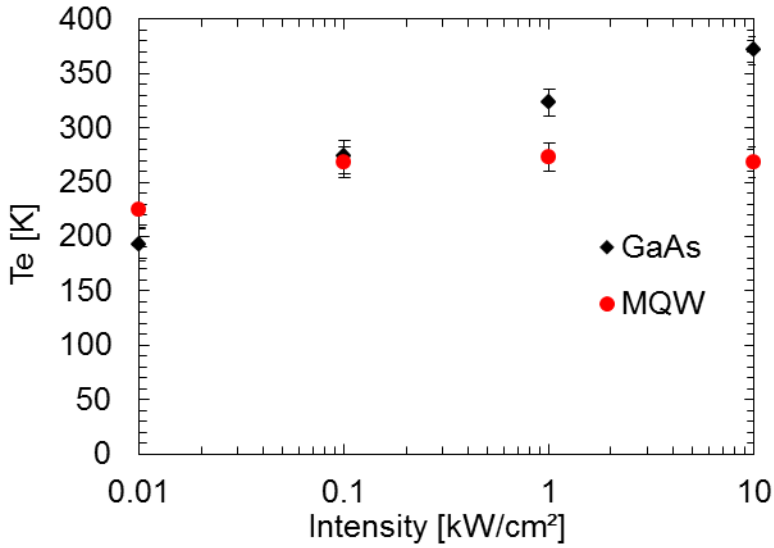

Figure 3-7. Electron temperature vs illumination intensity at a temperature of 93K with illumination at 660nm.

The linear increase in electron temperature with logarithmic increase in power for the GaAs region is the result of more energy being given to the carriers, as explained in section 2.1.1,

and a signature of hot carrier generation. It was verified that the peak energy itself did not shift, which would be attributable to an increase in the lattice temperature. Interestingly, the fact that the MQW electron temperature does not increase shows that this temperature is colder than the electrons in the GaAs absorber region and this structure is indeed acting as a heat engine with two electron populations at different temperatures. According to the presumed mode of operation, which is further revealed in the following sections, the temperature of the electrons in the MQW region should be defined by both the width of the resonance through which the electrons are being transferred to the MQW region and also the fact that they are not transferred at the conduction band minimum in to the MQW region but arrive with some extra energy in order to conserve momentum. The transmission as a function of potential is shown for the structure biased to V_{oc} (flat band) in Figure 3-8, showing that the full width at half maximum of the transmission from the GaAs to the MQW region is approximately 0.18meV. This would equate to a carrier temperature of around 3K, so it is likely that the biggest contribution to the carrier temperature in the MQW region is from the fact that these carriers are not transferred at the conduction band minimum.

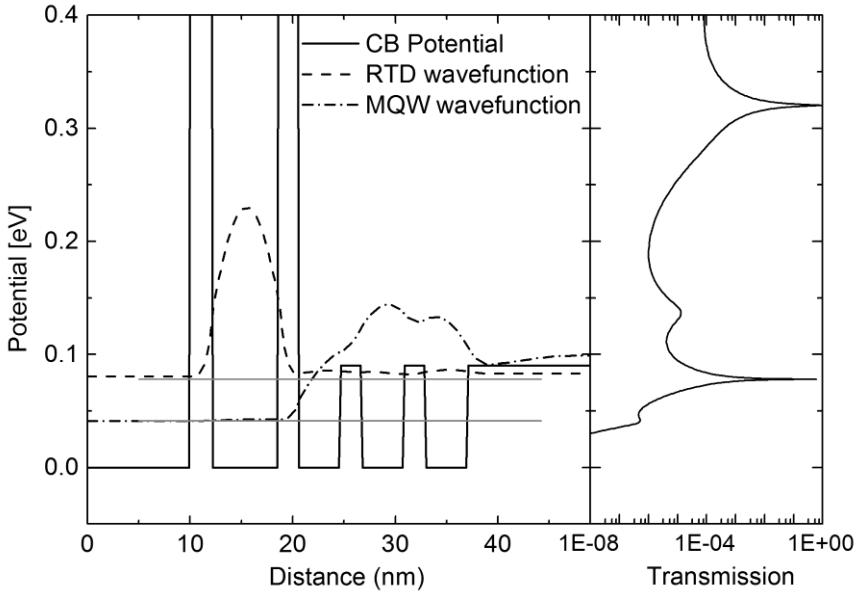

Figure 3-8. Band diagram and transmission as a function of potential.

These results should not be taken as an absolute temperature, as to obtain this detailed knowledge of the absorption is required and other considerations need to be made as discussed previously in section 2.1.1. However, if the absorption is unchanged over the range of intensities that are used (which is reasonable in this case) it can be used to compare the same structure at various states of illumination as carried out in this set of experiments.

3.5 Determination of carrier extraction speed by TRPL

In order to further explore the carrier transport properties in HYL5 TRPL was carried out at temperatures from 10K-270K using a Ti–sapphire laser at 720nm and with a pulse width of 30ps to excite the sample. The sample was cooled in a closed cycle helium cryostat and the time resolved PL spectra were recorded on a Hamamatsu streak camera.

The obtained images were all similar to Figure 3-9, with the previously assigned peaks marked on, but now with information as to the temporal dependence of their luminescence decay.

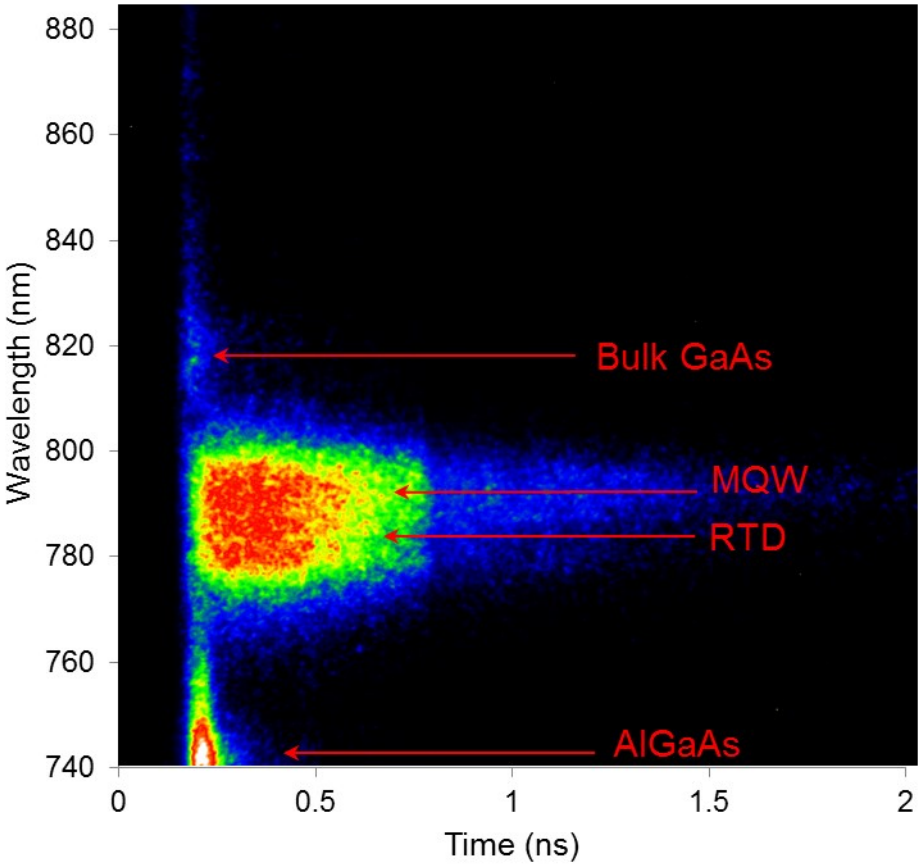

Figure 3-9. Streak camera plot of the emission from the MQW structure at a temperature of 93K.

The intensity at each peak was integrated over 5nm either side of the assigned peak, giving a "one dimensional" value, which could be compared with other peaks as a function of time. Figure 3-10 shows such a plot, with the normalized peak intensities for the GaAs, RTD and MQW PL emission plotted as a function of time at a lattice temperature of 10K. The time dependence of these peaks follows our expectations from section 3.3, with a very

fast decay for the GaAs PL giving further evidence to the proposed quenching mechanism of tunnelling through the RTD state. In comparison with the GaAs PL decay, the RTD and MQW states decay significantly more slowly as one would expect for radiative recombination in these regions. De-convoluting the laser signal from the GaAs signal reveals that the characteristic decay time for PL from this region is 10ps; combined with the evidence presented in section 3.3 this indicates carrier escape from the GaAs region through the RTD state via tunnelling. This is the designed mode of operation for our hot carrier cells, required for energy selective extraction, and it is on a timescale that is competitive with hot carrier decay in the GaAs region [26].

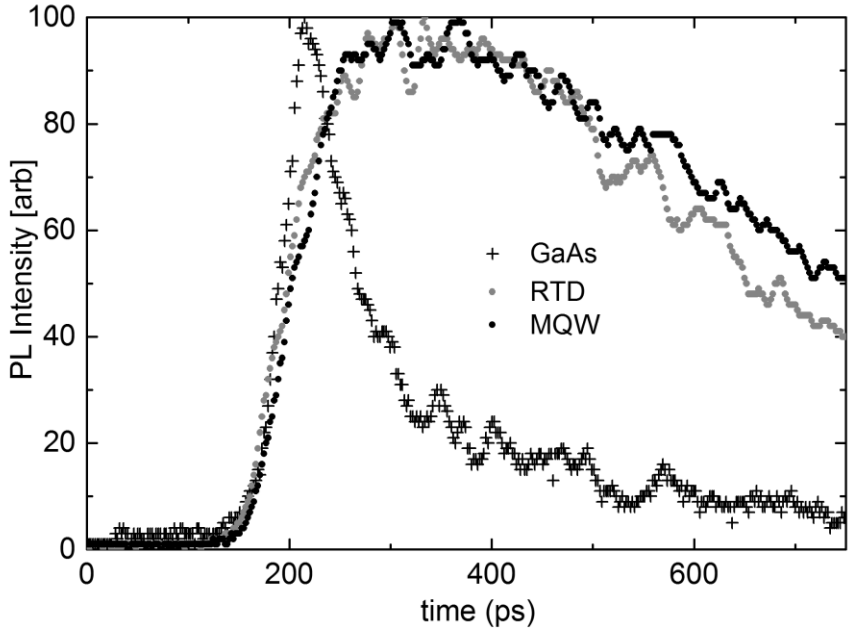

Figure 3-10. Time resolved photoluminescence data at 10K for the peak intensity as a function of time for the GaAs, RTD and MQW peaks

Figure 3-10 also reveals a small time difference between the peak PL observed in the GaAs region and the peak PL observed in the MQW and RTD regions. In order to investigate this further we fitted a bi-Gaussian equation to the TRPL data (to smooth over the periodic oscillations) and extracted the time difference (dt) between the GaAs PL peak intensity and the peak intensity for the MQW and RTD peaks over all the temperatures studied. This data is shown in Figure 3-11, revealing a constant temporal offset between the RTD and MQW PL peak intensity at low temperature, and between both these peaks and the GaAs peak intensity. This is further support for the suggested mode of operation of the cell, which is

transfer of carriers from the GaAs via the RTD state followed by scattering from the RTD state into the MQW state.

Figure 3-11 shows that this scattering occurs on a timescale of 30-40ps, agreeing with the TRPL decay oscillation period, which would result in the quenching of the RTD PL already observed in Figure 3-5. This total scattering time from RTD state to MQW state is long relative to the expected direct scattering time (approximately the LO phonon emission time). This is probably attributable to scattering occurring via the MQW+ state, since the overlap integral of the MQW+ and RTD wavefunctions is over four times larger than the overlap integral of the MQW and RTD wavefunctions. Further evidence for this carrier transfer from RTD to MQW can be seen in Figure 3-10 in the faster decay of the PL from the RTD state than the MQW state. This difference in PL decay also shows a similar dependence on temperature to that observed in the peak PL intensity shown in Figure 3-11.

Importantly the dt between the GaAs and RTD and MQW states reduces once the temperature exceeds 140K, tending towards zero; again supporting the interpretation that above 140K carriers are no longer confined in the RTD state in the MQW region and thus the majority of PL from the MQW and RTD regions at higher temperatures is attributable to direct photoexcitation in these regions.

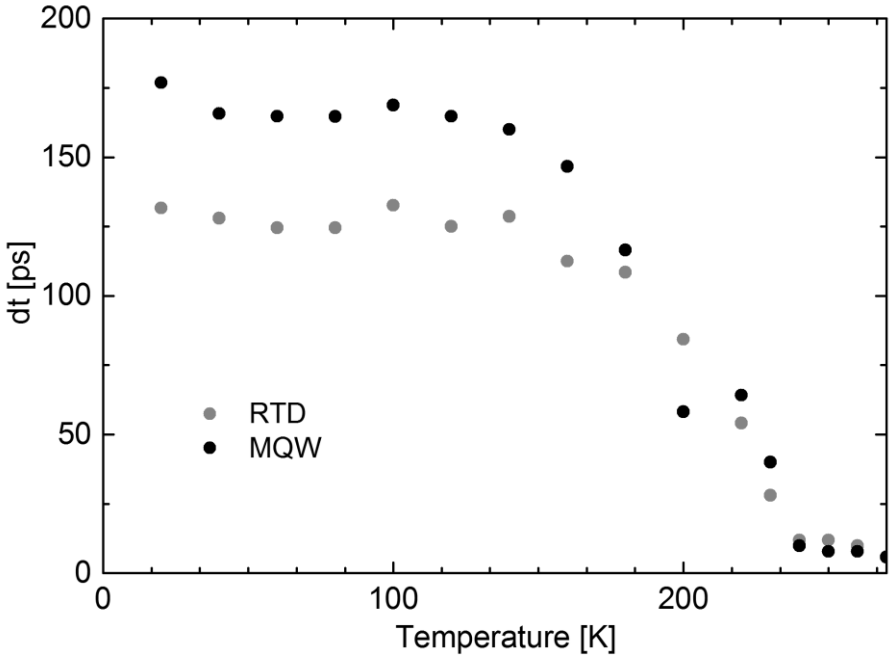

Figure 3-11. Time difference between peak PL intensity of GaAs peak and RTD peak (grey) and MQW peak (black)

3.6 Summary and problems with realising a hot carrier photovoltaic cell in a semiconductor

The TDPL and TRPL data presented in sections 3.3 and 3.5 has demonstrated that carriers are photogenerated in the GaAs absorber region of these structures and are extracted from this region via resonant tunneling on a timescale of 10ps. Furthermore, the carrier temperature measurements in section 3.4 confirm that the carriers in the absorber region are hotter than the carriers in the collector region. These pieces of data provide good evidence that this cell is indeed acting as an electron based heat engine, confirming the hot carrier photovoltaic device operation inferred from IV studies previously [40].

Both TDPL and TRPL data support the mode of operation such that at lattice temperatures below 140K carriers are extracted from the absorber region via a transmissive state and are scattered into a non-transmissive state. This temperature could be increased by further optimization of barrier heights. The fast extraction via tunneling is a requisite for hot carrier photovoltaic operation, allowing extraction of carriers before they thermalize. The transmission via a transmissive state followed by scattering into a non-transmissive state was used primarily as a signature to investigate the carrier dynamics in our cell, but could also be an important feature of an improved hot carrier cell, providing some directionality to the device, akin to a ratchet [14].

In addition to these optical assessments we have shown a low temperature IV characteristic of an improved prototype structure hot carrier photovoltaic cell structure, showing that such a cell supports a photocurrent density greater than $3A/cm^2$ and has a V_{oc} in excess of 1V.

While these improvements are promising, it is clear that a semiconductor-based hot carrier photovoltaic cell still has a variety of problems, which may prove challenging to overcome, in particular:

3.6.1 Low Absorption

The absorber section in a hot carrier cell is necessarily thin, to allow extraction of hot carriers before cooling. However, this also results in low total optical absorption, so the first key issue to overcome is how to make the cell “optically thick”, while being “electronically thin”.

3.6.2 Low temperature operation

Low temperature operation seems important to the first incarnation of hot carrier absorbers, since the rate of electron cooling ($\dot{Q}$) is heavily dependent on lattice temperature through its dependence on the number of LA phonon modes. The cooling rate equation for electrons in a thin semiconductor layer is presented as equation 3-1, as derived in appendix 3, showing its dependence on the population of phonons through the Bose-Einstein function (n) and hence its exponential temperature dependence.

$$\dot{Q} = Z(Z-1)\frac{D_i^2 k_B T_a m_e^2 (2+\delta_{fi})\Omega}{2\pi\hbar^3 \rho w^2 (\hbar\omega)} \left\{ \begin{array}{l} n\int f(E)(1-f(E+\hbar\omega)dE - (n+1)\int f(E+\hbar\omega)(1-f(E)dE \\ -(n+1)\int f(E)(1-f(E-\hbar\omega)dE + n\int f(E-\hbar\omega)(1-f(E)dE \end{array} \right\} \quad (3\text{-}1)$$

This equation can be compared to Marti's equivalent work for 3D "bulk" absorbers as equation 16 in his paper [24], with the key difference being that the scattering increases quadratically as the well width (w) decreases. The symbols follow his conventions and are fully described in appendix 3.

3.6.3 Narrowband operation

The absorption in the devices presented in [40], [78] and in this chapter is necessarily narrow band, with absorption allowed in the narrow band gap absorber, but not the wider band gap material. In order to create a high efficiency device it is necessary that absorption occur across the entire solar spectrum. The optimum hot carrier solar cell would have a band gap of zero, allowing it to absorb light of all wavelengths.

3.6.4 Improved methods for realising a hot carrier cell

The following two chapters build on the proof of principle for a hot carrier solar cell that we have already presented and focus on a way to address the above highlighted issues with the current design by using a metal as an absorbing region rather than a semiconductor.

4 THEORETICAL DEVELOPMENT OF A METALLIC HOT CARRIER CELL

In order to realise the maximum efficiency achievable with a hot carrier solar cell under full concentration it has already been stated that the optimum band gap is zero, favouring a metallic or semi-metallic absorber over a semiconductor absorber. This might appear to have drawbacks not only in terms of light absorption and the creation of energy selective contacts, but also in terms of electron scattering due to the high electron density in metals. However, with careful choice of both material and structure it will be shown that high absorption of light and good extraction of hot electrons is not only possible, but can be much better in metallic structures than in semiconductors.

Section 4.1 justifies the choice of a metal absorber for the hot carrier solar cell, based on a review of their known properties, providing a context for our choice of a metallic absorber. This section in particular overviews the mechanism of light absorption and hot carrier generation in metals, which can be subtly different from the dominant mechanism in semiconductors. From section 4.3 onwards we present our work theoretically optimising the absorbing layer of metal used in these cells and developing the conceptual device architecture that can be used for hot carrier generation and extraction in metals. More detailed modelling of the metallic solar cell is carried out at the end of the chapter in section 4.4, predicting features that should be observed in an operational cell.

4.1 Justification of metals for a hot carrier PV cell

4.1.1 The photovoltaic benefits of a metallic absorber

The primary benefit of a metallic or semi-metallic absorber for a solar cell is that, in principle, it has an effective band gap of zero; in as much as there are empty electron states infinitesimally close to occupied states, allowing arbitrarily small excitations of the electron gas. Whether these excitations can be exploited in a solar cell is covered in section 4.1.2, but for the sake of an initial justification, this is a good first step as it allows absorption of a very broad spectrum of light.

In addition to this, perhaps obvious, benefit of using a metallic absorber there is a subtler reason highlighted by Würfel [84], which is often overlooked. Würfel makes the point that demanding energy and particle conservation in a hot carrier solar cell leads to physically nonsensical results, in particular that the extraction of carriers must happen precisely at the average photon energy of the incident light in order that the temperature and chemical potential of the carrier distribution do not diverge. This absolute requirement would make any cell based on this principle so ludicrously inflexible it would be practically inoperable. Rather than using this as evidence that the hot carrier solar cell concept was doomed, Würfel instead suggests that to allow for physically sensible parameters to emerge it is necessary that impact ionisation and Auger recombination are included in models. This weakens the particle conservation requirements and allows some flexibility in the relationship between the average photon energy of the incident light and the average electron energy of the resulting hot carrier distribution.

The benefit to cell operation provided by Auger recombination and impact ionisation in the hot carrier cell means that these processes are likely to be fundamental to any highly efficient cell. This is in stark contrast to standard photovoltaics, in which Auger recombination is generally viewed as a significant loss mechanism. In terms of the discussion in section 1.5.3.1, what these processes allow is rapid redistribution of the hot carrier energy to allow repopulation of the energy level from which carriers are extracted. As long as these processes are all faster than the irreversible loss of energy to the lattice the cell will operate effectively. The benefit of metals in this context is that the scattering (impact ionisation) rate of high energy electrons is significantly higher than in semiconductors, allowing much faster redistribution of electron energy.

With these indications that realising a hot carrier solar cell in a metal might be a promising route, the following subsections of this section examine in more detail how this could be achieved.

4.1.2 The microscopic theory of metallic optical absorption

For the semiconductor structures mentioned in previous chapters, absorption occurs primarily through excitation of an electron from the valence band into the conduction band of a material. For metals, four different absorption mechanisms are possible [85]: interband absorption and three types of intraband absorption, in which momentum is conserved by either phonon emission, electron-electron scattering or surface plasmon-polariton generation.

In the optical and NIR wavelengths investigated in this work, the metals that we use show little interband absorption, and they are not structured or illuminated in such a way to make the generation of surface plasmon-polaritons likely. Therefore, direct absorption, with momentum conservation through either electron-electron scattering or phonon emission, are the key absorption pathways. Direct excitation with momentum conservation through phonon emission, through what is generally termed Drude or free-carrier absorption, is important to understand microscopically in order to determine whether and how it can be exploited and how our choices of materials and structures can influence this.

Light incident on a metal will interact with the electron population by causing it to oscillate at the same frequency as the incident field. This oscillation in an idealised metal results in the reflection of the incident beam, and does not lead to absorption as there is no mechanism for the loss of energy from a free electron gas interacting with an electromagnetic field. In particular, an oscillating electron, or gas of electrons, has no momentum associated with it, unlike the electrons which contribute to the photocurrent in a material. Holstein [86] set out the mechanism by which this interaction could lead to absorption, maintaining conservation of momentum through the interaction of the oscillating electrons with either the surface of the material [87] or the ions in the lattice [88]. This latter process is essentially inverse Bremsstrahlung and involves the oscillating electron absorbing the incident energy in the electromagnetic field by simultaneously emitting a phonon to conserve momentum.

The absorption through bulk phonon emission, often termed the volume absorption (A_v), is inversely dependent on the electron density (n) and the conductivity relaxation time (τ_e), as given in equation 4-1:

$$A_v = \left(\frac{m^*}{4\pi n e^2}\right)^{1/2} . \frac{2}{\tau_e} \tag{4-1}$$

Given that the electron density and conductivity relaxation time are also factors which linearly contribute to the conductivity of a metal, it is clear that the best metals for high absorption are likely to be those at the lower end of the conductivity spectrum, such as Lead and Chromium. Chromium in particular shows appreciable free carrier absorption in addition to some very complex absorptions due to an antiferromagnetic transition, interband absorptions and excitations from the fermi surface to some very flat bands less than 1eV away [89]. Irrespective of the precise mechanism, bulk Chromium shows a relatively flat and very broadband absorption of 30-50% from 0.4eV-5eV, highlighting its promise as a metallic absorber.

These materials will form the focus of optimised devices presented in the following chapter, but prototype devices fabricated from Silver will also be shown as these were used to prove the principle of the metallic solar cell, for simplicity and robustness of fabrication, and still show absorption on the order of 10-15%.

4.1.3 Benefits of thin films of metal

Following on from the previous analysis, inspecting the form of the equation for the surface absorption [87] of metals gives an indication that further absorption enhancements can be gained by thinning the metal absorber such that two interfaces (top and bottom) can be active in the electron scattering process in addition to phononic scattering. This necessitates films that are of the order of the metallic skin depth and so would look semi-transparent as an isolated film. A thin film is also necessary from the perspective of electrical extraction of hot carriers, as the metallic layer must be thinner than the electron-phonon mean free path.

While thick metals are generally highly reflective due to the electron plasma effectively screening the electromagnetic field from the bulk, various groups have already experimentally shown the benefit of using thin films for light absorption. Ahmad [90] has shown that 46% of total solar radiation is able to be absorbed in a thin film (13nm) of nickel with no anti-reflection coating. In addition, Hilsum [91] showed as long ago as 1954

that the addition of simple dielectric layers to thin metallic layers could enhance this absorption, by setting up a resonant optical cavity, leading to over 70% absorption. With improved antireflection coatings this absorption figure can be improved further to over 99% between 400-800nm [92], allowing significant absorption across the full solar spectrum through what is effectively impedance matching free space and a thin metallic film. The high absorption possible in thin films of metal is further investigated in section 4.2, where the microscopic absorption mechanism already described is related to macroscopic material quantities and optimum materials properties and dimensions are calculated for a good optical absorber.

4.1.4 Exploitation of a hot carrier distribution

Having shown that strong light absorption is possible in metals, the question is then whether intraband absorption can create useful hot carrier distributions, from which electrical extraction is possible. To answer this question it is necessary to determine the timescale over which the distribution cools. With reference to the discussion in section 1.4.1, this timescale is not the scattering time of electrons with each other, which can be ~10-100fs in metals [93], it is instead the rate at which the entire electron distribution loses energy to the lattice. This occurs through interaction with longitudinal ionic modes in metals [94], similar to the LA phonon modes in non-polar semiconductors, allowing direct dissipation of electron energy to the lattice. This timescale is related to the conductivity relaxation time (τ_e), as at each phonon emission the electrons will lose energy to the lattice, so optimising this timescale so it is short enough to allow light absorption but long enough to allow electron extraction is the balance the must be struck in developing the metallic hot carrier photovoltaic cell.

Fann et al [95] performed a Time Resolved Photoemission Spectroscopy experiment, illuminating gold with a 180fs pulse of 1.84eV light and determining the electron distribution as a function of time after this initial illumination. They showed an initial non-thermal distribution was generated followed by thermalisation (through e-e and e-p interactions) to a heated Fermi distribution within ~1ps, Figure 4-1.

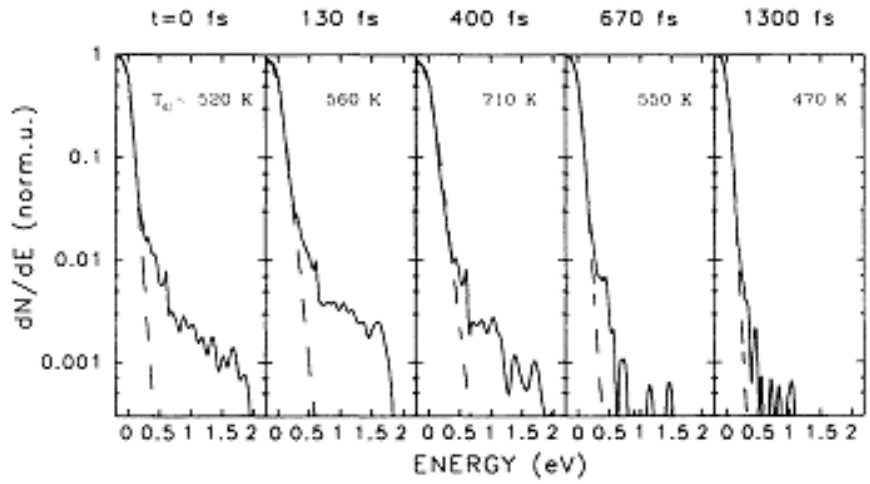

Figure 4-1. Evolution of the electron temperature in Gold from [95] showing a 1ps timescale to reach a hot fermi distribution after initial excitation of a non-thermal distribution by a 1.84eV laser.

This experiment took place at room temperature, demonstrating the existence of a heated electron distribution was still present after 1.3ps, an encouraging timescale for electrical extraction, especially given the thin film requirement for high absorption in metals. A relatively crude estimate using the thermal velocity of electrons (v_t~10^6m/s from [96]) shows that electron extraction from a 20nm thick film of Gold will happen on a timescale of ~0.02ps, long enough for electron-electron interactions to equilibrate electrons in a population, but short enough to extract them before they lose appreciable energy to the lattice. This crude estimate actually provides quite a reasonable comparison with experimental results investigating the extraction of electrons from thin films [97].

This justification for Gold also holds for Cr, but Cr actually has some further improved properties in that it can achieve a hot, but thermalised, population in as little as 100fs [98] with hot electron thermalisation with the lattice still taking longer than the timescale required to remove electrons from the metal layer.

The combination of high intraband absorption, a hot electron lifetime on the timescale of ps and rapid electron equilibration to a hot thermal distribution are encouraging, and show that there are no fundamental reasons why a hot carrier cell should not be possible using a metallic absorber. The loss of energy to the lattice after photoexcitation of a metal occurs on a timescale that is an order of magnitude slower than the likely extraction time from a thin film, so extraction of useful energy should be possible.

With this initial feasibility assessment showing the promise of such a cell, the following sections will present our work showing how the absorption of light in such a cell can be optimised (section 4.2), the conceptual structure for hot carrier extraction (section 4.3) and the signatures that can be expected from the IV characteristic of such cells if they are operating as a hot carrier cell (section 4.4).

4.2 Modelling of absorption in metals

4.2.1 Optimising the absorber properties

The microscopic mechanism for light absorption in a thin metallic film has already been discussed in section 4.1.2; however, it is important to understand how this microscopic mechanism manifests itself in the macroscopic properties of the material. The macroscopic quantities associated with the absorption of light in any medium are the extinction coefficient and refractive index, so it is important to examine how varying these quantities impacts the absorption of light in a thin film in order to optimise our material choice.

Using the transfer matrix solver described in chapter 2 and appendix 5 the absorption in a 10nm film of material held between two dielectric media of refractive index 1.47 (representing SiO_2) was studied as a function of its refractive index and extinction coefficient. A contour plot showing the absorption in the film at 500nm illumination is shown in Figure 4-2, demonstrating that the highest absorption in a thin film occurs when the refractive index and extinction coefficient are both approximately 3-4. Reassuringly, this macroscopic assessment yields the same favoured material of Chromium as did the microscopic analysis. Various materials used in this work are plotted in Figure 4-2 for reference. In particular, it is interesting to note that a 10nm thick film of GaAs and Au have similar total absorptions at 500nm, but for very different reasons. Macroscopically, GaAs has too low an extinction coefficient which microscopically leads to low absorption and high transmission, while Au has too low a refractive index, given its extinction coefficient, which leads to strong reflection.

The thickness of the metal layer will also influence the results shown in Figure 4-2, though not particularly strongly for the structure explored here (10nm layer between SiO_2 regions). Figure 4-4 shows how sensitive the absorption of Cr is on the thickness of the layer for the structure explored here (b) and once it is formed into a resonant structure (d), which is why the identification of promising materials was not carried out using a resonant structure.

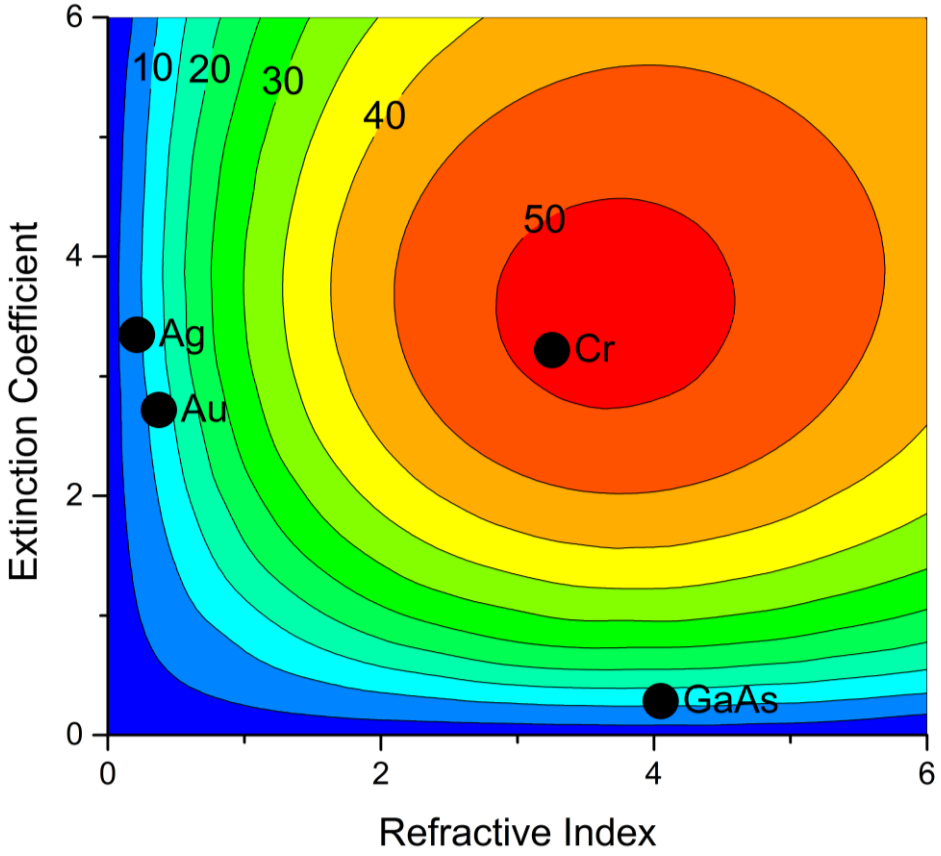

Figure 4-2. The absorption in a 10nm thick layer with the specified refractive index at 500nm, embedded between two SiO2 regions of 1000nm thickness. Various real materials used in this work are plotted for reference

With the optimised absorber provided by a thin film of Chromium (or another metal with similar refractive index and extinction coefficient, like Molybdenum) it is now worth optimising the structure to enhance this absorption further.

4.2.2 Improving absorption with resonance

In order to improve upon the absorption of light in a thin metallic film we can make use of two effects, reducing the reflection from the top surface and creating a resonant cavity in what is effectively an optical frequency Jaumann layer [99] (as used in early anti-radar coatings). These improvements are made by adding a thin layer of dielectric to each side of the thin metallic film and also adding a highly reflective back surface on the side furthest from the incident light. To demonstrate the benefit of an optimal thickness dielectric coating on each side of the metal thin film and a back surface reflector, the absorption/reflection/transmission properties of four structures were modelled, schematically illustrated in Figure 4-3.

The structure shown in a) gives the baseline absorption attributable to the good optical absorption properties of Chromium, structure b) shows the benefit of reducing the reflection from the top surface, structure c) shows the benefit of a back surface reflector which turns the region in between the Chromium and back reflector into an optical cavity and structure d) shows the benefit of preceding this with another layer of SiO_2 such that reflections from all surfaces are matched in antiphase.

A schematic illustration showing the phase of the reflected electric fields is shown in c) and d) to explain how reflection is reduced in these structures. Adding a further SiO_2 layer effectively gives an extra degree of freedom, allowing better phase cancellation between the reflected waves, resulting in a double minimum in the reflection profile as a function of wavelengths, as presented in Figure 4-5, yielding a low reflectivity over a much broader range of wavelengths.

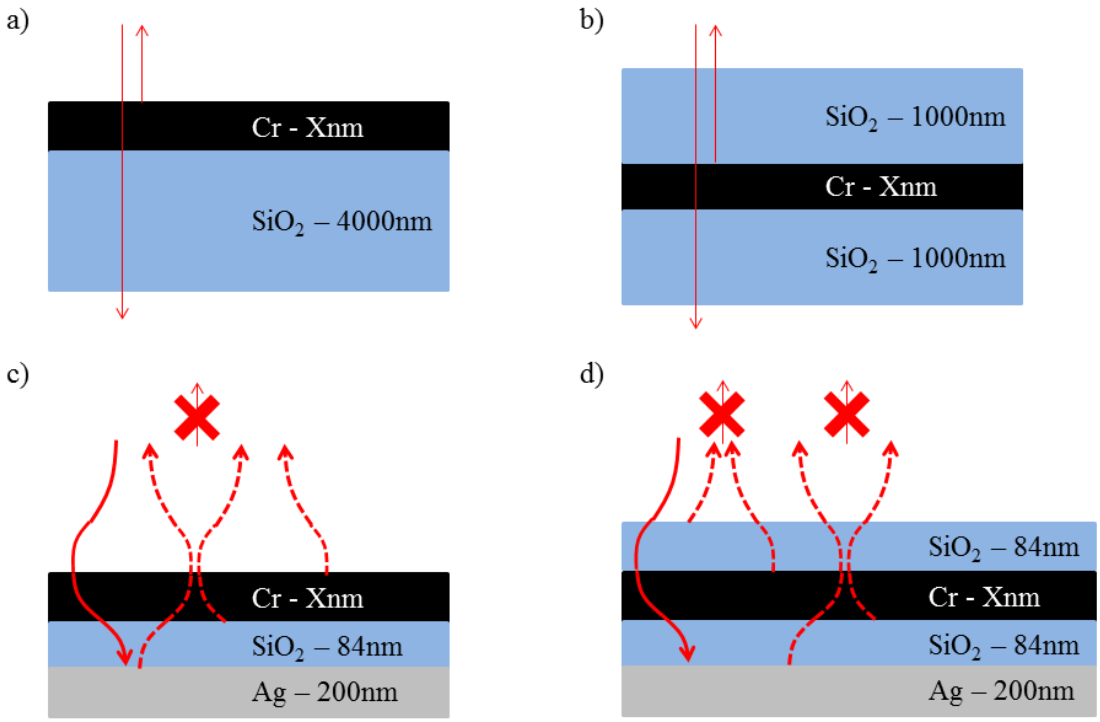

Figure 4-3. The four structures modelled to reveal the benefits of a) a Chromium absorber b) a SiO2 coupler c) A back reflector to provide a cavity d) a back reflector combined with an anti-reflective coating to provide a broadband cavity. The arrows for c and d show the phases of the electric field of the reflected light to explain the anti-reflection property.

Each of these structures was modelled for a varying chromium thickness, the absorption, reflection and transmission through each of these structures is shown in Figure 4-4 at a wavelength of 500nm. The absorption of structure a) for large Cr thickness was compared with the literature to ensure the accuracy of the model, literature values of absorption for such Cr films range from 35-40% [89], [100] agreeing well with these results. Adding a top surface dielectric in b) to reduce the reflection increases the Cr absorption by 10% absolute. The benefit of the cavity is then clear in the results from structure c) showing a 95% absorption is possible with an optimised Cr thickness of 6nm.

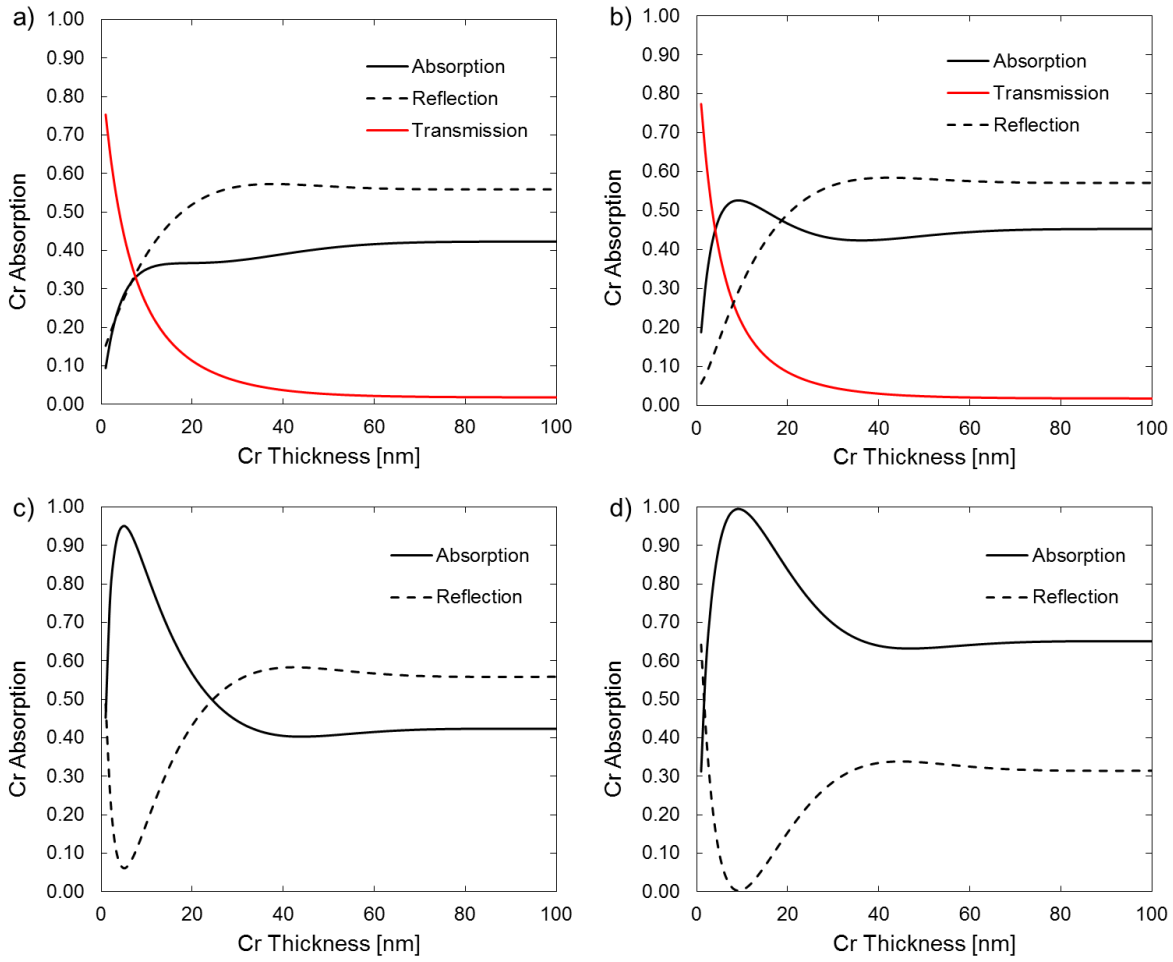

Figure 4-4. Fractional absorption, reflection and transmission of light at 500nm in a thin film of Cr shown as a function of Cr layer thickness for four different layer structures, as graphically illustrated in Figure: a) Cr on 4000nm of SiO_2. b) Cr sandwiched between two 1000nm thick SiO_2 regions. c) Cr/SiO_2-84nm/Ag d) SiO_2-84nm/Cr/SiO_2-84nm/Ag.

The absorption in the Cr layer of structure c) is already appreciable, at 95%, and the addition of a further SiO_2 layer in structure d) only adds a further 4% to this. However the benefit of this extra layer becomes clear when the wavelength dependent reflection is

plotted for each of these two structures, as in Figure 4-5. Structure d) has a reflection lower than 5% over the entire range from 450nm-1100nm, exhibiting the double reflection minimum characteristic of a Jaumann bi-layer [99]. Intuitively, the ultra-low, broadband reflection in this structure can be understood from the fact that as the wavelength of light increases, while this increases the optical pathlength from reflections of the interfaces either side of the rear dielectric, the same path length increase occurs for the reflections from the interfaces either side of the front dielectric, maintaining the antiphase relationship between these reflections. Thus if the Chromium layer is such that it allows approximately 50% transmission these two effects cancel out, allowing absorption over a much wider range of wavelengths than a standard *λ/4* antireflection layer.

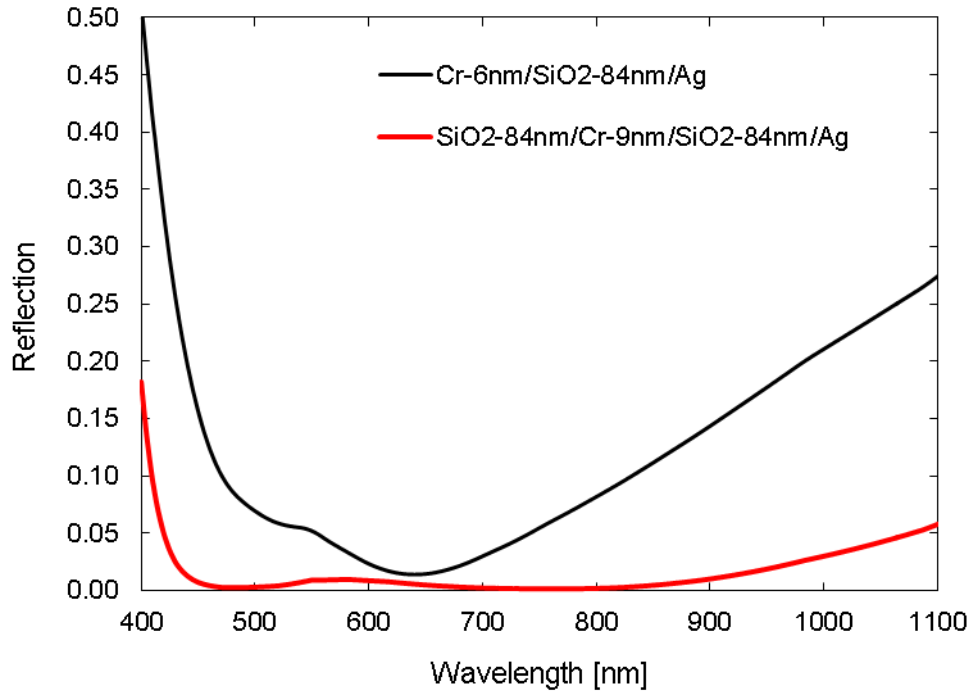

Figure 4-5. A comparison between the reflection as a function of incident wavelength for a structure with and without a top anti-reflection coating: Red: SiO2-84nm/Cr-9nm/SiO2-84nm/Ag Black: Cr-6nm/SiO2-84nm/Ag

To perform a simple verification of this modelling we grew and characterised a sample based on the above geometry. Gold was used in this case as it is a more common back contact metallisation, which will be more appropriate for the later fabrication of metallic solar cells. The intended structure was SiO_2-80nm/Cr-10nm/SiO_2-80nm/Au-150nm, with Au thermally evaporated on a glass substrate, followed by PECVD SiO_2 deposition, thermal evaporation of Cr and further subsequent PECVD SiO_2. All layers were within ~10% of intention with the exception of the top SiO_2 surface, which deposited more slowly

than expected on the Cr surface. The actual layer structure was examined by cross-sectional SEM, Figure 4-6, to assist future fabrication and to allow accurate comparison with the optical model. A Chromium layer of 10nm was intended, rather than the optimal thinner layers, due to fabrication constraints. Planar layers of Chromium thinner than 10nm are virtually impossible to achieve and normally result in island formation; this is based on prior experience of thermal evaporation of Cr films and is backed up extensively in the literature e.g. [101]. The planar layer of Cr in this sample is clear in Figure 4-6.

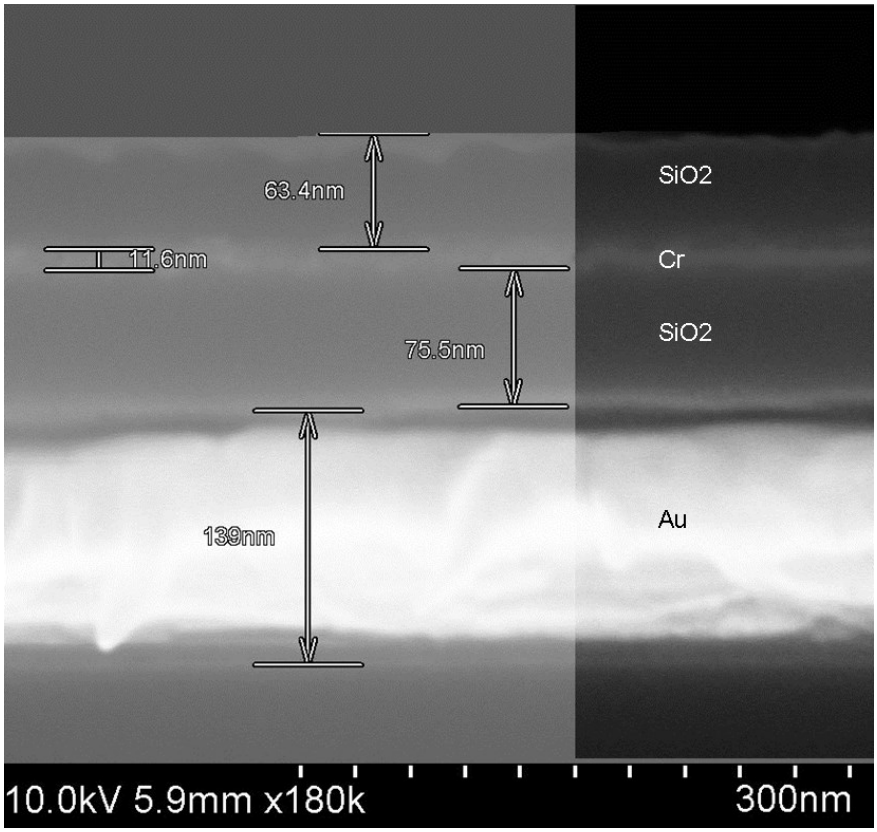

Figure 4-6. Cross sectional SEM image of a SiO_2/Cr/SiO_2/Au absorption structure

The reflectivity as a function of wavelength of this sample was measured with reference to a calibrated Silver mirror, with wavelength discretisation achieved through use of a monochromated Xe source. Measured reflectivity as a function of wavelength compared well with the transfer matrix model, Figure 4-7, and the resulting visual appearance of the structure is shown inset, confirming its high absorption with a black appearance. The top right corner of the sample shows the absence of Cr, as this was where the substrate was clamped during Cr deposition, thus it is clear the impact such a thin layer of Cr has on the optical properties of the sample. It should be noted that in modelling the Cr layer a 1nm Chromium Oxide layer is assumed to have formed at the top surface of the Cr. This assumption follows suggestions from the literature [102] that such a layer is likely to form

and protects against further film degradation, and also ellipsometry and reflectivity data of a control sample that was grown with 100nm of Cr evaporated onto a SiO_2 substrate.

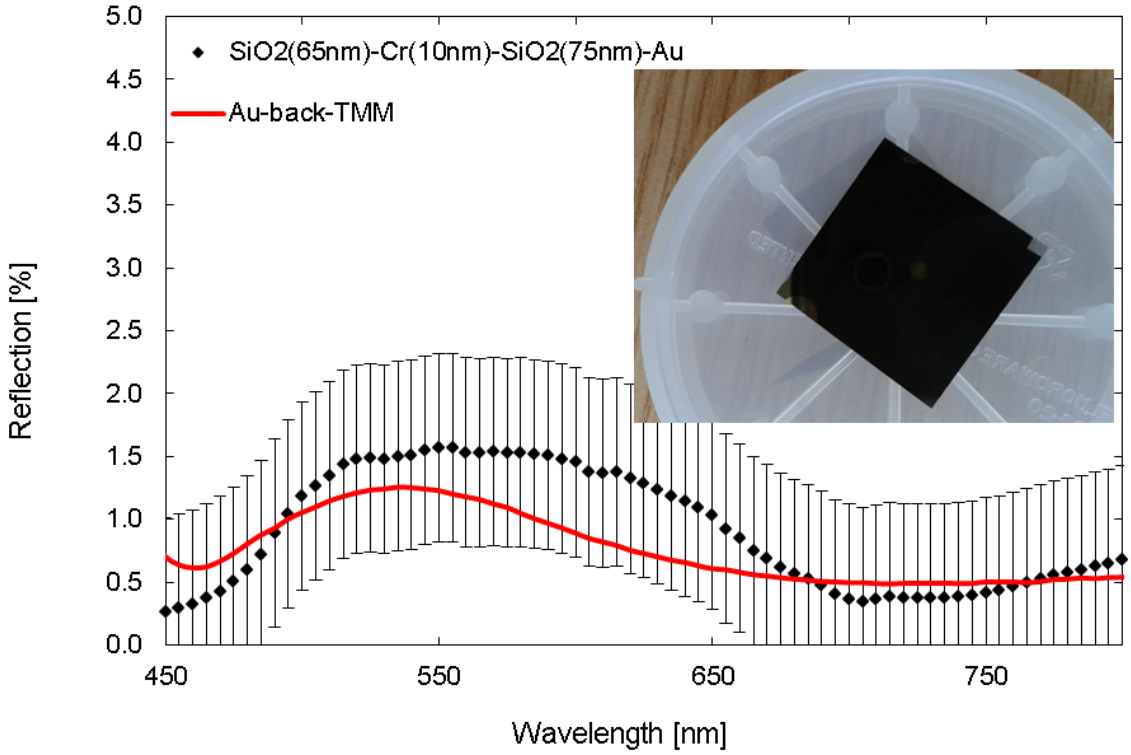

Figure 4-7. Reflection as a function of wavelength for the sample absorption structure. Inset: Sample structure fabricated on a glass substrate

This initial experimental feasibility shows the promise that thin films of metal hold in the strong absorption of a broadband of light. With this aspect of the cell proven, we will now concentrate on how such absorption can be exploited to develop a hot carrier solar cell.

4.3 Concept of a hot carrier metallic PV cell

While we, and others, have shown that thin films of metal can absorb strongly and have sufficient hot carrier lifetimes to permit hot carrier extraction, what has not been shown is how one could fabricate a hot carrier cell to exploit this. With the structures previously presented in this chapter the metallic absorber is held between two dielectric films, as such there is no way to extract electrons from the hot population that is generated.

A simple way to extend this is to replace one of the films with a semiconductor layer, which can support electron transport and offer a method to remove hot electrons from the metallic layer. One important feature of this film is that it should be optically transparent at

the wavelengths of interest, i.e. it should ideally have a wide band gap; AlGaAs and AlInAs are two easily grown wide band gap semiconductors, lattice matched to common growth substrates, which fulfil this requirement. Figure 4-8 shows one possible structure using 35nm of AlInAs in place of the second dielectric layer and using Au as the back reflector, as this can also operate as a contact material for a wide range of semiconductors.

Figure 4-8 shows the modelled reflection as a function of wavelength for this new structure, demonstrating that replacing the dielectric layer with a semiconductor layer does not significantly increase its reflection, which still averages only 5% over the range shown.

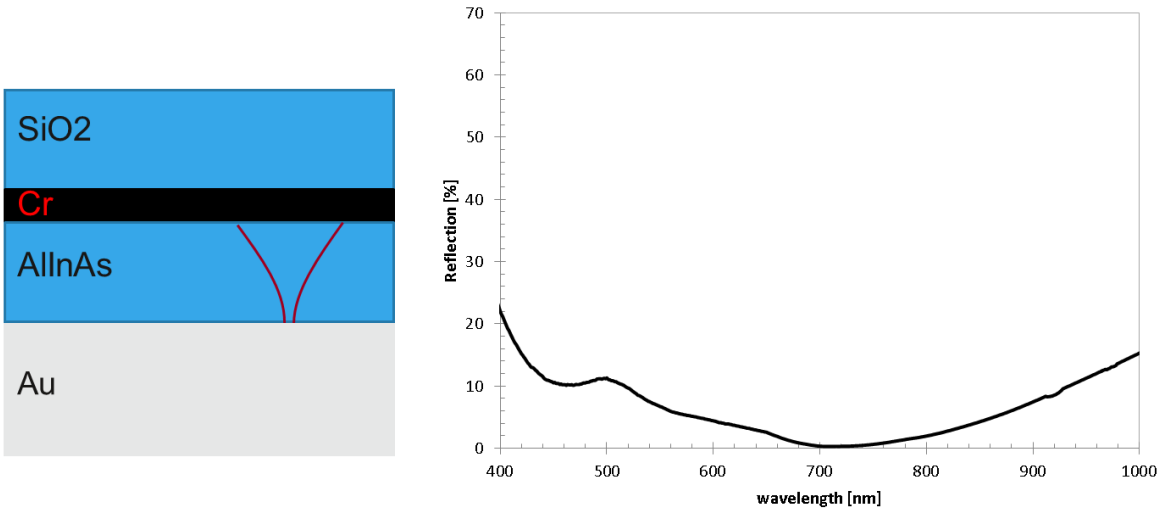

Figure 4-8. Left: A structure with a 35nm layer of a wide bandgap semiconductor (AlInAs) following a thin layer of Chromium, showing broadband absorption in the Cr layer. Right: Reflection as a function of wavelength for this structure.

Demonstrating that a thin semiconductor layer can replace one of the dielectric films, while still maintaining high absorption in the metallic thin film is important as it allows construction of structures using metal/semiconductor junctions in order to extract carriers from the metal layer. As already explained in section 1.5.3 some form of energy selective extraction is required in order to exploit a difference in electron temperature between two regions, so the following two sections present two different methods to achieve this extraction at a metal/semiconductor junction. The first method, presented in section 4.3.1, is to exploit a Schottky barrier at this interface to provide a semi-selective contact between the metal and the semiconductor, allowing electrons with an energy in excess of the Schottky barrier height to escape the metal. The second method, presented in section 4.3.2, is to extract electrons by tunnelling from the metallic layer through a quantum well to allow full energy selectivity.

4.3.1 Schottky barrier extraction

Placing a metal and an n-doped semiconductor adjacent to each other results in the formation of a Schottky barrier [103], a rectifying junction which has very low current from the metal to the semiconductor at all biases and only permits a current from the semiconductor to the metal when a sufficiently high bias is applied.

For the proposed metallic solar cell, the method of operation is such that light incident on the metal film will be absorbed in the electron distribution in the metal, heating the electrons from T_c to T_h as in Figure 4-9. The electrons in this heated distribution can then traverse the Schottky barrier resulting in a current at zero applied bias due to the electronic temperature difference between the metal and the semiconductor. Any electrons below the Schottky barrier height can still contribute to device efficiency by scattering with higher energy electrons.

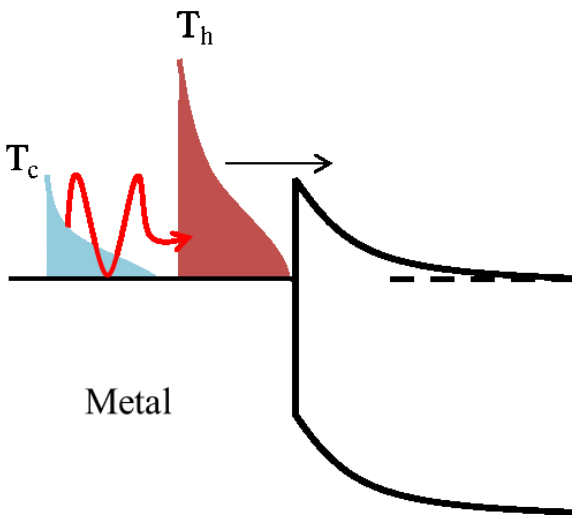

Figure 4-9. The metallic solar cell concept with Schottky type extraction of hot electrons

This method of hot electron extraction will be explored in more detail in section 4.4 where the IV characteristics of a cell operating by this principle will be modelled.

4.3.2 Tunnelling extraction

Simply placing a metallic layer next to a semiconductor layer creates a semi-selective contact, however, as stated in section 1.5.3, increasing the selectivity of the contact brings large benefits to the efficiency of the device through reduced heat loss from the electron distribution. To effect such selectivity in the metallic cell one can imagine placing a

quantum well in the semiconductor region close to the metal/semiconductor interface, schematically shown in Figure 4-10.

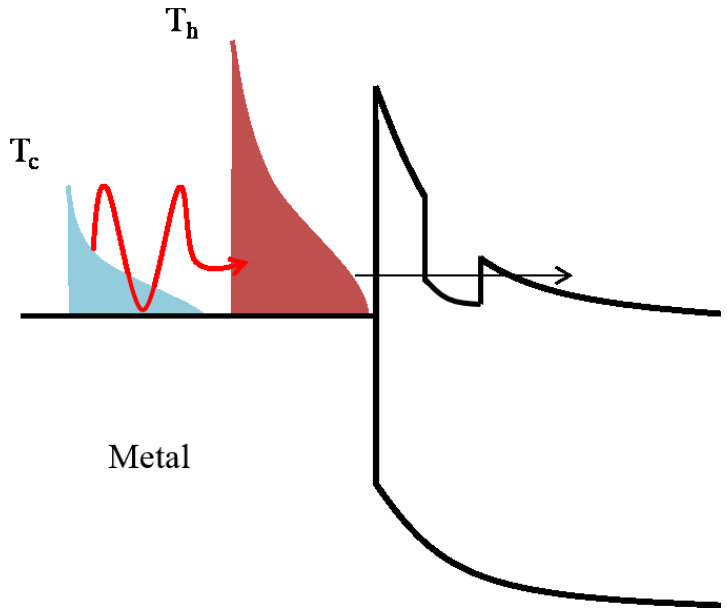

Figure 4-10. The metallic solar cell concept with tunnelling extraction of hot electrons

With extraction through the confined state in the quantum well fully energy selective extraction can be realised, but clearly the design and realisation of such a structure is not trivial. In particular the Schottky barrier height and width are determined by the semiconductor doping density, the metallic layer properties and the interface properties in combination. As such, the quantum well extraction structure only forms the required band structure when a metallic film is deposited on to the semiconductor layers. This makes intermediate characterisation of the semiconductor structure difficult. For this reason the modelling in the rest of this section starts with the simpler Schottky structure, as does the experimental development of the metallic solar cell in chapter 5. The tunnelling cell is then explored theoretically at the end of this chapter in section 4.4.4, with its experimental development ending the next chapter in section 5.5, using the results and understanding gained through the theoretical and experimental work carried out on simpler Schottky structure. In particular, knowledge of the Schottky barrier height was experimentally determined for the Schottky structure and then used to design the tunnelling structure. We have applied for a patent [104] to protect this idea for creating a hot carrier solar cell with tunnelling extraction from a metallic layer.

4.4 Modelling of hot carrier metallic cells

The method of Schottky barrier extraction of hot electrons will be explored further in this section, revealing the signatures of hot carrier extraction that we can expect in the IV characteristics of a metallic solar cell. We will first examine the intuitive expectations that we have for a metallic cell in section 4.4.1 and then model this cell numerically for different carrier and lattice temperatures in section 4.4.2 using the Schrödinger-Poisson framework developed in section 2.4 and appendices 6 and 7.

4.4.1 Intuitive expectations for the metallic solar cell

In order to understand the IV characteristics of the metallic solar cell, we must first understand what it is *not*. It is not, or should not be, a traditional Schottky solar cell. While the bandstructure looks trivially similar, the large difference in operation and expected characteristics is clear when we examine the differences between the two; in particular how absorption in the metallic region rather than the semiconductor region affects the device properties.

In a traditional n-semiconductor Schottky cell the absorption of light occurs in the semiconductor region, as such electrons are driven from the metal/n-Semiconductor contact into the semiconductor bulk by the field created by the depletion of electrons from this region, see Figure 4-11. Since holes in the valence band experience a field driving them into the metallic region this creates a negative current (electron flow in the opposite direction to potential). As the potential on the metal layer is increased (as defined in the figure) the barrier height is reduced, until the point at which the electrons flow into the metal rather than into the semiconductor. At this point the current abruptly turns positive as the photogenerated electrons and the pre-existing dopant electrons in the n-Semiconductor now contribute to a large forward biased diode current.

This mechanism of current generation results in several important features of the Schottky solar cell IV:

- A reverse bias current which saturates at the value of the incident photon flux (until breakdown of the junction at significantly large reverse bias)
- dI/dV in forward bias, but before V_{oc}, determined by shunt resistance and, ideally, zero in a perfect cell.

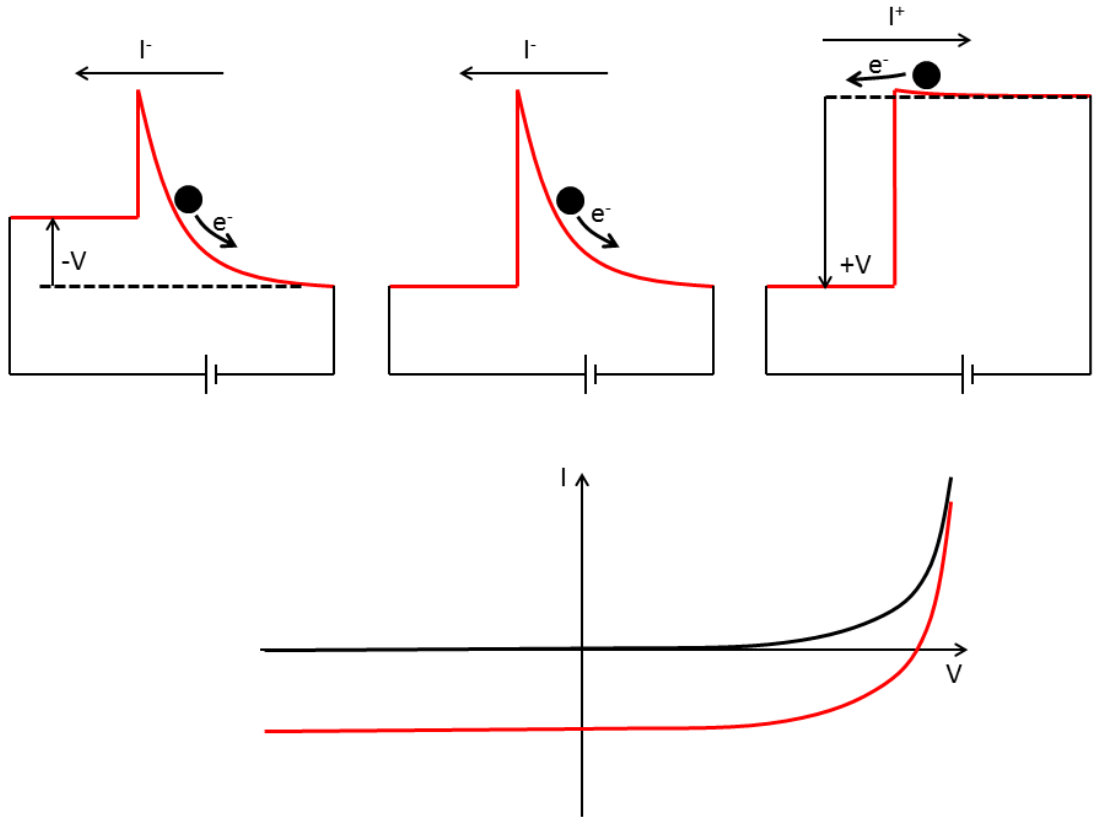

Figure 4-11. Top: Schematic band diagram under different biases corresponding to parts on the IV characteristic shown below for a standard Schottky Barrier photovoltaic cell. Bottom: IV characteristic for a Schottky Barrier photovoltaic cell in the dark (black) and illuminated (red)

Contrast this operation with the case of the metallic cell, where the absorption of light occurs in the metallic region, as schematically illustrated in the band diagrams of Figure 4-12. The creation of a heated distribution in the metallic region results in carriers being transferred, e.g. by thermionic emission, from the heated metal region to the semiconductor. Only carriers with an energy in excess of the Schottky barrier height can contribute to the current and as such the current, figuratively, traces out the shape of the fermi distribution as the bias changes. This results in two large changes in contrast to the IV characteristics of the Schottky solar cell:

- A reverse bias current which does not saturate
- dI/dV in forward bias, but before V_{oc}, determined by the shape of the Fermi distribution even in the case of infinite shunt resistance

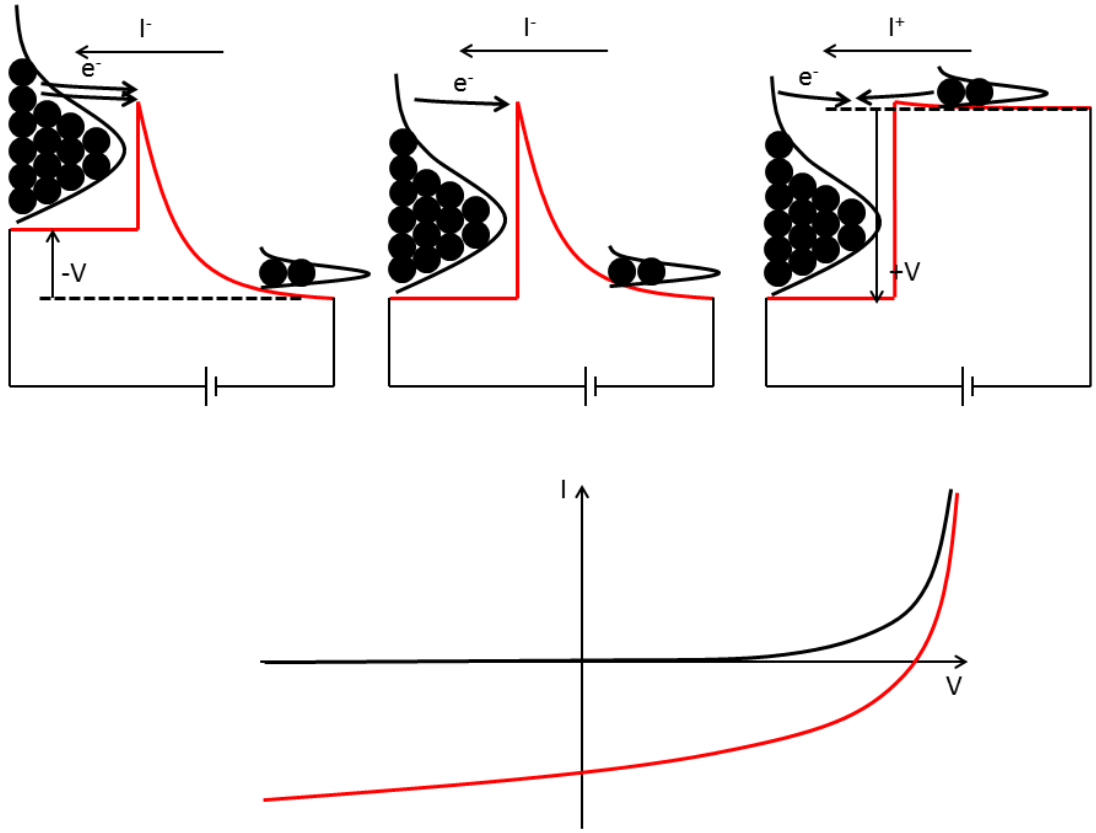

Figure 4-12. Top: Schematic band diagrams at different biases and IV characteristic in the dark (black) and under illumination (red) of the metallic solar cell with Schottky barrier rectification

Theoretical modelling of this metallic cell is presented in the following section (4.4.2) to build on this intuitive understanding with results using the metallic solar cell model based on the work presented in chapter 2.

4.4.2 Modelling of the metallic solar cell with Schottky extraction

Using the formalism developed in section 2.4, the metallic Schottky cell was modelled in order to understand how hot carrier operation will manifest itself in the IV characteristic of this cell.

The semiconducting region was taken to be at lattice temperature, while the metallic region was taken to be at a fixed higher temperature, caused by illumination, giving a temperature gradient in the cell. This approach provides a simple method to analyse the qualitative features of the IV characteristic for such a cell and how they change as the carrier temperature in the metallic region is varied. In this case the semiconductor properties used in the modelled structure were those of GaAs, from the IOFFE database [82], and the metal

properties were those of Chromium. A doping density of $5x10^{17}cm^{-3}$ was used for the nGaAs region and an effective Schottky barrier height of 0.8eV was used.

Figure 4-13 shows the outcomes of this modelling for two scenarios, firstly for the case of varying semiconductor temperature (T_s) for a fixed electron temperature in the metal (T_e) and secondly for the case of varying electron temperature in the metal for a fixed semiconductor temperature. Schematics of the electron distributions and bandstructure at different biases are presented at the top of the figure to describe the mechanism of current generation in this cell.

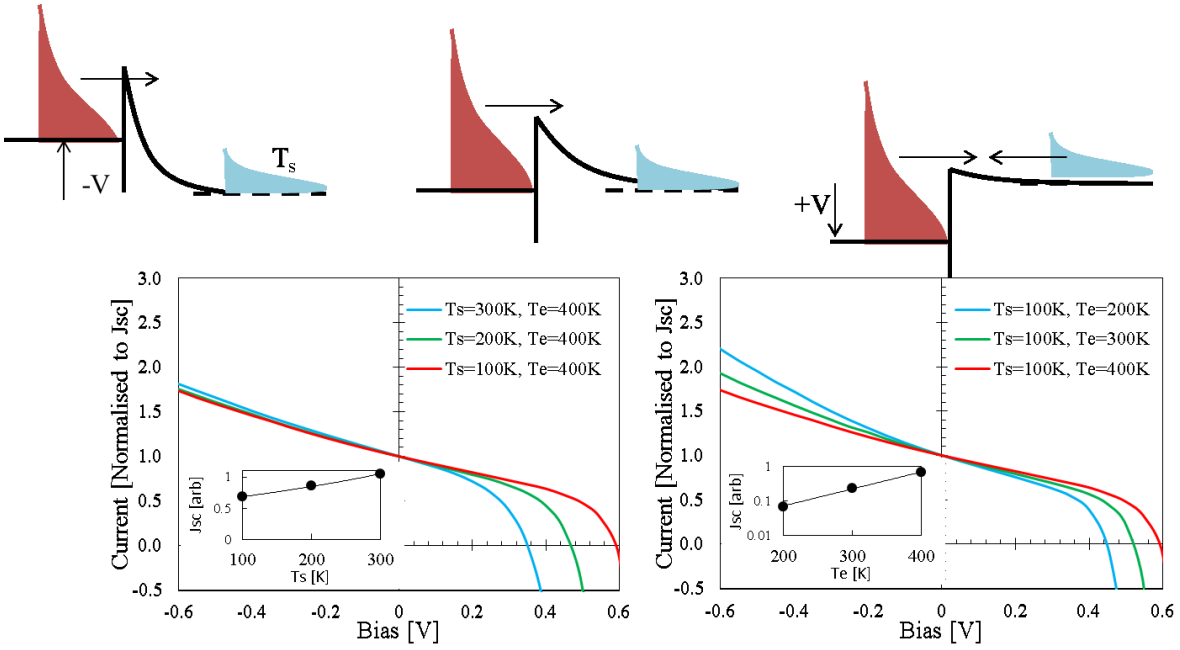

Figure 4-13. Top: Schematics of the electron distributions in the metal and semiconductor regions and bandstructure at different biases Left: Normalised IV characteristics for the metallic cell for constant metal electron temperature (400K) and different semiconductor temperature (100K, 200K, 300K) as in the legend. Right: Normalised IV characteristics for the metallic cell for constant semiconductor temperature (400K) and different metal electron temperature (100K, 200K, 300K) as in the legend. Inset to both graphs shows the relative values of the J_{sc} as a function of temperature for the plotted normalised graphs.

There are several interesting features shown in these IV characteristics which we can compare with the experimental IV characteristics in the following chapter. These IVs have been normalized such that the current is divided by the current at zero applied bias (J_{sc}). In this chapter and the following experimental chapter these normalised IVs therefore have power generation in the positive quadrant of the figure, as solar cells are often plotted, in contrast to the raw data which is generally plotted "as generated" like a diode, with power

generation in the positive voltage/negative current quadrant. This normalisation allows us to compare the slope of the IV characteristic in the reverse bias region without the concern of the absolute value of the current. This is the interesting figure of merit, which reveals useful information about the electron distribution in the metal.

One interesting feature of the un-normalised data is how the J_{sc} changes as a function of either metal or semiconductor temperature, this is plotted as an inset graph for both graphs in Figure 4-13. For the case where the metal electron temperature is raised, the J_{sc} increases exponentially, caused by an increasing temperature yielding exponentially more filled electron states at energies exceeding the Schottky barrier. For the case where the semiconductor temperature is raised, the J_{sc} increases approximately as $T^{3/2}$. This can be explained because the biggest effect of the increase in temperature of the moderately doped semiconductor on the extraction of carriers from the metal is to increase the density of states to which electrons can transfer; with density of states dependent on temperature according to $T^{3/2}$. Other effects on the simulated IV characteristics, such as the change in V_{oc} and IV gradient, are discussed for normalised data in the rest of this section.

For the normalised data, Figure 4-13 (left) shows that as semiconductor temperature is lowered for a fixed metal temperature the V_{oc} of the cell is expected to increase, while the gradient of the IV characteristic in the reverse bias region is expected to stay broadly unchanged. Figure 4-13 right shows that as metal temperature is lowered for a fixed semiconductor temperature the V_{oc} of the cell is expected to decrease, while the gradient of the IV characteristic in the reverse bias region is expected to increase.

These features can be understood by analyzing the changes in the electron distributions in the metal and semiconductor region for these cases, and understanding how they determine the current in these cells. Firstly the V_{oc} is determined by the voltage at which balance is achieved between the current resulting from electrons being emitted into the semiconductor from the metal and the current resulting from electrons being emitted into the metal from the semiconductor. For this reason, a higher relative metal temperature than semiconductor temperature results in an increased V_{oc} since the higher metal temperature means higher current emitted from the metal into the semiconductor and thus the semiconductor needs to be at a higher bias level to achieve a balancing current. Secondly the gradient of the IV in the reverse bias region is dominated by the change in electron density with energy in the metal region; with a higher temperature distribution having a lower decline in electron density as electron energy increases. This lower decline in electron density with electron

energy for a higher temperature metal results in a smaller change in current as a reverse bias voltage is applied.

Figure 4-14 gives us further understanding of the expected shapes and features of the IV characteristics of these cells, which we can apply to the experimental results in the following chapter. In these IV characteristics the semiconductor temperature and metal electron temperature are both increased in steps of 100K, while maintaining a 100K temperature differential between them. This is equivalent to some of the experiments that will be performed in the following chapter, in which a constant laser intensity is used, but the lattice temperature is varied by mounting the samples on a cryogenic temperature stage.

It can be seen in Figure 4-14 that we should expect that as lattice temperature is increased, the reverse bias gradient should decrease, the V_{oc} should decrease and this should result in the IV characteristics crossing over in the forward bias region. This is due to the normalisation such that at J_{sc} the current is 1, but the fact that the highest temperature IV characteristic has both the shallowest gradient and the lowest V_{oc}.

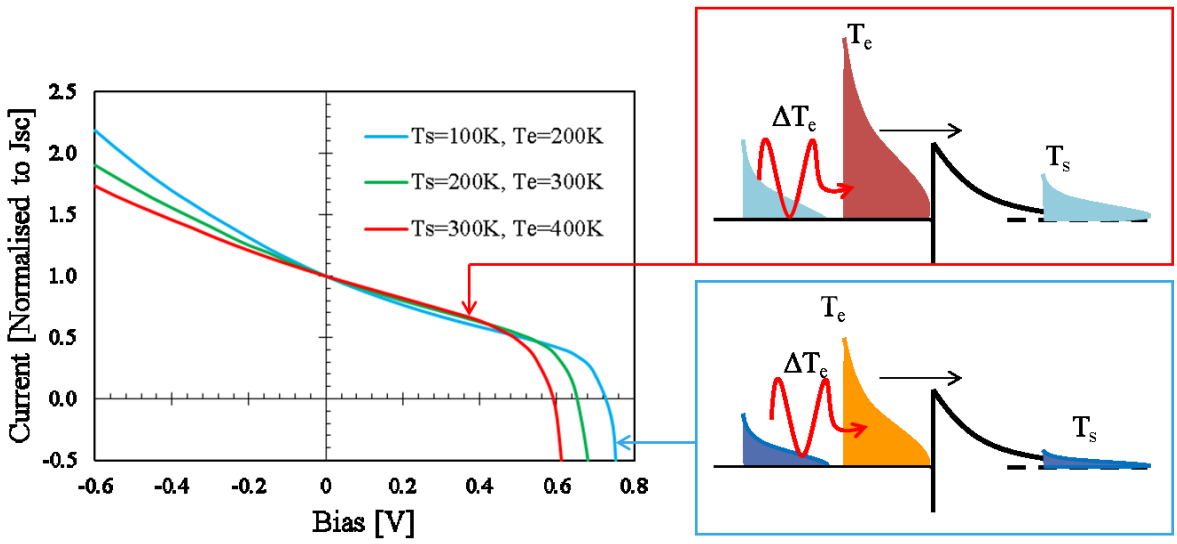

Figure 4-14. Normalised IV characteristics for the metallic cell with a fixed temperature gradient between the metal and semiconductor region (100K) at three different lattice temperatures (100K, 200K, 300K) as in the legend. Inset schematic explains the electronic reasons for these differences.

This modelling and the qualitative features described in this section will be referred to extensively in the experimental chapter 5.

4.4.3 Efficiency and comparison with an IPE cell

Recent theoretical work has been carried out into a device which looks superficially similar to this device called the Internal Photoemission (IPE) Cell [44], [105]–[108], in which a photogenerated electron from a metal is excited over the top of a Schottky barrier in to an adjacent semiconductor. Maximum efficiencies for such a device were shown to be limited to 7-22% (depending on assumptions made about the density of states), a long way short of the hot carrier results predicted by the semi-selective contact (shown as ~50% in Figure 1-10 of section 1.5).

The reason for this difference becomes clear when examining the mechanism by which carriers are excited in their models. The calculations presented by White and Catchpole [44] use the Fowler equation [109] to calculate the photo-emission yield, requiring the conservation of carriers and an assumption that only light in excess of the barrier height can contribute useful energy to the electrons, with energy below the barrier height wasted. Their work assumes that electrons are generated at the same energy as the incident light and that carrier-carrier scattering is an entirely dissipative process and in [106] it is explicitly stated that scattering between hot electrons will reduce the yield for such a cell.

This mechanism is summarised in Figure 4-15 b) in contrast to our proposed hot carrier mechanism, Figure 4-15 a), in which the entire electron population is warmed, a mechanism supported by the conclusions drawn in section 4.1.4. In particular, it seems unlikely that electrons will be extracted prior to any scattering events, except perhaps in ultra-thin layers of noble metals. This metallic hot carrier mechanism (Figure 4-15 a) can result in a higher efficiency, as it avoids the necessity for particle conservation (between photons in and current out), already described as a benefit in section 4.1.1. It also allows photons which excite electrons to energies below the barrier height to contribute to the efficiency through warming the electron distribution. Essentially, it allows the re-circulation of electron energy.

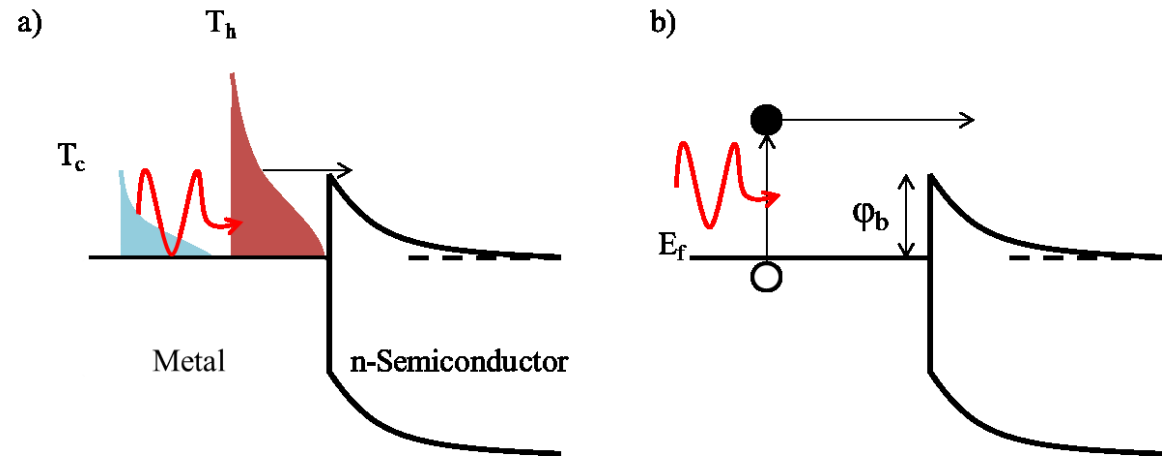

Figure 4-15. A Schematic illustration of the function of our proposed metallic solar cell (a) and the proposed IPE cell (b)

In addition to the differences in efficiency, there will also be clear differences in the IV characteristics of the IPE cell as compared to the metallic cell. Since the IPE cell operates by ballistic carriers[2] overcoming the Schottky barrier there will be several key differences in these cells:

- There should be saturation of photocurrent once all carriers can overcome the barrier
- There should be no impact on device current from illumination with energies below the barrier height when in combination with illumination at energies in excess of the barrier height (since there are assumed to be no e-e interactions).

Neither of these statements describes the cell characteristics that are observed in the experimental work of chapter 5.

In addition to our work, Konovalov [110] has recently investigated semi-selective hot carrier cells, arguing that the reduction in efficiency for a semi-selective cell is a price worth paying for a device which can achieve high power densities; likening the loss mechanism to a hot exhaust in a combustion engine. This "hot exhaust" in the terms of a

[2] We define "ballistic carriers" as those electrons which have not undergone any scattering events, either by electrons or phonons

hot carrier solar cell leads to a low fill factor, a high open circuit voltage and a slope in the IV characteristic in reverse bias which is caused by high temperature electrons, rather than the presence of shunting. These predictions compare well with our calculations in this chapter and the experimental evidence presented in chapter 5.

4.4.4 Modelling of the metallic solar cell with tunnelling extraction

To compare with the modelling of the metallic cell with Schottky extraction in section 4.4.2 the Schrödinger-Poisson model was also used to model the metallic cell with tunnelling extraction. This modelling helps us to understand the critical features of this cell and how its IV characteristics compare with the metallic cell with Schottky extraction.

In this case the same Schottky barrier height and width was used as previously in section 4.4.2, but a 12nm quantum well was placed 4nm from the metal/semiconductor interface. In designing this structure it was found to be necessary to grade the well, such that the potential offset is largest at the side nearest to the metal/semiconductor barrier, and least at the side furthest from this barrier. This grading mitigates the band bending of the semiconductor region following the barrier, allowing a flat band in this well region. Without this grading, the well region has the same band gradient as the barrier semiconductor regions, resulting in a triangular potential well at the side furthest from the barrier. This results in terrible IV characteristics, since it effectively increases the barrier width through which the electrons must tunnel to get from the metal layer into the well. The necessity of a flat band in the well region at operating biases was used as a design rule for these structures and is used in section 5.1.3 where the layer structure for the tunnelling cell that is grown is designed.

Figure 4-16 illustrates the operation of the tunnelling cell by showing the modelled transport of electrons through this structure at a forward bias of 0.15V. On either side of the central figure are the electron fermi distributions in the contact regions, the left hand distribution represents the (heated) metal and the right hand side the semiconductor; the semiconductor distribution is offset by 0.15V to give the correct biasing condition. The central figure represents an effective electron occupation (with the band structure overlaid in grey) as a function of energy and location, calculated by multiplying the wavefunction value at a location by the fermi distribution and density of states in either contact at that energy, as given by equation 4-2:

$$n(x_i, E(k)) = |\psi_k(x_i)|^2 \left[\rho^L f_k^L - \rho^R f_k^R\right] \qquad (4\text{-}2)$$

This value is normalised to 1 in the figure for clarity, but it is also shown summed over energy to give an absolute value of the electron density as a function of distance in Figure 4-17 for various different applied biases to the cell.

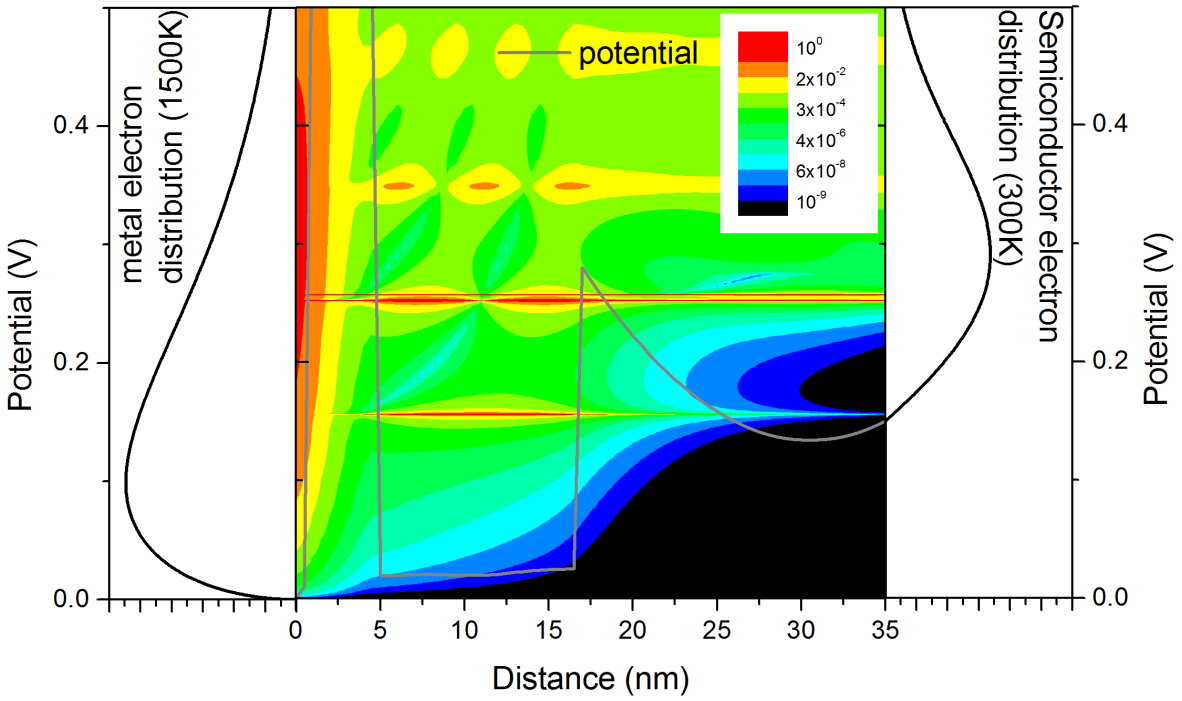

Figure 4-16. The value of the electron wavefunction multiplied by the electron fermi function (colour-mapped, normalised to a maximum of 1, as per the legend) as a function of distance and energy overlaid onto the conduction band potential (black) at an applied bias of 0.15V. Left and right graphs show the electron fermi distributions in the metal and semiconductor for temperatures of 1500K and 300K respectively.

From Figure 4-16 we can infer the following operational principles for this cell:

- The current is dominated by tunnelling transport through the well region
- The density of electrons at the energy of transmission (~0.23eV in this example) in the semiconductor compared with the metal layer determines the V_{oc} point. i.e. once the semiconductor band is biased sufficiently high above the metal the density of electrons in the semiconductor at the transmission energy will be sufficiently large to reverse the direction of current.
- The state which would be the first confined state (if this were an isolated quantum well) contributes very little to the current due to the depth of the well, so for an improved design at lower temperatures the offset between the well and the

collector side could be reduced. This could be optimised for the desired operational electron temperature.

Figure 4-17 further reveals the operation of this cell in by showing its conduction band profile and electron density profile at a variety of biases.

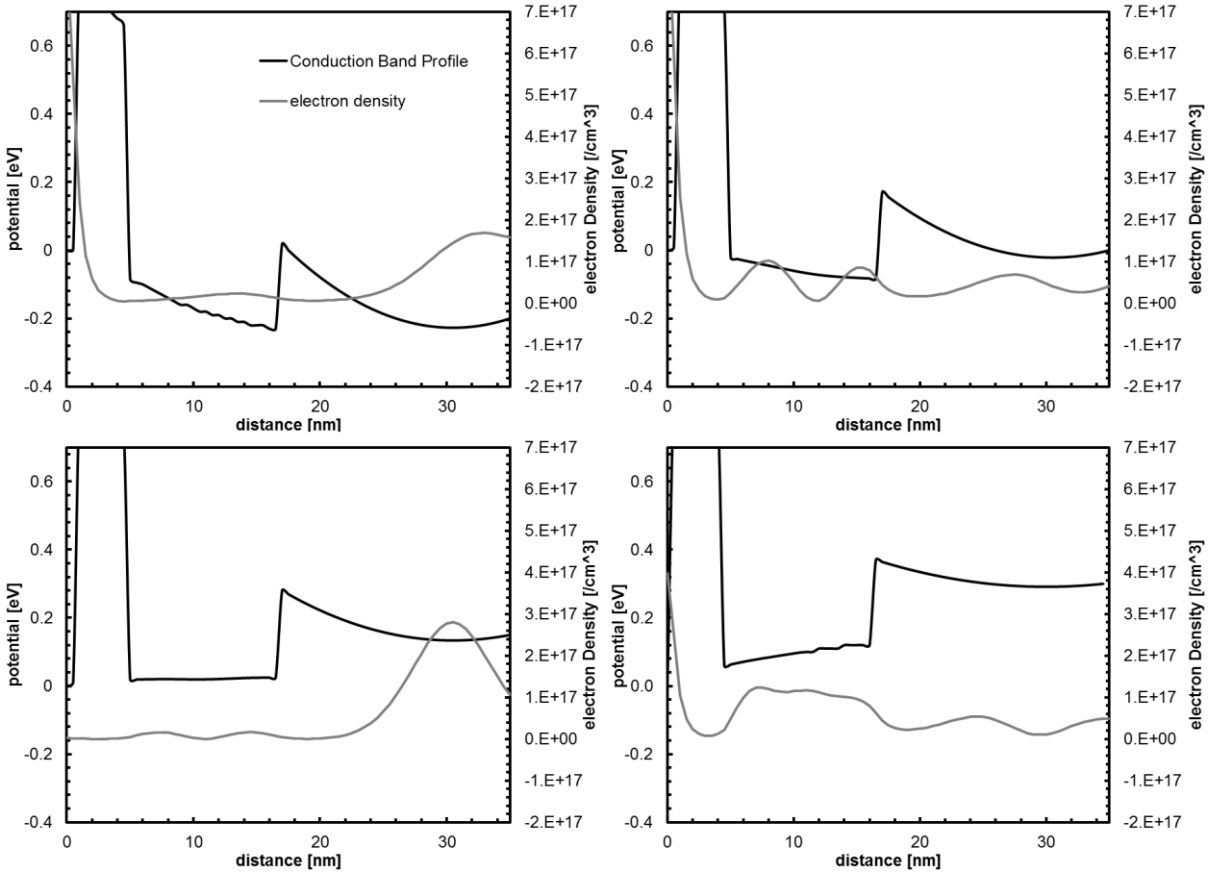

Figure 4-17. The conduction band profile and electron density for the tunnelling structure as calculated by the Schrödinger-Poisson program at various different biases (top left: -0.2V, top right: 0V, bottom left: 0.15V, bottom right: 0.3V)

At negative bias the current is predominantly by tunnelling through the first barrier and by thermionic emission over the barrier, leading to a large electron density in the regions at either end of the device, but little in the middle. As the bias is increased the current becomes dominated by tunnelling and a significant population of electrons in the well region occurs. As the bias is further increased the population in the well builds, eventually reversing the current flow once the injection from the semiconductor at the transmission energy is greater than the injection from the heated metallic layer.

The temperatures previously used to show the schematic operation of tunnelling cell (1500K metallic absorber and 300K semiconductor) were simply used to provide a clear

illustration of the operating principles of this cell. To show what we might expect from a cell with this tunnelling feature in comparison with the previously presented cell with Schottky extraction the same temperatures as in section 4.4.2 were used so that a comparison could be drawn.

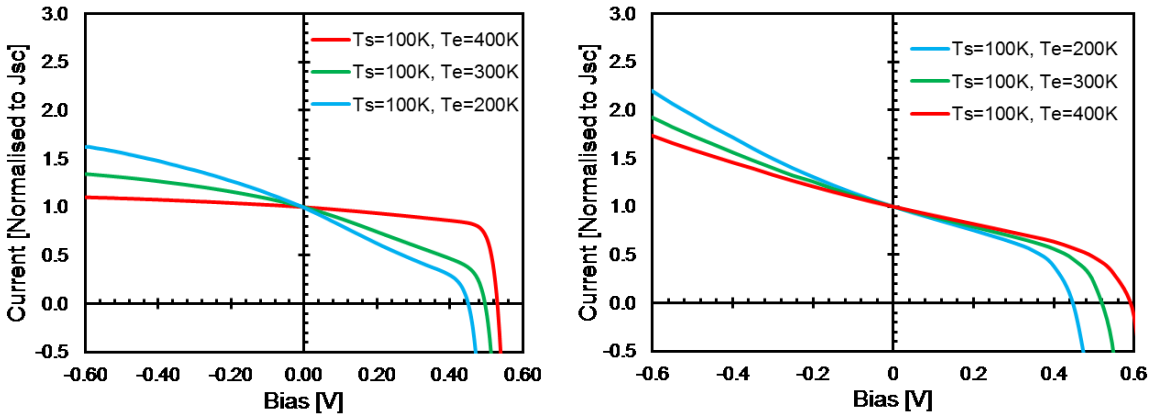

Figure 4-18. The modelled IV characteristics of the tunnelling extraction cell (left) and the Schottky extraction cell (right).

It is not expected that this modelling will be quantitatively comparable with the experimental data presented in the following section, as modelling tunnelling features quantitatively requires a more sophisticated theoretical treatment, such as non-equilibrium green's functions [111]. Even with such a sophisticated theory, to achieve a numerical match with data generally also requires fitting parameters to take into account e.g. series resistance effects [112]. However, the qualitative trends shown in the modelling should be reproduced and the modelling should allow us to understand the features that are observed. In particular, these qualitative features from Figure 4-18 should be observed in the experimental data if the cells are operating as intended:

- Higher temperature electrons in the metal (either through higher lattice temperature or illumination with shorter wavelengths or higher power) should lead to a shallower gradient in the reverse bias IV characteristic for both Schottky and tunnelling cells.
- The tunnelling cell should show a lower V_{oc} than the Schottky cell under identical illumination conditions. This is because the electrons can transfer from the semiconductor to the metal through the well rather than needing the biasing to overcome the field of the Schottky barrier.
- The tunnelling cell should show a shallower reverse bias gradient than the Schottky cell under identical illumination conditions. This is because in these conditions the

only barrier to electron transfer is the 4nm AlGaAs barrier, whereas for the Schottky cell the barrier is thicker. This means that in the tunnelling cell the transfer at these biases is from tunnelling through the barrier, whereas in the Schottky cell the transfer of electrons is still mostly through thermionic emission over the barrier.

With these features to look for, and the theoretical work to aid their design, the following chapter will discuss the experimental realisation of these cells.

5 EXPERIMENTAL EVALUATION OF METALLIC HOT CARRIER CELLS

Following the justification and modelling of the metallic solar cell concept presented in chapter 4, experimental results from various realised cells are presented in this chapter, with evidence that they are indeed operating as a hot carrier photovoltaic cell by absorption of light in the metallic layer. The design of the structures under investigation and their fabrication is presented in section 5.1, followed by the experimental methods that were used to characterise them in section 5.2. The results of this characterisation for various cells, to make the case for a metallic solar cell, are presented in the remainder of the sections of this chapter:

- Section 5.3 starts with a simple proof of principle in an Ag/GaAs cell.
- Section 5.4 builds on this with further experiments in an improved Cr/GaAs cell, including comparing the response of the cell above and below the GaAs band gap to contrast "metallic" operation with "Schottky" operation.
- Section 5.5 then shows a cell in Cr/AlGaAs with Schottky extraction compared with a Cr/AlGaAs cell with tunnelling extraction. This section includes results of dual wavelength illumination of the cells, showing that a photo-response can be observed from illumination at 642nm+1550nm when illumination at 1550nm alone results in no photo-response.

5.1 Design of a metallic solar cell

Twelve metallic cells were fabricated during this project, the characteristics of four of the cells will be described in this chapter. The structures of these four cells and notes on their design and fabrication are described in the subsections below: ICL4 (Ag/GaAs Schottky), ICL9 (Cr/GaAs Schottky), HYL11 (Cr/AlGaAs QW) and HYL12 (Cr/AlGaAs Schottky). The four cells reported in detail in this report all showed good repeatability of results after repeated IV sweeps and over a period of months. Other cells were fabricated, based on other materials (e.g. Al was used as the metallic absorber in ICL1 and ICL2) and using alternative fabrication processes (e.g. a surface oxide removal step was implemented in ICL3), but these devices yielded results that were not sufficiently repeatable to justify inclusion. These intermediate devices were used to refine the processes and materials selection that enabled good quality, repeatable results that were observed in the cells presented in this chapter.

5.1.1 ICL4: Silver/GaAs Schottky

The first cell to be presented in this chapter has a Silver absorber region deposited by thermal evaporation on to a GaAs substrate, with thicknesses and doping levels as shown in Table 2. This cell was designed to give a Schottky barrier for electron extraction from the metal (when illuminated) into the semiconductor. Silver was used for the initial prototype device due to existing processing techniques and robust device characteristics, which did not degrade with time, illumination or during processing.

Table 2. Layer structure of the ICL4 structure

Layer	**Material**	**Doping [cm^{-3}]**	**Thickness [nm]**
Absorber	Silver	-	22nm
Collector	GaAs	$2.1x10^{17}$ (Si)	Substrate (300um)

The cell was processed into the structure shown in cross-section in Figure 5-2 with the following important features in its processing, some of which are also important for the structures that follow, and most of which were determined through experimental variations:

- Moderately doped nGaAs was found to be necessary to create a good quality Schottky contact following measurement of the Schottky barrier height for various wafer dopings in the range of 10^{17}-10^{18} cm^{-3}. In excess of $7x10^{17}cm^{-3}$ generally produced an unacceptable amount of current in reverse bias, indicating the contact was starting to become ohmic (presumably due to tunnelling through a thinner Schottky barrier region). The dark IV characteristics of the two extreme doping values that were tested in this brief study, used to find an acceptable doping level to produce a good quality Schottky contact, are shown in Figure 5-1. This figure shows good diode behaviour at $2.3x10^{17}cm^{-3}$ and an excess reverse bias dark current for a doping level of $1.5x10^{18}cm^{-3}$.

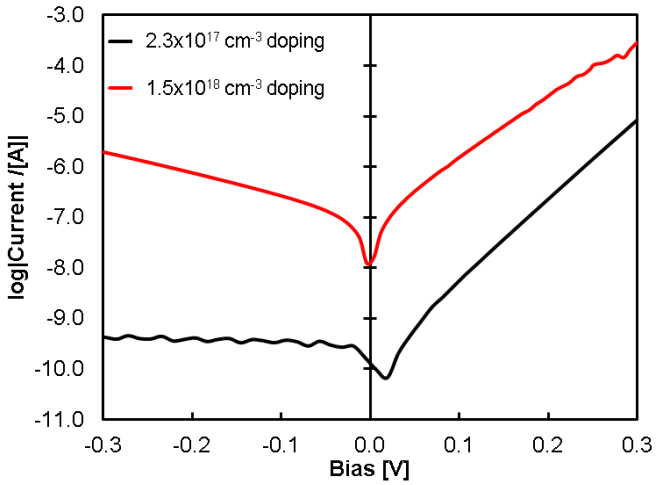

Figure 5-1.The dark IV characteristic of a 20nm layer of Cr deposited onto an nGaAs wafer with doping density of $2.3x10^{17}cm^{-3}$ (black) and $1.5x10^{18}cm^{-3}$ (red)

- An annealed InGe/Au ohmic back contact provided a contact resistance below $10^{-5}\Omega cm^2$
- 50um diameter regions of contact for active device area (Silver on to GaAs), the rest isolated by SiO_2 to reduce the dark current contribution to device characteristics. Illumination only occurred over this active area (illustrated in Figure 5-2).
- No surface oxide removal prior to silver deposition. This was tried, but resulted in less stable device characteristics in ICL3. The surface oxide thickness was determined by ellipsometry to be 1.3nm.
- Deposition of Ti between SiO_2 and Silver absorber layer, and between Silver and Gold top contact in order to provide good adhesion of the metallic layers.
- A thick layer of Gold (>150nm) to allow easy wire-bonding with a good yield of devices

The device structure shown in Figure 5-2 was common among all the devices presented in this chapter. A small active area was defined and the rest of the substrate was isolated from the contacts by SiO_2 deposition. The active area itself could then be illuminated, reducing the impact from dark current contributions to device behaviour, which would affect device characteristics much more if the illumination area were only a small fraction of the device area.

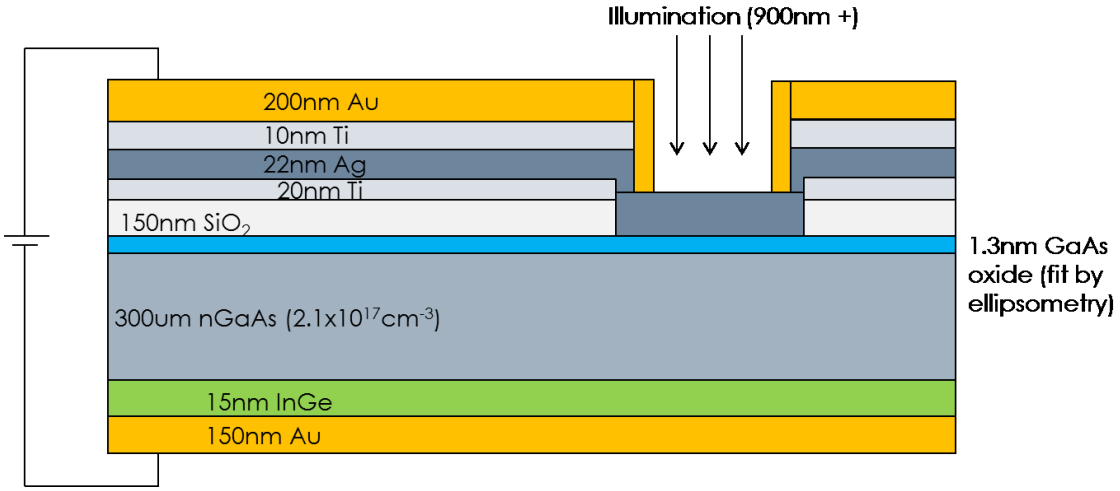

Figure 5-2. A schematic of the as processed structure of ICL4, showing the region of illumination and contacts.

5.1.2 ICL9: Cr/GaAs Schottky

This device was processed similarly to ICL4, but with a Cr absorber layer to enhance absorption. The use of Cr had the added benefit of simplifying the layer structure, since Cr is already oxygen active [113] it provides a very good adhesion to most layers it is deposited on (and certainly on GaAs), removing the necessity of a Ti interlayer.

ICL9 had the thinnest possible layer of Cr which could still form a planar layer and not islands; this was 8nm. The layer structure and substrate properties for ICL9 are shown in Table 3.

Table 3. Layer structure of the ICL9 structure

Layer	**Material**	**Doping [cm^{-3}]**	**Thickness [nm]**
Absorber	Chromium	-	8nm
Collector	GaAs	$1.8x10^{17}$ (Si)	Substrate (300um)

A microscope image of the processed structure is shown in Figure 5-3, showing the device active region contacted by a hook shaped contact, attached to a larger bond pad, from which electrical connections via ultrasonic wire bonding are made. This geometry is standard across all samples in this chapter, with optional extra steps to deposit e.g. antireflection coatings. This image is of a variant of ICL9, which had an amorphous Silicon antireflection coating deposited on the active area, showing a darker central region due to higher absorption. The devices electrically tested in this chapter in section 5.4 did not have this extra layer, because of some problems it generated due to shorting, but were otherwise identical.

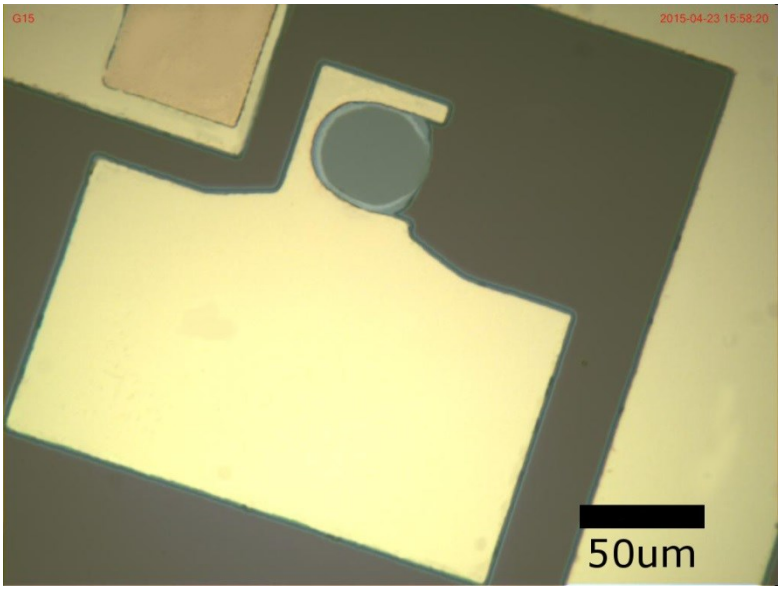

Figure 5-3. A microscope image of the processed ICL9, but with an additional aSi antireflection coating deposited (showing a deeper coloured region with high absorption in the centre of the active device region).

The surface roughness of the metal layer is a key factor in the magnitude of the current passed from the metallic absorber to the semiconductor for two reasons:

1. Increased light scattering by a roughened interface
2. A smooth Schottky contact experiences suppression of the Schottky current because of conservation of linear momentum for electrons passing from the metal to the semiconductor [114]. A roughened interface for the absorber layer allows linear momentum conservation to by broken by scattering the electrons from the metallic layer into the semiconductor and allowing internal quantum efficiencies to increase

by up to 2 orders of magnitude when compared with contacts with smooth interfaces [115].

Control of the Cr surface roughness was obtained by varying the deposition rate of the Cr by thermal evaporation. A deposition rate of 0.01nm/s gave a 4.2nm RMS roughness and a 0.2nm/s deposition rate gave a 1.9nm RMS roughness as shown in the AFM images of these surfaces shown in Figure 5-4 and Figure 5-5 respectively. A slower deposition rate gives a greater surface roughness because it allows the growth of islands of Cr.

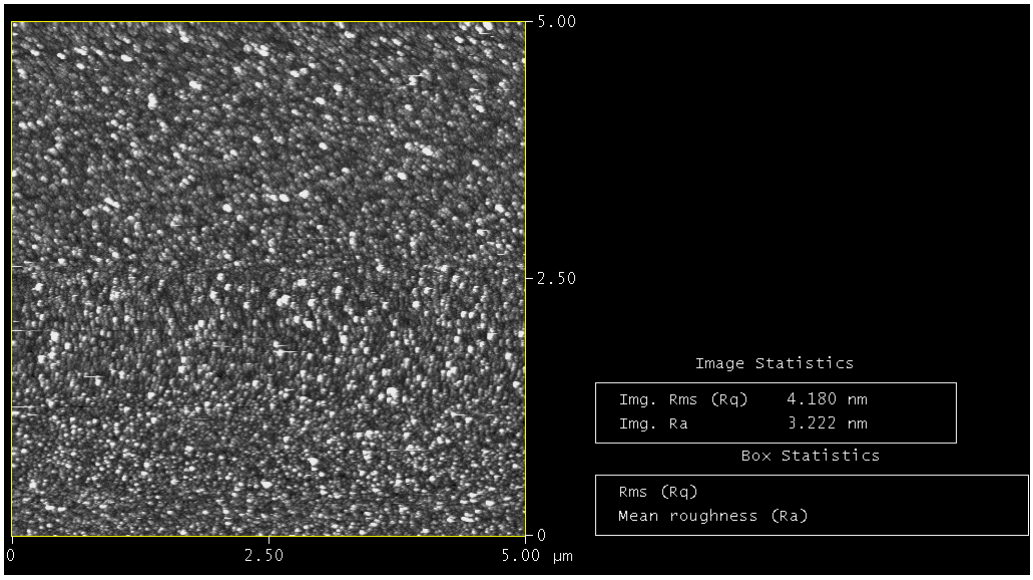

Figure 5-4. AFM image of slow deposition (0.01nm/s) of Cr on GaAs giving a rougher surface

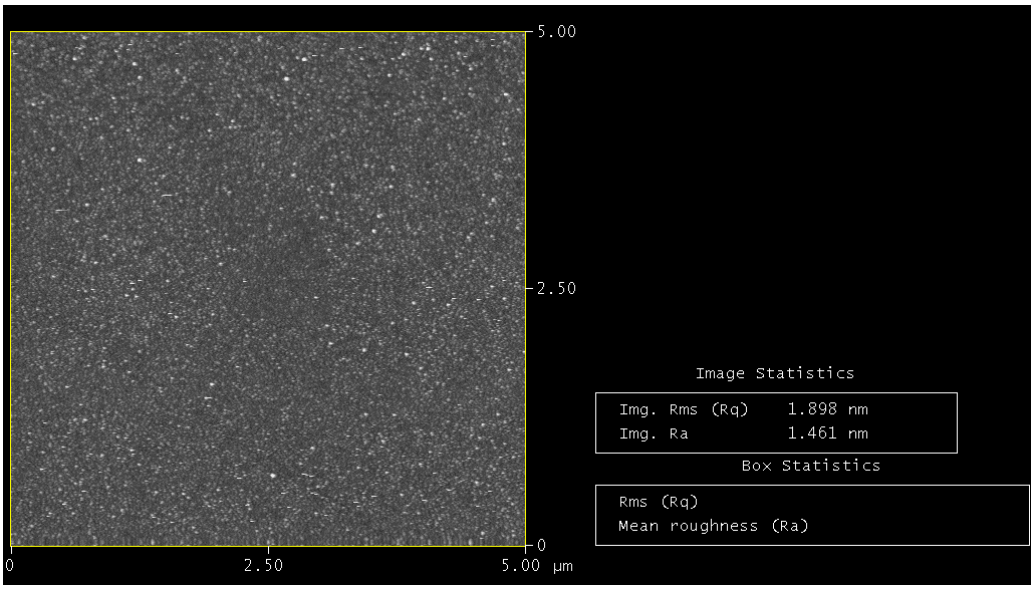

Figure 5-5. AFM image of fast deposition (0.2nm/s) of Cr on GaAs giving a smoother surface

A comparison of the IV characteristics under the same intensity broadband illumination for these samples in Figure 5-6 reveals that the sample with the slower deposition rate, and hence rougher surface, has a short circuit current of approximately 7 times greater than the faster deposited sample. As such, this sample will be used in the analysis presented in section 5.4. The reason for the IV shape will also be explained in this section, but is essentially attributable to contributions to the IV characteristic from Schottky-like operation (with absorption in the semiconductor) rather than metallic operation, as described in the theoretical section 4.4.1.

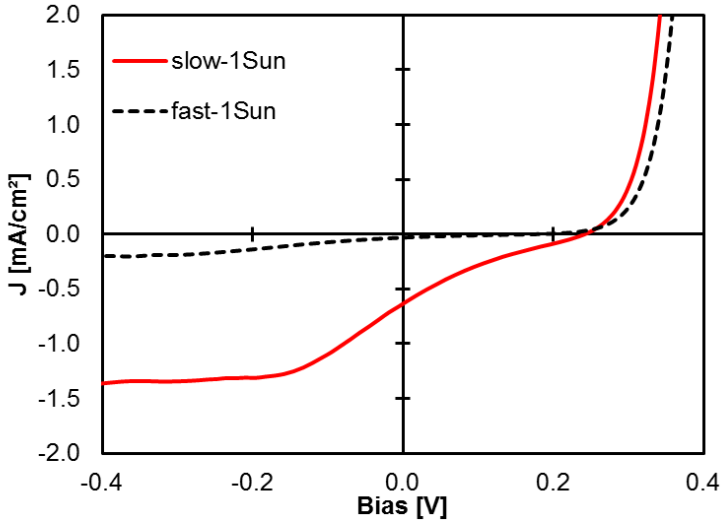

Figure 5-6. The current density of devices illuminated with a standard "1 Sun" intensity and spectrum to compare the effect of surface roughness. The red line shows the IV characteristic of the slow deposited (rough) sample and the black dashed line should the IV characteristic of the fast deposited (smooth) sample

All depositions on future samples followed this slower deposition rate for enhancement of the photocurrent.

5.1.3 HYL11: Cr/AlGaAs QW

Following the design rules laid out in section 4.3.2, and using the described theoretical tools, a tunnelling structure was designed with an AlGaAs barrier and a graded AlGaAs well region. The graded well region was designed to have a flatter band at operating bias while still maintaining a 0.1eV barrier to the AlGaAs region at the interface furthest from the metal/semiconductor barrier.

The structure for the cell, as designed and grown is presented in Table 4 and the bandstructure, as calculated, is shown in Figure 5-7. The energy of the confined electron

state through which electron tunnelling can occur from the metal is shown as a blue dashed line, the corresponding hole confined state is shown in red.

Table 4. Layer structure of the HYL11 structure

Layer	**Material**	**Doping [cm^{-3}]**	**Thickness [nm]**
Absorber	Chromium	-	30nm
Barrier	$Al_{0.4}Ga_{0.6}As$	$5x10^{17}$ (Si)	4nm
Well	$Al_xGa_{(1-x)}As$: $x=0 \rightarrow 0.3$	$5x10^{17}$ (Si)	15nm
Collector	$Al_{0.4}Ga_{0.6}As$	$5x10^{17}$ (Si)	150nm

The "as grown" structure had a 20nm GaAs cap layer to prevent oxidation of the AlGaAs top barrier. The GaAs cap was selectively etched away with a citric acid based etch before immediately loading the remaining structure into the thermal evaporator to prevent oxidation. This was also the case for the comparison "Schottky" cell presented in the following subsection 5.1.4.

This structure has a thicker chromium layer (30nm) than ICL9 to ensure no oxidation of the AlGaAs region, which was an issue affecting the robustness of other fabrications with an AlGaAs region and a thinner metallic layer.

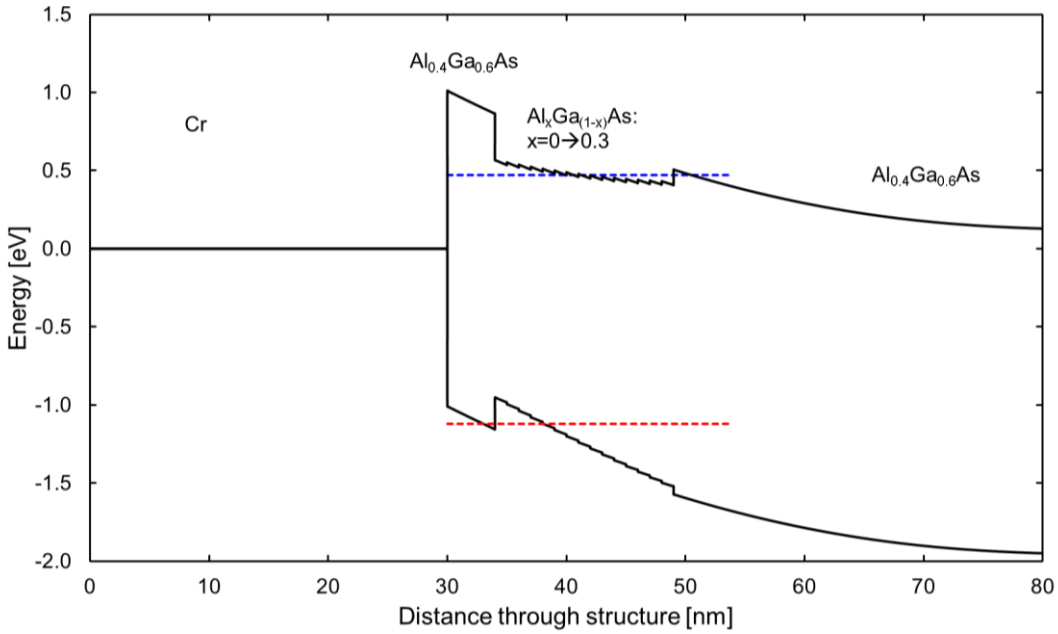

Figure 5-7. The calculated band structure of the HYL11 tunnelling structure, showing the Schottky barrier to the Chromium layer

5.1.4 HYL12: Cr/AlGaAs Schottky

To compare with the tunnelling cell presented in the previous subsection (HYL11) a control structure was grown, with the aim of operating similarly to ICL4 and ICL9 (i.e. without tunnelling extraction) but to have the same interface properties as the tunnelling cell (i.e. Cr/AlGaAs). This allows a fairer comparison of the IV characteristics of the two modes of operation. The layer structure of this cell is shown in Table 5.

Table 5. Layer structure of the HYL12 structure

Layer	**Material**	**Doping [cm^{-3}]**	**Thickness [nm]**
Absorber	Chromium	-	30nm
Collector	$Al_{0.4}Ga_{0.6}As$	$5x10^{17}$ (Si)	169nm

5.2 Experimental set up

The choice of wavelength, power and whether to use pulsed or continuous wave illumination can reveal or conceal important information about these cells, so choosing the correct operating conditions was critical.

For silver, interband absorptions start to become an important effect from 3.8eV [116] whereas for Chromium absorption of energy occurs in the electrons at the fermi surface up to 2.3eV [117], at which point critical point absorptions between various bands become important. For these reasons, the illumination wavelengths in this work were kept to wavelengths longer than those required to excite these interband transitions. Additionally the wavelengths were generally also kept below the band gap of the semiconductor layer, unless the experiment was designed to compare metallic cell operation with standard Schottky cell operation, as in section 5.4.3.

5.2.1 Illuminated IV measurement

Illuminated IV characteristics were obtained by illuminating the cells with various laser beams focused onto the fabricated cell mesa. A confocal system with an objective lens was used to both image the cell and to focus the light to a spot onto the active region. The sample was mounted on a cryogenic microscope stage (Linkam THMSE600 cryogenic microscope stage) to provide temperature dependent light IV measurements from 80K to room temperature. Three different illumination sources were used as an input light source for this confocal system:

1. A wavelength tuneable (700-950nm) Ti:Al_2O_3 laser with a minimum pulse width of 1.2ps and an 80MHz repetition rate. (Spectra-Physics: Millennia pumped Tsunami)
2. A variety of laser diodes driven by a variable pulse width and duty cycle driver, minimum 100ns pulse width and 1% duty cycle up to continuous wave. (ILX Lightwave LDP-3840B)
3. Eight fibre-coupled diode lasers from 642nm-1550nm which can be combined in a wavelength multiplexer to allow simultaneous illumination with up to three separate laser wavelengths on the same focused spot. The power of each fibre-coupled laser can be modulated separately for lock-in measurements. (THORLABS MCLS1 system)

A schematic of the optical illumination set up with illumination source 3 (fibre-coupled diodes) is shown in Figure 5-8, with images of a representative mesa structure with and without focused laser illumination.

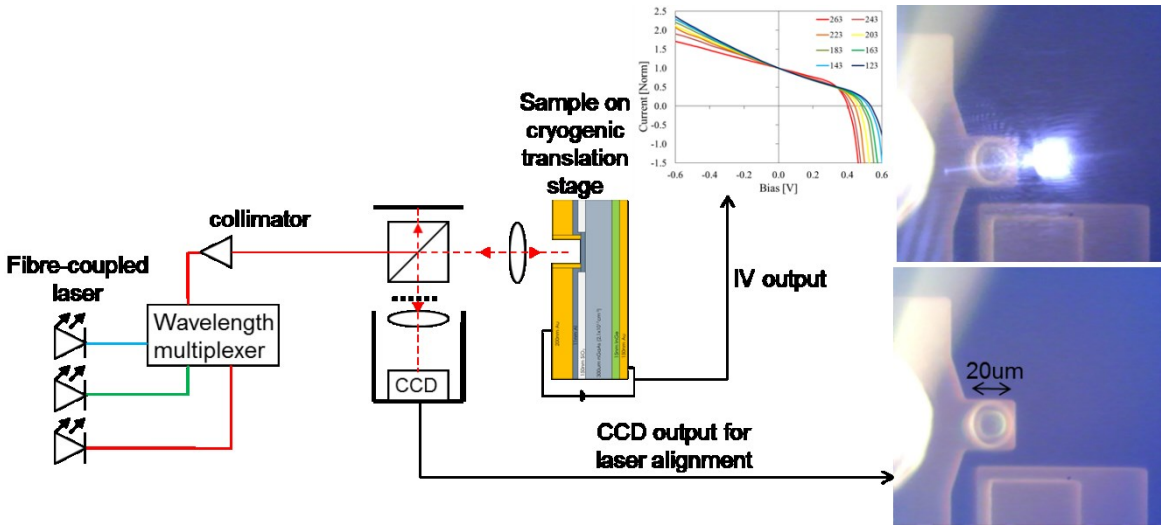

Figure 5-8. The experimental set-up used to illuminate our samples with up to three laser beams simultaneously and extract illuminated IV characteristics

The laser wavelengths of all sources were measured with a calibrated Anritsu MS9710C spectrum analyser to ensure uniformity of output.

5.3 Results ICL4 – Silver based cells

The initial "proof of concept" metallic solar cell was ICL4, some of the results of which have been presented previously [118]. This section (5.3) documents the characterisation of this cell, including some of the basic techniques which were repeated on all cells (such as dark current measurements, Schottky barrier height computation and reflection measurements) but which will only be documented briefly in the sections on the other cells.

5.3.1 Dark current and Schottky barrier height

The dark current as a function of temperature was taken for all cells after initial fabrication and also approximately one month post-fabrication. Measuring the dark current as a function of temperature allows an estimation of the Schottky barrier height, as outlined in this subsection. In addition to revealing this important device characteristic, any changes observed in the dark current after one month of experimentation reveal important information about device stability and therfore the reliability of results. All devices presented in this thesis suffered an RMS current difference of less than 5% over the range -0.5V/+0.5V at room temperature after one month of testing (Figure 5-9 left). It is for this

reason that samples fabricated from Aluminium were not pursued after ICL5 and ICL6, as the device characteristics degraded significantly on a timescale of ~3 days. This was presumably due to a surface reaction between the GaAs and Al layer, which did not occur with the more robust and inert Cr or Ag layers. It has been recorded that the surface of Al on GaAs is not particularly stable at elevated temperatures (perhaps present during laser illumination) due to the reaction of Al with either Ga_2O_3 or direct replacement of Ga [119].

Figure 5-9 right was used to compute the Schottky barrier height for ICL4, in a process that was repeated for all cells investigated in this chapter. This was carried out by comparing the IV characteristic as a function of temperature with the theoretical expression for the dark IV of a Schottky diode, equation 5-1:

$$I = AA^{*}T^{2}\exp\left(\frac{-\phi_b}{k_B T}\right)\left[\exp\left(\frac{V}{k_B T}\right)-1\right] \tag{5-1}$$

Where A is the cell area, A^* is the Richardson constant for the device and ϕ_b is the Schottky barrier height.

For a fixed voltage in the linear portion of the ln(V) vs I characteristic (i.e. after turn-on, but before the effects of series resistance become apparent) we can determine the Schottky barrier height at that bias by plotting $\ln(I/T^2)$ against $-1/k_BT$ as a function of temperature in what is generally termed a Richardson plot [120]. Rearranging equation 5-1 into equation 5-2 shows that the gradient of this plot is equal to the barrier height at that voltage (ϕ_b-V_a):

$$\ln\left(\frac{I}{T^2}\right) = \left(\phi_b - V_a\right)\left(\frac{-1}{k_B T}\right) + \ln(AA^{*}) \tag{5-2}$$

Plotting these Schottky barrier heights against the applied voltage and then extrapolating to zero bias yields the Schottky barrier height for the device. This plot is shown in Figure 5-10 for ICL4, giving a Schottky barrier height of 0.8eV for this structure.

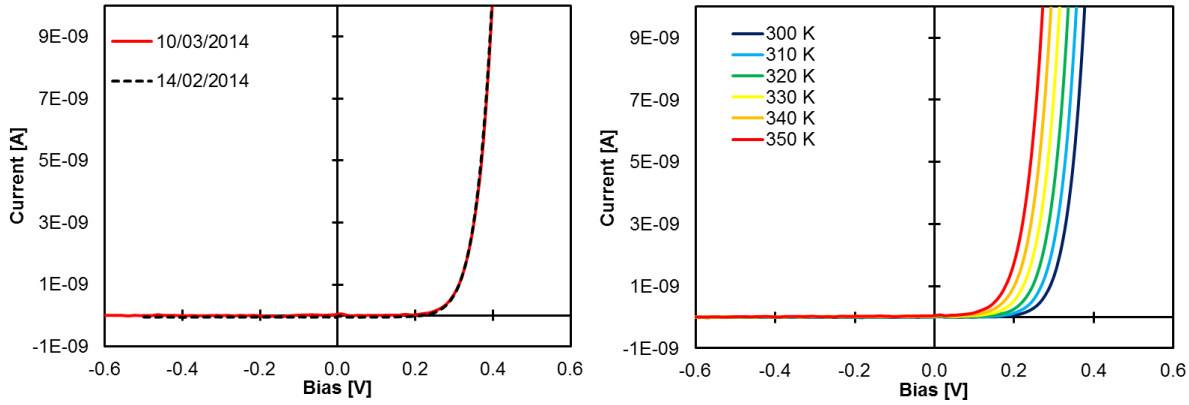

Figure 5-9. Left: The dark IV characteristics for ICL4 after fabrication and one month after fabrication following experimental work, showing a 4% RMS difference in current over the range. Right: The dark IV characteristics as a function of temperature, from which the Schottky barrier height is computed.

This value of the inferred Schottky barrier height depends sensitively on the surface preparation, making it difficult to theoretically predict. In the various Silver/GaAs structures fabricated during this project we have observed Schottky barrier heights from 0.65eV-0.85eV, in line with the variation found in the literature e.g. [119], [121], [122]. This variation is attributable to the impact of Fermi level pinning of the GaAs by surface states [123], and is what makes the semi-empirical modelling of these structures a necessity.

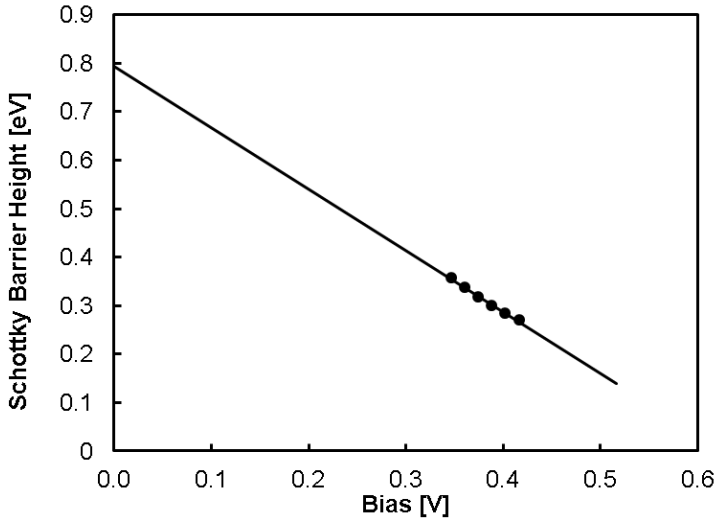

Figure 5-10. The inferred Schottky barrier height as a function of applied bias for the Ag/GaAs barrier in sample ICL4

5.3.2 Silver layer reflection

For a fair comparison of the IV characteristics for different wavelengths, it is important to know that the absorption for these wavelengths is comparable. For this reason, the reflection as a function of wavelength below the band gap of GaAs was measured at room temperature for ICL4. This was carried out by using the wavelength tuneable laser (source 1) and comparing the responses of two photodetectors as shown in Figure 5-11.

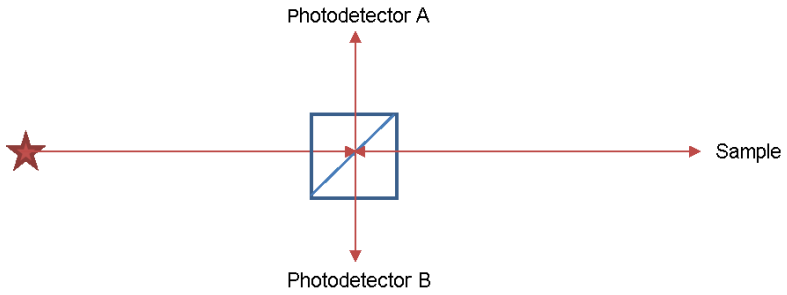

Figure 5-11. A schematic of the setup to measure reflection of a sample using a tuneable wavelength laser source

The reflection as a function of wavelength from an identically deposited silver film on GaAs is presented in Figure 5-12, and compared with the values determined by the transfer matrix program described in section 2.3.1, showing a reasonable quantitative agreement.

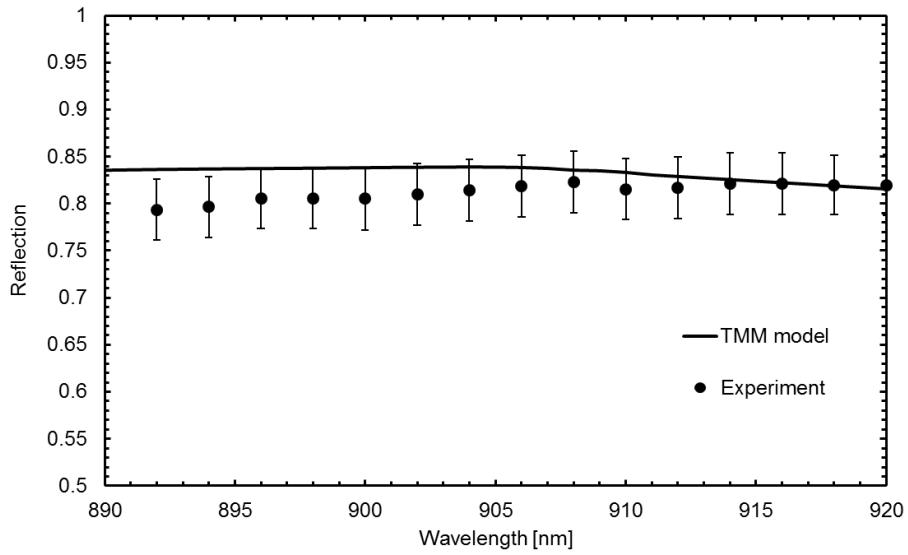

Figure 5-12. Reflection from a 22nm Silver film on a thick GaAs substrate in comparison with the Transfer matrix model

The TMM model and the experimental data are within error of each other from 900nm over the range shown. For this reason, illuminated IV characteristics in the initial investigation

of the following section were carried out between 900-918nm, which is below the GaAs band gap and for which the reflection was reasonably constant.

5.3.3 Light IV results

ICL4 was illuminated with the pulsed Ti:Al_2O_3 laser as the input source (source 1 from section 5.2.1). Figure 5-13 shows the temperature dependent IV characteristics of the cell at two different wavelengths, 900nm and 918nm. These were the widest separated wavelengths for which the fractional absorption was shown experimentally to be identical in section 5.3.2. The time-averaged power for the laser was kept constant at 1mW (focused to provide an intensity of 8.8W/cm^2) for both wavelengths and over the range of temperatures studied. The currents as a function of bias have been normalized to one at the zero bias point to allow comparison between the different wavelengths and temperatures used, and also to ease comparison with the theoretical results shown in section 4, for which the same normalization was applied. The absolute value of the J_{sc} as a function of temperature is plotted inset in each graph to show the expected exponential increase in current caused by the increase in carrier temperature, as discussed in section 4.4.2.

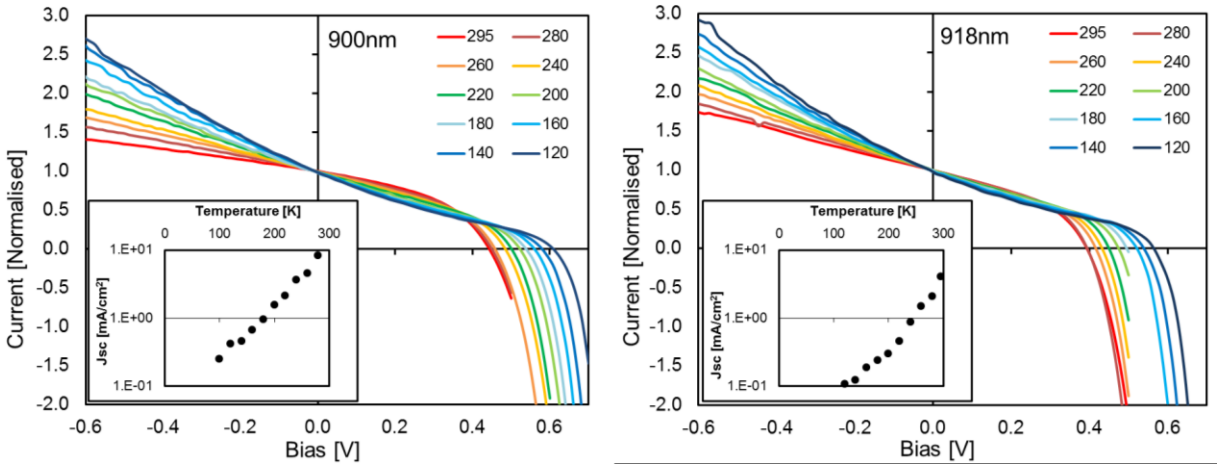

Figure 5-13. The normalised experimental IV characteristics for ICL4 under two different laser illuminations, 900nm and 918nm, at lattice temperatures from 120-295K Inset on each graph shows absolute value of J_{sc} as a function of device temperature.

The experimental temperature dependent IV characteristics shown in Figure 5-13 show a variety of the features already explored in the theoretical IV characteristics of section 4.4.2. These IV characteristics show a change in both the gradient of the current in the reverse bias region and also in the V_{oc} as the lattice temperature is reduced. The change is qualitatively similar to that produced in the theoretical model and gives evidence that the

photocurrent is attributable to absorption in the metallic region followed by extraction to the semiconductor region, since free-carrier absorption in the semiconductor could not explain the magnitude, direction or trend with temperature shown by the experimental IV characteristics. This possibility was discounted experimentally by etching the Silver from the illuminated region and observing no photo-current. The possibility of band-to-band absorption in the GaAs, as in a standard Schottky cell, and how this changes the IV characteristic is explored in section 5.4.3.

The increase in the gradient of the IV curve in the reverse bias region as the temperature of the lattice is reduced is a result of the associated reduction in electron temperature in the metal, as previously explained in section 4.4.2. Illuminating with the same wavelength of light, but for a lower initial lattice temperature will result in a cooler electron distribution, giving rise to a steeper gradient, as observed in Figure 5-13, in which the current (relative to J_{sc}) is nearly twice as large when the lattice is at 120K compared to room temperature.

These features are apparent for illumination at both 900nm and 918nm. Comparing the IV characteristics for each of these wavelengths shows that the longer wavelength illumination results in an IV characteristic with both a lower V_{oc} and a steeper gradient in reverse bias over the full temperature range explored. This is as one might expect from the results in section 4.4.2 if the shorter wavelength of illumination is resulting in hotter electrons in the metal and is a good start to proving the principle of the metallic hot carrier photovoltaic cell.

5.3.4 IV results with variable pulse width

The previous section showed that the gradient in the reverse bias region of the IV characteristic responded to changes in temperature, as predicted theoretically, however it was not shown that this electron temperature was different from the lattice temperature, though with picosecond timescale pulses of illumination repeating every 12.5ns this is highly likely. To explore this further the illumination source was changed to a variable pulse-width and duty cycle source (source 2 described in section 5.2.1) to determine whether increasing the time of continuous illumination affected the IV characteristics. The illumination wavelength was 894nm (the nearest wavelength diode laser to match the Ti:Al_2O_3 output) with an instantaneous power of 10mW (giving a time averaged power of 0.5-2mW depending on the duty cycle, equating to time averaged intensities of between 4.4-17.6W/cm^2).

Figure 5-14 compares the normalised IV characteristic for illumination at four different duty cycles (5-20%) for two different pulse widths (200ns and 10us) and all for the same instantaneous power (i.e. the same current used to drive the diode, but for a varying pulse duration and repetition rate). Using the same instantaneous power means the (as generated) electron temperature should be identical, but varying the pulse width and duty cycle allows us to probe the effect of energy loss from the electron population in this cell.

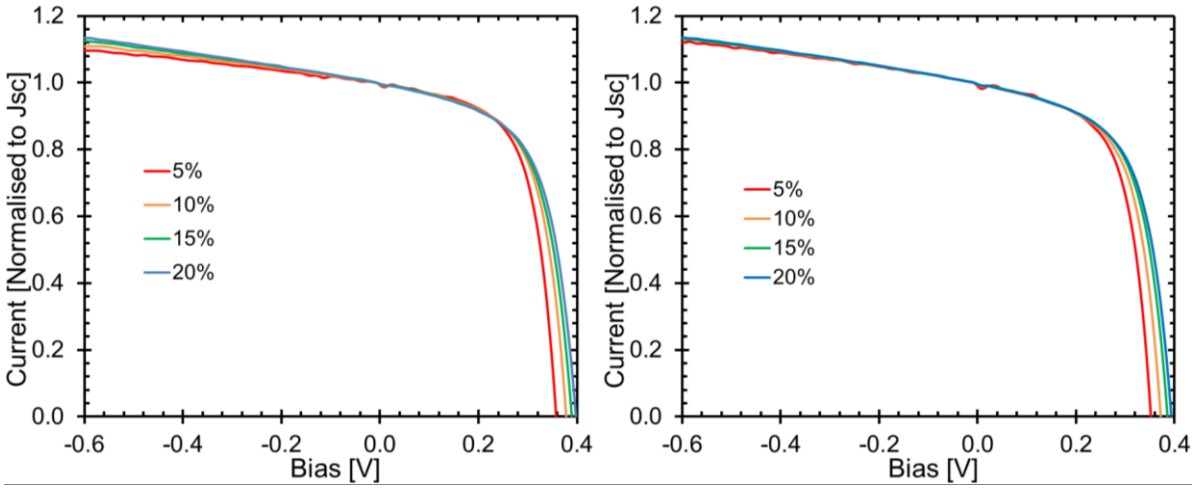

Figure 5-14. Illumination of ICL4 with different duty cycles of 894nm light with pulse widths of 200ns (left) and 10us (right). With the same instantaneous power and the sample at 295K.

A decrease in the V_{oc} is seen for both pulse-widths (200ns and 10us) as the duty cycle is reduced from 20% to 5%. For the 200ns case this change in V_{oc} is logarithmically dependent on the change in the J_{sc} for different duty cycles (Figure 5-15, red line), so this change can be explained as simply the increase in the relative importance of the dark current as the photocurrent is reduced. This is evident from an analytical rearrangement of the diode equation, yielding a simplistic linear relationship between V_{oc}, $\ln(J_{sc})$ and temperature, equation 5-3:

$$V_{oc} \approx \frac{k_B T}{q} \ln\left(\frac{J_{sc}}{J_0} + 1\right) \tag{5-3}$$

The good linearity shown in the results for a 200ns pulse-width implies that there is no substantial change in the lattice temperature, which would result in a larger increase in dark current (as is also apparent in the modelling shown in Figure 4-13 left) when the lattice temperature is changed and would affect the linearity of V_{oc} vs J_{sc}.

This gives good evidence that the lattice temperature of the GaAs region is not increased during this illumination period. However, for the 10us pulse-width the change in V_{oc} is no longer logarithmically dependent on the change in J_{sc}. Figure 5-15, black line, shows that as the intensity is increased the V_{oc} is reduced, relative to the straight-line dependence we would expect if the temperature were constant. This indicates that there is a change in lattice temperature for this set of duty cycles at this pulse-width, with increasing lattice temperature for increasing intensity.

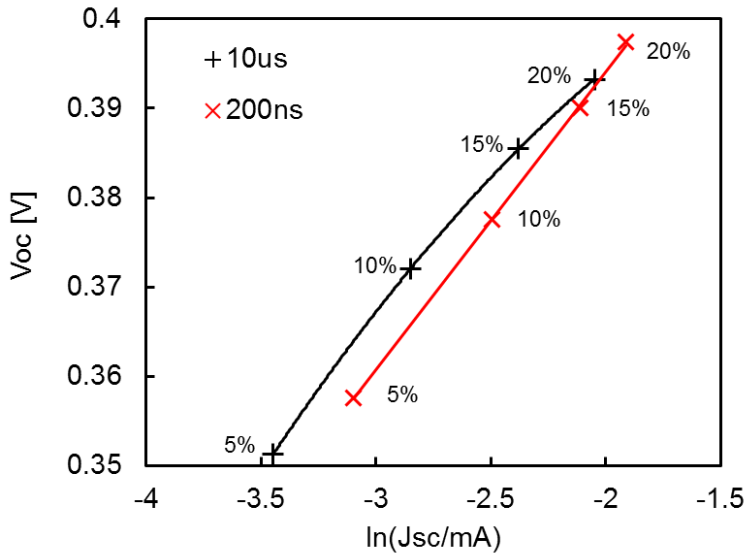

Figure 5-15. Ln(J_{sc}) vs V_{oc} for the IV characteristics shown in Figure 5-14, demonstrating a lattice heating effect for illumination with a pulse-width of 10us, but not for 200ns

The change in the reverse bias current gradient as a function of duty cycle between these two pulse-widths in Figure 5-14 shows some interesting differences, which give further information about this lattice heating effect. For the shortest pulse width (200ns) it is observed that as the duty cycle is reduced (from 20% to 5%), while the instantaneous power is kept constant, the reverse bias gradient decreases. For the longest pulse width (10us) a change in the reverse bias gradient with duty cycle is not observed. These changes imply that for the shortest pulse width the electrons in the metal are at a lower temperature for higher duty cycles, implying that electrons are cooling (losing energy) over longer illumination periods. However, for the longest pulse width, the results suggest that the electrons are achieving equilibrium with the metallic lattice during one cycle, so changing the duty cycle does not affect the (temperature dependent) IV characteristics.

To explore this further the interesting "figure of merit" from these graphs, the dI/dV gradient in the reverse bias region, is compared across three orders of magnitude of pulse

width (100ns-100us[3]) and the four stated duty cycles (5-20%). The dI/dV from each combination of pulse-width and duty cycle was calculated and plotted in Figure 5-16 to illustrate the change that is observed.

The trend is such that a smaller duty cycle, or a shorter pulse duration is required in order to observe the hottest carrier temperatures (lowest dI/dV). For the 5%, 10% and 15% duty cycles the gradient of the reverse bias current decreases as the pulse duration is reduced, indicating an increase in electron temperature. The decrease of dI/dV with shortening pulse duration reduces as the duty cycle is increased and is not observed for the case of a 20% duty cycle.

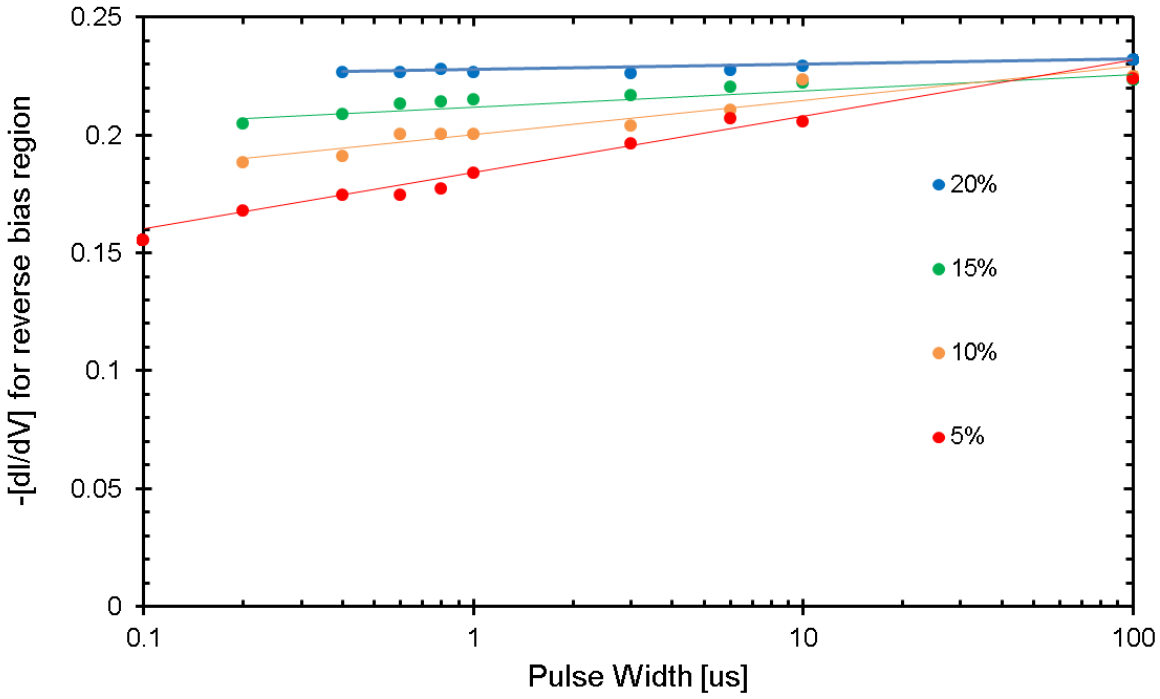

Figure 5-16. -dI/dV of reverse bias region plotted for different duty cycles (5-20%) as a function of laser illumination pulse width (for the same time averaged power in all cases).

[3] The ILX Lightwave LDP-3840B can only achieve the shortest pulse width (100ns) with duty cycles of 5% and below, the achievable pulse-width increases as duty cycle increases. A 100ns pulse-width is not available for 10% and 15% duty cycles and a 200ns pulse-width is not available for a 20% duty cycle.

These changes imply that as the pulse duration and duty cycle is increased, a greater transfer of energy from the photogenerated electron population is occurring, which is warming the lattice and contributing to a reduction in the V_{oc}, as observed in Figure 5-15.

5.3.5 Conclusions for a silver based metallic cell

This cell has proven an important principle, that the concept of a metallic solar cell works and that we can change the temperature of the absorber region by altering the wavelength of light, illumination duty-cycle and pulse-width, and the lattice temperature. However, it suffers from two key drawbacks. Firstly, the cell appears to heat, and so only operates properly under pulsed illumination. Secondly, it is not particularly efficient due to the low absorption of silver. The absolute value of the photocurrent (J_{sc}) for 900nm illumination at 295K (as shown normalised in Figure 5-13) is 12mA/cm², while our light intensity is 8.8W/cm², giving an external quantum efficiency (EQE) for this device of ~0.1%.

To improve upon this we shall extend this work using a more optimised absorber, chromium, as the metallic absorber. Silver was used in our prototype metallic cell because of simple fabrication and the robust Schottky junction, which did not degrade with time, unlike the Aluminium layers tested. However, as already mentioned, Cr has better properties for a hot carrier cell, so the remainder of this chapter shows results from cells with a Cr absorber and also looks at a cell with tunnelling based extraction in addition to the previously presented Schottky based extraction.

5.4 Results from ICL9 Cr/GaAs

In this section, the results of ICL9 are discussed. This is a cell based on an 8nm layer of Cr deposited on GaAs as described in section 5.1.2. As with ICL4 the repeatability, dark current and Schottky barrier height were measured. These are briefly summarised in section 5.4.1, followed by an analysis of the J_{sc} vs V_{oc} characteristic of this cell as a function of light intensity to verify that the lattice is not heating, similar to that for ICL4 in section 5.3.4. We will then discuss the illuminated IV properties of this ICL9 in section 5.4.3, with a particular comparison of its IV characteristics when illuminated with light of an energy above and below the band gap of GaAs. This will show the differences between the response of a metallic solar cell and one operating as a Schottky barrier solar cell, in which absorption occurs in the semiconductor region rather than the metal region.

5.4.1 Repeatability, dark current and Schottky barrier height

The Chromium on GaAs device ICL9 showed excellent repeatability over a one month period and also across different devices processed on a die, allowing confidence that the obtained results are representative of the structure. The device pitch is ~400um, yielding 225 devices on a 1cm^2 die, measuring two devices on opposite sides of the die shows excellent uniformity in device response (Figure 5-17).

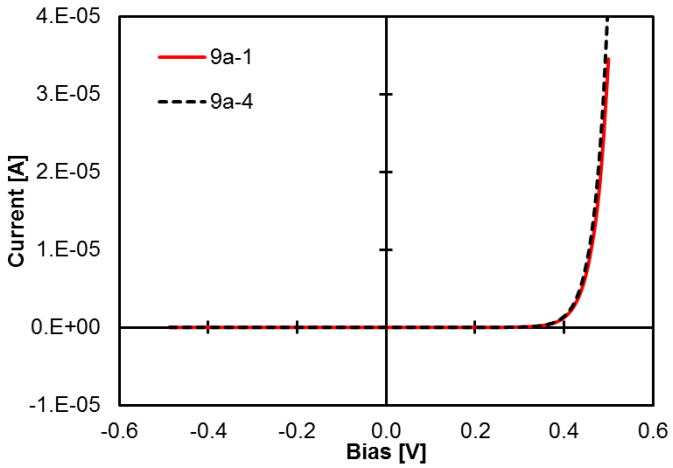

Figure 5-17. Dark IV characteristics of two wire-bonded devices on opposite sides of a processed die, 1cm apart, showing good reproducibility across the processed region.

The dark current response of this device showed excellent rectification properties with the rectification ratio between ±0.5V averaging over 10^5. Using the same technique outlined in section 5.3.1 the Schottky barrier height was computed to be 0.78eV for ICL9.

5.4.2 Change in V_{oc} with J_{sc}

Using the same method as with ICL4 outlined in section 5.3.4 it is important to firstly measure the IV characteristic as a function of light intensity in order to show linearity of the V_{oc} vs $\ln(J_{sc})$ response and ensure that any results we observe are not caused by direct lattice heating. Figure 5-18 shows the light IV characteristic of ICL9 at a lattice temperature of 243K under illumination at a wavelength of 890nm with a laser power of 30-150mW (focused to provide intensities between 16-80W/cm^2).

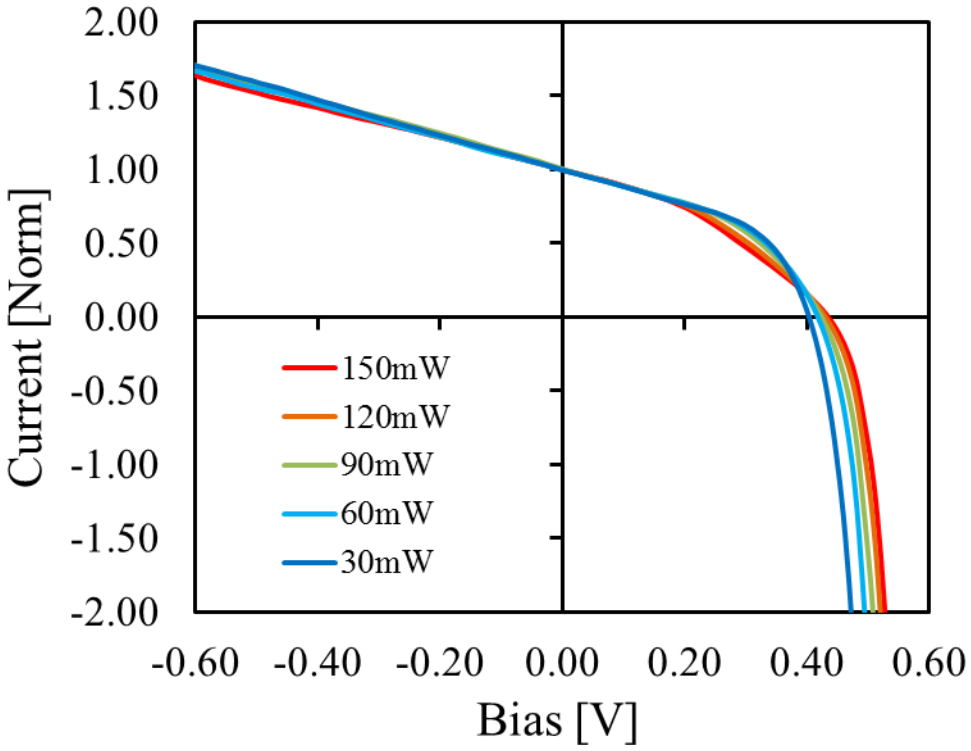

Figure 5-18. The light IV characteristic of ICL9 under illumination at 890nm and 243K for incident laser powers from 30-150mW, as in the legend.

The reverse bias IV shows a small decrease in its gradient as the power is increased from 30-150mW in line with expectations if increasing the illumination power results in an increase in electron temperature. The total decrease in gradient over this range is consistent with an increase in electron temperature of 10K according to our modelling. This agrees with the degree of heating caused by a given laser pulse calculated via the electronic heat capacity, as per the method of Groeneveld [124], with the exception being that for algebraic simplicity we assume that the result is a fully thermalized Fermi distribution so that this temperature can be input to our model.

As previously, to determine whether this increase in temperature is a global increase in lattice temperature, or local to the electrons in the thin metallic region, we compared the Jsc and Voc for each illumination power.

Our device results, extracted from Figure 5-18, are shown as the black crosses on Figure 5-19 along with two different fits. The black solid line shows a linear relationship between V_{oc} and J_{sc} assuming a constant lattice temperature of 243K. The red dashed line shows the modelled effect of increasing the lattice temperature in line with our findings from Figure 5-18, which suggested an increase in electron temperature of 10K from 30mW-150mW excitation.

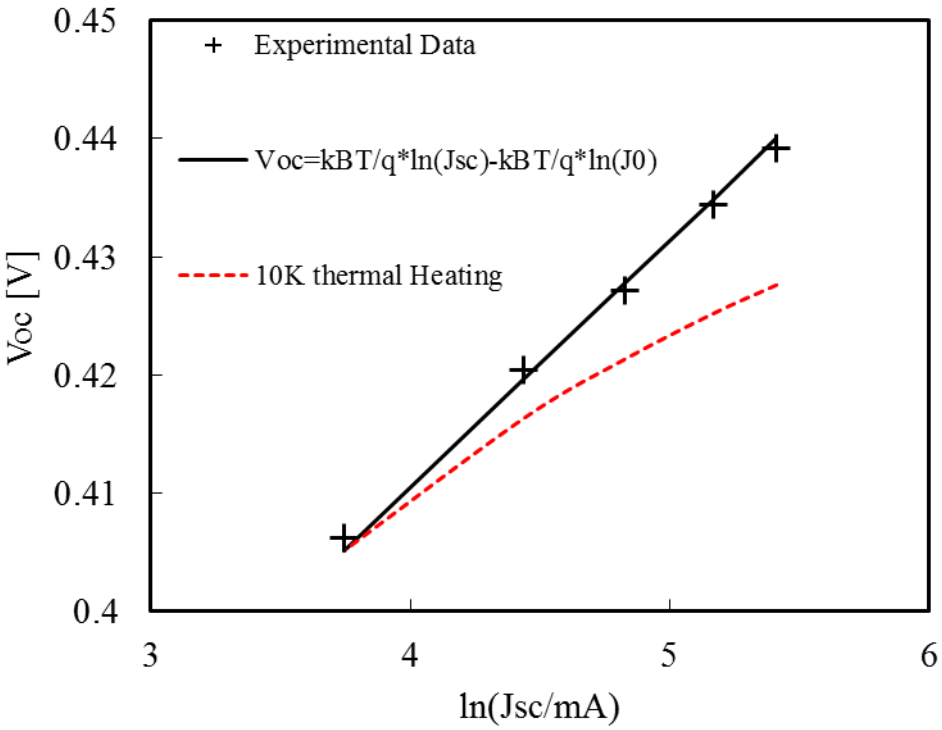

Figure 5-19. Ln(J_{sc}) vs V_{oc} for a Cr/GaAs metallic cell under illumination at 890nm and 243K for incident laser powers from 30-150mW, as in Figure 5-18.

No sub-linear trend is observed in Figure 5-19, therefore no lattice heating greater than 1K occurs in this cell as the laser illumination is increased from 30mW-150mW. This result, combined with the observation of a decrease in reverse bias gradient in Figure 5-18, caused by an increase in electron temperature, is evidence that we are seeing hot carrier extraction from the thin metallic layer. A non-linear change in V_{oc} vs ln(J_{sc}) starts to occur for lattice temperatures above 263K for this cell, so for this reason we only present results in the following section up to this temperature.

5.4.3 Schottky Response compared with metallic response

ICL9 was illuminated with laser wavelengths of 870nm and 890nm, using source 1 described in section 5.2.1, chosen to allow us to tune either side of the GaAs absorption edge by varying lattice temperature. The beam was focused to provide an intensity of 16W/cm^2.

The normalized IV characteristics are presented in Figure 5-20, for temperatures from 123-263K and at a fixed wavelength of 890nm. The results are normalized as conventional in this work, but the absolute values of J_{sc} for all temperatures studied are plotted as insets to each graph. The interesting feature to recognise from the relationship between the J_{sc} and

temperature is that for metallic absorption in Figure 5-20 and Figure 5-21 the exponential increase in J_{sc} with temperature is observed, which then increases with $T^{3/2}$ in Figure 5-22 and Figure 5-23 for the temperatures for which band edge absorption occurs in the GaAs. This is in line with theoretical predictions for both these regimes and for the reasons discussed in section 4.4.2.

Studying Figure 5-20, it is apparent that increasing the temperature of the sample for a fixed illumination intensity and wavelength has two key effects, firstly it reduces the open circuit voltage (V_{oc}) and secondly the gradient of the slope in the reverse bias region of the IV characteristic reduces. These features in the IV are similar to the already presented theoretical work and also with the results seen for the silver based cell ICL4 in the previous section.

Further to the previous explanations, the fact that we see a slope in the reverse bias region demonstrates the device operation is by emission from the metal region into the semiconductor, rather than showing any problems with shunt resistance. It is caused by the large difference in electron density in the metal region and the semiconductor, resulting in the fact that increasing the reverse bias (raising the metal potential higher than the semiconductor potential) will result in an incremental increase in current in this region. This is confirmed later by comparison with illumination at 870nm in Figure 5-21.

The reduction in the gradient of the reverse bias region IV as the temperature is increased is due to the reduction in photo-excited carrier temperature in the metal region, as confirmed previously through modelling in chapter 4. A lower substrate temperature means that for the same additional energy input a lower carrier temperature is reached. The lower the carrier temperature the greater the decrease in the density of electrons with respect to energy in the metal region (i.e. the electron Fermi distribution is sharper for colder temperatures). Given that the current, and the rate of change of current with bias, is governed by the density of these electrons at the energies at which they can overcome the Schottky barrier, a colder distribution will result in a greater change in current for a given change in bias. This is as observed as the steeper gradient for the colder temperatures in Figure 5-21.

The second feature of Figure 5-21, which is more straightforwardly explained, is the decrease in Voc as the temperature is increased. This is similar to a traditional photovoltaic cell and is caused by a reduction in the rate of electrons from the GaAs being transferred to the metal at a given bias. A lower temperature will cause the electron density distribution in

GaAs to have a lower peak energy and therefore require a higher bias to be equal to the electron density in the heated distribution in the metal, i.e. the V_{oc} condition of matched carrier flux from metal to GaAs and vice versa

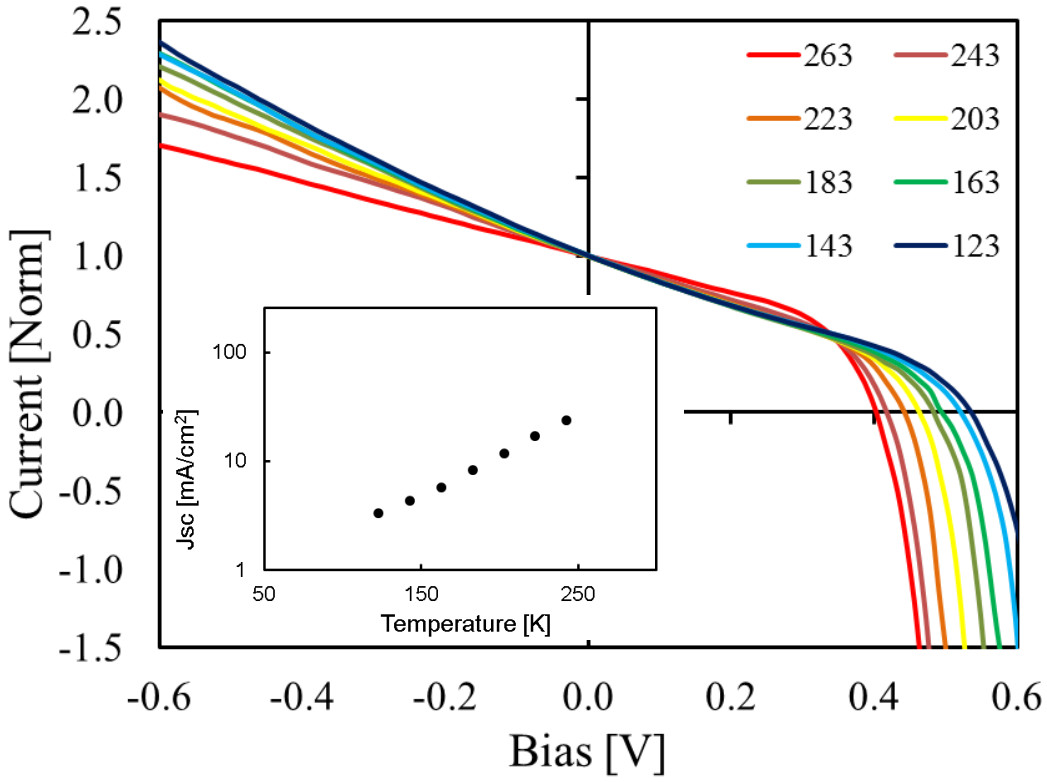

Figure 5-20. The light IV characteristic of a Cr/GaAs metallic cell under illumination at 890nm, below the GaAs band gap over the range of temperatures investigated here (Legend: Temperature/K). Inset shows absolute value of J_{sc} at each temperature

This mode of device operation can be further illustrated by varying the wavelength of illumination around the band gap of GaAs, as shown in Figure 5-21. Figure 5-21 shows the normalized IV characteristics of the device under illumination at the shorter wavelength of 870nm. At this wavelength and over the temperature range from 123-263K the illumination can be tuned above and below the absorption edge of the bulk GaAs. For the illuminated device at temperatures lower than 263K “metallic solar cell” IV characteristics are observed, as with the illumination at 890nm, with a slope in the reverse bias region. This is due to the electrons being excited by light in this region and heating this layer, with no other current creating mechanism involved.

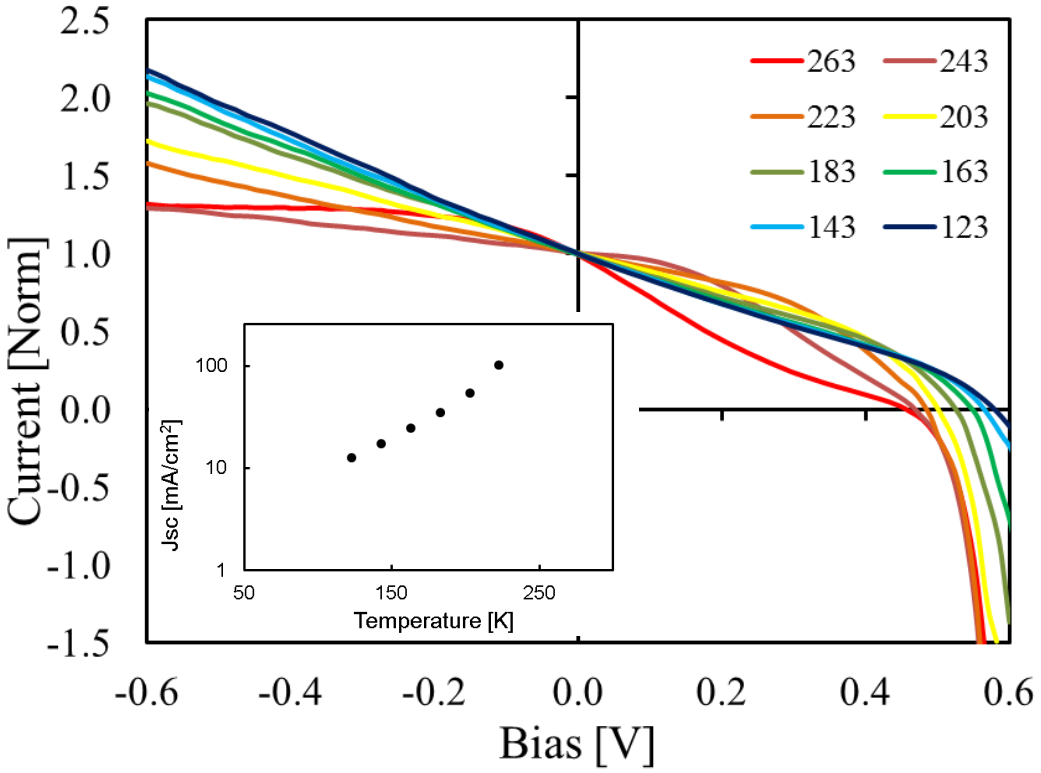

Figure 5-21. The light IV characteristic of a Cr/GaAs metallic cell under illumination at 870nm, using temperature to tune the GaAs band gap above and below the illumination energy (Legend: Temperature/K). Inset shows absolute value of J_{sc} at each temperature

As the temperature of the cell is increased the band gap narrows and carriers can be photo-generated in the GaAs. Under these conditions the device starts to operate like a standard Schottky solar cell, with the Schottky barrier at the Cr/GaAs interface now acting to separate electrons and holes that are photo-generated in the GaAs (as described in the theoretical section 4.4.1). This mechanism (a standard Schottky cell) results in the current in reverse bias saturating, as the current can now only be as high as the photo-generated current in the GaAs, rather than continually increasing if it is due to an increase in electron temperature in the metal region. This saturation is clearly observed in the IV characteristic for a lattice temperature of 263K. Another notable feature of this IV characteristic is the particularly low fill factor for the Schottky operation in comparison with the fill factor observed for metallic operation. This is attributable to the high dark current from the metal region, as this region will still be absorbing light in addition to the GaAs absorption and thus heating up.

Further evidence of these effects, with the same justification, can be seen in Figure 5-22 and Figure 5-23, presenting illumination at shorter wavelengths still (850nm and 785nm).

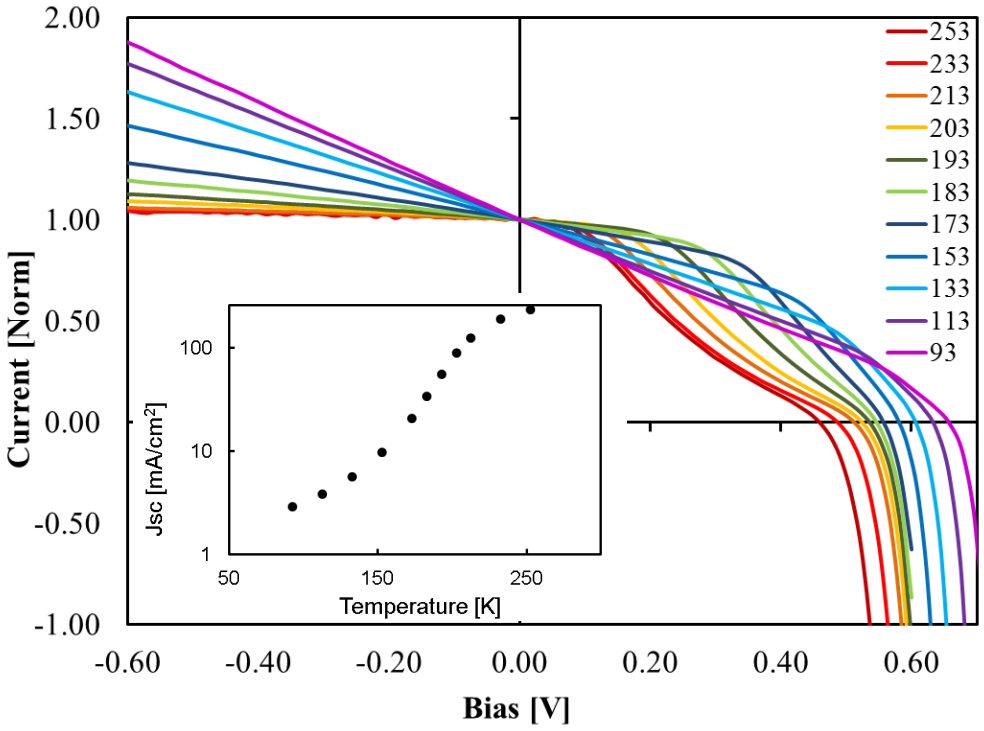

Figure 5-22. The light IV characteristic of a Cr/GaAs metallic cell under illumination at 850nm, using temperature to tune the GaAs band gap above and below the illumination energy (Legend: Temperature/K). Inset shows absolute value of J_{sc} at each temperature

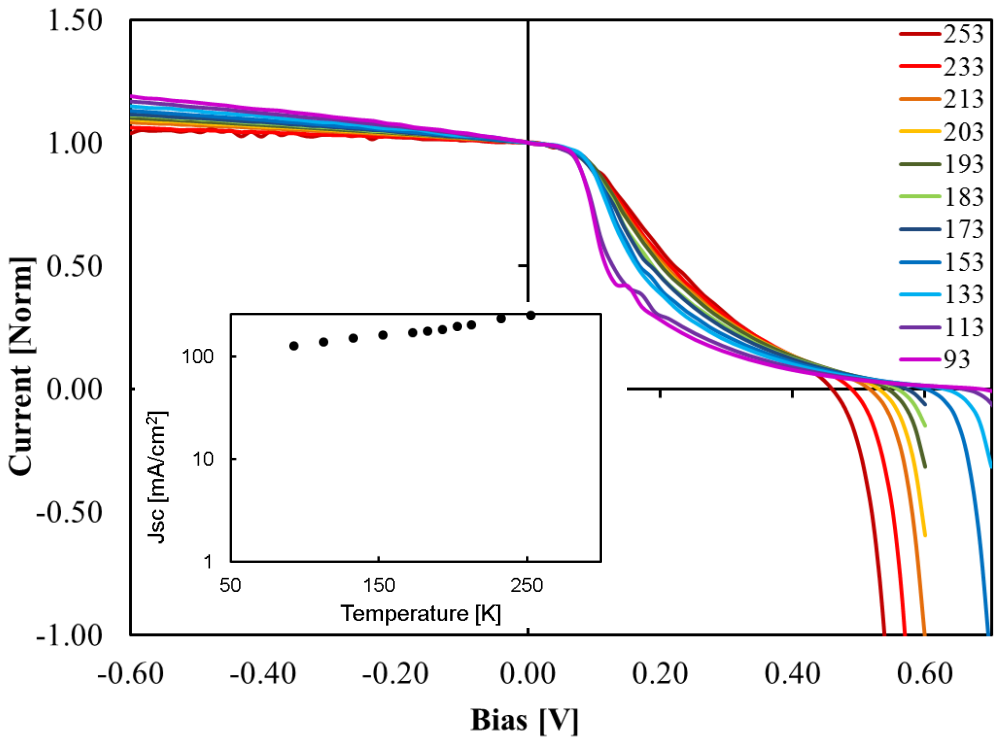

Figure 5-23. The light IV characteristic of a Cr/GaAs metallic cell under illumination at 785nm. Inset shows absolute value of J_{sc} at each temperature

It was necessary to lower the temperature to 93K in order to see the cross-over between metallic operation and Schottky operation with illumination at 850nm in Figure 5-22, however, no temperature reduction is able to tune the band gap of GaAs to absorb at 785nm, so Schottky operation is observed at all temperatures in Figure 5-23. In particular in Figure 5-23 the great heating of the metal layer with the shorter wavelength light, combined with the absorption in the semiconductor layer, leads to a particularly low fill factor, showing a clear progression of the device characteristics from illumination at 890nm to 785nm.

Importantly, in comparing Figures 5-20, 5-21, 5-22 and 5-23 it is evident that the gradient of the reverse bias slope is decreasing for shorter wavelengths. This is as observed for ICL4 and due to the increase in carrier temperature for shorter wavelengths, as argued previously both in theory and experiment. To explore this further we plotted the increase in current at -0.6V relative to 0V as a measure of the reverse bias gradient in Figure 5-24, this was carried out for illumination at 850nm and785nm as a function of temperature, and also for the two wavelengths simultaneously (using source 3 from section5.2.1).

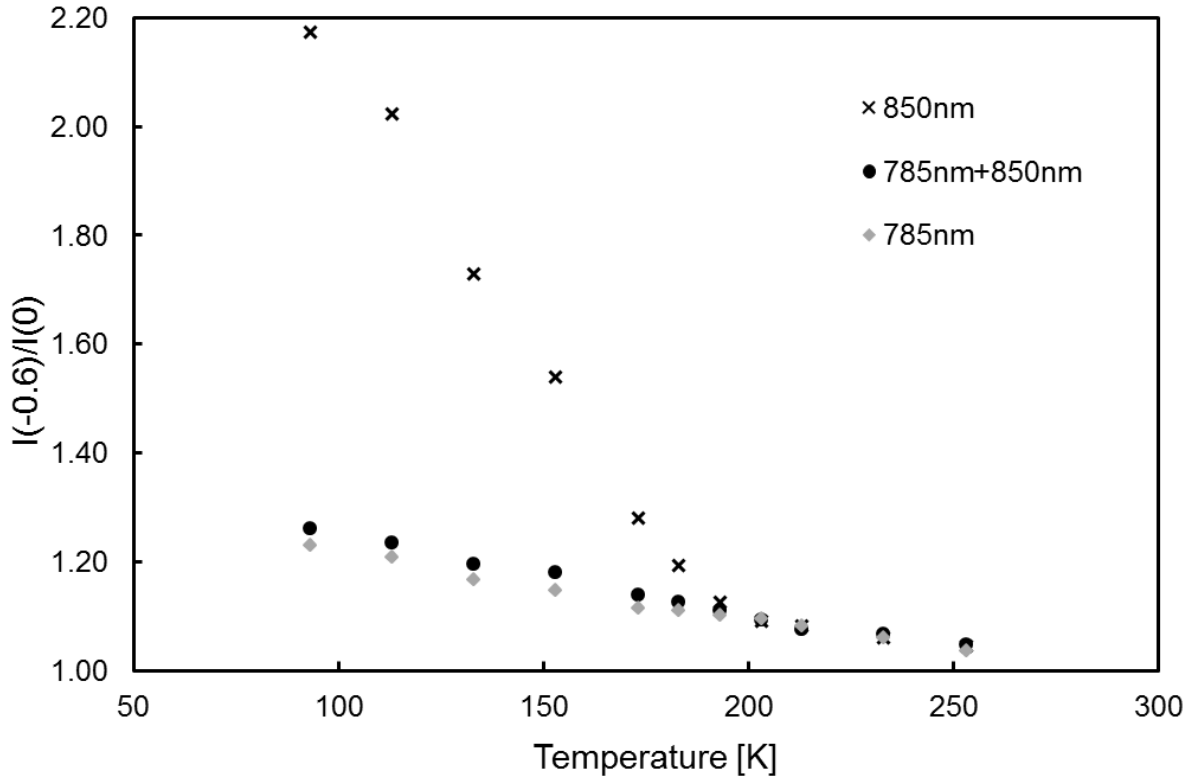

Figure 5-24. Increase in current at -0.6V relative to 0V plotted as a function of temperature for illumination at 850nm, 785nm and a combination of the two

Illumination with either 785nm, 850nm or a combination of the two provides an identical IV response in terms of the gradient of the reverse bias slope until ~190K, in which all cells can absorb in the GaAs region and are operating as a Schottky barrier solar cell. At temperatures below 190K the 850nm light is not strongly absorbed in the GaAs (shown with our TMM modelling to reduce from 9% of total absorption occurring in the GaAs region at 213K, reducing to less than 2% at 173K), giving further evidence for the metallic absorption in this cell and the dependence of the IV characteristic on temperature.

Interestingly, the combination of a 785nm and 850nm illumination results in an intermediate gradient being observed in Figure 5-24. This is important for the concept of carrier equilibration for carriers excited with different wavelengths of light, and will be explored further in section 5.5.3.

In providing an illustration of the cross-over between the metallic cell and Schottky cell regimes it is clear from Figures 5-21, 5-22 and 5-23 that the device characteristics presented in Figure 5-20 represent features caused by absorption of light in the metallic layer and demonstrate that we are observing extraction of carriers from this layer and not a shunted cell with some anomalous long wavelength absorption in the semiconductor itself. As previously mentioned, this is also supported by the fact that etching off the absorber region metal results in no observable photo-response for this device below the GaAs band edge. This explains the IV characteristic mentioned in section 5.1.2, in which the roughness of the cell was assessed through illumination with broadband light. Illumination with broadband light inevitably causes carrier generation in the GaAs region and leads to Schottky type behaviour contributing to the IV characteristics rather than pure hot carrier metallic operation.

5.5 Comparison of HYL11 and HYL12: tunnelling vs Schottky

Having proved the principle of the metallic hot carrier cell in both silver and chromium deposited on GaAs, the ultimate test of this concept is to extract carriers photogenerated in a metal through tunnelling; figuratively, combining the previous hot carrier design in a semiconductor tunnelling structure (chapter 3) with the promise of higher absorption in a thin metallic film. This combination is realised in HYL12, in which an AlGaAs/GaAs quantum well is used as the energy selective contact to remove hot electrons from a Cr region by tunnelling. HYL11 is the comparison cell, for which extraction of electrons is over a Schottky barrier, created between an adjacent Cr layer and an AlGaAs layer.

The Cr layer thickness in HYL11 and HYL12 was non-optimal in terms of its light absorption properties in order to counter the degradation that we observed for cells with an AlGaAs semiconductor region and a thinner Cr layer. This resulted in a reflectivity for these cells of 65% at 850nm (in line with the expectations of a film of Cr reported in section 4.1.2). Comparing this with the reflectivity for silver of 83%, we can infer that approximately double the absorption is occurring in a 30nm Cr structure than the 22nm Ag structure at this wavelength. This agrees with results from our TMM modelling. Dark IV measurements were repeatable in HYL11 and HYL12 across different devices on a die and over a period of one month, with an RMS current difference of less than 5% as specified in section 5.3.1, so the devices were deemed stable and repeatable.

5.5.1 Schottky barrier height

The Schottky barrier height was measured for both HYL11 and HYL12, although it only has true physical significance for HYL12, since HYL11 should have extraction by both resonant tunnelling and thermionic emission, so the equations used to compute the Schottky barrier height are only strictly accurate for HYL11. A Schottky barrier height of 1.0eV was measured for HYL12, while HYL11 had an "effective" Schottky barrier height of 0.8eV, as plotted in Figure 5-25.

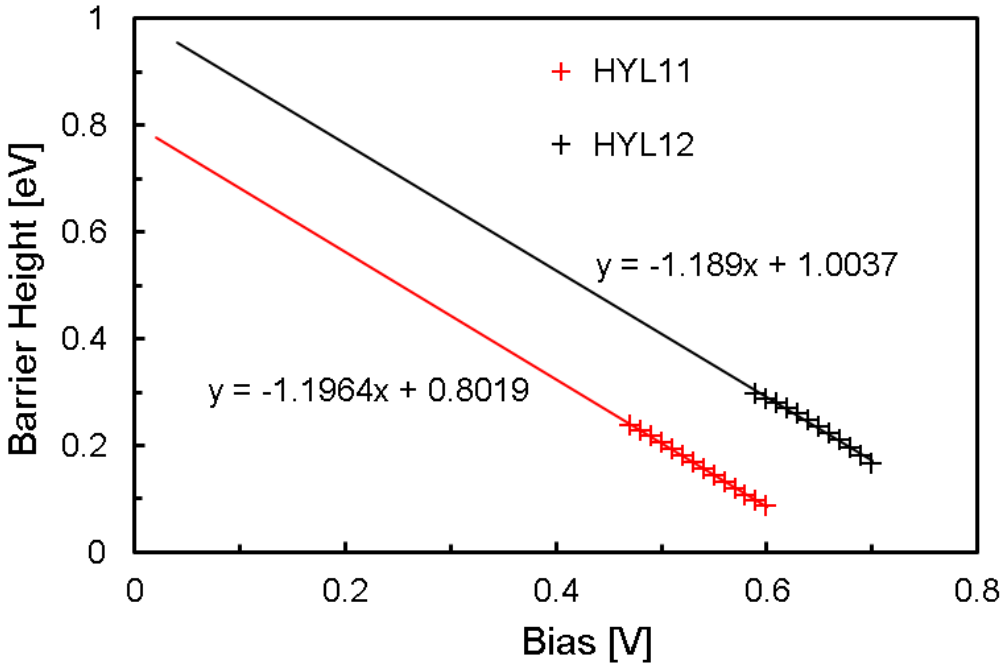

Figure 5-25. The inferred Schottky barrier height as a function of applied bias for the HYL11 (tunnelling) and HYL12 (Schottky), with fits showing extrapolation to zero bias.

The gradient of the fit in each case is almost identical, showing that as the bias is changed, the Schottky barrier changes by the same absolute amount in each case. This is a good sign that the ohmic contact and Schottky contact are of the same quality in each device, presenting the same resistivity and responding similarly to biasing.

We carried out the same effective "experiment" on structures representing HYL11 and HYL12 in our Schrödinger-Poisson model, i.e. changing the cell temperature and simulating the dark current to compute a Schottky barrier height. This method yielded similar results, but when the Schottky barrier height was fixed at 1eV in the potential profile, the computed value from the temperature variations was actually 1.1eV for the modelled HYL12 structure and 0.9eV for the modelled HYL11 structure. This was due to space-charge effects, as mentioned in chapter 2, shifting the response to higher voltages. This implies that the actual Schottky barrier height in the real cell may actually be higher due to this effect.

While there was a difference in the quantitative comparison, qualitatively the theoretical results were in good agreement with the experimental results, predicting a lower effective Schottky barrier height for HYL11 and also revealing a plausible mechanism for this. In the model, the tunnelling extraction provides an additional path at a lower potential energy for the electrons, this results in a lower "activation energy" (or voltage) for current transfer and thus gives an effective lower Schottky barrier height. This mechanism is the desired mode of operation for HYL11 and so is a promising sign that it is working as intended. Further information about this mechanism can be gathered by observing and comparing the cells' IV response under different illumination conditions, presented in the following sections.

5.5.2 Light IV as a function of temperature

Source 3 was used to illuminate HYL11 and HYL12 to allow multiple simultaneous wavelengths of excitation. Prior to multiple wavelength excitation, power and temperature dependent IV characteristics were taken. HYL11 and HYL12 can both be illuminated with shorter wavelength light than ICL4 and ICL9, as the band gap of $Al_{0.4}Ga_{0.6}As$ at room temperature is 0.5eV higher than GaAs. As such, the shortest wavelength used in light IV characterisation is 642nm. In addition to the incorporation of AlGaAs, the thicker Cr layer also lets close to 0% of the incident light through to the AlGaAs, being much more reflective than the 8nm of Cr used in the previous section on GaAs.

As previously, we verified the linearity of the $\ln(J_{sc})$ vs V_{oc} dependence with power. This was carried out at 642nm and linearity of response was confirmed over incident powers of 8-80W/cm² up to a device temperature of 290K.

The (un-normalised) response of HYL11 and HYL12 is shown in Figure 5-26 for illumination at 785nm and 642nm. The un-normalised responses are shown here in order that we can compare the efficiency of these two cells, revealing a 4x higher photocurrent under illumination at 642nm and a 10x higher photocurrent at 785nm for tunnelling extraction (HYL11) compared with thermionic emission over a Schottky barrier (HYL12).

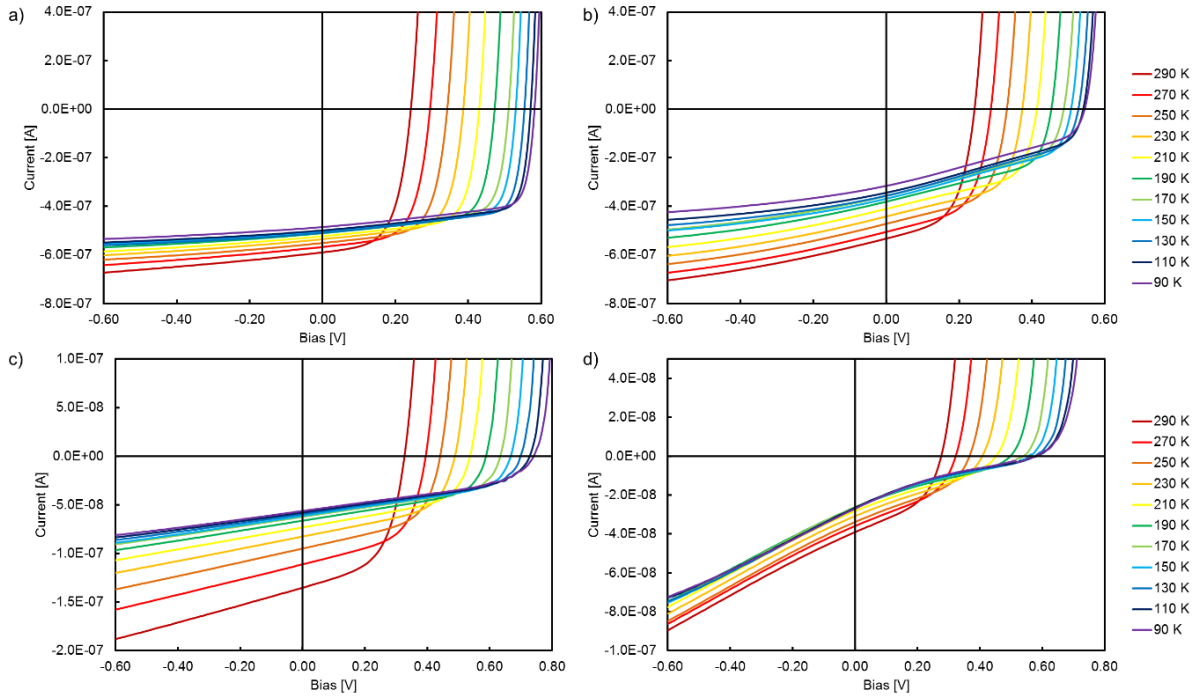

Figure 5-26. IV characteristics as a function of temperature (shown in legend) for illumination of the two Chromium based cells: a) HYL11 (tunnelling) illuminated at 642nm b) HYL11 illuminated at 785nm c) HYL12 (Schottky) illuminated at 642nm d) HYL12 (Schottky) illuminated at 785nm

Converting these values to an effective EQE at this wavelength (642nm) and intensity (8 W/cm²), HYL12 has an EQE of 0.19%, while HYL11 has an EQE of 0.78%. At this early stage, the absolute efficiencies are not particularly impressive, but indicate the improvements available by optimising the structure with a better absorber material (Ag→Cr ~2x increase) and a better extraction method (thermionic emission→tunnelling ~4-10x increase). Further improvements could be made by optimising the Cr layer thickness and adding an anti-reflection coating, which, beyond a few trials, were not pursued in this work.

This is because we are primarily focusing on the physics of the extraction mechanism rather than the optimisation of the device at this stage.

These graphs are in agreement with the expectations from the modelled results in section 4.4.4 and Figure 4-18, with a shallower gradient for HYL11 and a lower V_{oc}. Importantly, the V_{oc} changes by less than the change in the effective barrier height (e.g. at 90K and 642nm illumination HYL11: V_{oc}=0.59V, HYL12: V_{oc}=0.74V giving a V_{oc} reduction of 0.15V compared to the effective barrier height reduction of 0.2V). Therefore, we are not just observing a trade-off between J_{sc} and V_{oc} between these cells, as we do in first generation photovoltaic cells, where a reduction in bandgap inevitably leads to a lower V_{oc} but a higher J_{sc}. Other features of these graphs, such as the change in reverse bias gradient with temperature, are similar to previous devices and will not be discussed further.

To reveal information about operation of these cells we probe them with dual wavelength illumination in the following section to show how exciting electrons to two different energies impacts the IV characteristics. From this, we can infer details of the extraction mechanism and speed in each cell.

5.5.3 Dual wavelength illumination

Illuminating the cells with two wavelengths of light simultaneously reveals information about how electrons excited to two different energies interact before extraction. In particular we will be examining how the cells respond to a single wavelength of light (e.g. 785nm and 852nm separately) and how this compares with the response to both wavelengths together. If the IV characteristics of the single wavelength illumination simply linearly superpose to give the IV characteristic of the dual wavelength illumination then this is evidence that the carriers are behaving ballistically and being extracted before any equilibrating interactions occur. This is the scenario that is imagined in the IPE cell discussed in section 4.4.3. If, instead, the carriers are interacting, we should expect to see a non-linear contribution from the combination of two beams with different wavelengths.

Figure 5-27 shows the IV characteristics of HYL11 and HYL12 under illumination with 642nm (blue line), 785nm (green line) and 852nm (red line) laser light and also combinations of 785nm+852nm (green dashed) and 642nm+852nm (blue dashed).

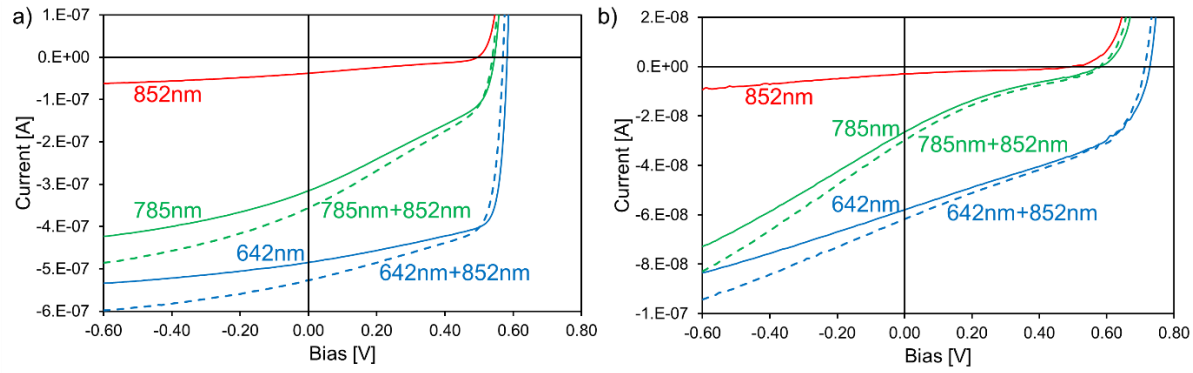

Figure 5-27. IV characteristics at 90K for a) HYL11 (tunnelling) and b) HYL12 (Schottky) at 5 different wavelength combinations: single wavelength illumination at 852nm (red), 785nm (green) and 642nm (blue) and dual wavelength illumination at 785nm+852nm (green dash) and 642nm+852nm (blue dash)

In order to determine whether the increase in current observed under dual illumination is linear or non-linear, the current of each of the single beam illuminated IVs is subtracted from the dual beam IV and the result is divided by the value of the current of the combined beams. This computed value gives a positive value when the current under dual beam illumination shows an increase over the linear addition of the two single beam illuminations and a negative value if there is a reduction in current. Division by the dual beam current gives the impact of the "non-linearity" as a fraction of the total current, so comparison can be made between temperatures and wavelengths.

The results of this calculation for 785nm+852nm and 642nm+852nm for the temperature range of 90K-290K for HYL12 are shown in Figure 5-28.

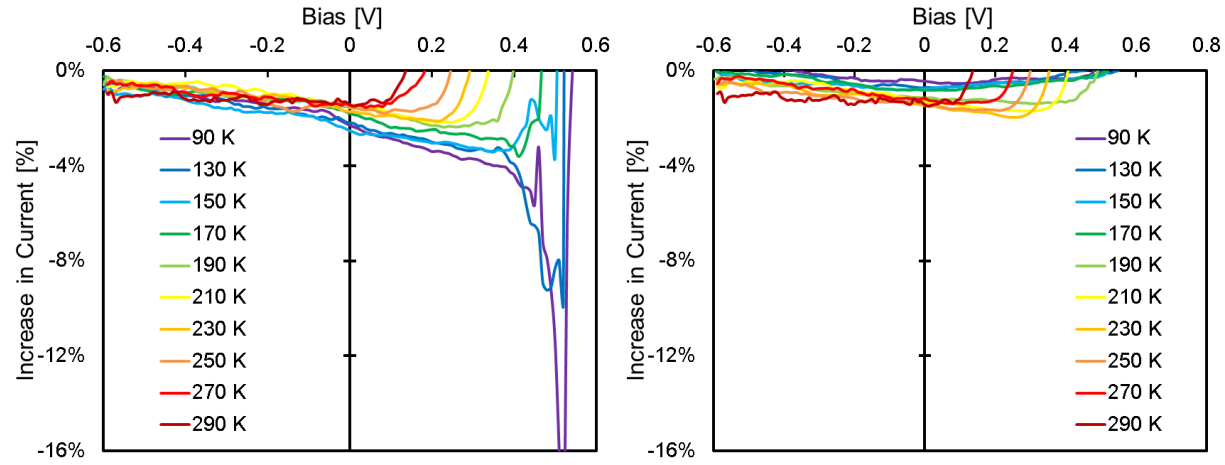

Figure 5-28. Percentage increase in current when HYL12 is illuminated with: Left: 852nm+785nm compared with the individual beams on their own Right: 852nm+642nm compared with the individual beams on their own

This can be compared to the same calculation carried out for HYL11 which is presented in Figure 5-29.

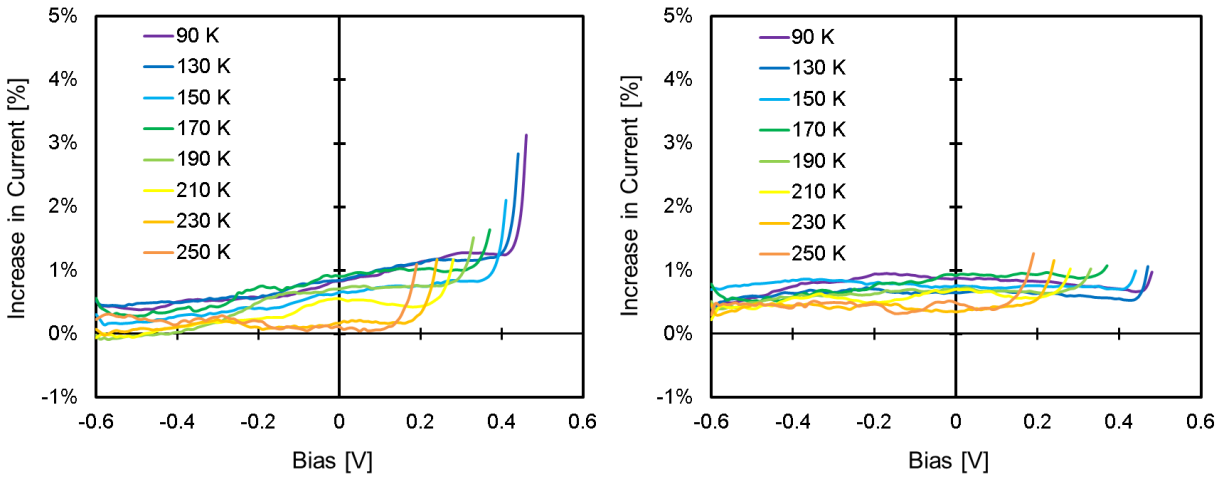

Figure 5-29. Percentage increase in current when HYL11 is illuminated with: Left: 852nm+785nm compared with the individual beams on their own Right: 852nm+642nm compared with the individual beams on their own

The most striking difference between the response for HYL11 and HYL12 is that the addition of illumination at 852nm results in a relative decrease to the photocurrent in HYL12 but results in a relative increase in the current for HYL11. The second difference in response is in the comparison of the addition of the 852nm illumination to either 642nm or 785nm. For the addition of 852nm to a 642nm illumination the relative increase (HYL11) or decrease (HYL12) is uniform with voltage, implying that the excitation is creating carriers so far in excess of the Schottky barrier that changing the voltage has a negligible impact on their extraction. This is not the case for the addition of 852nm to a 785nm illumination, in which the increase (HYL11) or decrease (HYL12) in relative current becomes more pronounced as the effective Schottky barrier height (presented to the metal) is increased (going to positive bias).

The most pronounced effect of the dual wavelength illumination comes at voltages prior to the V_{oc} point and with longer wavelengths (780nm + 852nm) that excite carriers that only just overcome the Schottky barrier. For this reason, we have compared the response of HYL11 and HYL12 at -0.2V before the V_{oc} point over the full temperature range. To reduce the noise present in the subtracted data in Figure 5-28 and Figure 5-29 we modulated the illumination intensity of the 852nm beam to allow us to lock-in to the related changes in current at this applied voltage. This was carried out for both HYL11 and HYL12

and Figure 5-30 shows the relative percentage increase/decrease in the combined illumination current for each of these cells as a function of temperature.

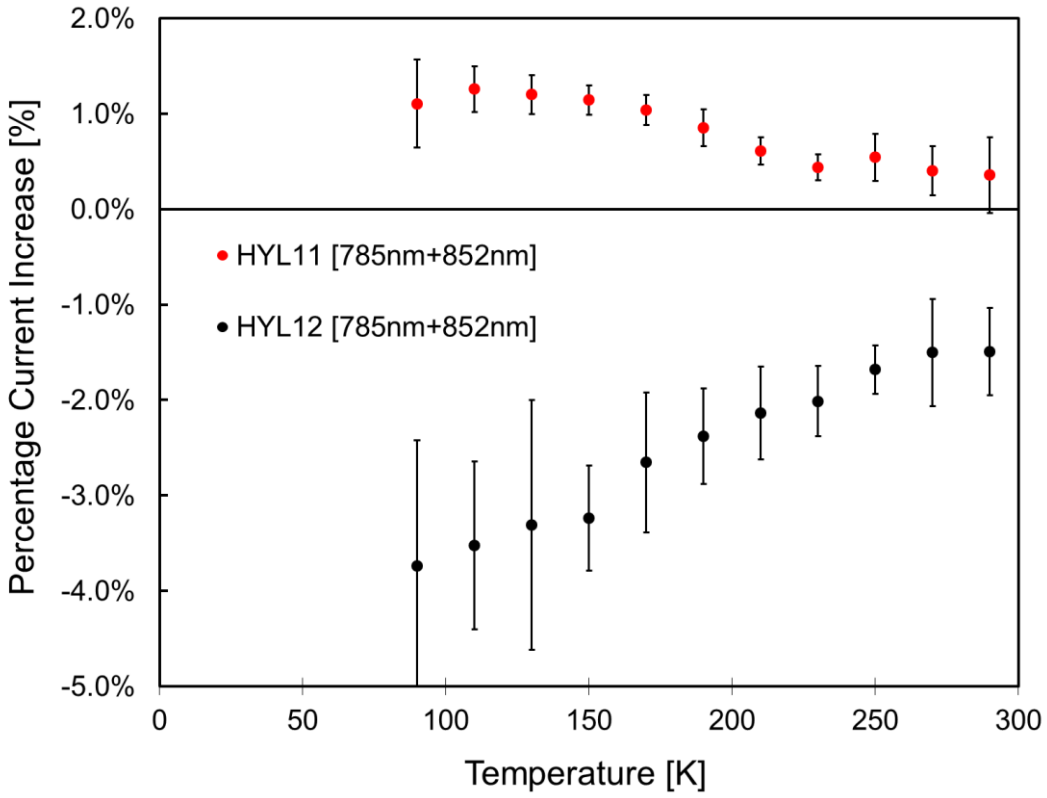

Figure 5-30. Percentage current increase for the tunnelling (HYL11) and Schottky (HYL12) structures for dual beam illumination (785nm+852nm) when compared with the photocurrent generated by each beam independently (measured at V_{oc}-0.2V).

This increase/decrease in the relative current can be explained by the schematics shown in Figure 5-31.

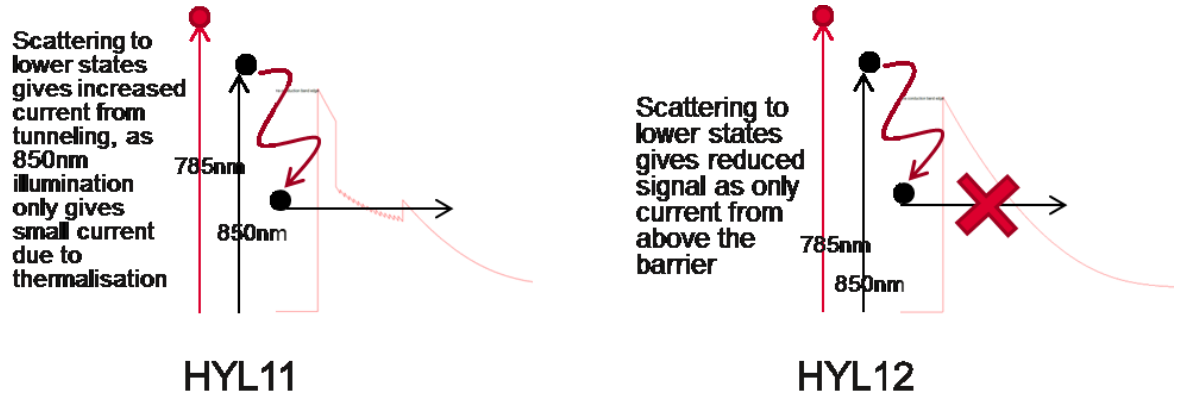

Figure 5-31. A schematic showing the cause of the relative gain of current when illuminating HYL11 with 850nm + 780nm light but the relative loss of current under the same illumination conditions for HYL12

Illumination with two wavelengths of light results in scattering between the generated electrons, equilibrating them to a fermi distribution, which was discussed in section 4.1.4 to occurs on a timescale of 10-100fs [93]. This scattering will result in the population of states below the Schottky barrier height, with more states being filled in this region (as a proportion of the total states filled) when a longer wavelength illumination is used.

For the case of Schottky barrier extraction (HYL12), this results in a reduction in the relative current. However, for the case of tunnelling extraction (HYL11) these carriers can be extracted through the tunnelling resonance and so results in an increase in the relative current. These schematics explain the principle, but are very simplistic, and to understand these effects it is best to imagine the combination of two fermi distributions of different temperatures into a third distribution at an intermediate temperature. The fermi distribution created by a 785nm illumination combines with a fermi distribution created by an 852nm illumination to create a distribution with fewer carriers above the top of the Schottky barrier, but more above the top of the tunnelling resonance.

Taking this experiment to the logical extreme, we illuminated the cells with 1550nm light in addition to 642nm light in order to observe whether any increase in the photo-response is seen when the additional wavelength itself (1550nm) has no photo-response. Figure 5-32 shows that the dark current (black) and current under illumination with 1550nm (red) is identical over the range of voltages at 90K. However, adding illumination at 1550nm to a beam at 642nm shows that an additive photo-response (green dashed line) is observed for the case of HYL11, but not for the case of HYL12.

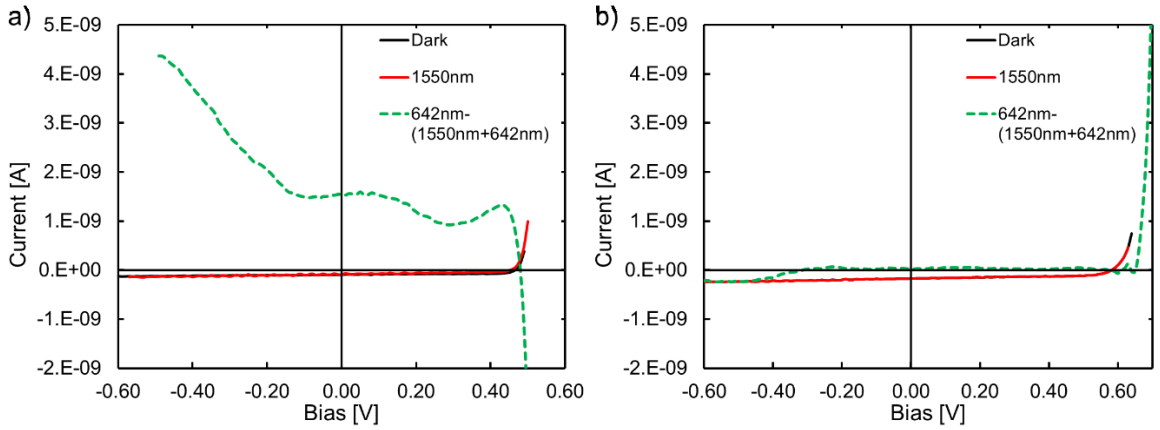

Figure 5-32. IV characteristics at 90K under dark conditions (black) and under 1550nm illumination (red) for HYL11 (a) and HYL12 (b).

This can be understood, as previously, from the addition of a fermi distribution generated by 1550nm light adding to a fermi distribution generated by 642nm light to give a (small) additional current increase through tunnelling for HYL11. The current generated by the additional illumination at 1550nm is around 1% of the magnitude of the current generated by illumination at 642nm For HYL 12 no benefit is seen, and at more negative voltages a small decrease in current is observed.

This dual wavelength work shows an important proof of principle for the concept of the hot carrier metallic cell over the IPE cell, demonstrating that a "sub-band gap" photon can contribute to the photocurrent, as required in a hot carrier cell and forbidden in an IPE cell.

5.6 Summary of metallic solar cells and further work

Four different cells have been presented in this chapter, based on the principle of absorption of light in a metallic layer followed by extraction to a semiconductor region. This work has shown that these cells are absorbing light in the metallic layer, which is heating up the electron distribution and that these heated carriers can be extracted over either a Schottky barrier or through a tunnelling resonance. We have shown the following important features, agreeing with our theoretical work and giving evidence for this mode of operation:

- Higher temperature electrons can be generated by either shorter pulse-widths, higher substrate temperatures, shorter wavelength illumination or more intense illumination. This gives rise to a shallower gradient of the IV characteristic in the reverse bias region.
- Illumination with wavelengths shorter than the band gap energy of the semiconductor region causes these cells to operate as standard Schottky barrier photovoltaic cells, rather than purely metallic cells.
- The cells do not operate as IPE cells, but instead equilibration amongst the electrons is inferred from dual wavelength illumination experiments.

However, due to the inability to obtain PL from a metal and the inaccessibility of transmission measurements on the processed samples, obtaining an independent measurement of the electron temperature has not been possible with the metallic cells, as it was with the semiconductor cells. In this chapter, we used comparisons between the modelled IV characteristics and experimental IV characteristics to demonstrate that hot

carrier operation was consistent with the observations, but it would be useful to have an independent measure of this using a complimentary technique.

One such complimentary technique is using a two dimensional photo-current (2DPC) measurement [125] which can be understood with reference to other multidimensional coherent optical spectroscopic techniques [126]. It measures the photocurrent generated from coherent illumination with four broadband laser pulses of approximately 20fs in duration and separated from each other by between 20fs and 10ps. In varying the separation of the pulses it is possible to observe carrier dynamical properties of the cell.

In collaboration with Carlos Silva and Ella Olejnik at the University of Montreal, this technique has been used on HYL11 to reveal information about the electron dynamics and infer information about the carrier extraction timescales in this structure. The initial results are shown in Figure 5-33, giving some further experimental validation for the proposed extraction mechanisms and their timescales.

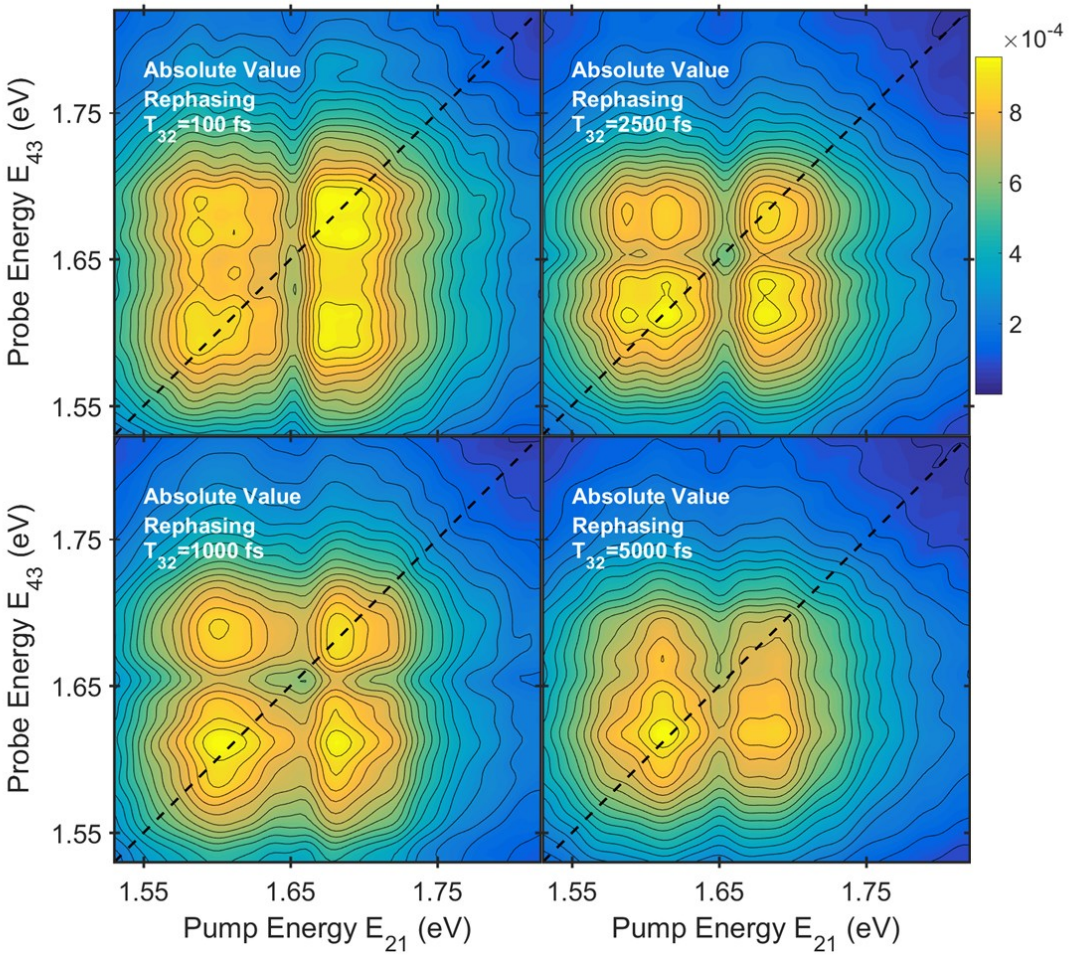

Figure 5-33. Plots of the absolute value of the rephasing signal from two dimensional photocurrent spectroscopy performed on the HYL11 structure for different delay times, T_{32}=100fs, 1000fs, 2500fs and 5000fs

We believe that the vertical reduction of the signal observed at 100fs and 1.65eV is a result of thermionic emission, giving a timescale for this process. Further, the presence of the horizontal reduction at the same energy but at a timescale of 2.5ps gives evidence that tunnelling extraction is occurring on this timescale. The absolute value of the signal and its changing distribution should also give us an indication of the carrier cooling dynamics in this sample.

This work is still at a preliminary stage, but is revealing further interesting properties from these cells. A full comparison of HYL11 and HYL12 using this technique is ongoing and will continue after this PhD to explore the differences between these two cells.

In addition to this future experimental work, further theoretical work to model the dual laser beam experiments has been proposed using a more sophisticated theoretical method (NEGF) [127], which was out of scope for the purposes of this PhD. This method includes self-consistent electron-electron and electron-phonon interactions and would therefore allow precise numerical comparisons between the experimental results and theoretical expectations, to support the qualitative justifications presented in this thesis.

6 CONCLUSIONS AND FUTURE WORK

We have shown the evolution of our concept for a hot carrier solar cell from its theoretical justification through to its experimental realisation in four different conceptual forms:

- Prior to this PhD, and reviewed in chapter 2, we demonstrated an n-i-n contacted hot carrier cell with extraction by resonant tunnelling from a narrow band gap semiconductor to a wider band gap semiconductor. This contacting scheme gave the purest information about the hot carrier extraction properties of this contact, being solely driven by the temperature difference between electrons on either side of a selective contact. However, this design suffered from a limited Voc, due to the fact that this device only operated in the conduction band.
- In chapter 3, we improved upon this initial design with a p-i-n contacted device. This was more complicated to understand, due to its sensitivity to the photogenerated carrier density in the absorber region, but IV and optical characterisation showed its promise as a hot carrier cell. In particular, this device showed the benefit of combining a heat driven current with a field driven current. However, both these semiconductor devices were still limited by the total amount of light that they could absorb, due to the necessity of a thin semiconductor layer to allow extraction of electrons prior to their thermalisation.
- The metallic cell was proposed in chapter 4, allowing a very high absorption (>99%) in a thin film, less than 10nm thick. This could, in principle allow ultrafast extraction of carriers and solve the absorption problem associated with the previously developed semiconductor based cells. This cell extracted carriers over a Schottky barrier between the metallic layer and the semiconductor region, so only

semi-selective operation was possible. This limited the potential maximum efficiency of this device from 85% for a fully selective device to 50-60% for a semi-selective device. Such a cell was realised in three different metal/semiconductor combinations in chapter 5, demonstrating operation by absorbing light in a metallic layer and the extraction of heated electrons.

- To combine the high absorption promised by a metallic layer and the high selectivity provided by resonant tunnelling, the final structure investigated in this project was a metallic cell in which extraction of the electrons from the metallic layer occurred through resonant tunnelling. The cell was shown to operate successfully in chapter 5 and, importantly, it was shown that it operated as a hot carrier cell rather than an IPE cell. We showed that electron equilibration occurs in this cell rather than simply the emission of photo-excited electrons prior to electron-electron interactions, showing that the cell could use wavelengths of light which were nominally "sub-bandgap"

Through these four structural concepts, we have shown that the realisation of a hot carrier cell is possible and shown structures in which this extraction occurs, and methods through which we can observe it.

Hot carrier solar cells have been shown to be a viable option for converting sunlight in to usable electrical energy, however, key limitations are still present, primarily due to materials properties. While we showed that prototype cells can already be realised in a variety of materials, they are still limited by the loss of energy of electrons through thermalisation. However, what we intended to show in this project was that prototype cells could be made, even in these imperfect materials. Given the large body of work that is ongoing, investigating new materials and structures with reduced carrier thermalisation rates [27], [34], [35], [62] and the promise of future materials by inverse design [51], with properties tailored to a devices requirements, the combination of these proposed structures and ever improving materials shows great promise for the future of hot carrier solar cells.

7 REFERENCES

[1] "International Energy Outlook 2016 - Energy Information Administration." [Online]. Available: http://www.eia.gov/forecasts/ieo/. [Accessed: 12-Jul-2016].

[2] "Solar photovoltaics deployment - Publications - GOV.UK." [Online]. Available: https://www.gov.uk/government/statistics/solar-photovoltaics-deployment. [Accessed: 12-Jul-2016].

[3] A. Becquerel, "Mémoire sur les effets électriques produits sous l'influence des rayons solaires," *Comptes Rendus Séances Hebd.*, vol. 9, pp. 561–567, 1839.

[4] L. C. Hirst and N. J. Ekins-Daukes, "Fundamental losses in solar cells," *Prog. Photovolt. Res. Appl.*, vol. 19, no. 3, pp. 286–293, May 2011.

[5] J. Nakamura, N. Asano, T. Hieda, C. Okamoto, H. Katayama, and K. Nakamura, "Development of Heterojunction Back Contact Si Solar Cells," *IEEE J. Photovolt.*, vol. 4, no. 6, pp. 1491–1495, Nov. 2014.

[6] K. Masuko *et al.*, "Achievement of More Than 25% Conversion Efficiency With Crystalline Silicon Heterojunction Solar Cell," *IEEE J. Photovolt.*, vol. 4, no. 6, pp. 1433–1435, Nov. 2014.

[7] E. Yablonovitch, O. D. Miller, and S. R. Kurtz, "The opto-electronic physics that broke the efficiency limit in solar cells," in *2012 38th IEEE Photovoltaic Specialists Conference (PVSC)*, 2012, pp. 001556–001559.

[8] C. A. Gueymard, D. Myers, and K. Emery, "Proposed reference irradiance spectra for solar energy systems testing," *Sol. Energy*, vol. 73, no. 6, pp. 443–467, Dec. 2002.

[9] W. Shockley and H. Quiesser, "Detailed Balance Limit of Efficiency of p-n Junction Solar cells," *J. Appl. Phys.*, vol. 32, no. 3, pp. 510–519, 1961.

[10] T. Markvart and G. H. Bauer, "What is the useful energy of a photon?," *Appl. Phys. Lett.*, vol. 101, no. 19, p. 193901, 2012.

[11] F. Dimroth *et al.*, "Four-Junction Wafer-Bonded Concentrator Solar Cells," *IEEE J. Photovolt.*, vol. 6, no. 1, pp. 343–349, Jan. 2016.

[12] A. Luque and A. Martí, "Increasing the Efficiency of Ideal Solar Cells by Photon Induced Transitions at Intermediate Levels," *Phys. Rev. Lett.*, vol. 78, no. 26, pp. 5014–5017, Jun. 1997.

[13] A. S. Brown and M. A. Green, "Intermediate band solar cell with many bands: Ideal performance," *J. Appl. Phys.*, vol. 94, no. 9, p. 6150, 2003.

[14] M. Yoshida, N. J. Ekins-Daukes, D. J. Farrell, and C. C. Phillips, "Photon ratchet intermediate band solar cells," *Appl. Phys. Lett.*, vol. 100, no. 26, p. 263902, Jun. 2012.

[15] M. C. Beard, A. G. Midgett, M. C. Hanna, J. M. Luther, B. K. Hughes, and A. J. Nozik, "Comparing Multiple Exciton Generation in Quantum Dots To Impact Ionization in Bulk Semiconductors: Implications for Enhancement of Solar Energy Conversion," *Nano Lett.*, vol. 10, no. 8, pp. 3019–3027, Aug. 2010.

[16] A. J. Nozik, M. C. Beard, J. M. Luther, M. Law, R. J. Ellingson, and J. C. Johnson, "Semiconductor Quantum Dots and Quantum Dot Arrays and Applications of Multiple Exciton Generation to Third-Generation Photovoltaic Solar Cells," *Chem. Rev.*, vol. 110, no. 11, pp. 6873–6890, Nov. 2010.

[17] M. C. Beard, J. C. Johnson, J. M. Luther, and A. J. Nozik, "Multiple exciton generation in quantum dots versus singlet fission in molecular chromophores for solar photon conversion," *Phil Trans R Soc A*, vol. 373, no. 2044, p. 20140412, Jun. 2015.

[18] R. M. Swanson, "Proposed Thermophotovoltaic Solar Energy Conversion System," *Proc IEEE U. S.*, vol. 67, pp. 446–447, Mar. 1979.

[19] N.-P. Harder and P. Würfel, "Theoretical limits of thermophotovoltaic solar energy conversion," *Semicond. Sci. Technol.*, vol. 18, no. 5, p. S151, 2003.

[20] R. T. Ross and A. J. Nozik, "Efficiency of hot-carrier solar energy converters," *J. Appl. Phys.*, vol. 53, no. 5, pp. 3813–3818, May 1982.

[21] P. Würfel, "Solar energy conversion with hot electrons from impact ionisation," *Sol. Energy Mater. Sol. Cells*, vol. 46, no. 1, pp. 43–52, 1997.

[22] D. König, Y. Yao, and R. Patterson, "Shortcomings in efficiency modelling of hot carrier solar cells: Considering device concepts and hot carrier absorber materials from a practical viewpoint," *Jpn. J. Appl. Phys.*, vol. 53, no. 5S1, p. 05FV04, May 2014.

[23] A. L. Bris and J.-F. Guillemoles, "Hot carrier solar cells: Achievable efficiency accounting for heat losses in the absorber and through contacts," *Appl. Phys. Lett.*, vol. 97, no. 11, p. 113506, Sep. 2010.

[24] A. Luque and A. Martí, "Electron–phonon energy transfer in hot-carrier solar cells," *Sol. Energy Mater. Sol. Cells*, vol. 94, no. 2, pp. 287–296, Feb. 2010.

[25] Y. Takeda, "Requisites for Highly Efficient Hot-Carrier Solar Cells," in *Quantum Dot Solar Cells*, vol. 15, J. Wu and Z. M. Wang, Eds. New York, NY: Springer New York, 2014, pp. 187–232.

[26] Y. Rosenwaks, M. C. Hanna, D. H. Levi, D. M. Szmyd, R. K. Ahrenkiel, and A. J. Nozik, "Hot-carrier cooling in GaAs: Quantum wells versus bulk," *Phys. Rev. B*, vol. 48, no. 19, pp. 14675–14678, Nov. 1993.

[27] L. C. Hirst, H. Fujii, Y. Wang, M. Sugiyama, and N. J. Ekins-Daukes, "Hot Carriers in Quantum Wells for Photovoltaic Efficiency Enhancement," *IEEE J. Photovolt.*, vol. 4, no. 1, pp. 244–252, Jan. 2014.

[28] J. A. Kash, J. C. Tsang, and J. M. Hvam, "Subpicosecond Time-Resolved Raman Spectroscopy of LO Phonons in GaAs," *Phys. Rev. Lett.*, vol. 54, no. 19, pp. 2151–2154, May 1985.

[29] P. G. Klemens, "Anharmonic Decay of Optical Phonons," *Phys. Rev.*, vol. 148, no. 2, pp. 845–848, Aug. 1966.

[30] K. T. Tsen, R. P. Joshi, D. K. Ferry, and H. Morkoc, "Time-resolved Raman scattering of nonequilibrium LO phonons in GaAs quantum wells," *Phys. Rev. B*, vol. 39, no. 2, pp. 1446–1449, Jan. 1989.

[31] D. von der Linde, J. Kuhl, and H. Klingenberg, "Raman Scattering from Nonequilibrium LO Phonons with Picosecond Resolution," *Phys. Rev. Lett.*, vol. 44, no. 23, pp. 1505–1508, Jun. 1980.

[32] B. K. Ridley, *Electrons and Phonons in Semiconductor Multilayers*. Cambridge University Press, 2009.

[33] S. K. Shrestha *et al.*, "Evaluation of Hafnium Nitride and Zirconium Nitride as Hot Carrier Absorber," in *Proceedings of the 40th IEEE Photovoltaic Specialists Conference*, Denver, CO, 2014.

[34] Y. Zhang *et al.*, "Extended hot carrier lifetimes observed in bulk In0.265±0.02Ga0.735N under high-density photoexcitation," *Appl. Phys. Lett.*, vol. 108, no. 13, p. 131904, Mar. 2016.

[35] A. Le Bris, L. Lombez, S. Laribi, G. Boissier, P. Christol, and J.-F. Guillemoles, "Thermalisation rate study of GaSb-based heterostructures by continuous wave photoluminescence and their potential as hot carrier solar cell absorbers," *Energy Environ. Sci.*, vol. 5, no. 3, p. 6225, 2012.

[36] P. A. Snow, D. J. Westland, J. F. Ryan, T. Kerr, H. Munekata, and L. L. Chang, "Hot carrier cooling in GaSb: Bulk and quantum wells," *Superlattices Microstruct.*, vol. 5, no. 4, pp. 595–598, 1989.

[37] L. C. Hirst, R. J. Walters, M. F. Führer, and N. J. Ekins-Daukes, "Experimental demonstration of hot-carrier photo-current in an InGaAs quantum well solar cell," *Appl. Phys. Lett.*, vol. 104, no. 23, p. 231115, Jun. 2014.

[38] G. J. Conibeer, C.-W. Jiang, D. König, S. Shrestha, T. Walsh, and M. A. Green, "Selective energy contacts for hot carrier solar cells," *Thin Solid Films*, vol. 516, no. 20, pp. 6968–6973, Aug. 2008.

[39] J. A. R. Dimmock, S. Day, K. Smith, J. Heffernan, and M. Kauer, "A Hot Carrier Photovoltaic Cell by Offset Resonant Tunneling," in *Proceedings of the 40th IEEE Photovoltaic Specialists Conference*, Denver, CO, 2014.

[40] J. A. R. Dimmock, S. Day, M. Kauer, K. Smith, and J. Heffernan, "Demonstration of a hot-carrier photovoltaic cell," *Prog. Photovolt. Res. Appl.*, vol. 22, no. 2, pp. 151–160, Feb. 2014.

[41] J. Shah, A. Pinczuk, A. C. Gossard, and W. Wiegmann, "Energy-loss rates for hot electrons and holes in GaAs quantum wells," *Phys. Rev. Lett.*, vol. 54, no. 18, p. 2045, 1985.

[42] F. A. Riddoch and B. K. Ridley, "Electron scattering rates associated with the polar optical phonon interaction in a thin ionic slab," *Phys. BC*, vol. 134, no. 1, pp. 342–346, Nov. 1985.

[43] Y. Imry and R. Landauer, "Conductance viewed as transmission," *Rev. Mod. Phys.*, vol. 71, no. 2, pp. S306–S312, Mar. 1999.

[44] T. P. White and K. R. Catchpole, "Plasmon-enhanced internal photoemission for photovoltaics: Theoretical efficiency limits," *Appl. Phys. Lett.*, vol. 101, no. 7, p. 073905, 2012.

[45] F. D. M. Haldane, "'Luttinger liquid theory' of one-dimensional quantum fluids. I. Properties of the Luttinger model and their extension to the general 1D interacting spinless Fermi gas," *J. Phys. C Solid State Phys.*, vol. 14, no. 19, p. 2585, 1981.

[46] Y. Harada, N. Kasamatsu, D. Watanabe, and T. Kita, "Nanosecond-scale hot-carrier cooling dynamics in one-dimensional quantum dot superlattices," *Phys. Rev. B*, vol. 93, no. 11, Mar. 2016.

[47] P. J. Price, "Theory of resonant tunneling in heterostructures," *Phys. Rev. B*, vol. 38, no. 3, pp. 1994–1998, Jul. 1988.

[48] T. Tada, A. Yamaguchi, T. Ninomiya, H. Uchiki, T. Kobayashi, and T. Yao, "Tunneling process in AlAs/GaAs double quantum wells studied by photoluminescence," *J. Appl. Phys.*, vol. 63, no. 11, pp. 5491–5494, Jun. 1988.

[49] J. Shah, *Ultrafast Spectroscopy of Semiconductors and Semiconductor Nanostructures*. Springer Science & Business Media, 2013.

[50] S. M. Goodnick and P. Lugli, "Effect of electron-electron scattering on nonequilibrium transport in quantum-well systems," *Phys. Rev. B*, vol. 37, no. 5, pp. 2578–2588, Feb. 1988.

[51] L. Yu, R. S. Kokenyesi, D. A. Keszler, and A. Zunger, "Inverse Design of High Absorption Thin-Film Photovoltaic Materials," *Adv. Energy Mater.*, vol. 3, no. 1, pp. 43–48, Jan. 2013.

[52] Z. Vardeny and J. Tauc, "Hot-Carrier Thermalization in Amorphous Silicon," *Phys. Rev. Lett.*, vol. 46, no. 18, pp. 1223–1226, May 1981.

[53] K. G. Kiriluk *et al.*, "Highly efficient charge transfer in nanocrystalline Si:H solar cells," *Appl. Phys. Lett.*, vol. 102, no. 13, p. 133101, Apr. 2013.

[54] A. Bhattacharyya, "Influence of diffusion of hot carriers on collection efficiency of solar cells:a-Si:H," *J. Phys. Appl. Phys.*, vol. 16, no. 2, p. 181, 1983.

[55] J. Shah and R. C. C. Leite, "Radiative recombination from photoexcited hot carriers in GaAs," *Phys. Rev. Lett.*, vol. 22, no. 24, p. 1304, 1969.

[56] R. Ulbrich, "Energy relaxation of photoexcited hot electrons in GaAs," *Phys. Rev. B*, vol. 8, no. 12, p. 5719, 1973.

[57] C. L. Tang and D. J. Erskine, "Femtosecond Relaxation of Photoexcited Nonequilibrium Carriers in Al x Ga 1- x As," *Phys. Rev. Lett.*, vol. 51, no. 9, p. 840, 1983.

[58] D. H. Auston, S. McAfee, C. V. Shank, E. P. Ippen, and O. Teschke, "Picosecond spectroscopy of semiconductors," *Solid-State Electron.*, vol. 21, no. 1, pp. 147–150, 1978.

[59] T. Brazzini *et al.*, "Electroluminescence of hot electrons in AlGaN/GaN high-electron-mobility transistors under radio frequency operation," *Appl. Phys. Lett.*, vol. 106, no. 21, p. 213502, May 2015.

[60] I. Gierz *et al.*, "Snapshots of non-equilibrium Dirac carrier distributions in graphene," *Nat. Mater.*, vol. 12, no. 12, pp. 1119–1124, Dec. 2013.

[61] J. Kanasaki, H. Tanimura, and K. Tanimura, "Imaging Energy-, Momentum-, and Time-Resolved Distributions of Photoinjected Hot Electrons in GaAs," *Phys. Rev. Lett.*, vol. 113, no. 23, p. 237401, Dec. 2014.

[62] J. Tang *et al.*, "Effects of localization on hot carriers in InAs/AlAsxSb1–x quantum wells," *Appl. Phys. Lett.*, vol. 106, no. 6, p. 061902, Feb. 2015.

[63] A. Le Bris, "Étude de faisabilité d'un dispositif photovoltaïque à porteurs chauds," Ecole Centrale Paris, 2011.

[64] L. C. Hirst, "A spectroscopic study of strain-balanced InGaAs/GaAsP quantum well structures as absorber materials for hot carrier solar cells," Imperial College London, 2012.

[65] F. Gibelli, L. Lombez, and J.-F. Guillemoles, "Two carrier temperatures non-equilibrium generalized Planck law for semiconductors," *Phys. B Condens. Matter*, vol. 498, pp. 7–14, Oct. 2016.

[66] H. Mizuta and T. Tanoue, *The Physics and Applications of Resonant Tunnelling Diodes*. Cambridge University Press, 2006.

[67] O. Vanbésien, R. Bouregba, P. Mounaix, and D. Lippens, "Temperature Dependence of Peak to Valley Current Ratio in Resonant Tunneling Double Barriers," in *Resonant Tunneling in Semiconductors*, L. L. Chang, E. E. Mendez, and C. Tejedor, Eds. Springer US, 1991, pp. 107–116.

[68] S. Yagi, Y. Hijikata, Y. Okada, and H. Yaguchi, "Quantum well double barrier resonant tunneling structures for selective contacts of hot carrier solar cells," 2011, pp. 003309–003312.

[69] J. A. R. Dimmock, S. Day, K. Smith, J. Heffernan, and M. Kauer, "Hot Carrier Solar Cells: Efficiency Limits and Realisation," in *Proceedings of the 10th Photovoltaic Science Applications and Technology Conference*, Loughborough, UK, 2014.

[70] L. A. A. Pettersson, L. S. Roman, and O. Inganäs, "Modeling photocurrent action spectra of photovoltaic devices based on organic thin films," *J. Appl. Phys.*, vol. 86, no. 1, p. 487, 1999.

[71] "Synopsys Sentaurus Device," *Synopsys*. [Online]. Available: http://www.synopsys.com/Tools/silicon/tcad/device-simulation/Pages/sentaurus-device.aspx. [Accessed: 04-Nov-2016].

[72] M. Paxman *et al.*, "Modeling the spectral response of the quantum well solar cell," *J. Appl. Phys.*, vol. 74, no. 1, pp. 614–621, Jul. 1993.

[73] R. Tsu and L. Esaki, "Tunneling in a finite superlattice," *Appl. Phys. Lett.*, vol. 22, no. 11, pp. 562–564, Oct. 1973.

[74] J. N. Schulman, "Extension of Tsu-Esaki model for effective mass effects in resonant tunneling," *Appl. Phys. Lett.*, vol. 72, no. 22, pp. 2829–2831, 1998.

[75] M. Cahay, M. McLennan, S. Datta, and M. S. Lundstrom, "Importance of space-charge effects in resonant tunneling devices," *Appl. Phys. Lett.*, vol. 50, no. 10, pp. 612–614, Mar. 1987.

[76] T. B. Boykin, J. P. Van der Wagt, and J. S. Harris Jr, "Tight-binding model for GaAs/AlAs resonant-tunneling diodes," *Phys. Rev. B*, vol. 43, no. 6, p. 4777, 1991.

[77] K. F. Brennan, "Self-consistent analysis of resonant tunneling in a two-barrier–one-well microstructure," *J. Appl. Phys.*, vol. 62, no. 6, pp. 2392–2400, Sep. 1987.

[78] J. A. R. Dimmock, M. Kauer, K. Smith, H. Liu, P. N. Stavrinou, and N. J. Ekins-Daukes, "Optoelectronic characterization of carrier extraction in a hot carrier photovoltaic cell structure," *J. Opt.*, vol. 18, no. 7, p. 074003, Copyright IOP Publishing. Reproduced with permission. All rights reserved 2016.

[79] S. Kettemann and J.-F. Guillemoles, "Thermoelectric field effects in low-dimensional structure solar cells," *Phys. E Low-Dimens. Syst. Nanostructures*, vol. 14, no. 1–2, pp. 101–106, Apr. 2002.

[80] D. Masson, F. Proulx, and S. Fafard, "Pushing the limits of concentrated photovoltaic solar cell tunnel junctions in novel high-efficiency GaAs phototransducers based on a vertical epitaxial heterostructure architecture," *Prog. Photovolt. Res. Appl.*, vol. 23, no. 12, pp. 1687–1696, Dec. 2015.

[81] Y. P. Varshni, "Temperature dependence of the energy gap in semiconductors," *Physica*, vol. 34, no. 1, pp. 149–154, 1967.

[82] "IOFFE Semiconductor Database," *http://www.ioffe.ru/SVA/NSM/Semicond/index.html*. .

[83] E. C. Le Ru, J. Fack, and R. Murray, "Temperature and excitation density dependence of the photoluminescence from annealed InAs/GaAs quantum dots," *Phys. Rev. B*, vol. 67, no. 24, p. 245318, Jun. 2003.

[84] P. Würfel, A. S. Brown, T. E. Humphrey, and M. A. Green, "Particle conservation in the hot-carrier solar cell," *Prog. Photovolt. Res. Appl.*, vol. 13, no. 4, pp. 277–285, Jun. 2005.

[85] J. B. Khurgin, "How to deal with the loss in plasmonics and metamaterials," *Nat. Nanotechnol.*, vol. 10, no. 1, pp. 2–6, 2015.

[86] T. Holstein, "Theory of transport phenomena in an electron-phonon gas," *Ann. Phys.*, vol. 29, no. 3, pp. 410–535, 1964.

[87] T. Holstein, "Optical and Infrared Reflectivity of Metals at Low Temperatures," *Phys. Rev.*, vol. 88, no. 6, pp. 1427–1428, Dec. 1952.

[88] T. Holstein, "Optical and Infrared Volume Absorptivity of Metals," *Phys. Rev.*, vol. 96, no. 2, pp. 535–536, Oct. 1954.

[89] L. W. Bos and D. W. Lynch, "Optical properties of antiferromagnetic chromium and dilute Cr-Mn and Cr-Re alloys," *Phys. Rev. B*, vol. 2, no. 11, p. 4567, 1970.

[90] N. Ahmad, J. Stokes, N. A. Fox, M. Teng, and M. J. Cryan, "Ultra-thin metal films for enhanced solar absorption," *Nano Energy*, 2012.

[91] C. HILSUM, "Infrared Absorption of Thin Metal Films," *J. Opt. Soc. Am.*, vol. 44, no. 3, pp. 188–188, Mar. 1954.

[92] S.-H. Cho *et al.*, "A black metal-dielectric thin film for high-contrast displays," *J. Korean Phys. Soc.*, vol. 55, no. 2, pp. 501–507, 2009.

[93] S. Pawlik, M. Bauer, and M. Aeschlimann, "Lifetime difference of photoexcited electrons between intraband and interband transitions," *Surf. Sci.*, vol. 377, pp. 206–209, 1997.

[94] J. Bardeen and D. Pines, "Electron-Phonon Interaction in Metals," *Phys. Rev.*, vol. 99, no. 4, pp. 1140–1150, Aug. 1955.

[95] W. S. Fann, R. Storz, H. W. K. Tom, and J. Bokor, "Electron thermalization in gold," *Phys. Rev. B*, vol. 46, no. 20, pp. 13592–13595, Nov. 1992.

[96] T. Juhasz, H. E. Elsayed-Ali, G. O. Smith, C. Suárez, and W. E. Bron, "Direct measurements of the transport of nonequilibrium electrons in gold films with different crystal structures," *Phys. Rev. B*, vol. 48, no. 20, pp. 15488–15491, Nov. 1993.

[97] C. Suárez, W. E. Bron, and T. Juhasz, "Dynamics and Transport of Electronic Carriers in Thin Gold Films," *Phys. Rev. Lett.*, vol. 75, no. 24, pp. 4536–4539, Dec. 1995.

[98] H. Hirori, T. Tachizaki, O. Matsuda, and O. B. Wright, "Electron dynamics in chromium probed with 20-fs optical pulses," *Phys. Rev. B*, vol. 68, no. 11, p. 113102, Sep. 2003.

[99] L. Ke, Z. Xin, H. Xinyu, and Z. Peng, "Analysis and design of multilayer Jaumann absorbers," in *2011 IEEE International Conference on Microwave Technology Computational Electromagnetics (ICMTCE)*, 2011, pp. 81–84.

[100] M. A. Lind, "The infrared reflectivity of chromium and chromium-aluminum alloys," 1972.

[101] A. I. Usoskin and I. N. Shklyarevskii, "Optical properties of thin chromium films," *J. Appl. Spectrosc.*, vol. 20, no. 3, pp. 398–399, 1974.

[102] K. a. Repa and D. b. Williams, "Fabrication of a Cr thin-film AEM characterization standard," *J. Microsc.*, vol. 192, no. 1, pp. 1–6, Oct. 1998.

[103] E. H. Rhoderick and R. H. Williams, *Metal-semiconductor contacts*. Clarendon Press, 1988.

[104] J. A. R. Dimmock, M. Kauer, N. J. Ekins-Daukes, and P. N. Stavrinou, "Energy Selective Photodetector," Application 15/269168, 19-Sep-2016.

[105] Y.-J. Chang and K.-H. Shih, "Solar energy conversion via internal photoemission in aluminum, copper, and silver: Band structure effects and theoretical efficiency estimates," *J. Appl. Phys.*, vol. 119, no. 18, p. 183101, May 2016.

[106] A. J. Leenheer, P. Narang, N. S. Lewis, and H. A. Atwater, "Solar energy conversion via hot electron internal photoemission in metallic nanostructures: Efficiency estimates," *J. Appl. Phys.*, vol. 115, no. 13, p. 134301, Apr. 2014.

[107] E. W. McFarland and J. Tang, "A photovoltaic device structure based on internal electron emission," *Nature*, vol. 421, no. 6923, pp. 616–618, 2003.

[108] K. J. Russell *et al.*, "Room-temperature electro-optic up-conversion via internal photoemission," *Appl. Phys. Lett.*, vol. 82, no. 18, p. 2960, 2003.

[109] R. H. Fowler, "The analysis of photoelectric sensitivity curves for clean metals at various temperatures," *Phys. Rev.*, vol. 38, no. 1, p. 45, 1931.

[110] I. Konovalov, V. Emelianov, and R. Linke, "Hot carrier solar cell with semi infinite energy filtering," *Sol. Energy*, vol. 111, pp. 1–9, Jan. 2015.

[111] R. Lake, G. Klimeck, R. C. Bowen, and D. Jovanovic, "Single and multiband modeling of quantum electron transport through layered semiconductor devices," *J. Appl. Phys.*, vol. 81, no. 12, pp. 7845–7869, 1997.

[112] J. P. Sun, G. I. Haddad, P. Mazumder, and J. N. Schulman, "Resonant tunneling diodes: models and properties," *Proc. IEEE*, vol. 86, no. 4, pp. 641–660, 1998.

[113] J. Vancea, G. Reiss, F. Schneider, K. Bauer, and H. Hoffmann, "Substrate effects on the surface topography of evaporated gold films—A scanning tunnelling microscopy investigation," *Surf. Sci.*, vol. 218, pp. 108–126, Aug. 1989.

[114] A. Giugni *et al.*, "Hot-electron nanoscopy using adiabatic compression of surface plasmons," *Nat. Nanotechnol.*, vol. 8, no. 11, pp. 845–852, Oct. 2013.

[115] I. Goykhman, B. Desiatov, J. Khurgin, J. Shappir, and U. Levy, "Waveguide based compact silicon Schottky photodetector with enhanced responsivity in the telecom spectral band," *Opt. Express*, vol. 20, no. 27, pp. 28594–28602, Dec. 2012.

[116] A. Marini, R. Del Sole, and G. Onida, "First-principles calculation of the plasmon resonance and of the reflectance spectrum of silver in the GW approximation," *Phys. Rev. B*, vol. 66, no. 11, p. 115101, Sep. 2002.

[117] E. Colavita, A. Franciosi, C. Mariani, and R. Rosei, "Thermoreflectance test of W, Mo, and paramagnetic Cr band structures," *Phys. Rev. B*, vol. 27, no. 8, pp. 4684–4693, Apr. 1983.

[118] J. A. R. Dimmock, M. Kauer, P. N. Stavrinou, and N. J. Ekins-Daukes, "A metallic hot carrier photovoltaic cell," in *Proc. SPIE 9358, Physics, Simulation, and Photonic Engineering of Photovoltaic Devices IV*, 2015, p. 935810.

[119] R. van de Walle, R. L. Van Meirhaeghe, W. H. Laflère, and F. Cardon, "On the relationship between interfacial defects and Schottky barrier height in Ag, Au, and Al/n-GaAs contacts," *J. Appl. Phys.*, vol. 74, no. 3, p. 1885, 1993.

[120] S. J. Pilkington, M. Missous, and D. A. Woolf, "On the Richardson constant of intimate metal-GaAs (111)B Schottky diodes grown by molecular beam epitaxy," *J. Appl. Phys.*, vol. 74, no. 10, pp. 6256–6260, Nov. 1993.

[121] R. D. Baertsch, "An Ag[Single Bond]GaAs Schottky-Barrier Ultraviolet Detector," *J. Appl. Phys.*, vol. 40, no. 1, p. 229, 1969.

[122] R. Ludeke, T. -C. Chiang, and T. Miller, "Schottky barrier formation of Ag on GaAs(110)," *J. Vac. Sci. Technol. B Microelectron. Nanometer Struct.*, vol. 1, no. 3, pp. 581–587, 1983.

[123] S. Birner, *Modeling of semiconductor nanostructures and semiconductor-electrolyte interfaces*, 1. Aufl. Garching b. München: Verein zur Förderung des Walter Schottky Instituts der Technischen Universität München, 2011.

[124] R. H. M. Groeneveld, R. Sprik, and A. Lagendijk, "Femtosecond spectroscopy of electron-electron and electron-phonon energy relaxation in Ag and Au," *Phys. Rev. B*, vol. 51, no. 17, pp. 11433–11445, May 1995.

[125] A. A. Bakulin, C. Silva, and E. Vella, "Ultrafast Spectroscopy with Photocurrent Detection: Watching Excitonic Optoelectronic Systems at Work," *J. Phys. Chem. Lett.*, vol. 7, no. 2, pp. 250–258, Jan. 2016.

[126] G. Nardin, "Multidimensional coherent optical spectroscopy of semiconductor nanostructures: a review," *Semicond. Sci. Technol.*, vol. 31, no. 2, p. 023001, 2016.

[127] U. Aeberhard and R. H. Morf, "Microscopic nonequilibrium theory of quantum well solar cells," *Phys. Rev. B*, vol. 77, no. 12, p. 125343, Mar. 2008.

[128] P. T. Landsberg and T. Markvart, "The Carnot Factor in Solar-Cell Theory," *Solid-State Electron.*, vol. 42, no. 4, pp. 657–659, Apr. 1998.

[129] L. C. Hirst *et al.*, "Hot-Carriers in InGaAs Quantum Wells: Generation and Extraction," in *Proceedings of the 40th IEEE Photovoltaic Specialists Conference*, Denver, CO, 2014.

[130] X. Luo, C. Li, N. Liu, R. Li, J. He, and T. Qiu, "The impact of energy spectrum width in the energy selective electron low-temperature thermionic heat engine at maximum power," *Phys. Lett. A*, vol. 377, no. 25–27, pp. 1566–1570, Oct. 2013.

[131] M. F. O'Dwyer, T. E. Humphrey, R. A. Lewis, and C. Zhang, "Electronic and thermal transport in hot carrier solar cells with low-dimensional contacts," *Microelectron. J.*, vol. 39, no. 3–4, pp. 656–659, Mar. 2008.

[132] M. Lundstrom, *Fundamentals of Carrier Transport*. Cambridge University Press, 2009.

[133] W. R. Frensley, "Wigner-function model of a resonant-tunneling semiconductor device," *Phys. Rev. B*, vol. 36, no. 3, pp. 1570–1580, Jul. 1987.

8 APPENDICES

APPENDIX 1 DETAILED BALANCE

The detailed balance model [9] is a way to find the highest efficiency for a solar cell assuming only the absolutely necessary radiative recombination, such that in thermal equilibrium no power is produced (because of balance of influx and outflux of photons).

The photon flux from a hot source (at temperature T_h) at a particular energy E is given the symbol $\Gamma(E,T_h)$ (in units of $\#m^{-2}s^{-1}J^{-1}$). This photon flux is absorbed at an absorber subtending some angle θ of the hot source with the absorber at some lower temperature T_c. The absorber then re-radiates some photon flux $\Gamma(E,T_c,V)$ where V is the bias across the cold source. The total power obtainable from such a device is then given by the net current multiplied by the applied voltage, equation A1-1:

$$P = q\left[\int_{E_g}^{\infty}\Gamma(E,T_h)dE - \int_{E_g}^{\infty}\Gamma(E,T_c,V)dE\right].V \tag{A1-1}$$

Where E_g is the energy above which the absorber can absorb (e.g. the band gap for a PV cell). If we model the input spectrum as a black body and the re-radiated energy as a boson gas with chemical potential qV we obtain:

$$P = \frac{q}{\hbar^3 c^2}\left[2\pi\sin^2\theta\int_{E_g}^{\infty}\frac{E^2}{e^{E/k_BT_h}-1}dE - 2\pi\int_{E_g}^{\infty}\frac{E^2}{e^{(E-qV)/k_BT_c}-1}dE\right].V \tag{A1-2}$$

Dividing this by the power input then gives us the efficiency of the system:

$$\eta(E_g,V) = \frac{q\left[2\pi\sin^2\theta\int_{E_g}^{\infty}\frac{E^2}{e^{E/k_BT_h}-1}dE - 2\pi\int_{E_g}^{\infty}\frac{E^2}{e^{(E-qV)/k_BT_c}-1}dE\right].V}{2\pi\sin^2\theta\int_{0}^{\infty}\frac{E^3}{e^{E/k_BT_h}-1}dE} \tag{A1-3}$$

This efficiency is then maximised with respect to V for a given E_g to give the maximum efficiency of a solar cell with a particular band gap (e.g. 31% for a Silicon cell with bandgap 1.12eV).

This basic framework is easily extended to take in to account absorption as a function of wavelength and also other loss mechanisms. We can also input a different spectrum for $\Gamma(E,T_h)$ if e.g. the cell is operating in space.

Würfel [21] and Landsberg and Markvart [128] have further generalised this equation so that the voltage is generated by extracting an electron and hole separated by some energy, which is in excess of the band gap, and modulating this with the temperature of the carriers by a Carnot factor. They propose an optimum voltage for the cell equal to:

$$V = \frac{E_{eh}}{q}\left(1 - \frac{T_a}{T_c}\right) \tag{A2-1}$$

Where E_{eh} is the energy difference between the extraction points for electrons and holes in the cell, in which they are at a temperature T_{hc} and extracted to a region which is at a temperature T_a. Using this value for the voltage in equation A1-3 yields equation A1-4:

$$\eta(E_g, T_c) = \frac{\left[2\pi \sin^2\theta \int_{E_g}^{\infty} \frac{E^3}{e^{E/k_B T_h} - 1} dE - 2\pi \int_{E_g}^{\infty} \frac{E^3}{e^{E/k_B T_c} - 1} dE + \dot{Q}(T_c)\right]\left(1 - \frac{T_a}{T_c}\right)}{2\pi \sin^2\theta \int_0^{\infty} \frac{E^3}{e^{E/k_B T_h} - 1} dE} \tag{A1-4}$$

This gives the efficiency obtainable from hot carriers when the Fermi function for the electrons is at T_c and the surroundings are at T_a. In this case, we maximise for T_c, rather than V, giving an upper bound on the efficiency of a hot carrier solar cell. This is an upper bound, since we are effectively assuming that we can extract all carriers at the exact energies that they are created with no thermalisation loss.

The cooling rate of hot carriers can be taken into account in the "Q" factor present in equation A1-4. This can either be theoretically deduced, as in appendix 3, or experimentally calculated, with the lowest figure experimentally calculated to date being 2.5W/K/m² for an InP Quantum well [129]. For the "optimal" value of efficiency presented in Figure 1-2 we use Q=0, such that no thermalisation occurs.

APPENDIX 2 HEAT FLUX CALCULATION

The Landauer formalism [43] is a method to calculate the particle flux between two reservoirs of particles over a set of allowed energy levels, given a probability for a particle of energy E transferring from one reservoir to another. Using this it can be shown that the net current of carriers moving from a reservoir with an energy distribution f_h to a reservoir with an energy distribution f_c is given by equation (A2-1):

$$I = \frac{2Nq}{h}\int \tau(E).\left(f_h\left(E,\mu_h,T_h\right) - f_c\left(E,\mu_c,T_c\right)\right)dE \qquad \text{(A2-1)}$$

With N representing an areal density of contacts between the two reservoirs, T_h and T_c representing the temperatures of the Fermi distribution of electrons in the hot and cold reservoir respectively, μ_h and μ_c the chemical potential of the hot/cold reservoirs and τ the probability of electron transfer between the reservoirs at a given energy level.

Following the method of Luo et al [130] and O'Dwyer et al [131], we assume energy, but not particle, conservation, balancing the different energy fluxes until a self-consistent solution is found. In this model the transmission probability (τ) for electrons is modelled as a top hat function of width ΔE and height E_{off}. In this way the energy flux from the hot to the cold reservoir is given by equation (A2-2):

$$\dot{Q}_h = \frac{2N}{h}\int_{E_{off}}^{E_{off}+\Delta E}\left(E-\mu_h\right).\left(f_h\left(E\right) - f_c\left(E\right)\right)dE \qquad \text{(A2-2)}$$

With a similar equation for transfer from the cold reservoir to the hot reservoir.

In the calculations in this work N is fixed for a given ΔE and E_{off} in order to maximize efficiency. A value is obtained for the hot carrier temperature (T_h) in f_h by equating $\dot{Q}_h$ to the net solar energy flux into the absorber, taking into account re-radiation from the absorber. In this way a self-consistent hot carrier temperature can be determined. In a similar way the power extractable from the cell is given by equation (A2-3).

$$P = \frac{2N}{h}\int_{E_{off}}^{E_{off}+\Delta E}\left(\mu_c-\mu_h\right).\left(f_h\left(E\right) - f_c\left(E\right)\right)dE \qquad \text{(A2-3)}$$

The bias condition (the difference between μ_h and μ_c) is then incremented in order to maximize the efficiency, with efficiency measured as the power (equation A2-3) divided by the incident solar flux. The incident solar flux is approximated by a blackbody distribution at 6000K, and full angular concentration, and the ambient is fixed at 300K.

APPENDIX 3 ELECTRON-PHONON SCATTERING

Using a similar method to Marti [24] for 3D electron phonon interactions, we extended this work to the 2D case to compare electron cooling rates between 2D and 3D absorbers based on acoustic phonons (so this treatment is only strictly valid for non-polar semiconductors, but gives a good start for comparing the electron cooling rates based only on dimensionality).

Fermi's Golden rule for transitions between energy states is:

$$S(\underline{p},\underline{p}') = \tfrac{2\pi}{\hbar}\left|H_{\underline{p},\underline{p}'}\right|^2 \delta\left(E(\underline{p}) - E(\underline{p}') - \Delta E\right) \tag{A3-1}$$

Where S is the transition rate between states with momentum $\underline{p}$ and $\underline{p}'$ separated by an energy ΔE. $H_{p,p'}$ is the matrix element joining the two states through their interaction via a potential U:

$$H_{\underline{p},\underline{p}'} = \left\langle \psi_{\underline{p}} \middle| \hat{U} \middle| \psi_{\underline{p}'} \right\rangle \tag{A3-2}$$

The perturbing potential is given by:

$$\hat{U} = K_\beta u_\beta \tag{A3-2}$$

Where u_β is a Fourier component of the lattice vibration and K_β is dependent on the interaction type (e.g. $K_\beta = \beta D_A$ for acoustic phonon scattering). $\hbar\beta$ is the phonon momentum throughout.

Evaluating $H_{p,p'}$ for some confined electron states in the z direction (and polar vector $\underline{\rho}$ in the plane) ($\left|\psi_{\underline{p}}\right\rangle = \psi_i(z)\frac{e^{i\underline{p}'_{\parallel}\cdot\frac{\underline{\rho}}{\hbar}}}{\sqrt{A}}$) we have:

$$H_{\underline{p},\underline{p}'} = \int_{-\infty}^{\infty} \psi_f^*(z)\frac{e^{-i\underline{p}'_{\parallel}\cdot\frac{\underline{\rho}}{\hbar}}}{\sqrt{A}}\left(A_\beta K_\beta e^{\pm i\underline{\beta}_{\parallel}\cdot\underline{\rho}} e^{\pm i\beta_z\cdot z}\right)\psi_i(z)\frac{e^{i\underline{p}'_{\parallel}\cdot\frac{\underline{\rho}}{\hbar}}}{\sqrt{A}}dz\,d\underline{\rho} \tag{A3-3}$$

With $\left|A_\beta\right|^2 = \frac{\hbar}{2\rho\Omega\omega_\beta}\left(N_{\omega\beta} + \frac{1}{2} \pm \frac{1}{2}\right)$ the quantum mechanical amplitude of the lattice vibration (with $N_{\omega\beta}$ the Bose-Einstein factor, ρ the crystal density and Ω the crystal volume) from p78 of Lundstrom [132].

The 2D unconfined direction integral (in $\underline{\rho}$) gives momentum conservation (a delta function) yielding:

$$H_{\underline{p},\underline{p}'} = A_\beta K_\beta \delta_{\underline{p}_{\|}',\underline{p}_{\|} \pm \hbar\beta_{\|}} \int_{-\infty}^{\infty} \psi_f^*(z) e^{\pm i\beta_z \cdot z} \psi_i(z) dz \tag{A3-4}$$

Putting this in to the transition rate gives:

$$S^{\pm}(\underline{p},\underline{p}') = \tfrac{2\pi}{\hbar}\left|A_\beta K_\beta \int_{-\infty}^{\infty} \psi_f^*(z) e^{\pm i k_z' \cdot z} \psi_i(z) dz\right|^2 \delta\left(E(\underline{p}) - E(\underline{p}') - \Delta E\right) \tag{A3-5}$$

$$S^{\pm}(\underline{k},\underline{k}') = \tfrac{2\pi}{\hbar}\left|A_\beta K_\beta\right|^2 \int_{-\infty}^{\infty} \psi_f^*(z) e^{\pm i \underline{k}_z' \cdot z} \psi_i(z) dz \int_{-\infty}^{\infty} \psi_f^*(z') e^{\pm i \underline{k}_z' \cdot z'} \psi_i(z') dz' \delta\left(E(\underline{k}) - E(\underline{k}') \pm \hbar\omega\right) \tag{A3-6}$$

The transfer of energy to a state $\underline{k}$ ($W(\underline{k})$) is then given by integrating this transfer rate over all states $\underline{k}$' to which and from which energy can be transferred to/from state $\underline{k}$ (multiplied by the amount of energy transferred ($n\hbar\omega$) and the occupation numbers of initial and final states $f(\underline{k})$:

$$W(\underline{k}) = \frac{2}{8\pi^3}\hbar\omega \left\{ \begin{array}{l} \int \left[S^-(\underline{k},\underline{k}') n f(\underline{k})(1 - f(\underline{k}')) - S^-(\underline{k},\underline{k}')(n+1) f(\underline{k}')(1 - f(\underline{k}))\right] d^3\underline{k}' - \\ \int \left[S^+(\underline{k},\underline{k}')(n+1) f(\underline{k})(1 - f(\underline{k}')) - S^+(\underline{k},\underline{k}') n f(\underline{k}')(1 - f(\underline{k}))\right] d^3\underline{k}' \end{array} \right\} \tag{A3-7}$$

We can perform the dk'_z integral of the $d^3\underline{k}'$ integral to simplify the z integral in $S^{\pm}(\underline{k},\underline{k}')$:

$$\int S^{\pm}(\underline{k},\underline{k}') dk_z = \tfrac{2\pi}{\hbar}\left|A_\beta K_\beta\right|^2 \int_{-\infty}^{\infty} \psi_f^*(z) \psi_i(z) dz \int_{-\infty}^{\infty} \psi_f^*(z') \psi_i(z') dz' \int_{-\infty}^{\infty} e^{\pm i k_z' \cdot (z - z')} dk_z \delta\left(E(\underline{k}) - E(\underline{k}') \pm \hbar\omega\right) \tag{A3-8}$$

$$\int S^{\pm}(\underline{k},\underline{k}') dk_z = \tfrac{4\pi^2}{\hbar}\left|A_\beta K_\beta\right|^2 \int_{-\infty}^{\infty} \psi_f^*(z) \psi_i(z) dz \int_{-\infty}^{\infty} \psi_f^*(z') \psi_i(z') dz' \delta\left(z - z'\right) \delta\left(E(\underline{k}) - E(\underline{k}') \pm \hbar\omega\right) \tag{A3-9}$$

$$\int S^{\pm}(\underline{k},\underline{k}') dk_z = \tfrac{4\pi^2}{\hbar}\left|A_\beta K_\beta\right|^2 \int_{-\infty}^{\infty} \left|\psi_f(z)\right|^2 \left|\psi_i(z)\right|^2 dz \delta\left(E(\underline{k}) - E(\underline{k}') \pm \hbar\omega\right) \tag{A3-10}$$

Now using sinusoidal functions in z for the confined electrons we have:

$$\int S^{\pm}(\underline{k},\underline{k}')dk_z = \tfrac{4\pi^2}{\hbar}\left|A_\beta K_\beta\right|^2 \frac{(2+\delta_{if})}{2w} dz\,\delta\left(E(\underline{k}) - E(\underline{k}') \pm \hbar\omega\right) \tag{A3-11}$$

with w as the well width and δ_{if} as the Kronecker delta for initial and final subbands (=1 for intra-subband scattering, =0 for inter-subband scattering).

Evaluating for acoustic phonon scattering: approximating $N_{\omega\beta} = \frac{k_B T}{\hbar\omega_\beta}$ in A_β and using $D_i = D_A\beta$ we obtain:

$$W(\underline{k}) = \frac{2\pi}{\hbar}\frac{2}{4\pi^2}\frac{D_i^2 k_B T_a (2+\delta_{if})}{4\rho\omega^2\Omega}\hbar\omega\begin{Bmatrix}\int\left[nf(\underline{k})(1-f(\underline{k}')) - (n+1)f(\underline{k}')(1-f(\underline{k}))\right]\delta\left(E(\underline{k}) - E(\underline{k}') - \hbar\omega\right)d^2\underline{k}' - \\ \int\left[(n+1)f(\underline{k})(1-f(\underline{k}')) - nf(\underline{k}')(1-f(\underline{k}))\right]\delta\left(E(\underline{k}) - E(\underline{k}') + \hbar\omega\right)d^2\underline{k}'\end{Bmatrix} \tag{A3-12}$$

Transferring to an energy integral, assuming parabolic bands, and applying the delta function energy conservation to remove the integral yields:

$$W(\underline{k}) = \frac{D_i^2 k_B T_a m_e (2+\delta_{fi})}{2\hbar^3\rho\omega^2 w}\begin{Bmatrix}\hbar\omega nf(E)(1-f(E+\hbar\omega) - \hbar\omega(n+1)f(E+\hbar\omega)(1-f(E) \\ -\hbar\omega(n+1)f(E)(1-f(E-\hbar\omega) + \hbar\omega nf(E-\hbar\omega)(1-f(E)\end{Bmatrix} \tag{A3-13}$$

Integrating over all $\underline{k}$ and multiplying by the number of degenerate valleys (Z) between which scattering takes place we then have the following for the cooling rate:

$$\dot{Q} = Z(Z-1)\frac{D_i^2 k_B T_a m_e^2 (2+\delta_{fi})\Omega}{2\pi\hbar^3\rho w^2(\hbar\omega)}\begin{Bmatrix}n\int f(E)(1-f(E+\hbar\omega)dE - (n+1)\int f(E+\hbar\omega)(1-f(E)dE \\ -(n+1)\int f(E)(1-f(E-\hbar\omega)dE + n\int f(E-\hbar\omega)(1-f(E)dE\end{Bmatrix} \tag{A3-13}$$

In this it must be stressed that the Fermi function (f) is at some (hot) electron temperature T_c while the lattice, and thus the Bose-Einstein factor (n), is at some cooler temperature T_a. To calculate efficiencies this cooling rate is then used in a detailed balance model, as in appendix 1.

The comparable rate for 3D interactions (as derived in Marti's work [24]) is:

$$\dot{Q} = Z(Z-1)\tfrac{D_i^2 k_B T_a m_e^2 \Omega}{\pi^3\hbar^5\rho(\hbar\omega)}\left[\int\sqrt{E}\sqrt{E+\hbar\omega}\left(n.f(E).(1-f(E+\hbar\omega) - (n+1).f(E+\hbar\omega).(1-f(E)\right)dE - \int\sqrt{E}\sqrt{E-\hbar\omega}\left((n+1).f(E).(1-f(E-\hbar\omega) - n.f(E-\hbar\omega).(1-f(E)\right)dE\right] \tag{A3-13}$$

The extra square root dependence on energy in the 3D form arises as a result of the difference in the density of states, which is larger for a 3D system than for a 2D system.

The density of states in 3D is:

$$g_c^{3D}(\mathrm{E}) = \frac{8\pi\sqrt{2}m^{*3/2}}{h^3}\sqrt{E - E_c} \tag{A3-14}$$

While the density of states in 2D (divided by the well width to maintain comparable units of $cm^{-3}eV^{-1}$) is:

$$g_c^{2D}(E) = \frac{4\pi m^*}{wh^2}\sum_n \Theta(E - E_n) \tag{A3-15}$$

Where Θ is the Heaviside unit step function.

Graphically represented in Figure 8-1 the difference in density of states is clear.

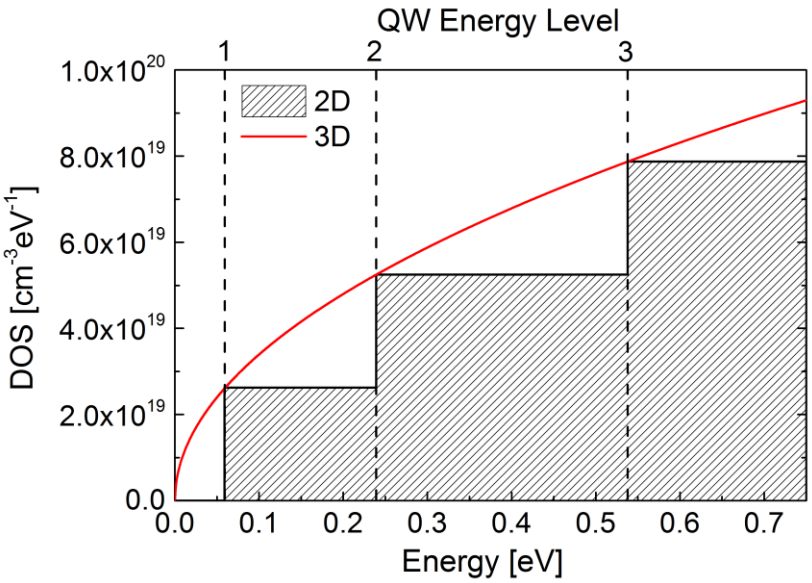

Figure 8-1. A comparison of the density of states for a 10nm quantum well compared with a 3D system.

Integrating both these density of states over energy to the bottom of a certain quantum well sub band (N) gives a volumetric density of states below a certain energy:

3D $$g_c^{3D} = \frac{8\pi\sqrt{2}m^{*3/2}}{h^3}\int_0^{\frac{N^2h^2}{8m^*w^2}}\sqrt{E}dE = \frac{\pi N^3}{3w^2} \tag{A3-16}$$

2D $$g_c^{2D} = \frac{4\pi m^*}{wh^2}\sum_1^N\sum_n \Theta(E - E_n) = \frac{\pi N}{12w^2}(4N + 1).(N - 1) \tag{A3-17}$$

Dividing the 2D case by the 3D case gives the fractional comparison between the integrated DOS in 3D with that in 2D (equation A3-18):

$$\frac{g_c^{2D}}{g_c^{3D}} = \frac{(4N+1).(N-1)}{4N^2} \qquad \text{(A3-18)}$$

N in this case is the highest sub-band of the well which can be filled by illumination with an incident light source $\left[N = \sqrt{\frac{8m^*c}{h\lambda}}w\right]$, so increasing *N* in this equation can either be viewed as making the well wider or illuminating with a shorter wavelength of light.

So as N→∞ (shorter wavelengths or wider wells) the difference between the scattering rates should disappear as the cumulative density of states in 2D and 3D is identical, but as N→0 (longer wavelengths and narrow wells) a difference in the scattering rates should be apparent due to the large difference in the cumulative density of states.

APPENDIX 4 ELECTRON-ELECTRON SCATTERING

For electron thermalisation we verified claims in the literature that "it turns out that the restriction of motion to one dimension completely eliminates any effect of the interaction, at least to lowest order" [p. 236 [32]]. This was verified by a quantum field theoretical analysis of the strongly interacting electron gas. The 2-body interaction Hamiltonian of electrons via a coulomb potential can be written as:

$$\hat{H} = \hat{H}^0 + \hat{V}_{coul} = \hat{H}^0 + \frac{1}{2}\int d\underline{x}\int d\underline{x}'\sum_{\sigma,\sigma'} c_\sigma^+(\underline{x})c_{\sigma'}^+(\underline{x}')\frac{e^2}{|\underline{x}-\underline{x}'|}c_{\sigma'}(\underline{x}')c_\sigma(\underline{x}) \tag{A4-1}$$

Where $\hat{H}^0$ is the non-interacting Hamiltonian for electrons in a lattice potential V_{latt}:

$$\hat{H}^0 = \int d\underline{x}\sum_\sigma c_\sigma^+(\underline{x})\left[\frac{\hat{p}^2}{2m} + V_{latt}(x)\right]c_\sigma(\underline{x}) \tag{A4-2}$$

With the standard quantum field theory notation of $\hat{p} = -i\hbar\nabla$, $c_\sigma^+(\underline{x})$ creating an electron of spin σ at x (and $c_\sigma(\underline{x})$ annihilating it) and the anti-commutation relation for spinful fermion (electron) states as $\left[c_\sigma(\underline{x}), c_{\sigma'}^+(\underline{x}')\right]_+ = \delta(\underline{x}-\underline{x}')\delta_{\sigma\sigma'}$.

For free electron like states (a good approximation for energetic conduction band electrons) the lattice potential tends to zero and we write the electron states in the Fourier basis $\left[c_\sigma^+(\underline{x}) = \frac{1}{\sqrt{V}}\sum_k c_{\sigma k}^+ e^{i\underline{k}\cdot\underline{x}}\right]$ giving the interaction potential of.

$$\hat{V}_{coul} = \frac{1}{2}\frac{1}{V^2}\int d\underline{x}\int d\underline{x}'\sum_{\sigma,\sigma',\underline{k}_1,\underline{k}_2,\underline{k}_3,\underline{k}_4} c_{\sigma,\underline{k}_1}^+ c_{\sigma',\underline{k}_2}^+ c_{\sigma',\underline{k}_3} c_{\sigma,\underline{k}_4}\frac{e^2}{|\underline{x}-\underline{x}'|}e^{-i.(\underline{k}_1-\underline{k}_4)\cdot\underline{x}}e^{-i.(\underline{k}_2-\underline{k}_3)\cdot\underline{x}'} \tag{A4-3}$$

Transforming to a centre of mass coordinate system $\underline{x} = \bar{\underline{x}} + \frac{\Delta x}{2}$ and $\underline{x}' = \bar{\underline{x}} - \frac{\Delta x}{2}$ gives us:

$$\hat{V}_{coul} = \frac{1}{2}\frac{1}{V^2}\int d\underline{\Delta x}\int d\bar{\underline{x}}\sum_{\sigma,\sigma',\underline{k}_1,\underline{k}_2,\underline{k}_3,\underline{k}_4} c_{\sigma,\underline{k}_1}^+ c_{\sigma',\underline{k}_2}^+ c_{\sigma',\underline{k}_3} c_{\sigma,\underline{k}_4}\frac{e^2}{|\underline{\Delta x}|}e^{-i.(\underline{k}_1-\underline{k}_4+\underline{k}_2-\underline{k}_3)\cdot\bar{\underline{x}}}e^{-i.(\underline{k}_1-\underline{k}_4-\underline{k}_2+\underline{k}_3)\cdot\underline{\Delta x}} \tag{A4-4}$$

Performing the $\underline{\bar{x}}$ integration delivers a delta function providing momentum conservation:

$$\hat{V}_{coul} = \frac{1}{2}\frac{1}{V}\int d\underline{\Delta x} \sum_{\sigma,\sigma',\underline{k}_1,\underline{k}_2,\underline{k}_3,\underline{k}_4} c^{+}_{\sigma,\underline{k}_1} c^{+}_{\sigma',\underline{k}_2} c_{\sigma',\underline{k}_3} c_{\sigma,\underline{k}_4} \delta_{\underline{k}_1+\underline{k}_2,\underline{k}_3+\underline{k}_4} \frac{e^2}{|\underline{\Delta x}|} e^{-i.(\underline{k}_1-\underline{k}_4-\underline{k}_2+\underline{k}_3)\cdot\underline{\Delta x}} \tag{A4-5}$$

Which yields the two body interaction potential of:

$$\hat{V}_{coul} = \frac{1}{2} \sum_{\sigma,\sigma',\underline{k}_1,\underline{k}_2,\underline{k}_3} c^{+}_{\sigma,\underline{k}_1} c^{+}_{\sigma',\underline{k}_2} c_{\sigma',\underline{k}_3} c_{\sigma,\underline{k}_1+\underline{k}_2-\underline{k}_3} \frac{1}{V}\int d\underline{\Delta x} \frac{e^2}{|\underline{\Delta x}|} e^{-i.2(\underline{k}_2-\underline{k}_3)\cdot\underline{\Delta x}} \tag{A4-6}$$

This is a Fourier transform integral and depends on the dimensionality of $\underline{x}$, this was evaluated in 1D, 2D and 3D to give:

$$\hat{V}^{3D}_{coul} = \frac{1}{2V} \sum_{\sigma,\sigma',\underline{k}_1,\underline{k}_2,\underline{Q}} c^{+}_{\sigma,\underline{k}_1+\underline{Q}} c^{+}_{\sigma',\underline{k}_2-\underline{Q}} c_{\sigma',\underline{k}_1} c_{\sigma,\underline{k}_2} \frac{\pi e^2}{Q^2} \tag{A4-7}$$

$$\hat{V}^{2D}_{coul} = \frac{1}{2V} \sum_{\sigma,\sigma',\underline{k}_1,\underline{k}_2,\underline{Q}} c^{+}_{\sigma,\underline{k}_1+\underline{Q}} c^{+}_{\sigma',\underline{k}_2-\underline{Q}} c_{\sigma',\underline{k}_1} c_{\sigma,\underline{k}_2} \frac{\pi e^2}{Q} \tag{A4-8}$$

$$\hat{V}^{1D}_{coul} = \frac{e^2}{2V} \sum_{\sigma,\sigma',\underline{k}_1,\underline{k}_2} c^{+}_{\sigma,\underline{k}_1} c^{+}_{\sigma',\underline{k}_2} c_{\sigma',\underline{k}_1} c_{\sigma,\underline{k}_2} \tag{A4-9}$$

(N.B V is implicitly a "volume" with the same dimensions as $\underline{x}$ [due to the Fourier expansion], so in 1D it is L, in 2D it is L^2 and in 3D it is L^3, this treatment has been carried out in "natural units" such that $\varepsilon_0 = 1$). Where Q is the momentum exchange occurring in this scattering interaction.

This scattering potential can be pictorially represented as the following scattering diagrams, Figure 8-2, with time running vertically upwards:

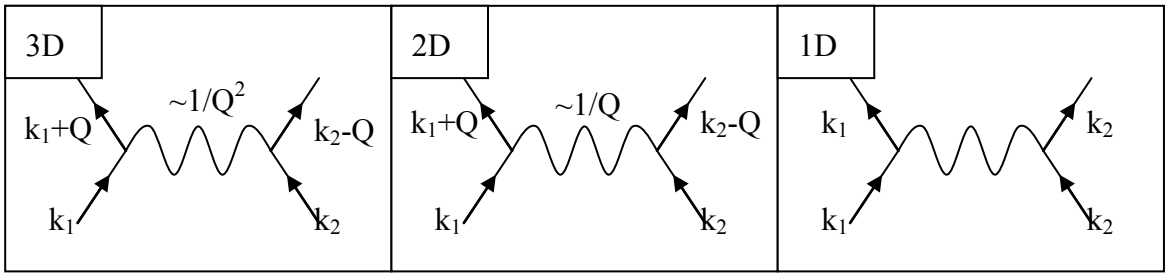

Figure 8-2. Scattering diagrams for electron-electron interactions in 3D, 2D and 1D

In 3D and 2D the electrons can scatter off each other and exchange momentum via a 1/Q or 1/Q² potential respectively. However, because the Fourier integral in 1D is imaginary for all

values $k_2 \neq k_3$ this results in a scattering potential that cannot result in a momentum exchange between incident electrons. This verifies the statement that momentum exchange between electrons cannot occur in a truly 1D electron system.

This can also be understood from an intuitive perspective by imagining the collision of billiard balls. A head on collision results in the velocities of two balls switching (equivalent to 1D interaction); whereas after a glancing collision the subsequent velocities depend on the angle of collision (equivalent to a 2D interaction).

APPENDIX 5 TMM

To calculate the expected absorption and reflection in a thin-film multi-layer stack a transfer matrix method (TMM) model was written in FORTRAN, following the work of Petterson et al [70] to calculate the absorption in each layer. It follows the scattering matrix approach in their work, allowing the electric field at the input side to be related to that at the substrate side through a series of matrices representing transfers from adjacent layers. With the photogeneration rate linked to the electric field (E_j) by equation A5-2, equating the energy dissipated at a location ($Q_j(x)$) through the imaginary part of the refractive index with an exciton generation rate ($G_j(x)$):

$$Q_j(x) = \frac{1}{2} c\varepsilon_0 \alpha_j(\lambda) n_j(\lambda) \left|E_j(x)\right|^2 \quad \text{(A5-1)}$$

$$G_j(x) = \frac{Q_j(x)\lambda}{hc} = \frac{1}{\hbar} \varepsilon_0 k_j(\lambda) n_j(\lambda) \left|E_j(x)\right|^2 \quad \text{(A5-2)}$$

where the subscript j is a material layer index, and the other symbols as conventional.

The following code is for a module with a subroutine to calculate the electric field profile through a multilayer stack for a given illumination wavelength. The subroutine in this module was called from various other programs to enable e.g. illumination with a broadband spectral source or for the output generation profile to feed in to a Poisson-Schrödinger solver to examine the illuminated IV characteristics of a structure (appendix 6).

```
module TMMmono

implicit none

!this module calculates the Electric field through a multilayer semiconductor stack using a transfer
matrix method

!GLOBAL VARIABLES

!double precision kind-set
integer, parameter :: dp=kind(1.0d0)! find the kind of a high precision variable, by finding the kind of
1.0d0

! Constants
complex(kind=dp), parameter :: i = (0.0d0,1.0d0) ! setting the imaginary unit as i
real(kind=dp), parameter:: h = 6.626d-34 ! planck [Js]
real(kind=dp), parameter :: c = 2.998d8 ! speed of light [m/s]
real(kind=dp), parameter :: pi = 3.14159265359d0

! input variables
integer, parameter :: dx = 1 !dx discretization of lengthscale (nm)

contains
  subroutine TMM(no_of_layers,thickness,nk_in,wavelength,power,x_points_size,x_points,El,Gen,Ref_Tot)

  !LOCAL VARIABLES
```

```
  ! read in variables for subroutine
  integer :: no_of_layers
  real(kind=dp), dimension(no_of_layers) :: thickness !layer thicknesses
  real(kind=dp), dimension(no_of_layers,200,3) :: nk_in
  real(kind=dp) :: wavelength ! wavelength to calculate electric field [nm]
  real(kind=dp) :: Power ! input intesnity of light mW/cm^2

  ! input variables
  real(kind=dp), dimension(no_of_layers) :: cumul_thickness
  complex(kind=dp), dimension(no_of_layers) :: n !refractive index

  ! evaluation parameters
  integer :: x_points_size !allocates the x_points dimension
  real(kind=dp), dimension(x_points_size) :: x_points ! discrete mesh for E-Field calculation
  real(kind=dp) :: x !position in each layer to calculate the E-field
  integer :: loop !generic loop integer
  integer :: mloop !loop integer for looping through materials
  integer :: xloop !loop integer for looping through meshpoints
  real(kind=dp) :: Trans_Top !incoherent transmission through the top layer
  real(kind=dp) :: Refl_Top !incoherent reflection from the top layer
  real(kind=dp) :: Ref !reflection from multilayer region
  real(kind=dp) :: Tra !Transmission
  complex(kind=dp) :: xi !2*pi*n/lamda for each layer (for the propagation matrix)
  integer ::res !specifies the array index at which we find the wavelength

  !Plotting Parameters
  real(kind=dp) :: Ref_Tot !total reflection from device (incoherent + coherent)
  complex(kind=dp), dimension(x_points_size) :: El !Electric field
  real(kind=dp), dimension(x_points_size) :: Gen ! Exciton Generation rate

  !Working Transfer Matrices
  complex(kind=dp),dimension(2,2) :: S ! system transfer matrix
  complex(kind=dp),dimension(2,2) :: I_mat ! layer transfer matrix
  complex(kind=dp),dimension(2,2) :: L_mat ! layer propagation matrix
  complex(kind=dp),dimension(2,2) :: S_1 ! system transfer matrix for the left hand side of a chosen
layer
  complex(kind=dp),dimension(2,2) :: S_2 ! system transfer matrix for the rhs of a chosen layer

!set refractive index for the given layer and wavelength
 res = minloc(nk_in(1,:,1),DIM=1,MASK = nk_in(1,:,1) .EQ. wavelength)
 do loop=1,no_of_layers
   n(loop) = CMPLX(nk_in(loop,res,2),nk_in(loop,res,3))
 end do

  cumul_thickness(1)=0.0d0
  do mloop=2,no_of_layers
    cumul_thickness(mloop)=cumul_thickness(mloop-1)+thickness(mloop)
  end do

  ! set-up discrete mesh for E-Field calculation
  x_points(1) = dx/2.0d0
  do loop=2,x_points_size
    x_points(loop) = x_points(loop-1)+dx
  end do

  !transmission and reflection from very top surface (air/thick layer interface)
  Trans_Top = abs(4.0d0*n(1)/(1.0d0+n(1))**2.0d0)
  Refl_Top = abs((1.0d0-n(1))/(1.0d0+n(1)))**2.0d0

  !incoherent transmission and reflection at the first interface
  I_mat(1,1)=0.5d0*(1.0d0+n(2)/n(1)); I_mat(1,2)=0.5d0*(1.0d0-n(2)/n(1))
  I_mat(2,1)=0.5d0*(1.0d0-n(2)/n(1)); I_mat(2,2)=0.5d0*(1.0d0+n(2)/n(1))
  S=I_mat

  do mloop=2,(no_of_layers-1)
    I_mat(1,1)=0.5d0*(1.0d0+n(mloop+1)/n(mloop)); I_mat(1,2)=0.5d0*(1.0d0-n(mloop+1)/n(mloop))
    I_mat(2,1)=0.5d0*(1.0d0-n(mloop+1)/n(mloop)); I_mat(2,2)=0.5*(1.0d0+n(mloop+1)/n(mloop))
    xi = 2.0d0*pi*n(mloop)/wavelength
    L_mat(1,1)= exp(-i*xi*thickness(mloop)) ; L_mat(1,2)= 0.0d0
    L_mat(2,1)= 0.0d0; L_mat(2,2)= exp(i*xi*thickness(mloop))
    S=matmul(S,matmul(L_mat,I_mat))
  end do

  Ref = abs(S(2,1)/S(1,1))**2 !reflection from multilayer stack
  Tra = abs(2.0d0/(1.0d0+n(1)))/sqrt(1.0d0-Refl_Top*Ref) !transmission into multilayer stack

  !calculate transfer matrices either side of each "active region" to generate the electric field
profile: JAP,86:487 (Eq 12,13)
  do loop=2,no_of_layers
    I_mat(1,1)=0.5d0*(1.0d0+n(2)/n(1)); I_mat(1,2)=0.5d0*(1.0d0-n(2)/n(1))
    I_mat(2,1)=0.5d0*(1.0d0-n(2)/n(1)); I_mat(2,2)=0.5d0*(1.0d0+n(2)/n(1))
    S_1=I_mat

    do mloop=3,loop
      I_mat(1,1)=0.5d0*(1.0d0+n(mloop)/n(mloop-1)); I_mat(1,2)=0.5d0*(1.0d0-n(mloop)/n(mloop-1))
      I_mat(2,1)=0.5d0*(1.0d0-n(mloop)/n(mloop-1)); I_mat(2,2)=0.5d0*(1.0d0+n(mloop)/n(mloop-1))
      xi = 2.0d0*pi*n(mloop-1)/wavelength
      L_mat(1,1)= exp(-i*xi*thickness(mloop-1)) ; L_mat(1,2)= 0.0d0
      L_mat(2,1)= 0.0d0; L_mat(2,2)= exp(i*xi*thickness(mloop-1))
```

```
      S_1=matmul(S_1,matmul(L_mat,I_mat))
    end do

    S_2(1,1) = 1.0d0 ; S_2(1,2) = 0.0d0
    S_2(2,1) = 0.0d0 ; S_2(2,2) = 1.0d0

    do mloop=loop,no_of_layers-1
      I_mat(1,1)=0.5d0*(1.0d0+n(mloop+1)/n(mloop)); I_mat(1,2)=0.5d0*(1.0d0-n(mloop+1)/n(mloop))
      I_mat(2,1)=0.5d0*(1.0d0-n(mloop+1)/n(mloop)); I_mat(2,2)=0.5d0*(1.0d0+n(mloop+1)/n(mloop))
      xi = 2.0d0*pi*n(mloop+1)/wavelength
      L_mat(1,1)= exp(-i*xi*thickness(mloop+1)) ; L_mat(1,2)= 0.0d0
      L_mat(2,1)= 0.0d0; L_mat(2,2)= exp(i*xi*thickness(mloop+1))

      S_2=matmul(S_2,matmul(I_mat,L_mat))
    end do

    xi = 2.0d0*pi*n(loop)/wavelength

    !calculate the total observed reflection from the device (incoherent + coherent)
    Ref_Tot = Refl_Top + Trans_Top**2*Ref/(1-Refl_Top*Ref) !full formula if top surface is incoherent

    !calculate the electric field and the exciton generation rate: JAP,86:487 (Eq 22)
    do xloop = INT(cumul_thickness(loop-1)/dx+1),INT(cumul_thickness(loop)/dx)
      x=xloop-(cumul_thickness(loop-1)/dx)
      El(xloop)=Tra*(S_2(1,1)*exp(-i*xi*(thickness(loop)-x))+S_2(2,1)*exp(i*xi*(thickness(loop)-x))) / &
      (S_1(1,1)*S_2(1,1)*exp(-i*xi*thickness(loop))+S_1(1,2)*S_2(2,1)*exp(i*xi*thickness(loop)))
      x=x+dx
      Gen(xloop)=pi*AIMAG(n(loop))*REAL(n(loop))*Power*abs(El(xloop)**2)/(h*c*2.5d4)
    end do

  end do
  end subroutine TMM
end module TMMmono
```

APPENDIX 6 SCHRÖDINGER-POISSON

The discretised Schrödinger equation approach that we have used to solve the current-voltage characteristics of heterostructures is functionally equivalent to (and based upon) the Wigner-function method described by Frensley [133], but is perhaps more intuitive since it remains in terms of the electron wavefunction and Schrödinger equation rather than the density matrix and the Liouville equation. We also include self-consistency with charge density in the structure, through the Poisson equation, which is not included in the former work. A grid is set up to describe the potential, wavefunction and hence electron density in the growth direction, as illustrated in Figure 8-3.

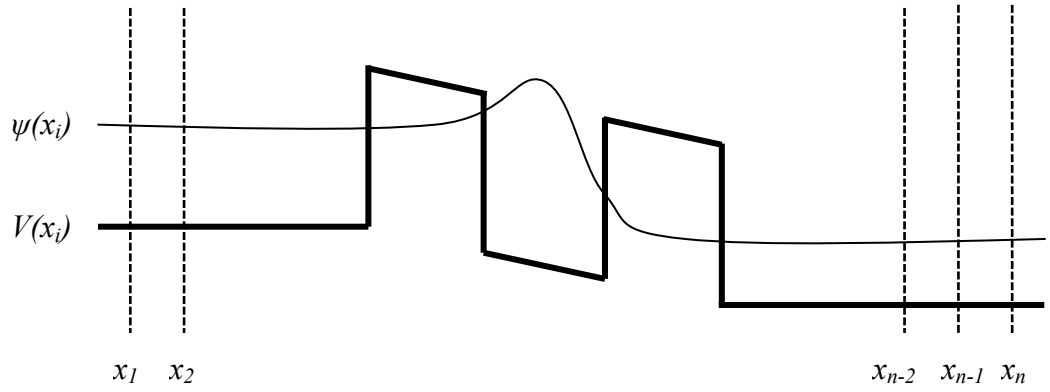

Figure 8-3. A schematic of the grid set up for the Poisson-Schrödinger solver

We assume carrier transport is only in the conduction band and use an effective mass approximation. Our starting point is to spatially discretise the stationary Schrödinger equation A6-1 (with "*x*" the growth direction, i.e. perpendicular to the layer structure of the device):

$$-\frac{\hbar^2}{2m^*}\frac{\partial^2\psi(x)}{\partial x^2}+V(x)\psi(x)=E\psi(x) \tag{A6-1}$$

$$\psi(x_{i+1})=\left\{\frac{2m^*(\Delta x)^2}{\hbar^2}(V(x_i)-E)+2\right\}\psi(x_i)-\psi(x_{i-1}) \tag{A6-2}$$

Equation A6-2 can be broken down further if there are differences in effective mass between the layers. The potential V has contributions from the potential due to band offsets (V_{bi}) and also from electron interactions (V_e), such that V= V_{bi}+V_e. The band offset

potential is fixed for each bias, whereas the electron interaction potential is solved self-consistently in the Poisson equation as well (later in the program).

Equation A6-2 now allows a known wavefunction at points x_i and x_{i-1} to the point x_{i+1}. The integer "i" runs from 1 (denoting the left hand boundary) to nx, the total number of points into which we have discretised the domain, with the discretisation length Δx. The discretisation length should be approximately equal to the distance between atoms. This bound is imposed as otherwise it allows for arbitrarily large kinetic energy terms ($\sim 1/\Delta x^2$) without a concomitantly large potential term, which is fixed and averaged over lattice points due to the effective mass approximation.

In order to form an "initial guess" at the form of the wavefunction to feed into this iterative formula we use a plane wave, since this is the correct solution at the boundary of the system in the absence of a potential. Other solutions were tried, such as sinusoidal functions and treating the system as closed, however the plane wave solutions allow us to model the system as open and calculate current in a more intuitive way. In this way the limiting form of the wavefunction is given by:

$$\psi(x_i) = Ae^{ik_x x} + Be^{-ik_x x} \lim x \longrightarrow 0 \tag{A6-3}$$

$$\psi(x_i) = Ce^{ik_x x} + De^{-ik_x x} \lim x \longrightarrow \infty \tag{A6-4}$$

Working in k-space we now split the propagation of electrons up into two directions, $k_j>0$ is electrons travelling from left to right in Figure 8-3 and $k_j<0$ is electrons travelling from right to left.

For electrons with $k_j<0$, we set the reference potential as the right hand boundary [i.e. $V_r(x)=V(x)-V(x_{nx})$] and set initial travelling wave solutions at the left hand boundary:

$$x = 0, A = 0, B = 1 \rightarrow \psi(x_1, k_j) = e^{-i.k_0.0} = 1 \tag{A6-5}$$

$$x = x_2, A = 0, B = 1 \rightarrow \psi(x_2, k_j) = e^{-i.k_0.dx} \tag{A6-6}$$

We start at the exit contact (left hand boundary) and work backwards, since we know that for electrons starting at x_{nx} and travelling left ($k_j<0$) the term at the exit contact with $k_j>0$ must be zero (A=0), however the reflection term ($Ce^{ik_x x}$) is non zero and unknown at the start of the simulation.

k_0 is the exit electron wave-vector, defined by the difference in potential between the left and right boundaries and the energy of the electron with wave-vector k_j at the input side:

$$k_0 = \sqrt{2 \cdot m_1 \cdot \left(E(k_j) - V_r(x_1)\right)} \Big/ \hbar \tag{A6-7}$$

$$E(k_j) = \frac{\hbar^2 k_j^2}{2m_2} \tag{A6-8}$$

These initial conditions $\psi(x_1, k_j)$ and $\psi(x_2, k_j)$ are then fed into equation A6-2 to iterate them through the structure to give a first guess for $\psi(x_i, k_j)$. Once $\psi(x_i, k_j)$ is calculated over all x_i the wavefunction is normalised at the right hand contact region, since we now have D relative to B. This process is repeated for all k_j <0 to build up the wavefunction over x for each k_j. Similarly for for electrons with k_j <0, we set the reference potential as the right hand boundary [i.e. $V_r(x)=V(x)-V(x_{nx})$] and set initial travelling wave solutions at the left hand boundary.

The potential energy (V_e) in the Schrödinger equation is then calculated self-consistently from the potential ($\Phi = -qV_e$) in a discretised Poisson equation:

$$-\nabla.(\varepsilon(x)\nabla\phi(x)) = \rho(x) \tag{A6-9}$$

Whereupon discretising again gives:

$$\left(\varepsilon(x_i) + \frac{\varepsilon(x_{i+1}) - \varepsilon(x_{i-1})}{4}\right)\phi(x_{i+1}) - 2.\varepsilon(x_i).\phi(x_i) + \left(\varepsilon(x_i) + \frac{\varepsilon(x_{i+1}) - \varepsilon(x_{i-1})}{4}\right)\phi(x_{i-1}) = q\Delta x^2(N(x_i) - n(x_i)) \tag{A6-10}$$

Where $\varepsilon(x_i)$ is the relative permittivity of layer i, $\Phi(x_i)$ is the potential, $N(x)$ is the fixed charge and $n(x_i)$ is the electron density. The electron density at each Δx slice is calculated from the wavefunction and the Fermi function in the contacts (L for contact at ground, R for contact at biased potential):

$$n(x_i) = \sum_k |\psi_k(x_i)|^2 \left[f_k^L - f_k^R\right] \tag{A6-11}$$

Assuming that the relative permittivities of the media are equal, Equation A6-10 can be specified as a matrix equation and simplified by inversion at the start of the program:

$$-\begin{bmatrix} 1 & 0 & 0 & 0 & 0 \\ 1 & -2 & 1 & 0 & 0 \\ 0 & \ddots & \ddots & \ddots & 0 \\ 0 & 0 & 1 & -2 & 1 \\ 0 & 0 & 0 & 0 & 1 \end{bmatrix} \begin{bmatrix} \varepsilon(x_1)\phi(x_1) \\ \varepsilon(x_2)\phi(x_2) \\ \dots \\ \varepsilon(x_{nx-1})\phi(x_{nx-1}) \\ \varepsilon(x_{nx})\phi(x_{nx}) \end{bmatrix} = q(N(x_i) - n(x_i)) \tag{A6-12}$$

In the case where the relative permittivities are not equal we can instead solve by guassian elimination. The '1' entry in the top left and bottom right of this matrix allows us to fix the correct boundary conditions on the potential, generally that $\Phi(x_0)=0$ and $\Phi(x_n)=-V_{applied}/q$.

We iterate these equations until the potential profile does not change by more than a threshold amount between iterations. This is shown schematically below in Figure 8-4.

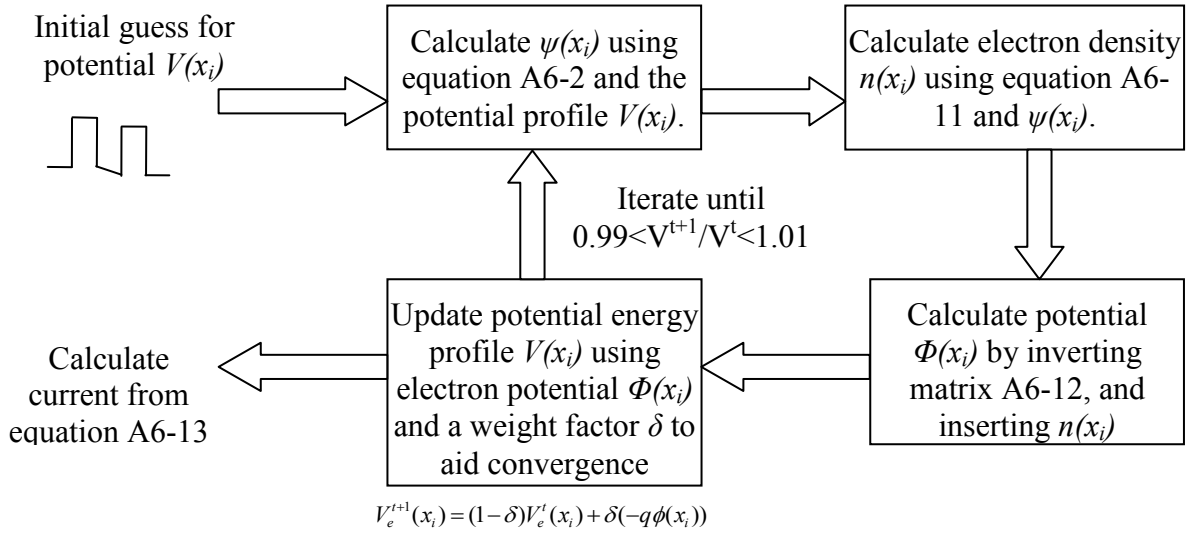

Figure 8-4. A schematic illustration of the discretised Schrödinger based program to calculate the current and electron distribution self-consistently

The current is calculated from the quantum mechanical particle flux derived from the wave-function, as given by equation A6-13:

$$I(x_i) = \frac{q\hbar}{m^*} \sum_k \mathrm{Im}(\psi_k^*(x_i)\nabla\psi_k(x_i)).(f_k^L - f_k^R) \tag{A6-13}$$

The current and the electron density are dependent on a three dimensional summation over k vectors. To speed computation this was simplified (see Appendix 7) by analytically integrating over heated Fermi distributions for y and z dependence (perpendicular to the growth direction) since the dispersion is taken to be parabolic in these directions. Leaving a

one-dimensional numerical summation in k_x for the program to give the electron density and current density:

$$n(x_i) = \sum_{k_x} A_{k_x} \left| \psi_{k_x}(x_i) \right|^2 \tag{A6-14}$$

$$J = \frac{q\hbar}{m_R} \sum_{k_x} A_{k_x} \operatorname{Im}(\psi_k^*(x_i) \nabla \psi_k(x_i)) \tag{A6-15}$$

$$A_{k_x} = \frac{m_R k_B T \Delta k_x}{\pi \hbar^2} \ln\left[\left(\frac{1 + e^{(E_{fL} - E_x - eV)/k_B T_1}}{1 + e^{(E_{fL} - \alpha E_x - eV)/k_B T_1}} \right)^{T_1/T_2} \cdot \left(\frac{1 + e^{(E_{fR} - \alpha E_x)/k_B T_2}}{1 + e^{(E_{fR} - E_x)/k_B T_2}} \right) \right] \tag{A6-16}$$

Where m_R is the absorber region electron mass and m_L is the electron mass in the emitter region, Δk_x is the discretisation in k_x, E_x is the x component of electron energy and $\alpha = \frac{m_R}{m_R - m_L}$.

A derivation for A_{kx} for the case where the fermi distributions in each contact are generally of different temperature and with a different electron mass is given in appendix 7.

APPENDIX 7 ESAKI-TSU TRANSMISSION

In equation A6-13 it was stated that the current is calculated from the quantum mechanical particle flux derived from the wave-function, repeated as equation A7-1:

$$I(x_i) = \frac{q\hbar}{m^*} \sum_k \mathrm{Im}(\psi_k^*(x_i) \nabla \psi_k(x_i)).(f_k^L - f_k^R) \tag{A7-1}$$

This equation involves a 3D summation over k vectors which would be very time consuming to compute numerically. Instead in this work we assume that the y and z directions (the unconfined directions) have a parabolic dependence of energy on momentum and can therefore be analytically integrated over. This approach follows the work of Esaki and Tsu [73] to calculate the current through a heterostructure, this has previously been expanded to take into account different effective masses [74], but here we extend it further to take into account different electron temperatures and fermi energies.

Equation A7-1 can be transformed into an integral in cylindrical polar coordinates, owing to the symmetry of the y,z plane, with x the confinement direction. The integral in A7-2 now gives a current density (J) travelling in the x direction because of the density of states factors in the summation→integral conversion $\left[\sum_k f_k = \frac{L^2}{(2\pi)^2} \iint f(k) dk\right]$:

$$J(x) = 2q \int_0^\infty \frac{dE_x}{2\pi\hbar} \mathrm{Im}(\psi^*(E_x) \nabla \psi(E_x)). \int_0^\infty \frac{2\pi k_\parallel dk_\parallel}{(2\pi)^2} \left[f^L(k_\parallel, E_x, V) - f^R(k_\parallel, E_x, 0)\right] \tag{A7-2}$$

The integral over (E_x) will remain, since this is the confined direction, but the integral over the parallel direction ($k_{||}$) is carried out analytically, depending on the exact nature of f. The two functions of f, for the left and right hand regions, have dependencies on the parallel wavevector($k_{||}$), the confined direction energy (E_x) and also on the applied voltage (V). In the first instance we assume these are fermi functions of electrons with temperatures T_L,T_R, fermi energies E_{fL}, E_{fR}, and masses m_L, m_R, which has the form given in equation A7-3.

$$f^L(k_\parallel, E_x, V) = \frac{1}{1 + e^{\left(E_x + \frac{\hbar^2 k_\parallel^2}{2m_L} - E_{fL} + eV\right) \Big/ k_B T_L}} \tag{A7-3}$$

The different masses on either side of an offset tunnelling region are a necessity, in order to conserve momentum for a change in energy relative to the band minimum. I.e. $m_R > m_L$ so that carriers that have a high energy relative to the conduction band energy in the absorber region can have a lower energy relative to the conduction band in the collector region and still conserve momentum and energy. These different masses result in a limit on the k|| integration to conserve momentum and energy, as schematically shown in Figure 8-5.

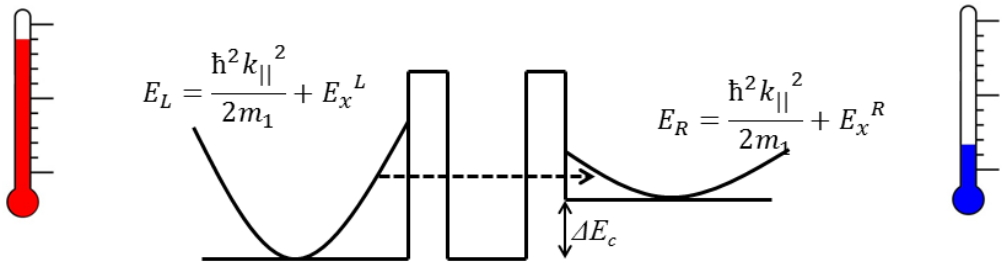

Figure 8-5. The energy of an electron on the right (R) and left (L) of an offset tunnelling region, with the confinement direction in *x*.

Conserving energy and momentum for this system requires that a maximum value of $k_{||}$ is dependent on E_R, such that:

$$k_{\parallel}^{\max} = \sqrt{\frac{2E_R}{\hbar^2}\left(\frac{1}{m_L} - \frac{1}{m_R}\right)^{-1}} \tag{A7-4}$$

And the integral should be taken from the bottom of the conduction band of the Right hand region.

With the definitions and simplifications of:

$$T(E_x) = \mathrm{Im}(\psi^*(E_x)\nabla\psi(E_x)) \tag{A7-5}$$

$$\alpha = \frac{m_R}{m_R - m_L} \tag{A7-6}$$

And taking the left hand region to be heated ($T_1 > T_2$) A7-2 can be readily integrated to give:

$$J = \frac{qm_R k_B T_2}{2\pi\hbar^3}\int_0^{\infty} dE_x T(E_x).\ln\left[\left(\frac{1+e^{(E_{fL}-E_x-eV)/k_B T_1}}{1+e^{(E_{fL}-\alpha E_x-eV)/k_B T_1}}\right)^{T_1/T_2}.\left(\frac{1+e^{(E_{fR}-\alpha E_x)/k_B T_2}}{1+e^{(E_{fR}-E_x)/k_B T_2}}\right)\right] \tag{A7-7}$$

This integral in E_x can now be turned back into a summation over k_x to be solved computationally:

$$J = \frac{q\hbar}{m_R}\sum_{k_x} A_{k_x}\ \mathrm{Im}(\psi_k^*(x_i)\nabla\psi_k(x_i)) \tag{A7-8}$$

With A_{kx} given by:

$$A_{k_x} = \frac{m_R k_B T \Delta k_x}{\pi\hbar^2}\ln\left[\left(\frac{1+e^{(E_{fL}-E_x-eV)/k_BT_1}}{1+e^{(E_{fL}-\alpha E_x-eV)/k_BT_1}}\right)^{T_1/T_2}\cdot\left(\frac{1+e^{(E_{fR}-\alpha E_x)/k_BT_2}}{1+e^{(E_{fR}-E_x)/k_BT_2}}\right)\right] \tag{A7-9}$$

The benefit of writing it in this way is that if we wish to model a different electron distribution the same summation can be used, but with a different A_{kx}. For example, with a ballistic electron distribution represented by a Gaussian distribution with width ΔE and positioned at some energy E_Γ, we would have the following A_{kx}.

$$A_{k_x} = \frac{m_R \Delta E \Delta k_x}{2\sqrt{\pi}\hbar^2}\,ERFC\left(\frac{E_x - E_\Gamma}{\Delta E}\right) \tag{A7-10}$$

This would be the case directly after laser illumination if the tunnelling (extraction) rate were faster than the electron-electron interaction.

9 REPUBLICATION PERMISSIONS

APS - FANN

Permission to republish the gold thermalisation graph from [95] as Figure 4-1.

18/11/2016 RightsLink Printable License

AMERICAN PHYSICAL SOCIETY LICENSE TERMS AND CONDITIONS

Nov 18, 2016

This Agreement between James Dimmock ("You") and American Physical Society ("American Physical Society") consists of your license details and the terms and conditions provided by American Physical Society and Copyright Clearance Center.

License Number	3991820386538
License date	Nov 18, 2016
Licensed Content Publisher	American Physical Society
Licensed Content Publication	Physical Review B
Licensed Content Title	Electron thermalization in gold
Licensed Content Author	W. S. Fann et al.
Licensed Content Date	Nov 15, 1992
Licensed Content Volume Number	46
Type of Use	Thesis/Dissertation
Requestor type	Student
Format	Print, Electronic
Portion	chart/graph/table/figure
Number of charts/graphs/tables/figures	1
Portion description	FIG. 1
Rights for	Main product
Duration of use	Life of Current Edition
Creation of copies for the disabled	no
With minor editing privileges	no
For distribution to	Worldwide
In the following language(s)	Original language of publication
With incidental promotional use	no
The lifetime unit quantity of new product	0 to 499
The requesting person/organization is:	James Palles-Dimmock
Order reference number	
Title of your thesis / dissertation	Realisation of a hot carrier photovoltaic cell
Expected completion date	Dec 2016
Expected size (number of pages)	190
Requestor Location	James Dimmock Sharp Labs Europe Ltd Edmund Halley Road Oxford, OX4 4GB

APS - ROSENWAKS

Permission to republish the electron cooling graph from [26] as Figure 1-8.

18/11/2016 RightsLink Printable License

AMERICAN PHYSICAL SOCIETY LICENSE TERMS AND CONDITIONS

Nov 18, 2016

This Agreement between James Dimmock ("You") and American Physical Society ("American Physical Society") consists of your license details and the terms and conditions provided by American Physical Society and Copyright Clearance Center.

License Number	3991830348621
License date	Nov 18, 2016
Licensed Content Publisher	American Physical Society
Licensed Content Publication	Physical Review B
Licensed Content Title	Hot-carrier cooling in GaAs: Quantum wells versus bulk
Licensed Content Author	Y. Rosenwaks et al.
Licensed Content Date	Nov 15, 1993
Licensed Content Volume Number	48
Type of Use	Thesis/Dissertation
Requestor type	Student
Format	Print, Electronic
Portion	chart/graph/table/figure
Number of charts/graphs/tables/figures	1
Portion description	FIG. 2
Rights for	Main product
Duration of use	Life of Current Edition
Creation of copies for the disabled	no
With minor editing privileges	no
For distribution to	Worldwide
In the following language(s)	Original language of publication
With incidental promotional use	no
The lifetime unit quantity of new product	0 to 499
The requesting person/organization is:	James Palles-Dimmock
Order reference number	
Title of your thesis / dissertation	Realisation of a hot carrier photovoltaic cell
Expected completion date	Dec 2016
Expected size (number of pages)	190
Requestor Location	James Dimmock Sharp Labs Europe Ltd Edmund Halley Road Oxford, OX4 4GB

IEEE - YAGI

Permission to republish the IV characteristic from [68] as Figure 2-2.

IOP - DIMMOCK

Permission to republish parts my first author publication [78] - into chapter 3. http://dx.doi.org/10.1088/2040-8978/18/7/074003

James Dimmock

From: Kathryn Shaw <Kathryn.Shaw@iop.org> on behalf of Permissions <permissions@iop.org>
Sent: 22 November 2016 10:19
To: James Dimmock
Subject: Re: Reuse of article for a thesis

Dear James Dimmock,

Thank you for your email and for taking the time to seek this permission.

Regarding:

James A R Dimmock et al 2016 J. Opt. 18 074003

When you transferred the copyright in your article to IOP, we granted back to you certain rights, including the right to include the Final Published Version of the article within any thesis or dissertation. Please note you may need to obtain separate permission for any third party content you included within your article.

Please include citation details, "© IOP Publishing. Reproduced with permission. All rights reserved" and for online use, a link to the Version of Record.

The only restriction is that if, at a later date, your thesis were to be published commercially, further permission would be required.

Please let me know if you have any further questions.

In the meantime, I wish you the best of luck with the completion of your dissertation.

Kind regards,

Kathryn Shaw

Copyright & Permissions Team
Gemma Alaway – Rights & Permissions Adviser
Kathryn Shaw - Editorial Assistant

Contact Details
E-mail: permissions@iop.org

For further information: http://iopscience.iop.org/page/copyright

Please see our Author Rights Policy http://ioppublishing.org/author-rights/

Please note: We do not provide signed permission forms as a separate attachment. Please print this email and provide it to your institution as proof of permission.

Please note: Any statements made by IOP Publishing to the effect that authors do not need to get permission to use any content are not intended to constitute any sort of legal advice. Authors must make their own decisions as to the suitability of the content they are using and whether they require permission for it to be published within their article.